UNIVERSITY COLLEGE LONDON

DOCTORAL THESIS

Inductive Links for Biomedical Wireless Power and Data Telemetry: Circuits and Methods

---

Author:
Matthew James SCHORMANS

Supervisors:
Prof. Andreas DEMOSTHENOUS
Dr. Virgilio VALENTE

A thesis submitted in partial fulfilment of the requirements
for the degree of Doctor of Philosophy

in the

Sensors, Circuits, and Systems Group
Department of Electronic and Electrical Engineering

September 2, 2019

Declaration of Authorship

I, Matthew James SCHORMANS, declare that this thesis titled, “Inductive Links for Biomedical Wireless Power and Data Telemetry: Circuits and Methods” and the work presented within are my own. I confirm that:

- Where I have consulted the published work of others, this is always clearly attributed.
- Where I have quoted from the work of others, the source is always given. With the exception of such quotations, this thesis is entirely my own work.

Signed:

Date:

“*The main problem [with Spice] is that people tend to trust its answers, as they trust most computers, long after the reason to trust it should have evaporated. I have come very close to fist fights and screaming contests when a person claims that such-and-such an answer is obviously right because Spice gave it to him.*”

Bob Pease

“*Digital? Every idiot can count to one!*”

Bob Widlar

Abstract

Inductive Links for Biomedical Wireless Power and Data Telemetry: Circuits and Methods

Implantable medical devices (IMDs) have been a subject of much commercial and academic interest and research since their inception in the form of the first pacemakers. Over time they have been developed to perform a wide range of functions, including neurostimulation, pressure sensing, and neural recording, to name a few. A key building block of IMDs is telemetry; they must have some way to receive power from, and communicate with, the outside world. One of the most common methods of providing this telemetry is through an inductive link. While inductive telemetry has existed in some form since the inception of IMDs, it is still a subject of research today; there is increasing pressure to design links that are more power efficient, more resilient, and that can carry more data.

This thesis contributes developments to the field of inductive link based telemetry for IMDs in the form of analyses and methods, as well as circuit and system designs. Firstly, the theory behind inductive links is extensively discussed and built upon, in order to provide a series of simple methods that can be used for inductive link design. A free software tool, the Coupled Coil Configurator (CuCCo) was produced to accompany the analyses, and aid in the design of inductive links. Secondly, a system was developed for tracking the optimum frequency of an inductive link, for use in powering passive implants. This system was fabricated and tested, and found to greatly improve the resilience of the link against coupling variations when overcoupled. Third, a methodology and system were developed together to allow a remote capacitive sensor to be easily interrogated through an inductive link. A proof-of-concept device was fabricated in 180 nm CMOS, and was found to agree well with the theory when measured, with a low power consumption. Fourth, the principles of stagger tuning for inductive links were investigated, and a dual-purpose power and data link was constructed using stagger-tuning. This approach was confirmed to greatly reduce the sensitivity of the link to coupling variations, as well as improving its performance when transferring data. Finally, a novel impulse-based system for data transfer via an inductive link was developed, allowing for high-speed low-power data transfer, without the need for carriers or local oscillators. This system was fabricated using 0.35 µm CMOS, and confirmed to achieve data transfer at up to 52 Mbps, with a power consumption of 8.11 pJ/b.

Impact Statement

The potential impact of the research presented in this thesis can be summarized as follows.

1. The work has directly led to the publication of several journal and conference publications. These publications directly add to the academic body of knowledge in the field of inductive link design and implementation for biomedical telemetry.
2. One of these publications is in the form of a tutorial [1], with accompanying software [2]. These both have the potential to greatly aid students new to the field of short range inductive telemetry. The software in particular could also be of use to businesses wishing to design products making use of inductive telemetry.
3. The novel circuit designs presented in this thesis have the potential to greatly impact both academia and industry, as they push the state of the art in the field, and can inform new research and development. Particularly in the case of the design of resilient, effective inductive power links; low-power, high-speed data links; as well as novel, direct-sensing methods employing inductive links.
4. The work has potential for impact in commercial implantable medical device designs, examples include implanted sensors wishing to employ compact interrogation systems, and neural recording implants wishing to transfer data at high rates. Applications are not limited to the medical field; the techniques and circuits could be readily applied to consumer electronics wishing to employ wireless power transfer, or efficient high-data rate data transfer.

Acknowledgements

Firstly, I must thank and acknowledge the Engineering and Physical Sciences Research Council (EPSRC) for funding my endeavours. Also I give thanks to the i-sense project[1], for additional funding used in chip fabrication. Without this support, none of my work would have gotten off the ground.

Second, I would like to thank Prof Andreas Demosthenous, for providing me with this opportunity, and fighting my corner when nobody else would. You have been a consistent guide, mentor, and friend to me for many years, and have endured far more nonsense from me than anyone should have to. For this I will always be grateful.

Third, I would like to thank Dr Virgilio Valente, for being a constant source of inspiration, guidance, and friendship throughout all these years. Without your help and companionship, I'm not sure where I would have ended up. You will always have my gratitude.

Fourth, I would like to thank Dr Dai Jiang; you have always been willing to lend a hand and offer advice. Without your assistance with all things digital, I'm sure things would have been a lot more painful along the way.

I would also like to thank the good people of the analogue and biomedical electronics group, the time we spent in the 7th and 10th floor offices has been overall a very positive experience.

My family and friends outside of UCL also are very deserving of thanks. In particular to my long suffering parents, thank you for everything; from putting up with me at home, to proofreading my work, you have always been there for me.

Finally, I extend my most heartfelt thanks to Meixuezi Tong. From the time I met you to the time of writing, you have brightened my life immeasurably, and made the second half of my PhD journey more joyful than I could have imagined.

There are certainly others deserving of thanks that I have neglected to mention through my own absent-mindedness, for this I apologize.

---

[1] `https://www.i-sense.org.uk`

Contents

Declaration of Authorship **iii**

Abstract **v**

Acknowledgements **vii**

1 Introduction **1**

- 1.1 IMDs and Inductive Telemetry 1
- 1.2 Challenges for Modern IMD Telemetry 5
- 1.3 Novel Contributions and Publications 7
  - 1.3.1 Publications 8
- 1.4 Thesis Summary 9

2 Coupled Inductors for IMDs: Theory and Practice **11**

- 2.1 Principles 12
- 2.2 Link Design 14
  - 2.2.1 Coil Modelling 15
    - Inductance 16
    - Series Loss 17
    - Litz Wire 20
    - Parasitic Capacitance 21
  - 2.2.2 Link Modelling 22
    - Mutual Inductance 22
    - Link Impedance 24
    - Gain 25
    - PDL and PTE 27
  - 2.2.3 Limitations of Analytic Modelling 28
- 2.3 Considerations for Power Transfer 28
  - 2.3.1 Frequency Splitting 29
  - 2.3.2 Maximizing the kQ Product 32
  - 2.3.3 Displacement Resilience 34
  - 2.3.4 Resonant Topologies: Which one to Use? 35
  - 2.3.5 Quality Factor Degradation (Q-loading) 36
  - 2.3.6 Refining Targets 37
- 2.4 Software and Design Example 38
  - 2.4.1 Design Example: Cochlear Implant 39

Constraints and Calculations 39
Experimental Validation 41
2.5 Concluding Remarks 43

3 Optimum Frequency Tracking for Power Transfer to Passive Implants 45
3.1 Introduction and Context 45
3.2 Frequency Splitting in Passive Implants 46
3.3 System Design 49
3.3.1 Integrated Class-D Power Amplifier 50
3.3.2 Phase and Lock Detection 50
3.3.3 Microcontroller Behaviour 52
3.3.4 Coil Design and Implementation 53
3.4 Measured Results 54
3.4.1 Test Procedure 54
3.4.2 Link Measurements 54
3.4.3 Realtime results 56
3.5 Concluding Remarks 57

4 A Self-Oscillator for Remote Capacitive Sensing 59
4.1 Context: Interrogating Remote Sensing Capacitors 59
4.2 Direct Inductive Sensing 61
4.2.1 The Phase-Dip Method 61
4.2.2 An Exact Method 62
4.2.3 Self-Oscillation 66
4.2.4 Link Coupling 68
4.2.5 Active Mode 68
4.2.6 Passive Mode 71
4.2.7 Errors due to coupling variations 71
4.2.8 Series Losses 72
4.3 System Design 74
4.3.1 Oscillator Circuit 74
4.3.2 Round Robin Sensing 76
4.3.3 Humidity Sensing Capacitors 78
4.4 Measured Results 79
4.4.1 Reduced Coupling 82
4.4.2 Power Consumption 83
4.5 Conclusion 83
4.6 Addendum: Application to Power Transfer 85

5 Power and Data Transfer using Stagger Tuning and PPSK 87
5.1 Data Transfer for IMDs 87
5.1.1 Shared Link Solutions 87
5.1.2 Dedicated Link Solutions 89

5.2 Problem Definition: NEUWalk 90
5.3 Passive Phase Shift Keying 92
5.4 Stagger Tuning for Power and Data Transfer 94
5.5 Link Design and Gain Measurements 95
5.6 AM Demodulator 97
5.7 Data Transfer Testing 98
5.8 Discussion and Conclusions 99

6 Shortrange Quality-Factor Modulation (SQuirM) 101

6.1 Existing Techniques 102
6.2 Theory 104
  6.2.1 Fundamentals 104
    PHM 104
    SQuirM 106
6.3 Transmitter and Receiver Circuit 108
  6.3.1 Transmitter Details 108
  6.3.2 Receiver Details 112
  6.3.3 Charge Injection When Damping 114
  6.3.4 Regulatory Considerations 115
6.4 Chip Measurements 115
  6.4.1 Experimental Setup 115
  6.4.2 Power Consumption 117
  6.4.3 Bit Error Rate and Resilience 118
6.5 Discussion and Conclusions 121
6.6 Addendum: Impulse-Driven Clock Generation 122
  6.6.1 Theory 122
  6.6.2 Circuit Details 123

7 Closing Discussion, Conclusions, and Future Work 127

7.1 Future Work and Outlook 129
  7.1.1 Further Coil Modelling 129
  7.1.2 Self-oscillating drivers for power transfer 130
  7.1.3 Improvements to SQuirM and Other Applications 130

A Useful Formulae for Link Design 133

A.1 Cumulative H-field Calculation 133
A.2 Table of Reference 134

B CuCCo: The Coupled Coil Configurator 137

B.1 Features 137
B.2 Function Descriptions 137
  B.2.1 Coil Object Definitions 137
  B.2.2 Link Parameter Functions 139

Bibliography **145**

List of Figures

1.1 Elmqvist's pacemaker, with visible recharging coil. Reproduced with permission.[2] . . . 2
1.2 The Chardack-Greatbatch pacemaker, (A) front and (B) side view. Reproduced with permission.[3] . . . 2
1.3 Modern IMDs, (A): A *Nucleus* cochlear implant, (B): An *Activa RC* neurostimulator from Medtronic, and (C): A prototype *Heartsaver* ventricular assist device (VAD).[4] . . . 3
1.4 General diagram for a cranially mounted implant. . . . 4
1.5 Power and data requirements for a range of implantables. . . . 5

2.1 Conceptual overview of ICPT. . . . 13
2.2 Comparison of NRIC link arrangements. (a) Series-Series (SS), (b) Series-Parallel (SP), (c) Parallel-Series (PS), (d) Parallel-Parallel (PP). . . . 13
2.3 General 2-port model. An appropriate source should be chosen depending on resonant configuration. . . . 13
2.4 General flow diagram for the initial design of inductive links. . . . 14
2.5 Solenoid and spiral structures. Geometric parameters are annotated. . . . 16
2.6 Solenoid and spiral structures. Geometric parameters are annotated. . . . 16
2.7 Skin effect manifestation in wire and PCB trace. . . . 18
2.8 Proximity effect causing uneven current crowding in adjacent conductors. . . . 18
2.9 A Litz wire bundle consisting of 7 strands, with strand diameter d_s and strand pitch p_s. . . . 20
2.10 General case of two coupled circular filaments F_1 and F_2, with coaxial, lateral, and angular displacement. Remastered from [105] . . . 22
2.11 The three important special cases of the general case in Figure 2.10. Figures here are also remastered from [105]. . . . 22
2.12 Simplified coupled circuit reflects an impedance in series with the primary. . . . 24
2.13 Example contents of Z_2 (see Figure 2.12) for a parallel resonant secondary coil. . . . 25
2.14 Frequency splitting in power output from an example SP link driven by a 1 V source. . . . 30
2.15 Frequency splitting in efficiency output for an example SP link driven by a 1 V source. . . . 31

2.16 Root paths showing frequency splitting in the link impedance of the example link. 31
2.17 Optimizing winding pitch to maximize Q comes at the cost of increased coil length. Pitch is normalized to the minimum pitch $p = d_0$. 32
2.18 Decrease in coupling coefficient between two identical coils as winding pitch is modified. 33
2.19 Changing Q-factor as winding pitch is modified, with respect to frequency. 33
2.20 Effect of increasing the number of turns on Q-factor and SRF. Parameters otherwise the same as in Table 2.3. 34
2.21 Curves of PDL and PTE for SS and SP configurations as Z_{load} is varied. Parameters are otherwise the same as in Table 2.3. D = 40mm. 35
2.22 *Left*: magnetic flux lines from an energized loop of wire, *right*: field strength for increasing distance from the loop in coaxial alignment. . 36
2.23 Loaded series (left) and parallel (right) secondaries. 37
2.24 Maximum theoretical link efficiency (according to Equation 2.49), as the coupling coefficient and average (geometric) Q-factor are varied. 38
2.25 Finding optimum Q-factor as wire diameter is varied, following diameter and length constraints. 39
2.26 Curves to show link efficiency and the required input voltage to achieve 40 mW output from an SP configured link, coil geometries in accordance with the text and Figure 2.25, wire diameters noted on the curves. 40
2.27 Diagram of the test arrangement, measured voltages are annotated. . 42
2.28 Measured and calculated link efficiency for the constructed link, maintaining 40 mW at a 2 kΩ load. 42

3.1 SP link with notation used throughout this chapter. 47
3.2 Relationship between coupling and distance, normalised. 48
3.3 (A): Gain vs coil spacing against γ variations, (B): Gain vs γ against coil spacing variations. 48
3.4 3-dimensional plot of the slices from Figure 3.3. 49
3.5 Block diagram to show the layout of the transmitter system. Inset: a compact transmitter prototype, with the chip fixed in the centre of the coil. 50
3.6 Details of the phase detection arbiter. 51
3.7 Flow diagram to show the behaviour of the microcontroller. 52
3.8 Diagram to demonstrate the geometry of a square spiral printed coil . 53
3.9 Plots to show experimental data against calculated behaviour for distance and load sweeps for the 5 MHz coils, with OFT enabled ($\omega = \omega_{opt}$) and OFT disabled ($\omega = \omega_0$) 55

3.10 Plots to show experimental efficiency data for distance and load sweeps, with OFT enabled ($\omega = \omega_{opt}$) and OFT disabled ($\omega = \omega_0$) . . . 56
3.11 Scope screenshots to show variation in output voltage against coil movement ((A),(B)), and the phase difference between V_{PLL} and V_{DIV} ((C),(D)), with OFT enabled and disabled. 57

4.1 Typical sensor architectures. (A): a typical remote sensor chain with digital wireless transmitter. (B): an inductive link based remote interrogator, using an impedance analyzer. 60
4.2 Passive and active sensor configurations with the proposed system. . 60
4.3 The phase-dip measurement approach for wireless capacitive sensing. $L_1 = 10\mu$H, $L_2 = 100\mu$H, $R_{1,2} = 2\Omega$, $M = 3.162\mu$H, $C_{SENS} = 3$ pF. 61
4.4 General case inductive link model. 62
4.5 Impedance plots for a symmetric link. $L_{1,2} = 10$ μH, $C_{1,2} = 10$ pF, $M = 1\mu$H, $R_{1,2} = 3\ \Omega$. 63
4.6 Magnitude of the link impedance for varying values of $C_{1,2}$. 64
4.7 Determining capacitance through resonant frequency. 65
4.8 Symmetric vs asymmetric link impedances, resonance points marked. 66
4.9 Lines of resonance and anti-resonance for an asymmetric link as C_2 is swept. Parameters are the same as in Figure 4.3 except $C_{stray} = 1.5$ pF. 67
4.10 Lines of resonance and anti-resonance for a symmetric link as C_2 is swept. Parameters the same as in Figure 4.5. 67
4.11 (A): Link gain vs coupling and frequency. Lines of resonance and anti-resonance are highlighted. (B):Planes of resonance against changes in C_2 and k. 69
4.12 Plots of (A) β_{active} and (B) $\beta_{passive}$ against variations in Δk and $\Delta C_{(1,2)}$. Nominal parameters again are the same as in Figure 4.5, $k_{(nom)} = 0.1$, $C_{(1,2)_{(nom)}} = 10$ pF. 70
4.13 Lines of resonance and anti-resonance against changes in R_1 and R_2. Other link parameters the same as in Figure 4.5. 73
4.14 More detailed link diagram, including series loss in capacitors. 74
4.15 *Top*: Cross-coupled oscillator circuit. C_1 is on or off chip depending on active or passive configuration. *Bottom*: Table of device dimensions. 75
4.16 Microscope (a) and ion-beam (b) images of the humidity sensing capacitor. (c) shows a close-up image of the fabricated circuits and their area, layout detail is highlighted. 76
4.17 Full chip architecture; including round-robin selector and bias control loop. 77
4.18 Output voltage at the transmission coil with 4 round robin oscillators running. 77

4.19 Post-layout simulated frequency spectra for each of the round robin bursts from Figure 4.18. Parasitic capacitance reduced the measured operating frequency to between 55 and 60 MHz. 78
4.20 Nominal geometric specifications of the fabricated link coils. Both coils are circular, identical, and coaxially aligned. 79
4.21 Test arrangements for the active and passive modes. 80
4.22 Raw relative humidity data from the system in active and passive mode, compared with calibration data from the capacitive sensor. . . 81
4.23 Capacitive deviation as a function of relative humidity for the active and passive modes. 81
4.24 Passive mode capacitance measurements for different coil spacings. . 82
4.25 Output spectra for different coil spacings. 83
4.26 Measured and simulated average current consumption (I_{avg}) and oscillator output amplitude (V_{out}) as V_{bias} is varied. 85

5.1 Simple overview of an OOK-LSK style shared link solution. 88
5.2 OOK modulation, 6.78 MHz carrier, 100 kHz datastream. Black trace is the envelope. 88
5.3 OOK modulation, 6.78 MHz carrier, 500 kHz datastream. Black trace is the envelope. 89
5.4 (A): Remastered from [179], an arrangement to minimize unwanted couplings between coils in a power + full duplex data link arrangement. (B): Circuit representation of the arrangement; desirable couplings are labelled, undesirable couplings are marked with thin dashed lines. . . 90
5.5 Adapted from [181], overview of the closed-loop spinal stimulator concept. 91
5.6 Implanted stimulator and external transmitter. 91
5.7 Block diagram of the transmitter/implant/link arrangement. 92
5.8 Circuit setup for LSK/PPSK simulation, R_L =1344 Ω, link specifications otherwise the same as in Table 5.1. 93
5.9 Simulated waveforms for an LSK arrangement. 93
5.10 Simulated waveforms for a PPSK arrangement. 93
5.11 Link gain responses for different stagger setups. Link arrangement is SP, $R_1 = 0.77\Omega$, $R_2 = 1.14\Omega$, $R_L = 1344\Omega$. Other specifications are given in Table 5.1. 94
5.12 Plot to show experimental values of V_{out} against coil separation d, with drive frequency $f = 9.6$ MHz. Black lines are calculations, red circles are measurements. 96
5.13 Plot to show experimental values of V_{out} against frequency f and coil separation d. 97
5.14 PPSK demodulation circuit. 97
5.15 Simulated demodulator waveforms. 98

5.16 PPSK modulator for BER testing. 98
5.17 BER test results, upper and lower bounds shown to 95% confidence. . 99

6.1 Neural implant diagram, with many recording electrodes, and a 'Utah' electrode array, for neural recording [185]. 101
6.2 Inductive WPT with (A): WiFi-style data link, (B): data-modulated power link, and (C): dedicated data link. 102
6.3 V_{rect} drooping due to high data rate 103
6.4 PHM system block diagram. 104
6.5 Pulse-driving mechanism for PHM, with tables of values for an example system. 105
6.6 (A): Ideal PHM waveforms, (B): Erroneous PHM waveforms. 105
6.7 (A): Block and (B): timing diagrams for SQuirM. 107
6.8 Microphotographs of the fabricated transmitter and receiver circuits, highlighting the active areas. 109
6.9 *Left:* Detailed transmitter circuit block diagram. *Right:* Expanded view of the output stage. M_{Tx} has 3 taps to alter the output power. The 3b trimcap is binary weighted, with 40,80, and 160 fF MIM capacitors. . . 110
6.10 Postlayout Monte Carlo spread of pulse widths from the impulse generator in Figure 6.9 111
6.11 A well-timed current pulse into a resonant circuit, f_0 = 205.5 MHz. . . 111
6.12 Simulated data of maximum amplitude seen at the receiver, for varying pulse widths and coupling factors, for two coupled tanks with f_0 = 205.5 MHz, $\tau_{pw(opt)} \approx$ 2.433ns. 111
6.13 Output voltage responses of the example link at low and high coupling factors. The response shows a mix of the two peak frequencies at high coupling. 112
6.14 Details of the receiver circuitry. 113
6.15 Trimmable peaking current source, with 3 equally weighted output taps. 113
6.16 Simulated voltages for the receiver chain, with a short delay set in the delay block. All vertical axis units are Volts. 114
6.17 (A): Regular receiver damping scheme, i_d injects a pulse into the coil. (B): Differential damping, equivalent i_d pulses cancel each other. . . . 115
6.18 Experimental setup. 116
6.19 Equipment setup for producing and recovering datastreams. 116
6.20 Measured and simulated power consumption per bit for (A): transmitter and (B): receiver circuits. The receiver consumes far more quiescent power than the transmitter. 117
6.21 Quiescent power draw in the overall circuit (A), and inferred measured power without quiescent draw (B). 117
6.22 Maximum coil distance vs Tx supply voltage. 119

6.23 Measured waveforms for a 40 Mbps pseudorandom data sequence, demonstrating a low level of jitter over time. 120
6.24 (A): BER results across a range of coil spacings and data rates. (B): Zoomed in view of the point at which many errors occur. The regions between the upper and lower confidence levels are shaded. In the case the lower bound is zero, the shaded area continues downward forever. 120
6.25 Damped vs continuous oscillations. $x(t)$ is the resonator current, $f(x)$ is the instantaneous frequency. 123
6.26 Simplified circuit diagram of the impulse-driven clock circuit. 123
6.27 Screenshot of circuit layout, key blocks are highlighted. 124
6.28 Simulated waveforms for the clock circuit. 124

7.1 Potential configuration of a self-oscillating driver, with an adjustable receiver capacitor. 130

List of Tables

1.1 Devices from Figure 1.5 and their functions 6

2.1 Coil Parameters 15
2.2 Link Impedances in Accordance with Figures 2.2 & 2.3 26
2.3 Example Link Specifications 29
2.4 Cochlear Implant Example Link Specifications. 41

3.1 Table listing the geometric parameters generated for the test coil pair 53
3.2 Measured coil parameters for operation at 5MHz. 54

4.1 Measured Nominal Link Parameters. 79
4.2 Summary of correlation and error between system measurements and calibration measurements. 82
4.3 Comparison with other recent wireless sensing systems. 84

5.1 Table of stagger configurations, with inductance and capacitance values. 95
5.2 Measured parameters of the link coils. Measurements were performed at 9.6 MHz. 96

6.1 Pros and cons for the schemes shown in Figure 6.2 103
6.2 Table of comparison for inductive data telemetry schemes. 121

A.1 Common Link Design Formulae: Table of Reference 135

List of Abbreviations

ASK	**A**mplitude **S**hift **K**eying
AM	**A**mplitude **M**odulation
BER	**B**it **E**rror **R**ate
CotS	**C**ommercial **o**ff **t**he **S**helf
CW	**C**ontinuous **W**ave
FEM	**F**inite **E**lement **M**ethod
FSK	**F**requency **S**hift **K**eying
ICPT	**I**nductively **C**oupled **P**ower **T**ransfer
IMD	**I**mplantable **M**edical **D**evice
IR	**I**mpulse **R**adio
ISI	**I**nter-**S**ymbol **I**nterference
LO	**L**ocal **O**scillator
LSK	**L**oad **S**hift **K**eying
MIM	**M**etal **I**nsulator **M**etal
NRIC	**N**earfield **R**esonant **I**nductive **C**oupling
OFT	**O**ptimum **F**requency **T**racking
OQPSK	**O**ffset **Q**uadrature **P**hase **S**hift **K**eying
PDM	**P**ulse **D**elay **M**odulation
PHM	**P**ulse **H**armonic **M**odulation
PSK	**P**assive **S**hift **K**eying
PPSK	**P**assive **P**hase **S**hift **K**eying
QPSK	**Q**uadrature **P**hase **S**hift **K**eying
SQuirM	**S**hort-range **Qu**al**i**ty-facto**r** **M**odulation
WPT	**W**ireless **P**ower **T**ransfer

Dedicated to inductors everywhere

Introduction

1

Implantable medical devices (IMDs) and their telemetry systems are the subject of much commercial and academic research interest; there are continuing efforts to improve and refine these devices to be more effective. This chapter discusses the history of IMDs, and the importance of effective telemetry systems for both power and data transfer.

1.1 IMDs and Inductive Telemetry

Perhaps the first successful IMD to be both created and implanted was Elmqvist's pacemaker [3]. Constructed hastily from available discrete components, the device consisted of a few transistors and passives, a battery of nickel-cadmium cells for power, and a coil of wire for recharging. The device itself was encapsulated in epoxy formed in a Kiwi boot polish tin (see Figure 1.1). The components are still visible through the clear epoxy, which maintains the shape of the tin.

Elmqvist's device was implanted in the engineer Arne Larsson, in October 1958, as a last resort treatment for otherwise untreatable heart malfunction. Despite initial difficulties, the device fundamentally proved successful; Larsson eventually died at age 86 of an unrelated malady [3].

Soon afterwards, in 1960, successful human implantation of a similar pacing unit was reported by Greatbatch [4], [5]. This led to the creation and patenting of the Chardack-Greatbatch pacemaker, shown in Figure 1.2. The Chardack-Greatbatch pacemaker operates on a similar principle to Elmqvist's; both use a simple oscillator made from discrete components, running from a battery and encapsulated in epoxy. A key difference between the two devices is that Greatbatch's device relies on its low power consumption and large battery for continued operation, whereas Elmqvist's employs a coil for wireless battery recharging.

Modern IMDs perform more functions than just cardiac pacing however; large implanted heart pumps can serve as heart replacements, cochlear and retinal implants can restore hearing and sight, and neural stimulators provide last-resort treatment for certain neurological conditions. These devices boast advanced integrated electronics, and impressive biocompatible packaging, however solutions to powering these devices

---

[1] `http://agentgallery.com/objects/1958-prototype-siemens-elima-cardiac-pacemaker`

[2] `https://www.flickr.com/photos/prutchi/9656000889/in/album-72157635214722957/`

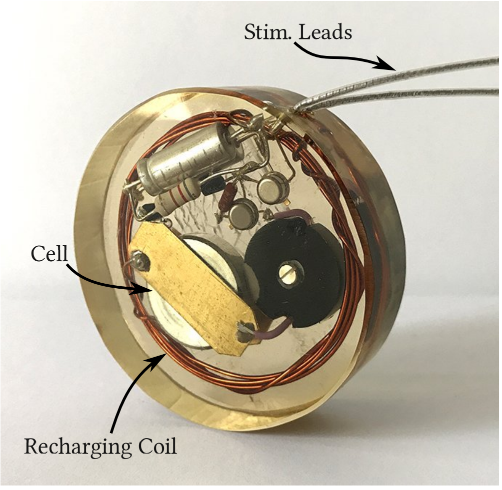

FIGURE 1.1: Elmqvist's pacemaker, with visible recharging coil. Reproduced with permission.[1]

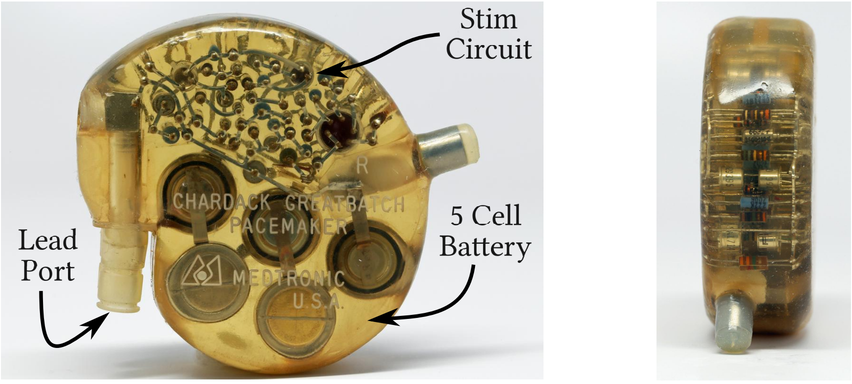

(A)

(B)

FIGURE 1.2: The Chardack-Greatbatch pacemaker, (A) front and (B) side view. Reproduced with permission.[2]

(A) (B) (C)

FIGURE 1.3: Modern IMDs, (A): A *Nucleus* cochlear implant, (B): An *Activa RC* neurostimulator from Medtronic, and (C): A prototype *Heartsaver* ventricular assist device (VAD).[3]

remain similar to early devices. Modern implants will often use a wireless power transmission method similar to the simple inductive recharging scheme employed by Elmqvist, either for battery recharging, or for providing continuous power from an external wearable battery.

Unlike their predecessors however, modern implants often require *data* telemetry in addition to power telemetry. For example a deep brain stimulator would require communication with an external programmer, in order to configure the stimulation parameters. Requirement for data telemetry adds a new design dimension, which is tackled in a variety of ways. A common approach for instance is to modulate data on top of an inductive power delivery system; a simple and compact approach well suited to implantables.

Figure 1.3 shows a selection of modern IMDs, each with a different application. Despite the fact that each IMD shown here has a different function, they share a similar scheme for power and data telemetry; they all use some form of inductive coupling. In the case of the cochlear implant, power is continuously supplied from outside the skull through the coil visible at the top of the image. In addition, data can be transferred bidirectionally by modulating this power carrier. The *Activa RC* uses a similar approach, but instead of continuous powering, it contains an internal battery that can be recharged periodically. The heart pump also uses this rechargeable battery approach, but does so with a much larger power budget, requiring several watts to operate compared to the milliwatt level operation of the other two implants.

Figure 1.4 shows an exploded overview of a typical cranial implant arrangement utilizing an inductive link, e.g. the cochlear implant from Figure 1.3. The external transmitter is mounted on the skin, and delivers power wirelessly from the external transmitter coil. This power is recovered at the implant through the receiver coil, allowing the implant to perform sensing, stimulation, or other functions.

---

[3] (A): `https://commons.wikimedia.org/wiki/File:Cochearimplants.JPG`,
(B): `http://www.medtronic.com/us-en/healthcare-professionals/products/neurological/deep-brain-stimulation-systems/activa-rc.html`,
(C): `https://commons.wikimedia.org/wiki/File:Prototype_of_the_HeartSaver_VAD,_Ottawa,_Canada,_1999_Wellcome_L0060516.jpg`

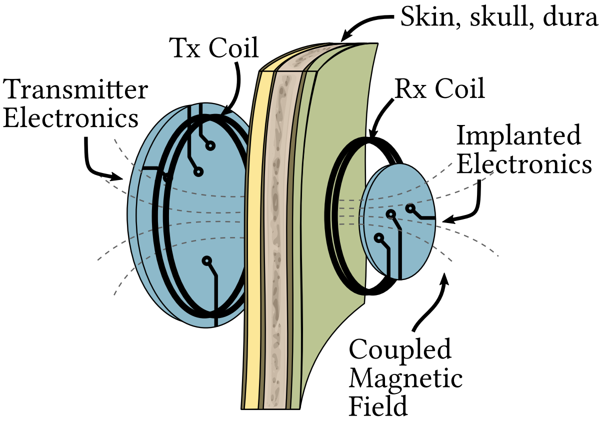

FIGURE 1.4: General diagram for a cranially mounted implant.

The implants in Figure 1.3 show only three different applications, but we can still observe how these different applications have different requirements when it comes to power budget, implant size, and data telemetry. The wide range of conditions that modern implants attempt to tackle necessitates a similarly wide range of designs and approaches; IMDs have come a long way from the early days, where the only real application was cardiac pacing. Figure 1.5 shows how the range of power and data requirements varies significantly for each application, with examples of both commercial and research IMDs. Implants within the same category form clusters, giving a general idea of the requirements of each class of IMD. The three biggest clusters for this range of modern IMDs are: *biosensing*, *neural recording*, and *neurostimulation*. The devices in Figure 1.3 would all cluster near the bottom right with the stimulators and heart pumps, requiring fairly significant power delivery, but with modest data transfer requirements.

Figure 1.5 also highlights the extremely wide range of power and data requirements needed by modern implantables. At the lowest end of the power spectrum, examples such as the Medtronic ‘Micra’ pacemaker[6] require only a few nanowatts of power. For this kind of sub-miniature device, a small, low-leakage battery is the best option for power delivery, rather than WPT. At the other end of the spectrum there are implantable heart pumps and neurostimulators, that would require milliwatt- to watt-level power delivery. WPT solutions tend to be employed mostly for devices closer to the centre-right of this map. Inductive links in particular excel in this domain; they are capable of delivering significant power levels efficiently, often with included data transfer.

Table 1.1 expands on some examples from Figure 1.5, giving further details about their implementations and functions. One example is taken from each category from Figure 1.5, and demonstrates how inductive links find application across a broad range of systems. Approaches such as long term stable batteries and RF harvesting begin to be used for applications where the power consumption drops to the region of microwatts and below [6], [18].

There exist other approaches for wireless power telemetry, such as ultrasound [21],

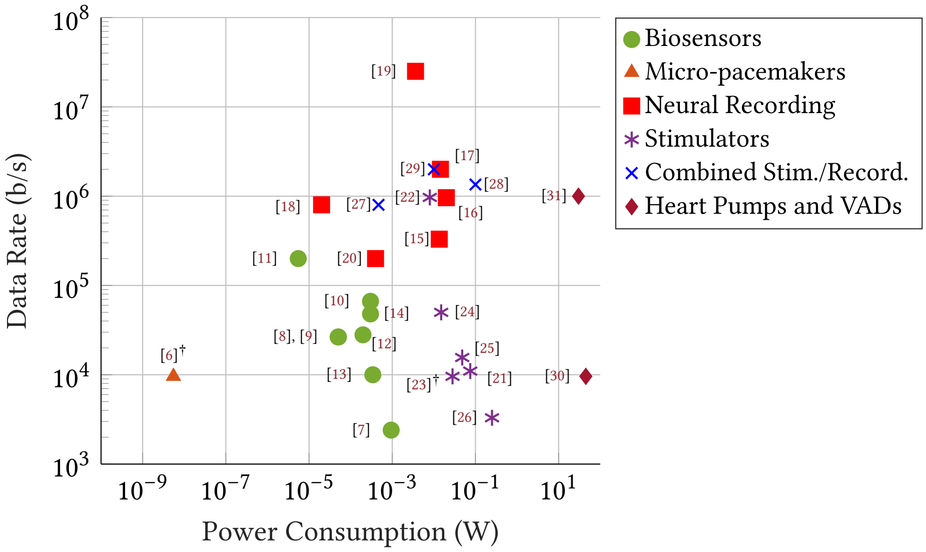

†These devices are commercial Medtronic designs. Data rate is secret, therefore RS-232 standard 9.6 kbps is assumed.

FIGURE 1.5: Power and data requirements for a range of implantables.

[32], high-frequency midfield beamforming [33], and multi-coil resonator arrays [34]. These methods enable power delivery to deeply implanted devices, or scattered arrays of small neural implants, with a greater efficiency than a traditional 2-coil inductive link would be capable of. While these systems show promise for the future direction of IMDs, they are currently at the early stages of development, with no commercial applications at present. The work in this thesis therefore focuses on two-coil inductive links, as they are widely applicable and effective in the majority of IMD applications. This shows, in some respect, that Elmqvist's inductive charging idea has stood the test of time. Despite the fact that inductive powering is not suitable for *all* modern applications, the method is still used in a wide range of IMDs to great effect.

1.2 Challenges for Modern IMD Telemetry

While telemetry initially referred to the transfer of data only, it has come to mean delivery of power and/or data. In the context of modern IMDs, it generally refers to both. Modern IMD designs face pressure to improve, particularly from the point of view of their telemetry subsystems. Power should be transferred as efficiently and safely as possible, over longer ranges, with more tolerance to environmental variations [31], [35]–[39]. Improvements of this kind prolong the battery life of external transmitters, and improve the quality of life of patients with these implants. Transferring data at higher rates with lower power consumptions is also very desirable; particularly in the case of implants for neural recording, where the requirement for high data-rate telemetry is crucial [17], [40]–[42].

A considerable source of difficulty when approaching these problems is power budget. IMDs must restrict the amount of power they dissipate, so as not to cause heating of the surrounding tissue. Power usage must therefore be carefully managed

TABLE 1.1: Devices from Figure 1.5 and their functions

Ref.	**Function**	**Telemetry**	**Details**
[6]	Implantable micro-pacemaker	• Power: Internal battery • Unspecified RF radio for data transfer. Likely used to update stimulation parameters.	State of the art commercial pacemaker in a pill-sized package. Very low power consumption allows multi-year operation from a battery of internal cells.
[7]	Low-power multi-target sensor SoC	• Power: Inductive link • Downlink: OOK modulated power link, 2.4 kbps • Uplink: 403 MHz low power transmitter	An implantable, integrated, CMOS system on chip for measuring temperature, glucose, protein presence, and pH. Powered through an inductive link, downlink through a longer range low power RF link.
[18]	20 µW wireless neural recording tag	• Power: RF Harvesting from 915 MHz • Downlink: ASK • Uplink: Backscatter OOK 150-800 kbps	An integrated implantable neural recording tag. Operates from 20 µW power budget, scavenges energy from 915 MHz carrier for low-duty operation.
[28]	Inductive link for neural stimulation and recording	• Power: 13.56 MHz inductive link • Downlink: OOK modulated ind. link • Uplink: LSK modulated ind. link, 1.35 Mbps	An integrated system for a combined implantable stimulator and neural recorder. Inductive link is used to deliver 100 mW of power, and modulated for bidirectional half-duplex data transmission.
[26]	Inductive link for powering a retinal implant	• Power: 1 MHz inductive link, 250 mW • Downlink: Separate link, not explained in detail • Uplink: LSK modulated ind. link, 3.3 kbps	An integrated system for a proposed retinal prosthesis. Back telemetry is used to provide information to the transmitter, and ensure efficient power delivery.
[31]	Inductive link for powering an implanted heart pump	• Power: 800 kHz inductive link, 5-30 W • 27.1 MHz RF radio for ind. link control, 100 kbps • 403.5 MHz RF radio used for sensor readout and pump control, up to 1 Mbps†	A high power high efficiency system for powering and controlling an implanted heart pump via inductive link, with two separate data links for power control, and pump/sensor control.

† Data subsystem information is not in the paper [31], but was confirmed through correspondence with the author.

to maximize efficiency, without compromising the functionality of the implant. For example, Lee and Ghovanloo [43] suggest an inventive scheme to efficiently charge an implant, to adjust for changing load conditions [44]. Another example from Lee et al. [24] proposes an adaptive rectifier that is controlled by the requirements of a neurostimulator, such that the rectifier only provides necessary power for the stimulator. When considering data transfer, power can be saved by combining wireless power and data transfer into one link [45]–[48], obviating the need for separate carriers to be generated and separate data links to be fabricated. Carrierless methods, such as pulse harmonic modulation [49] and pulse delay modulation [50] offer another low-power alternative.

Most of the telemetry solutions in the literature thus far attempt to attack these problems from either side of the inductive link, by improving the transmitter electronics, the receiver electronics, stimulation and sensing methods, and power management schemes. The focus in much of the existing work is on parts of the system *around* the inductive link, rather than the link itself, despite the fact that the inductive link has a key role in defining the limits of performance of the system.

The work in this thesis provides a series of analyses, methods, and circuits, that take a ‘link-first’ approach. By analysing link behaviour in detail, a thorough link model was developed, with accompanying software, and was used to great effect when developing the other systems and methods.

Using this link model, several systems and methods were devised that take advantage of the inherent properties of inductive links to achieve good performance. For power transfer, two systems were developed that both take advantage of the phenomenon of frequency splitting to improve the resilience of the system to variations in coupling and load. The phenomenon of frequency splitting was further investigated, and a method was developed that employs frequency splitting to perform remote capacitive sensing with a minimal number of components. Finally, a system was developed that takes advantage of high quality-factor inductive links to achieve high-speed, energy efficient data transmission.

1.3 Novel Contributions and Publications

The work presented in this thesis provides the following series of contributions to the field of inductive wireless telemetry for IMDs.

- A comprehensive review of existing approaches to analytic modelling of inductive link behaviour. This compilation is presented in a tutorial format, with additional analysis and insight, with reference to IMD applications, throughout.

- A methodology and system design for optimum frequency tracking in inductive links, with the aim of ensuring more reliable power transfer in the face of link coupling variations.

- A thorough analysis of inductive link splitting, that can be utilized for low-complexity direct sensing through an inductive link. This is accompanied by a proof of concept system.
- An implementation of a combined power and data transfer link for an existing implantable system, that demonstrates the strength of the principle of stagger tuning, and its applicability to modern IMD telemetry.
- An impulse-based high-speed low power wireless data transfer system, targeting IMDs for neural recording.
- A free software package written to aid the design of inductive links, based on simple analytic methods.

1.3.1 Publications

This work has specifically led to the publication of the following articles, including conference and journal papers.

1. **Intermittent Excitation of High-Q Resonators for Low-Power High Speed Clock Generation**, *Schormans, Matthew; Valente, Virgilio; Demosthenous, Andreas;* - IEEE International Symposium on Circuits and Systems (ISCAS), 2018.
2. **Practical Inductive Link Design for Biomedical Wireless Power Transfer: A Tutorial**, *Schormans, Matthew; Valente, Virgilio; Demosthenous, Andreas;* - IEEE Transactions on Biomedical Circuits and Systems, vol. 12, no. 5, pp. 1112-1130, 2018.
3. **A Low-Power, Wireless, Capacitive Sensing Frontend Based on a Self-Oscillating Inductive Link**, *Schormans, Matthew; Valente, Virgilio; Demosthenous, Andreas;* - IEEE Transactions on Circuits and Systems I: Regular Papers, vol. 65, no. 9, pp. 2645-2656, 2018.
4. **An Energy-Efficient 1.2 V 4-Channel Wireless CMOS Potentiostat for Amperometric Biosensors**, *Valente, Virgilio; Schormans, Matthew; Demosthenous, Andreas;* - Proceedings of the IEEE International Symposium on Circuits and Systems (ISCAS), 2018.
5. **An integrated passive phase-shift keying modulator for biomedical implants with power telemetry over a single inductive link**, *Jiang, Dai; Cirmirakis, Dominik; Schormans, Matthew; Perkins, Timothy A; Donaldson, Nick; Demosthenous, Andreas;* - IEEE Transactions on Biomedical Circuits and Systems, vol. 11, no. 1, pp. 64-77, 2017.
6. **Single-pulse harmonic modulation for short range biomedical inductive data transfer**, *Schormans, Matthew; Valente, Virgilio; Demosthenous, Andreas;* - Proceedings of the IEEE Biomedical Circuits and Systems Conference (BioCAS), 2017.

7. **Frequency splitting analysis and compensation method for inductive wireless powering of implantable biosensors**, *Schormans, Matthew; Valente, Virgilio; Demosthenous, Andreas;* - Sensors, vol. 16, no. 8, 2016.
8. **An implantable wireless multi-channel neural prosthesis for epidural stimulation**, *Jiang, Dai; Eder, Clemens; Perkins, Timothy A; Vanhoestenberghe, Anne; Schormans, Matthew; Liu, Fangqi; Valente, Virgilio; Donaldson, Nick; Demosthenous, Andreas;* - IEEE International Symposium on Circuits and Systems (ISCAS), pp. 2026-2029, 2016.
9. **Efficiency optimization of class-D biomedical inductive wireless power transfer systems by means of frequency adjustment**, *Schormans, Matthew; Valente, Virgilio; Demosthenous, Andreas;* - Proceedings of the 37th Annual International Conference of the IEEE Engineering in Medicine and Biology Society (EMBC), no. 1, pp. 5473-5476, 2015.

1.4 Thesis Summary

The contents of this thesis are arranged in chapters as follows:

Chapter 1 gives a brief history of IMDs, and considers the context and importance of the telemetry systems they require for both power and data transfer. It introduces the rest of the material in the thesis, and outlines novel contributions that were produced.

Chapter 2 presents a series of analyses and methods for analytic modelling of inductive links for wireless power transfer, with a focus on biomedical applications. This chapter focuses on extracting practical methods from the literature, and combining them to give the full picture of how to design an efficient power link.

Chapter 3 presents the design and implementation of a system for tracking the optimum frequency for driving an inductive power link for passive implants. By adjusting the drive frequency automatically to match the optimum frequency, frequency splitting can be compensated for, power delivery can be maintained at a constant level regardless of coupling, providing the link is overcoupled.

Chapter 4 presents the development of a method for measuring an unknown sensing capacitance at either side of an inductive link, and an accompanying system to prove the concept. Such a system allows for very simple remote sensing devices to be interrogated with a simple, low-power interrogation circuit. The system was fabricated and tested, and measurements taken that were found to agree well with theory.

Chapter 5 briefly discusses the problem of data telemetry for IMDs using inductive links, and some different approaches present in the literature. It then describes the design, build, and testing of a stagger-tuned inductive link, to provide coupling-insensitive power and data transfer to an implantable stimulator.

Chapter 6 describes the method of Short-range Quality-factor Modulation (SQuirM) for high data-rate low power data transmission through an inductive link. The method is described in detail, as well as an accompanying circuit that was designed, fabricated, and tested. The test results were found to be in good agreement with the simulated behaviour of the chip.

Chapter 7 concludes the thesis, with some discussion of the work presented and the associated results. It also covers potential future directions of the work.

Appendix A contains a reference sheet of useful formulae for link design, and Appendix B describes the Coupled Coil Configurator (CuCCo), software, written to aid the design of inductive links.

Coupled Inductors for IMDs: Theory and Practice

2

The work in this chapter was first published in IEEE Transactions on Biomedical Circuits and Systems [1]. This chapter contains further details not present in the original.

Chapter 1 presents how the principle of ICPT is used to great effect in a variety of IMD applications, across a wide range of power and data transfer targets. However, despite the flexibility, prevalence, and potential of ICPT, there is still no firm consensus regarding methods of inductive link design and optimization. Terman provides some of the earliest analysis of inductively coupled systems [51], [52]. Terman's analysis alone is insufficient to fully design an inductive link however; factors such as efficiency and resilience must also be considered. This is not factored into Terman's original work, as the focus was on receiver and filter circuits for early radio applications. Nonetheless it is an excellent starting point, considering the behaviour of coupled resonant circuits in more detail than most other sources, working from the ground up. There has been a lot of subsequent (more modern) analysis dedicated to characterizing and optimizing such links. These analyses have shortcomings however. For instance, they are often very focused on a specific aspect or design procedure, and so only provide insight into a small part of the design process [53]–[57]. For example, Ko et al. [54] provide a procedure for designing 'radio-frequency powered coils for implant instruments'; while the procedure is fairly clear, it is only applicable to small IMDs with a simple fixed frequency driver. Donaldson and Perkins [55] give a thorough analysis of the effects of varying coupling coefficients on link performance of series-parallel links; however, no other link configurations are considered. Jow and Ghovanloo [53] consider a detailed model of PCB based spiral coils, but the analysis is not immediately applicable to wirewound coils. Alternately, some analyses cover a wider range of aspects in great detail [58]–[60], but are often impractical. For instance Halpern and Ng [58] give a very detailed analysis of the limits of power delivery and efficiency of two-coil series-series and series-parallel configured links, but significant prior knowledge of the subject is required to apply it to a design process.

In addition, while these methods provide a good picture of link characteristics in the theoretical circuit domain, they assume the link parameters are known a priori. The problem with this assumption is that the electrical parameters of the coils must be determined through some means beforehand. This generally requires either fabrication and measurement, or finite element method (FEM) simulation [61]–

[64]. FEM simulations can allow link behaviour to be predicted more accurately than calculations alone. However, FEM software is often expensive, with a steep learning curve. Although fabrication and measurement is cheap, requiring measurements as part of the design procedure is time consuming and impractical. FEM can also be equally time consuming over many simulation iterations.

The full design process therefore requires more than just consideration of the electrical parameters of the link. There are inevitably design restrictions on elements such as coil size, materials, and separations/displacements. As a result, it is imperative to be able to easily convert between geometric and electrical parameters as part of an analytic design process. In addition, it is beneficial to consider a broader approach than those presented in older analyses (e.g. [51], [52], [65]), where assumptions are made to simplify the calculations, and parameters such as the frequency, coupling, losses, and load are considered constant [65].

The purpose of this chapter therefore is to provide a simple approach for the analysis and design of 2-coil inductive links, without requiring FEM solvers. The methods presented here are the result of the collection, review, and selection of the most relevant design approaches present in the literature; they are considered both sufficiently practical and accurate for the designing and prototyping process. In addition to specific methodology, useful rules for the designer to follow are included, to give a sense of how to apply theory to practice. The focus is on biomedical applications, but the principles can easily be applied to design inductive links for other purposes. The accompanying free software tool, ‘CuCCo’ [2], was written with the aim of giving the designer a set of easy to use scripts that perform all the necessary calculations required for designing an inductive link. CuCCo is described in more detail in Appendix B.

This chapter is structured as follows: Section 2.1 reviews the basic theory of operation for ICPT and reviews essential principles. Section 2.2 considers the problem of link design in detail, and presents analytical methods for geometric to electrical parameter conversion, as well as link characterization. Section 2.3 discusses important practical considerations and tradeoffs that should be considered to achieve efficient power transfer. Section 2.4 gives a design example for a simple power link, demonstrating the methods presented and usage of CuCCo.

2.1 Principles

Any WPT system that uses closely coupled inductive coils can be considered as some form of ICPT. Even though a wide variety of designs exists, all ICPT systems employ at least two coils that are separated by a short distance relative to the coil diameters. Although some designs use 3 or 4 coils [34], [61], [66]–[68], the analysis in this chapter is limited to the 2-coil case, as it is the most easily-implemented ICPT arrangement, and is still capable of achieving good performance. 3 and 4 coil systems are often superior in terms of power delivery and efficiency, but this comes at the cost of a much more complex design procedure.

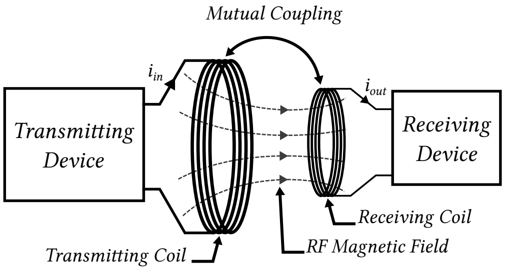

FIGURE 2.1: Conceptual overview of ICPT.

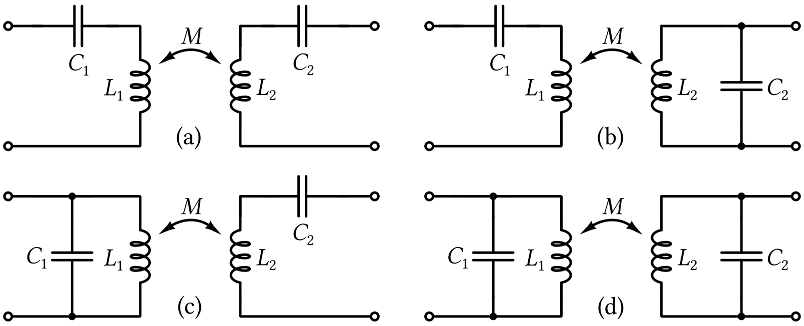

FIGURE 2.2: Comparison of NRIC link arrangements. (a) Series-Series (SS), (b) Series-Parallel (SP), (c) Parallel-Series (PS), (d) Parallel-Parallel (PP).

In the simplest case, ICPT can be achieved by aligning two inductive coils in close proximity, such that they are magnetically coupled. This principle is illustrated in Figure 2.1, where energy is transferred from the transmitting coil (Tx) to the receiving coil (Rx) due to the magnetic field of the Tx being coupled into the Rx. This can be considered as a pair of inductances L_1 and L_2, coupled by a mutual inductance M. Assuming that parasitic capacitance in the coils is negligible, this forms a non-resonant system. Non-resonant energy transfer is not generally used for WPT, as its efficiency is poor compared to resonant arrangements [65]. For non-resonant arrangements efficiency is proportional to the coil coupling k, whereas for resonant arrangements it is proportional to the kQ product. This is considered in more detail later in this chapter.

By adding capacitors in series or parallel with the coils resonant arrangements can be realised, referred to as near field resonant inductive coupling (NRIC) [69]. NRIC is a form of ICPT that can achieve increased efficiency compared to the non-resonant case. Figure 2.2 shows the four possible arrangements for two-coil NRIC; each coil has an accompanying capacitor, so each side of the link forms a resonant tank. Each

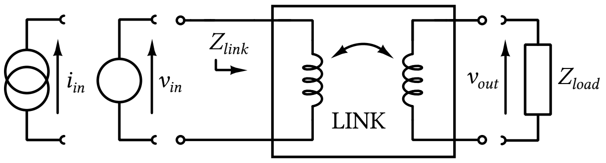

FIGURE 2.3: General 2-port model. An appropriate source should be chosen depending on resonant configuration.

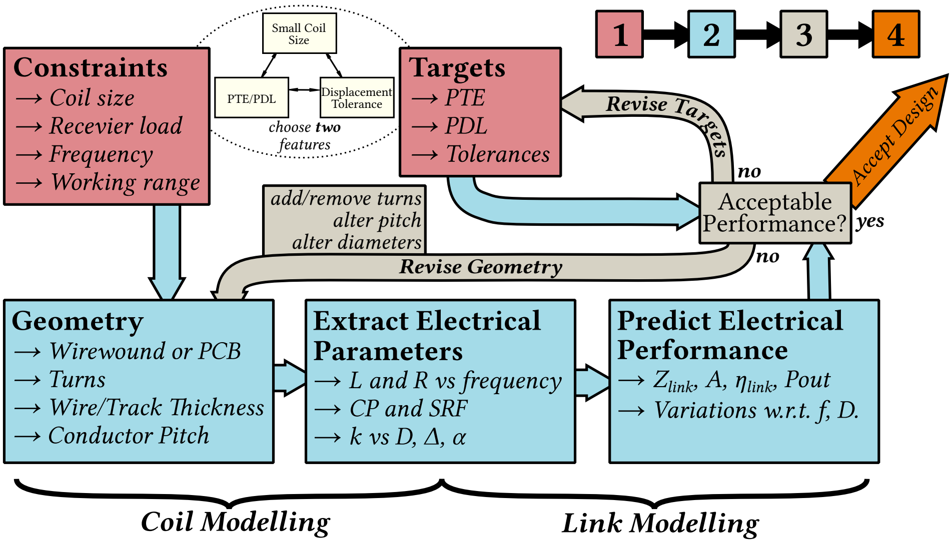

FIGURE 2.4: General flow diagram for the initial design of inductive links.

of the configurations in Figure 2.2 can be considered as a 2-port network, where the Tx (L_1) is driven by a power source and the Rx (L_2) is connected to a load. The 2-port representation is illustrated in Figure 2.3, where Z_{link} is the impedance looking into the link, and will depend on the topology chosen from Figure 2.2. Z_{load} is the impedance connected to the output port of the link. For good input matching, a series resonant primary (Figure 2.2(a,b)) is driven by a voltage source, and a parallel resonant primary (Figure 2.2(c,d)) is driven by a current source. The same principle can be applied to the receiving side; circuits with a large current draw would be driven better by a series resonant receiver, and lower power circuits would be better driven by a parallel resonant receiver.

Using the circuit analysis presented by Terman [51], [52], parameters such as the link gain and impedance can be determined for any of the link configurations in Figure 2.2. The link gain A_v is considered either as a unitless voltage gain (v_{out}/v_{in}), or as a transimpedance (v_{out}/i_{in}), depending on the driver. This analysis is developed further by Van Schuylenbergh and Puers, where equations for link efficiency and optimization procedures are developed and presented [65]. The link efficiency $\eta_{link} = P_{out}/P_{in}$ is of equal importance, defining the power gain of the link. Combining these analyses is sufficient to perform rudimentary analysis of an inductive link in terms of the electrical circuit parameters, extracting parameters such as the power delivered to the load (PDL) and power transfer efficiency (PTE). This forms the basis of the electrical parameter analyses in Section 2.2.

2.2 Link Design

This section summarizes the key analyses required for link design. By using the analyses in this section, it is possible to design links to achieve design targets for a given

Table 2.1: Coil Parameters

Geometric		Electrical†	
d	Diameter	L	Inductance
l	Length	R	Series Loss
n	Number of Turns	Q	Quality Factor
$d_0 = 2r_0$	Wire Diameter	C	Resonating Capacitance
p	Winding Pitch	C_P	Parasitic Capacitance
w	Track Width		
s	Track Spacing		

†These units are with reference to either the Tx or Rx coil, and are noted with subscript 1 or 2 respectively.

application. Figure 2.4 is an overview of a typical design flow for designing an inductive link. The process starts with constraints and targets. Constraints typically include geometric limits, e.g. the receiver coil size must fit within an implant's package, and targets describe the desired performance metrics. Examples include PTE, PDL, and tolerance to displacement and load variations. The process then involves determining geometry that fits the initial constraints, extracting the electrical parameters associated with that geometry, using these extracted parameters to predict the link performance, and then comparing that performance with the design targets. This process is then repeated, altering the geometry as necessary until the predicted performance is acceptable. The designer must tradeoff between small coils, PTE/PDL, and displacement tolerance; see the triad of features inset at the top of Figure 2.4. For example, to obtain good performance in PTE/PDL with small coils, the displacement tolerance will suffer, i.e. the link will only achieve the desired performance for a small range of displacement values. The rest of this section collects relevant design equations from the literature, and describes how they can be used according to the flow presented in Figure 2.4. This can be considered in two parts: *coil modelling*, where electrical parameters are extracted from the proposed geometry; and *link modelling*, where the performance of the link is predicted in terms of these extracted electrical parameters.

2.2.1 Coil Modelling

While any coil types can be used for WPT, in general the coil types used are short wire solenoids, printed circuit board (PCB) spirals, or 'pancake' coils. Figure 2.5 shows the structure of solenoid and PCB spiral coils, with their geometric parameters annotated. Pancake coils can be considered analogous to PCB spiral coils, but would use the d_0 and p parameters for wires, rather than the w and s parameters for PCB tracks. These geometric parameters must then be converted to electrical parameters: inductance, resistance, and capacitance, shown in Figure 2.6; a full list of parameters is given in Table 2.1.

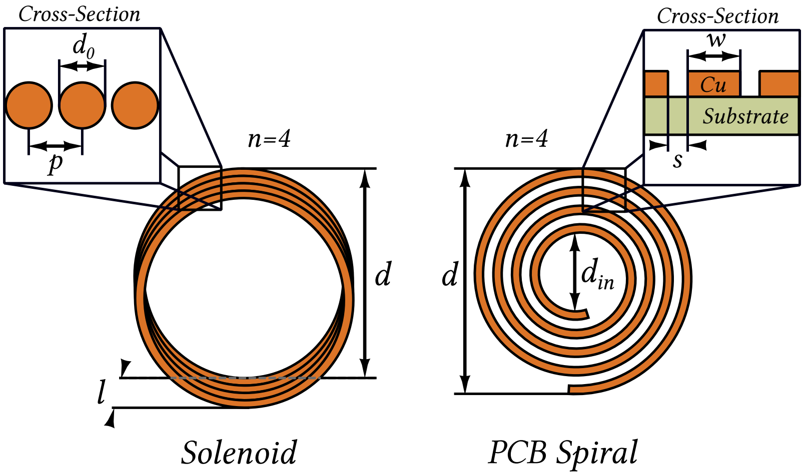

FIGURE 2.5: Solenoid and spiral structures. Geometric parameters are annotated.

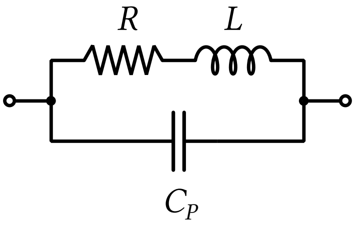

FIGURE 2.6: Solenoid and spiral structures. Geometric parameters are annotated.

Inductance

The procedure of analytic inductance calculation is well described in the literature. Wheeler [70] provides one of the earliest expressions for inductance calculation, where simple formulae are given for calculating the inductance of long radio coils. A development of this work is given by Grover [71], where a collection of tables and methods are presented; again the focus is on radio coil design. The subject has subsequently been reformulated and developed, generally building upon the work of Grover and Wheeler [72]–[74]. Hurley et al. in particular provide analysis of coil parameters in the context of WPT [73]. Perhaps the most thorough treatment of the subject to date however is attributable to Knight, where the inductor is considered from first principles, and the appropriate theory is developed in order to produce accurate expressions for calculating inductance [75]. Knight provides a continuous expression for calculating the inductance of solenoid coils of any proportion, based on the current-sheet inductance method:

$$L = \frac{\mu_0 \pi r^2 n^2 \kappa}{l} \tag{2.1}$$

where μ_0 is the permeability of free space, $r = d/2$, and κ is Nagaoka's coefficient, approximated as [75]:

$$\kappa = z_k \left(ln\left(1 + \frac{1}{z_k}\right) \frac{1}{\left(k_0 + k_1\left(\frac{l}{d}\right)\right) + k_2\left(\frac{l}{d}\right)^2 + \frac{w_1}{(|w_2|+d/l)^v}} \right) \tag{2.2}$$

where $z_k = l/(\pi r)$, $k_0 = 2.30038$, $k_1 = 3.437$, $k_2 = 1.76356$, $w_1 = -0.47$, $w_2 = 0.755$, and $v = 1.44$. By substituting this approximation for κ into Equation 2.1, L can be calculated to within ±20ppM. While it is possible to evaluate the appropriate line integral to obtain an exact result [72], the procedure is complex and can be computationally expensive over many design iterations. Equations 2.1 and 2.2 however are simple expressions that are both computationally efficient and practical. It should be noted that the inductance value produced by Equation 2.1 for a given geometry is valid only at low frequencies with respect to the self-resonant frequency (SRF) of the inductor. Determining the SRF is a complex topic itself, and is discussed further in Section 2.2.1.

For the case of PCB spiral coils, the inductance calculation is somewhat simpler. Mohan et al. give an expression based on the fill-factor $\beta = (d - d_{in})/(d + d_{in})$, and the average turn diameter $d_{avg} = 0.5(d + d_{in})$ [76]:

$$L_{spiral} = \frac{\mu n^2 d_{avg}}{2} \left(ln\left(\frac{2.46}{\beta}\right) + 0.2\beta^2 \right) \quad . \tag{2.3}$$

Equation 2.3 accurately predicts the inductance of a circular PCB spiral coil for most geometries (less than 8% error for $s \leq 3w$ [76]). The expression in Equation 2.3 can be modified for use with square, octagonal, and hexagonal coils, by adjusting the appropriate coefficients. This is detailed in Appendix A.

Series Loss

Determining the series loss R involves breaking down the loss into its constituent parts:

$$R = R_{DC} + R_{skin} + R_{prox} \tag{2.4}$$

where R_{DC} is the simple resistive loss of the conductor, R_{skin} is the loss due to the skin effect, and R_{prox} is the loss due to the proximity effect. The skin effect is the formation of a thin 'skin' of current at the edges of a conductor that is carrying high frequency current. The effect is well documented; procedures to calculate R_{skin} accurately for various conductor shapes appear as early as 1918 [77], [78]. Similar approaches have been used in recent years to predict skin effect losses in PCB spiral coils [37], [53], and wirewound coils [66] for biomedical WPT designs. Figure 2.7 illustrates the manifestation of the skin effect in conductors of different cross section. In the case of the axially symmetric circular wire, current shaped by the skin effect can be considered to flow in a layer of continuous depth δ. In the case of the PCB track, the distribution is less even, with current density being highest at the horizontal edges of the track.

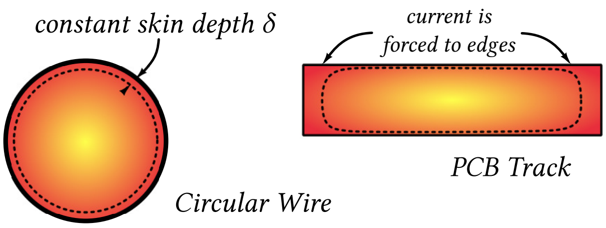

FIGURE 2.7: Skin effect manifestation in wire and PCB trace.

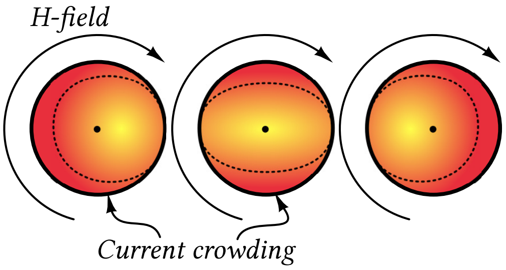

FIGURE 2.8: Proximity effect causing uneven current crowding in adjacent conductors.

To fully characterize the resistive losses however, the proximity effect must also be considered. The proximity effect describes the resistive loss that occurs due to adjacent current filaments flowing in the same direction. The closer the filaments, the greater the loss due to the proximity effect. Figure 2.8 shows how the H-field of one conductor interferes with the current density in adjacent conductors; the H-field generates an opposing current, which manifests as loss. Early work approximates the proximity effect losses as a constant proportion of the skin effect losses based on filament distance [72], [77]. Lammeraner and Stafl [79] consider the topic of both the skin and proximity effects in great detail from the perspective of Maxwell's equations, however the analysis is cumbersome and protracted. FEM based solutions are often used to predict proximity effect losses [80]–[83], or at least used to verify measurements [84]. More recently, the problem has been formulated into closed form expressions for the cases of round conductors; these solutions have been verified through both FEM simulation and measurements [85], [86]. The case of PCB spiral coils has also been considered, the proximity effect losses can be approximated using a similar process [37], [87]. Practical expressions for R_{DC}, R_{skin}, and R_{prox} are given below. Firstly, the DC loss can be considered a function of the conductor's geometry and resistivity:

$$R_{DC} = \rho \frac{l_c}{A_c} \quad , \tag{2.5}$$

where ρ is the resistivity of the material, l_c is the length of the conductor, and A_c is the cross-sectional area of the conductor. The length l_c can be determined by:

$$l_c = \pi d_{avg} n \tag{2.6}$$

where in the case of a single-layer solenoid $d_{avg} = d$, and in the case of PCB spirals:

$$d_{avg} = d - \frac{(w+s)n}{2} \quad . \tag{2.7}$$

In the case of pancake wire spirals, the $(w + s)$ term can be replaced with the winding pitch p to obtain the same result. R_{skin} is simple to calculate in the case of a circular conductor; first, the skin depth δ can be defined as a function of frequency:

$$\delta = \sqrt{\frac{2\rho}{\omega\mu}} \tag{2.8}$$

where $\mu \approx \mu_0$ for copper conductors. The loss due to the skin effect can therefore be considered in terms of the different cross sections of the full circular conductor and the current skin:

$$R_{skin} = \frac{l_c\rho}{\pi(d_0 - \delta)\delta} \quad . \tag{2.9}$$

For the case of a rectangular conductor, such as a PCB track, a convenient expression is given by Wheeler [88]:

$$R_{skin} = R_{DC}\frac{t_0}{\delta\left(1 - e^{-\frac{t_0}{\delta}}\right)}\frac{1}{1 + \frac{t_0}{w}} \tag{2.10}$$

where t_0 is the thickness of the PCB track (usually $\approx 35\mu$m for standard plated PCBs). An expression for R_{prox} is given by Kim et al. [86], which is applicable to any single-layer wire solenoid of otherwise arbitrary dimensions:

$$R_{prox} = \frac{2P_{prox}}{I_0^2} \approx 2R_{DC}\pi^2 r_0^2\left(\frac{2r_0}{\delta} - 1\right)\frac{H^2}{I_0^2} \tag{2.11}$$

where $r_0 = d_0/2$, P_{prox} is the power dissipation due to proximity effect losses, and H is the cumulative H-field experienced by the conductors in the solenoid. The analysis in [86] continues by describing a process for determining the H- field experienced by each conductor, normalized against I_0 (the current flowing in the coil), and as a function of the relative distance to the other conductors in the coil. In this way the total H-field can be determined as a function of the geometry of the coil. The process of calculating the cumulative H-field is detailed in Appendix A.1. In the case of PCB tracks, the significant asymmetry of the printed conductor cross-section (see Figure 2.7) renders the approach in Equation 2.11 inapplicable. An approximation by Kuhn et al. [87] defines the proximity effect loss in a printed spiral coil as:

$$R_{prox} = \frac{R_{DC}}{10}\left(\frac{\omega}{\omega_{crit}}\right)^2 \quad , \tag{2.12}$$

where ω_{crit} is the critical frequency at which current crowding begins to occur:

$$\omega_{crit} \approx \frac{3.1}{\mu_0}\frac{(w+s)\rho}{w^2 t_0} \quad . \tag{2.13}$$

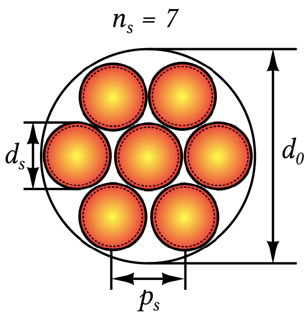

FIGURE 2.9: A Litz wire bundle consisting of 7 strands, with strand diameter d_s and strand pitch p_s.

It is important to note that the approximation in Equation 2.13 was initially specified for use with integrated coils; as a result it can lose accuracy at lower resisitivities. Utilizing Equations 2.4-2.13 as appropriate, the losses due to both the skin and proximity effect can be accurately modelled in a simple manner, for the most common cases of single-layer solenoids and PCB spirals.

Litz Wire

Section 2.2.1 considers coils constructed of single core magnet wire (copper wire coated with a few microns of insulating polymer), or PCB traces. However, for lower frequency systems (< 2 MHz [52]) attempting to maximize Q-factor, it may be desirable to construct a coil from Litz wire [31], [89]–[92]. Litz wire consists of one or more bundles of thin magnet wire strands connected in parallel, primarily to reduce skin effect losses. By reducing skin effect losses in this way, Litz wire links can achieve greater efficiency than solid wire links that would fit in the same geometry, as long as the frequency can be kept low enough. A cross-section of a Litz wire bundle is shown in Figure 2.9. Since each of the strands in a bundle is insulated from the others, each forms its own skin. As a result, a Litz coil will generally have a lower value of R_{skin} than a solid wire coil with the same value of d_0 [93]. While Litz wire is a useful means of reducing skin effect losses, the proximity effect becomes a bigger issue, particularly at higher frequencies [94]. Modelling losses in Litz wire is a difficult task, and FEM techniques are commonly employed to simulate them [85], [95]. However, there are also some fairly simple approximate methods to predict losses in Litz wire coils [93], [96]. By simplifying the analysis of Bartoli et al. [93] to consider a Litz wire solenoid of only a single layer, the total AC loss ($R_{skin} + R_{prox}$) can be approximated in terms of Kelvin functions[97] as:

$$R_{AC} \approx R_{DC}\frac{\gamma}{2}\left(A/n_s - 2\pi n_s\left(\zeta_1^2 + \zeta_2^2\frac{\psi}{2\pi n_s}\right)B\right) \quad ,$$
$$A = \frac{ber(\gamma)bei'(\gamma) - bei(\gamma)ber'(\gamma)}{ber'^2(\gamma) + bei'^2(\gamma)} \quad ,$$
$$B = \frac{ber_2(\gamma)ber'(\gamma) - bei_2(\gamma)bei'(\gamma)}{ber^2(\gamma) + bei^2(\gamma)} \quad , \tag{2.14}$$

where $R_{DC} = (4\rho l_c)/(n_s\pi d_s^2)$ is the DC loss, $\gamma = d_s/(\delta\sqrt{2})$, $\zeta_1 = (d_s/p)\sqrt{\pi/4}$ is an external porosity factor, $\zeta_2 = (d_s/p_s)\sqrt{\pi/4}$ is an internal porosity factor (p_s is the average strand pitch (see Figure 2.9)), and $\psi = (n\pi d_s^2)/(\pi d_0^2)$ is a packing factor. Equation 2.14 gives a good approximation of the total losses, as long as $\gamma \lesssim 1.2$ [93].

In all these cases, the calculated loss can be considered as a proportion of the coil's reactive impedance, in the form of its Q-factor:

$$Q = \frac{\omega L}{R} \quad . \tag{2.15}$$

An ideal coil would have zero loss, i.e. $Q = \infty$. The Q-factor is a useful parameter when considering PTE and PDL, and is discussed in Section 2.2.2.

Parasitic Capacitance

As the drive frequency of an inductor is increased, it presents a changing impedance as it approaches its SRF, appearing as if a capacitor C_P was connected in parallel. The source of this capacitance was originally considered to be the result of inter-winding capacitance [98]. The basis of the theory is that due to each coil winding laying parallel to its neighbors, there exists a capacitance between them. The idea can be extended to include printed spiral coils by including additional capacitances seen between PCB layers as well as tracks [37], [53]. This principle has been used for the purposes of approximation [99], [100], but FEM has proved necessary for accuracy [101]. The basis of the inter-winding capacitance theory has been brought into contention however, with an alternate method that considers the coil as a transmission line being developed by Knight [102]. This analysis has been corroborated by Payne, who gives simple approximations for determining the SRF (in MHz), providing measured results accurate to within 0.2% of the calculated values [103]:

$$f_{SRF(\lambda/4)} \approx \frac{\left(\frac{300}{4l_c(1+0.225d/l)}\right)^{0.8}}{(d^2/73p)^{0.2}} \tag{2.16}$$

Equation 2.16 gives the quarter wave resonant frequency in MHz. It is important to note that Equation 2.16 breaks down for coils with very few turns, since the approximation depends strongly on the pitch p and the ratio d/l. Equation 2.16 assumes that $\epsilon \approx \epsilon_0$. By determining f_{SRF} , it is possible to infer C_P using the standard resonance approximation equation [104]:

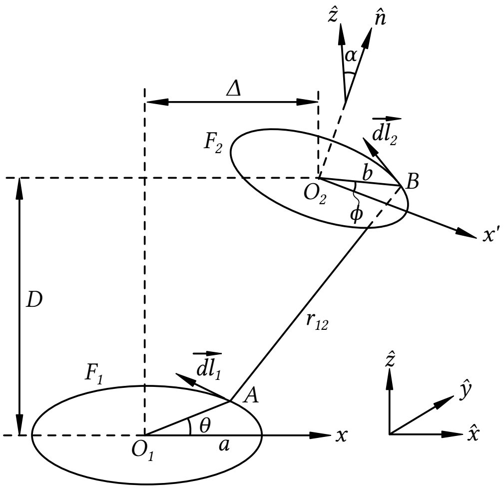

FIGURE 2.10: General case of two coupled circular filaments F_1 and F_2, with coaxial, lateral, and angular displacement. Remastered from [105]

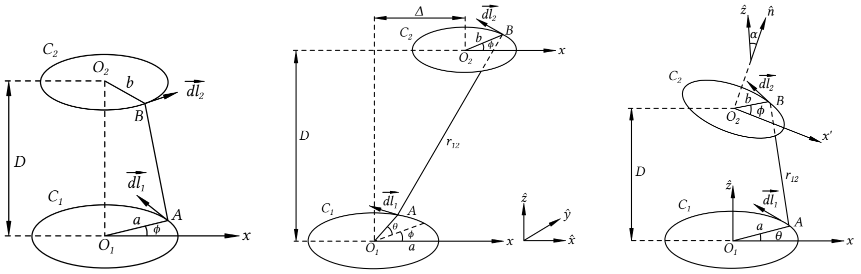

(A) Coaxial (B) Lateral (C) Angular

FIGURE 2.11: The three important special cases of the general case in Figure 2.10. Figures here are also remastered from [105].

$$C_P = \left(\frac{1}{2\pi f_{SRF}\sqrt{L}} \right)^2 \tag{2.17}$$

Generally, the quarter-wave SRF of Equation 2.16 can be considered to give the upper limit frequency for the usefulness of the lumped model. As a rule of thumb, C_P can be completely neglected if the SRF is much greater (10 × or so) than the operating frequency.

2.2.2 Link Modelling

With each coil modelled in accordance with Figure 2.6, the link itself must be modelled. This includes determining the mutual inductance of the link, as well as the gain, PTE, and PDL.

Mutual Inductance

A practical treatment of mutual inductance calculation is given by Soma and Galbraith, where each coil is considered as a series of circular filaments, each being coupled to all other filaments, dependent on their physical arrangement [105]. Figure 2.10 shows the general case of two filaments F_1 and F_2 with radii a and b, arranged with coaxial, lateral, and angular displacements, D, Δ, and α respectively. The general case can also be degenerated to three special cases, shown in Figure 2.11, where the displacement is purely coaxial, lateral, or angular.

It is important to note that these mutual inductance calculations assume that each coil turn can be approximated as a thin filament, i.e. $r_0 \ll r$. In the case of extremely compact coils [34], [106], the equations will progressively lose accuracy as r_0 approaches r.

The mutual inductance between these two filaments for purely coaxial displacement ($\Delta, \alpha = 0, D \neq 0$) is [105]:

$$M_{coax} = \mu_0 \sqrt{ab} G(\aleph)\,, \tag{2.18}$$

where

$$G(\aleph) = \left(\frac{2}{\aleph} - \aleph\right) K(\aleph) - \frac{2}{\aleph} E(\aleph) \tag{2.19}$$

$$\aleph = \sqrt{\frac{4ab}{(a+b)^2 + D^2}}\,, \tag{2.20}$$

where K and E are complete elliptic integrals of the first and second kind respectively. While the purely coaxial case is simple, it is more complex to describe the general case that includes lateral and angular displacements. Fortunately it is possible to separate the effects of lateral and angular misalignments, and consider them as essentially orthogonal [56], [105]. Soma presents expressions using numerical integration to calculate M for these cases, based on [107]. For the lateral misalignment case ($\alpha = 0, D, \Delta \neq 0$):

$$M_{lat} = \frac{\mu_0 ab}{2\pi} \oint \frac{cos\beta}{\sqrt{ab_{lat}}} G(\aleph_{lat}) d\phi\,, \tag{2.21}$$

where

$$\aleph_{lat} = \sqrt{\frac{4ab_{lat}}{(a+b_{lat})^2 + D^2}}\,, \tag{2.22}$$

$$b_{lat} = \sqrt{b^2 + \Delta^2 + 2\Delta b cos\phi}\,, \tag{2.23}$$

$$\beta = tan^{-1}\left(\frac{\Delta sin\phi}{b + \Delta cos\phi}\right)\,. \tag{2.24}$$

For the angular misalignment case ($\Delta = 0, D, \alpha \neq 0$):

$$M_{ang} = \frac{\mu_0 \sqrt{ab}}{\pi \sqrt{cos\alpha}} \int_0^{\pi} \left(\frac{cos\lambda}{cos\phi}\right)^{\frac{3}{2}} G(\aleph_{ang}) d\phi\,, \tag{2.25}$$

where

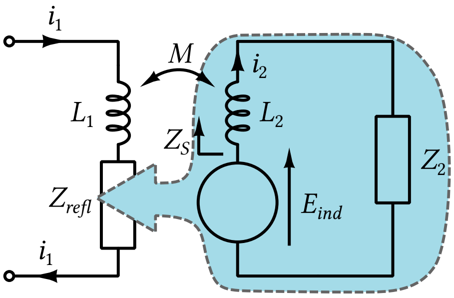

FIGURE 2.12: Simplified coupled circuit reflects an impedance in series with the primary.

$$\aleph_{ang} = \sqrt{\frac{\dfrac{4abcos\phi cos\alpha}{cos\lambda}}{a^2 + b^2 + D^2 - 2bDcos\phi sin\alpha + \dfrac{2abcos\phi cos\alpha}{cos\lambda}}} \,, \tag{2.26}$$

$$\lambda = tan^{-1}\left(\frac{sin\phi}{cos\phi cos\alpha}\right) . \tag{2.27}$$

Equations 2.18, 2.21, and 2.25 can be used to determine the mutual inductance between individual filaments; the total mutual inductance can be determined through summation across all the turns of each coil [108]:

$$M = \sum_{i=1}^{n_1} \sum_{i=1}^{n_1} M_{ij}(a, b, D, \Delta, \alpha) . \tag{2.28}$$

This mutual inductance can also be considered as a unitless coupling coefficient k:

$$k = M/\sqrt{L_1 L_2} . \tag{2.29}$$

Since k is normalized to the mean inductance of the two link coils, k values can be freely compared between links of arbitrary geometry.

Link Impedance

The previous sections have focused on converting geometric parameters to electrical parameters, aiming to determine all the parameters in Table 2.1. These electrical parameters can then be used to model the link in accordance with Figure 2.2. The element to consider first is the coupling of the secondary circuit into the primary, in order to determine the impedance presented by the link to the driver. The principle is described in detail by Terman as follows [51].

The current flowing in the primary coil will induce current in the secondary coil, since they are magnetically coupled. This current can be considered as resulting from a voltage in series with the secondary coil, shown as 'E_{ind}' in Figure 2.12. This now can be considered as a 'reflected load' at the primary side, allowing the the whole coupled secondary circuit to be considered simply as a complex impedance in series with the primary coil. The reflected load is defined as

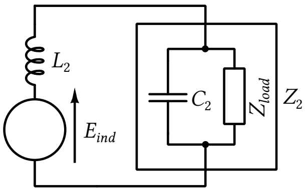

FIGURE 2.13: Example contents of Z_2 (see Figure 2.12) for a parallel resonant secondary coil.

$$Z_{refl} = \frac{(\omega M)^2}{Z_S} , \tag{2.30}$$

where Z_S is the impedance seen by the induced voltage E_{ind}, which is defined as

$$E_{ind} = -j\omega M i_1 = i_2 Z_S . \tag{2.31}$$

The principle is illustrated in Figure 2.12; the secondary side of the link can be transformed into the reflected impedance Z_{refl} in series with the primary coil. The true source of this apparent load that appears in the primary is the back-voltage induced from current flowing in the secondary. This back-voltage will oppose any voltage at the primary, and thus appears as if it is a complex load. Using this principle, the link impedance, gain, and efficiency can be readily calculated. For instance, the link impedance in the simplified case (as in Figure 2.12) is given by:

$$Z_{link(simple)} = j\omega L_1 + \frac{(\omega M)^2}{j\omega L_2 + Z_2} , \tag{2.32}$$

where Z_2 is the impedance seen by the coil L_2, usually formed of the resonating capacitor C_2 and output load Z_{load}. For the four NRIC configurations as in Figure 2.2, expressions for Z_{link} are given in Table 2.2, where Z_{L1} and Z_{L2} are the impedances of the coils including their parasitics, in accordance with Figure 2.6:

$$Z_{L1,L2} = \left(\frac{1}{j\omega L_{1,2} + R_{1,2}} + j\omega C_{P1,P2} \right)^{-1} . \tag{2.33}$$

If the operating frequency is well below the SRF of both coils, Equation 2.33 can be simplified to:

$$Z_{L1,L2} = j\omega L_{1,2} + R_{1,2} . \tag{2.34}$$

By substituting coil impedances from Equation 2.33 or 2.34 into the expressions in Table 2.2, Z_{link} can be calculated. With Z_{link} in place, gain, power, and efficiency figures can be determined.

Gain

While output power and link efficiency may at first seem like the most important parameters for a power transfer system, it is important to know the link gain in order

TABLE 2.2: Link Impedances in Accordance with Figures 2.2 & 2.3

Topology	Link Impedance Z_{link}
SS	$Z_{L1} + \frac{1}{j\omega C_1} + \frac{(\omega M)^2}{Z_{L2}+\frac{1}{j\omega C_2}+Z_{load}}$
SP	$Z_{L1} + \frac{1}{j\omega C_1} + \frac{(\omega M)^2}{Z_{L2}+\frac{1}{j\omega C_2+1/Z_{load}}}$
PS	$\left(j\omega C_1 + \frac{1}{Z_{L1}+\frac{(\omega M)^2}{Z_{L2}+\frac{1}{j\omega C_2}+Z_{load}}}\right)^{-1}$
PP	$\left(j\omega C_1 + \frac{1}{Z_{L1}+\frac{(\omega M)^2}{Z_{L2}+\frac{1}{j\omega C_2+1/Z_{load}}}}\right)^{-1}$

to determine power output, as well as to ensure sufficient voltage will be present at the receiver for the remote circuits to operate. As discussed in Section 2.2.1, the link gain A_v will either be a voltage gain or a transimpedance, depending on the primary tank configuration and primary driver. It is assumed that series-resonant primaries are driven by voltage sources and parallel-resonant primaries are driven by current sources. In both cases, the voltage output v_{out} (see Figure 2.3) can be defined in terms of the induced voltage E_{ind}, for SS and PS links:

$$v_{out} = \frac{E_{ind} Z_{load}}{Z_{L2} + \frac{1}{j\omega C_2} + Z_{load}}\ , \tag{2.35}$$

and for SP and PP links:

$$v_{out} = \frac{E_{ind}}{Z_{L2}\left(j\omega C_2 + 1/Z_{load}\right) + 1}\ . \tag{2.36}$$

Since E_{ind} can be determined in terms of the current i_1 flowing into Z_{refl}, see Equation 2.31, gains can be defined by expressing i_1 in terms of the input voltage or current. For SS and SP links:

$$i_1 = \frac{v_{in}}{Z_{link}}\ , \tag{2.37}$$

and for PS and PP links:

$$i_1 = \frac{i_{in} Z_{link}}{Z_{L1} + Z_{refl}}\ . \tag{2.38}$$

Therefore, the link gains for all four configurations can be defined:

$$A_{SS} = \frac{v_{out}}{v_{in}} = \frac{-j\omega M Z_{load}}{Z_{link}\left(Z_{L2} + \frac{1}{j\omega C_2} + Z_{load}\right)}\ , \tag{2.39}$$

$$A_{SP} = \frac{v_{out}}{v_{in}} = \frac{-j\omega M}{Z_{link}\left(Z_{L2}\left(j\omega C_2 + \frac{1}{Z_{load}}\right) + 1\right)}\ , \tag{2.40}$$

$$A_{PS} = \frac{v_{out}}{i_{in}} = \frac{-j\omega M Z_{load} Z_{link}}{\left(Z_{L1} + Z_{refl}\right)\left(Z_{L2} + \frac{1}{j\omega C_2} + Z_{load}\right)}\ , \tag{2.41}$$

$$A_{PP} = \frac{-j\omega M Z_{link}}{\left(Z_{L1} + Z_{refl}\right)\left(Z_{L2}\left(j\omega C_2 + \frac{1}{Z_{load}}\right) + 1\right)}\ . \tag{2.42}$$

PDL and PTE

Since the output voltage v_{out} is defined in Equation 2.35 and 2.36 as being across Z_{load}, the true power delivered to the load can be written simply as

$$P_{out} = \frac{|v_{out}|^2\ \Re\{Z_{load}\}}{|Z_{load}|^2}\ . \tag{2.43}$$

P_{out} will be maximized in the case that Z_{load} is purely real[1], i.e. the power factor is unity. If, for instance, the drive frequency differs from the resonant frequency of the receiving tank, v_{out} will have a phase lag/lead, which must be compensated for by adding a matching reactance to Z_{load}. Of course, the load matching theorem also applies; for SS and PS links where the receiving tank is resonating, Z_{load} should equal R_2, and for SP and PP links where the receiving tank is resonating Z_{load} should equal the parallel resistance of the receiving tank (R_{P2}). The parallel resistance of a coil can also be defined in terms of its series resistance and Q-factor (see Equation 2.15 and Figure 2.6):

$$R_P = R(Q^2 + 1)\ . \tag{2.44}$$

Calculating PTE is considered in detail in [65], where the link efficiency is considered in two parts: the efficiency from the transmitter to Z_{refl}, η_1, and the efficiency from the receiver to Z_{load}, η_2. Van Schuylenbergh assumes that both tanks are tuned to the operating frequency for the purpose of simplification [65], this is not assumed here for completeness. These efficiencies are defined as follows:

$$\eta_1 = \frac{P_{Z_{refl}}}{P_{in}} = \frac{|i_1|^2\Re\{Z_{refl}\}}{|i_{in}|^2\Re\{Z_{link}\}} = \frac{|i_1|^2\Re\{Z_{refl}\}|Z_{link}|^2}{|v_{in}|^2\Re\{Z_{link}\}}\ , \tag{2.45}$$

$$\eta_2 = \frac{P_{out}}{P_{Z_{refl}}} = \frac{|v_{out}|^2\Re\{Z_{load}\}}{|i_1|^2\Re\{Z_{refl}\}|Z_{load}|^2}\ . \tag{2.46}$$

---

[1] and by extension v_{out}, since v_{out} is dependent on Z_{load}

Equations 2.45 and 2.46 can be combined to determine the total link efficiency:

$$\eta_1 \eta_2 = \frac{P_{Z_{refl}} P_{out}}{P_{in} P_{Z_{refl}}} = \frac{P_{out}}{P_{in}} = \eta_{link} \, . \tag{2.47}$$

Considering the behavior of the link intuitively, if the coupling and load are such that Z_{refl} appears real, and both coils have high Q-factors ($R_{1,2} \longrightarrow 0$), then η_{link} will approach unity, assuming the power source is also impedance matched to Z_{link}. This behavior can be formalized in terms of the kQ product [109]–[111]:

$$k\sqrt{Q_1 Q_2} \, . \tag{2.48}$$

The Q part of the product is the geometric mean of the Q- factors of the two coils. The maximum theoretical efficiency can be shown to be directly proportional to Equation 2.48 [110]:

$$\eta_{link_{(max)}} = \frac{k^2 Q_1 Q_2}{\left(1 + \sqrt{1 + k^2 Q_1 Q_2}\right)^2} \, . \tag{2.49}$$

2.2.3 Limitations of Analytic Modelling

It is important to note that the analytic modelling techniques discussed in the previous subsections rely on the assumption that $\mu = \mu_0$ and $\epsilon = \epsilon_0$ everywhere in the system. As a result, they can be insufficient for modelling inductive links in complex environments containing combinations of tissue, electronics, epoxies, and other materials, all with different μ and ϵ values. Analytic methods can still be used to model simple muscular environments with good results however. For example, Jow et al. demonstrate errors of only a few percent between calculation and simulation for free space and muscle environments [53]. For these kinds of calculation, it is useful to note that, at lower frequencies, biological tissue can be considered to have $\mu = \mu_0$; ϵ however is more variable, and particularly dependent on tissue type [112], [113]. For environments containing layers of materials with many different permittivities, analytic calculations become more difficult to perform; as a result, therefore FEM simulations or physical measurements may be necessary in later design iterations if precise results are required.

2.3 Considerations for Power Transfer

When undertaking a link design, constraints and targets must be considered. Common constraints include the geometry, materials, and operating frequency; common targets include PTE, PDL, and misalignment tolerance. Considering the flow diagram in Figure 2.4, the main iteration is in coil geometry, as the geometry determines the electrical parameters, and thus the link performance. It is therefore crucial for the designer to understand how to adjust geometric parameters in order to obtain the desired change in electrical parameters. This section reviews a number of factors

TABLE 2.3: Example Link Specifications

Parameter	**Value**
Coil diameter ($d_{1,2}$)	20 mm
Wire diameter ($d_{0(1,2)}$)	0.3 mm
Winding pitch ($p_{1,2}$)	0.6 mm
Number of turns ($n_{1,2}$)	8
Inductance ($L_{1,2}$)	1.88 μH
Capacitance ($C_{1,2}$)	293 pF
Tuned frequency ($f_{0(1,2)}$)	6.78 MHz
Output load (Z_{load})	2.1 kΩ
Configuration	SP

that should be considered during this process, describes relations between geometric and electrical parameters, and discusses how to determine whether design targets are feasible or not.

2.3.1 Frequency Splitting

The previous analysis in Section 2.2 has implied that, in an NRIC link, both tanks should be tuned to the same frequency. This intuitively appears to be the best approach to maximize PDL and PTE, because if both tanks are driven at their resonant frequencies, they will appear to be real. The problem with this assumption is that it does not account for the fact that Z_{refl} appears as a complex impedance in series with the primary coil, whose value is dependent on the coupling. This manifests in the form of frequency-splitting, also known as pole-splitting, where the optimum drive frequency of the link varies from the tuned frequency as the coils are brought closer together [68], [114]–[120]. The effect can be observed directly by plotting parameters such as the link gain, impedance, and efficiency against changes in drive frequency and coupling. Figures 2.14 and 2.15 show the link efficiency and power output for an example link in SP configuration driven by an ideal 1V source, in accordance with Equation 2.43 and Equation 2.47. The link specifications that are independent of frequency and coupling are given in Table 2.3; both coils are identical wire solenoids, arranged in coaxial alignment ($\Delta, \alpha = 0$). Figures 2.14 and 2.15 clearly show that, despite both sides of the link being tuned to resonate at 6.78 MHz, reducing the separation distance to below 20 mm induces splitting in both the PDL and PTE responses. While it is possible to maintain a high PTE with a fixed frequency of 6.78 MHz up to very short spacing distances (see Figure 2.15), the accompanying PDL drops significantly (see Figure 2.14). It should be noted that the efficiency plot in Figure 2.15 assumes the link is being driven by an ideal source; for a real source, the efficiency at the center frequency will likely drop due to the change in Z_{link}. For links with variable separation,

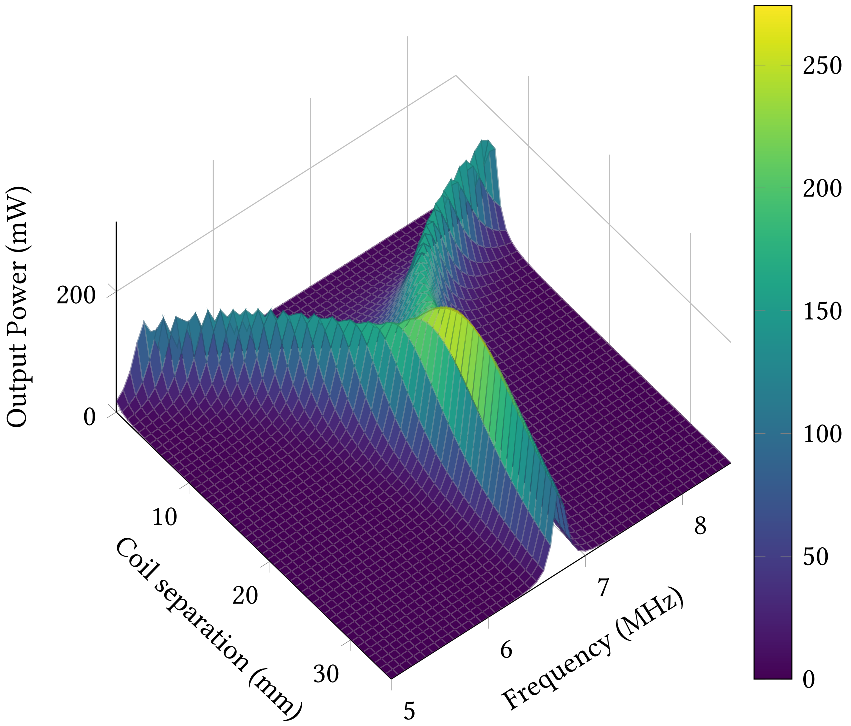

FIGURE 2.14: Frequency splitting in power output from an example SP link driven by a 1 V source.

frequency splitting must be considered if both high PTE and PDL are to be maintained. Splitting is generally tackled by implementing an adjustable frequency drive to track the optimum frequency [59], [119], [120], or adjustable link components to force the optimum frequency back to the drive frequency [114], [118], [121].

The exact optimum frequencies can be determined by partial differentiation. For instance, solving

$$\left.\frac{\partial P_{out}}{\partial \omega}\right|_{M_{min}<M<M_{max}} = 0\,, \tag{2.50}$$

(where $M_{min} < M < M_{max}$ describes the desired range of mutual inductances) will produce a series of positive real root frequencies; odd roots correspond to peaks and even roots correspond to troughs. Equation 2.50 can be most easily solved through symbolic mathematical software in order to find the root paths. An alternative approach is given by Niu et al. [59], where direct expressions are given for root paths for an ‘SS’ link. By controlling a variable frequency drive in accordance with odd roots from Equation 2.50, the power output can be maximized regardless of coil separation. These odd roots can be automatically tracked using a zero-phase-tracking system, to ensure the system remains in resonance [120].

Equation 2.50 shows partial differentiation of P_{out} w.r.t. ω, but other link parameters (e.g. η_{link}, Z_{link}, A) can be treated in the same way to obtain the splitting characteristic. Figure 2.16 shows the three root paths that can be obtained by partially differentiating Z_{link} w.r.t. ω.

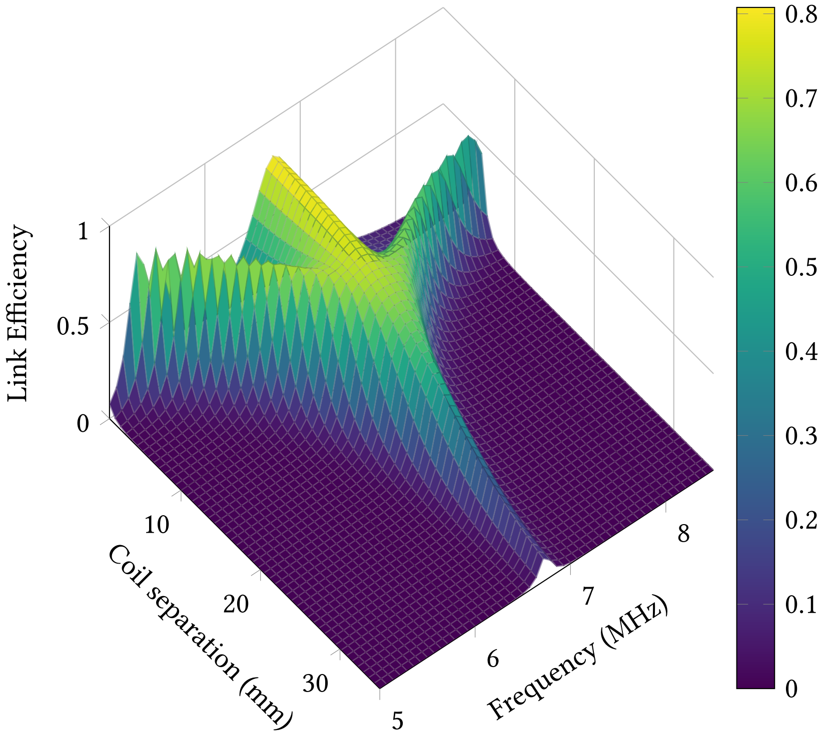

FIGURE 2.15: Frequency splitting in efficiency output for an example SP link driven by a 1 V source.

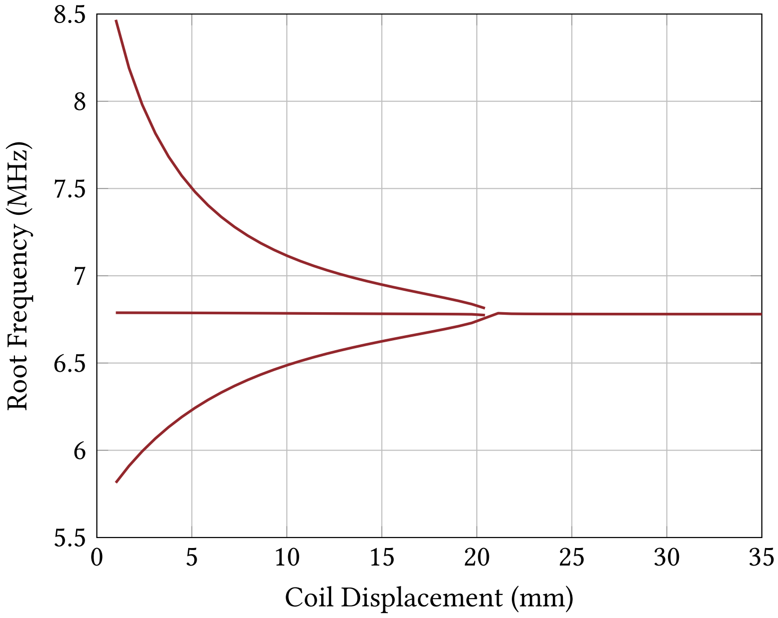

FIGURE 2.16: Root paths showing frequency splitting in the link impedance of the example link.

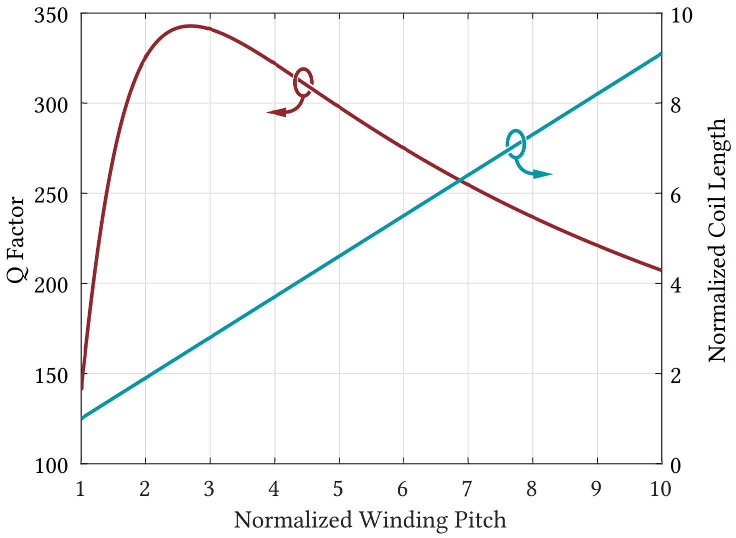

FIGURE 2.17: Optimizing winding pitch to maximize Q comes at the cost of increased coil length. Pitch is normalized to the minimum pitch $p = d_0$.

2.3.2 Maximizing the kQ Product

Considering the kQ product from Equation 2.48 as a figure of merit, an ideal link can be considered as one with a kQ product that tends to infinity. Adjusting geometric parameters with the aim of maximizing kQ however is largely an exercise in tradeoffs. For instance, Figure 2.17 shows the effect of adjusting the winding pitch of a solenoid (with otherwise the same geometry as in Table 2.3) on its Q-factor and length. By packing the windings as close as possible, the Q-factor will be suppressed by proximity effect losses, but if the pitch is too large, the Q-factor drops due to reduced inductance. In this example, to maximize Q by increasing the pitch requires an increase in the coil length of 2.5 × , which will have a detrimental effect on the coupling k, assuming the edge to edge separation D remains the same. This is illustrated in Figure 2.18; increasing the pitch effectively increases the mean distance between turns, reducing the coupling coefficient. Maintaining a winding pitch that is greater than the minimum can also pose a practical problem; the coil must be constructed with a former or glue such that the desired pitch is maintained. This is not a problem for PCB based coils; the tracks are fixed in place on the substrate, guaranteeing the desired pitch.

It is important to note also that Q-factor optimization by pitch adjustment is affected by operating frequency. This is particularly important to consider in variable frequency drive systems, as it will dictate the optimum splitting root path to follow. This can be seen in Figures 2.14 and 2.15; the lower frequency splitting path gives slightly higher power output and efficiency figures than the higher frequency path, due to the dependence of Q-factor on frequency. The effect of frequency on Q-factor is further highlighted in Figure 2.19; as the operating frequency increases, the optimum winding pitch also increases.

Similar to varying the winding pitch, varying the number of turns in each coil also

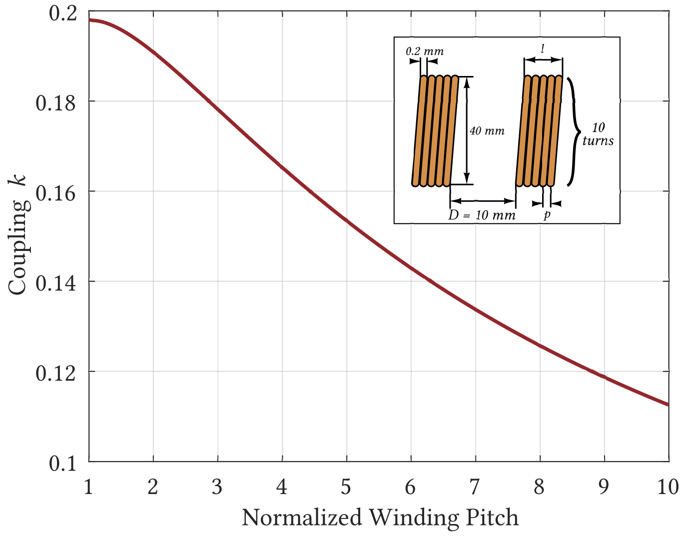

FIGURE 2.18: Decrease in coupling coefficient between two identical coils as winding pitch is modified.

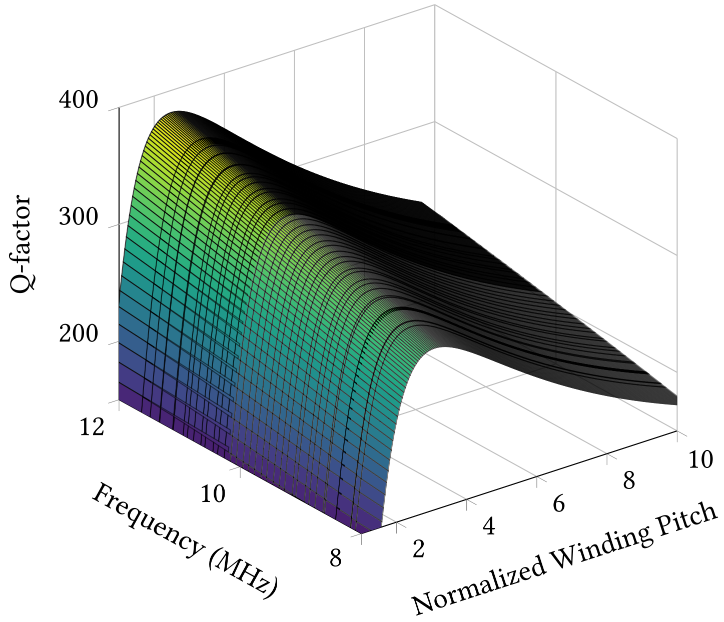

FIGURE 2.19: Changing Q-factor as winding pitch is modified, with respect to frequency.

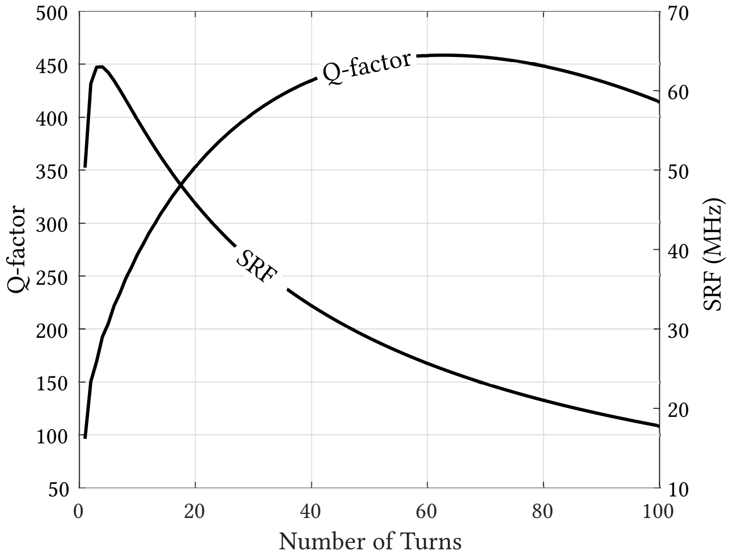

FIGURE 2.20: Effect of increasing the number of turns on Q-factor and SRF. Parameters otherwise the same as in Table 2.3.

reveals tradeoffs. Considered qualitatively, increasing the number of turns has the effect of increasing the length, inductance, and Q-factor up to a limit; it also affects the SRF. Figure 2.20 shows how increasing the number of turns increases the Q-factor, up until the point at which the increased losses outweigh the increased inductance. Similar to the case of winding pitch, the increase in length also causes a decrease in k, so it is better to adjust turns aiming to maximize kQ, rather than just the Q-factor. Since increasing the number of turns also reduces the SRF, the point at which the SRF approaches the operating frequency can be considered a hard limit on the allowed number of turns in either coil.

2.3.3 Displacement Resilience

Resilience to displacement, particularly in the lateral and angular sense, is a target that depends strongly on application. In cochlear implants for instance, link coaxial alignment can be assumed, as the coils are magnetically aligned [122]. In the case of spectacle-mounted retinal stimulator links however, this alignment cannot be guaranteed [26]. In such cases, it is more desirable to ensure that an inductive link is resilient to displacement variations than solely focusing on maximizing PTE and PDL. A simple method of improving displacement tolerance is described by Donaldson and Perkins [55], based on the work of Ko et al. [54], where it is suggested that by determining a ratio of coil diameters that maximizes k for a given D, resilience to displacement in general will be maximized. This conclusion can be explained by the fact that any displacements, axial, lateral, or angular, will reduce k, and so by maximizing k for a given arrangement, this reduction can be mitigated. Ko gives the

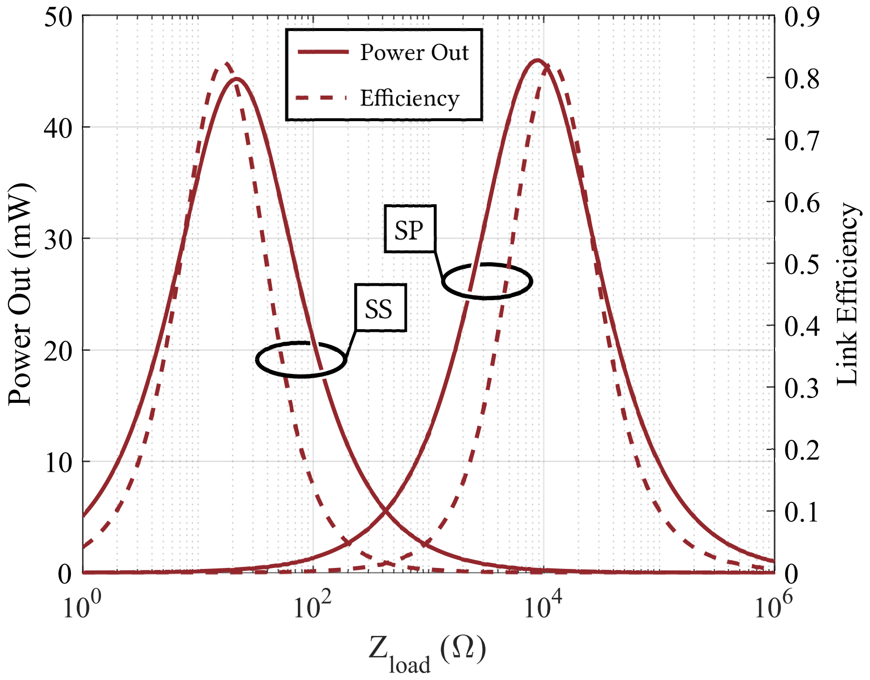

FIGURE 2.21: Curves of PDL and PTE for SS and SP configurations as Z_{load} is varied. Parameters are otherwise the same as in Table 2.3. D = 40mm.

ideal transmitter coil diameter d_1 for maximum resilience in terms of a given receiver coil diameter d_2 and coaxial distance D [54]:

$$d_1 = \sqrt{d_2^2 + 4D^2}\,. \tag{2.51}$$

In addition to resilience considerations, since k is maximized by selecting diameters in accordance with Equation 2.51 the kQ product is increased, boosting PTE and PDL.

By increasing the ratio d_1/d_2 even further, k can be kept very stable against displacements, at the cost of the absolute value of k. This strategy is employed in wireless powering of endoscopic capsules, where the receiver is subject to significant movement, and PTE and PDL are not inherently critical [123]–[125].

Adaptive systems are also popular for improving displacement tolerance. Figures 2.14 and 2.15 show how coupling changes due to displacement can result in a change in optimum frequency; by adapting the operating frequency or resonant capacitance, such systems are more resilient to these changes in displacement [62], [63], [121], [126]–[128].

2.3.4 Resonant Topologies: Which one to Use?

In addition to optimizing the coil geometry for a given application, a resonant topology that is appropriate to the application must also be selected. Each of the four resonant topologies as shown in Figure 2.2 suits a different application, since each topology presents a different impedance. The problem of topology selection has been considered

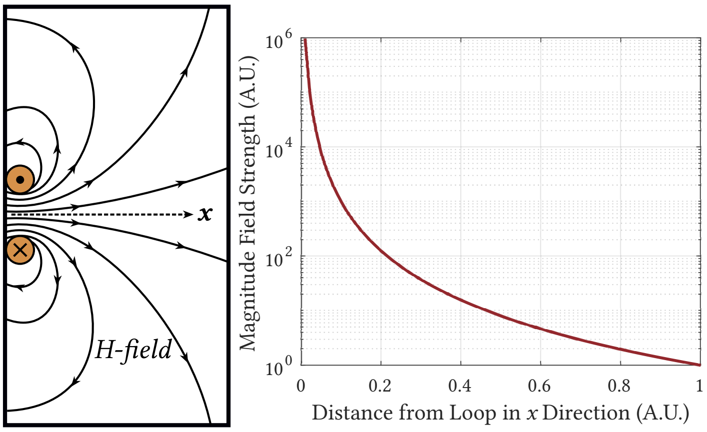

FIGURE 2.22: *Left*: magnetic flux lines from an energized loop of wire, *right*: field strength for increasing distance from the loop in coaxial alignment.

in the literature, with differing conclusions about when to use series- and parallel-resonant topologies [38], [58], [129].

Considering the link as two coupled resonant tanks, the appropriate topology can be determined by observing the impedance of each tank relative to the impedance of the power amplifier and the receiver, and matching them. In Figure 2.2, series-resonant primaries are driven by voltage sources, and parallel-resonant primaries by current sources for this reason. The principle holds when considering the secondary side of the link; for high output impedances, a parallel-resonant secondary will improve PTE and PDL, and vice-versa. This difference is demonstrated in Figure 2.21; an otherwise identical link will have very different optimum load conditions depending on its resonant topology. Here the SP link works best for a Z_{load} that is 3 orders of magnitude greater than the optimum Z_{load} for the SS configuration.

It is for this reason that the SP link configuration is common for biomedical inductive links [55], [130]–[133]. The receiver will commonly have a relatively high input impedance, and the driver will often be a Class-D or -E amplifier, suited to driving low impedances [26], [123], [134], [135]. If maximizing PTE and PDL are crucial, it is possible to determine the optimum load impedance for a given topology analytically [44]. This analysis has been adopted for the design of adaptive rectification circuits, that aim to present an optimum impedance to the link at all times by varying the rectification parameters (duty cycle, frequency etc.) [136]–[138].

2.3.5 Quality Factor Degradation (Q-loading)

After determining the appropriate resonant topology, it is important to consider the effect that the load of the link has on the Q-factor of the secondary.

Considering Figure 2.23, it is clear that the load at the output adds to the coil loss resistance directly. In the case of the series secondary, the loaded Q is simply:

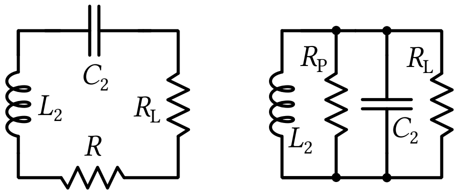

FIGURE 2.23: Loaded series (left) and parallel (right) secondaries.

$$Q_{2(loaded)} = \frac{\omega L_2}{R + R_L}\,. \tag{2.52}$$

It is less simple for the parallel secondary however. By rearranging the definition from Equation 2.44, it becomes clear that once Q is large enough, the following simplification can be made:

$$R_P = \omega L\,(Q + 1/Q) \approx \omega LQ\Big|_{Q>10} \therefore Q \approx R_P/\omega L\,. \tag{2.53}$$

This allows the loaded Q for the parallel secondary to be defined as follows:

$$Q_{2(loaded)} \approx \frac{1}{1/R_L + 1/R_P}\frac{1}{\omega L} = \frac{R_L Q}{R_L + Q\omega L}\,. \tag{2.54}$$

Equations 2.52 and 2.54 show that Q suffers as the load increases and decreases for series and parallel links respectively. It is also important to note that the Q-loading effect applies in the same way to the transmitter side; instead of considering the load resistance, the output resistance of the driver should be considered. It can usually be safely assumed that the driver will have a far smaller effect than the load however.

Once loaded Q-factors have been determined, they should be substituted back into the efficiency equations, such as Equation 2.49, to get a more realistic estimate of link efficiency.

2.3.6 Refining Targets

During the design process, it may become apparent that the design targets are impossible to achieve given the initial design constraints. For example, if both coils are limited to a diameter of 10 mm, and the target axial distance is 50 mm, it will be impossible to achieve a high PDL and PTE. The triad inset in Figure 2.4 qualitatively shows three desirable design features that must be traded off against each other. At most, two out of three of the features can be achieved; sacrificing one feature will often improve the other two. This triad should be considered when determining an initial link specification, in order to ensure that the desired targets are reasonable given the constraints. When trying to determine if a target coil separation distance is reasonable, a useful rule to remember is the fact that the magnetic field strength from an energized coil decays proportional to the inverse cube of the coaxial distance from its center. This is illustrated in Figure 2.22; the current- carrying loop is essentially a magnetic dipole, and shows the characteristic divergence in its flux lines as

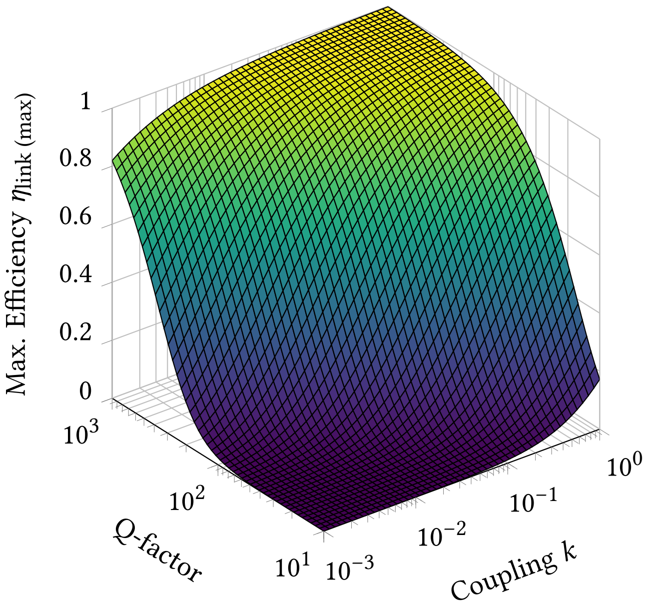

FIGURE 2.24: Maximum theoretical link efficiency (according to Equation 2.49), as the coupling coefficient and average (geometric) Q-factor are varied.

distance from the loop increases. The number of flux lines captured by the receiving coil will determine the coupling coefficient k between the two coils. Since NRIC does not require extremely high coupling for high PTE and PDL, the coils do not have to be extremely close to each other, as in non-resonant coupling[2].

The exact minimum value of k to maintain a given target value of PTE therefore depends more on the average Q of the two coils. Figure 2.24 shows how the maximum theoretical PTE can remain high even for very low coupling coefficients, providing the average Q-factor is high. The maximum obtainable Q-factor will depend on the available materials, operating frequency, dimensions etc, as discussed in the previous sections.

This principle also applies when considering coil size and displacement tolerance. Smaller coils will generally have a lower Q and worse overall displacement tolerance; the smaller coil size makes the loop appear less like a dipole.

2.4 Software and Design Example

To automate some of the processes in Figure 2.4, the Coupled Coil Configurator (CuCCo) software has been developed for MATLAB [2]; an early version of the software is currently available for download, is in active development at the time of writing, and is licensed under the GNU GPLv3 [139]. The aim of CuCCo is to provide functions that perform geometric to electrical parameter conversion, and link performance prediction purely through analytical calculation. The motivation

---

[2] Referring back to Equation 2.49: for *resonant* systems as $Q \longrightarrow \infty$, high efficiency can be achieved, even with low coupling factors. Non-resonant systems must instead rely *only* on high coupling to achieve good efficiency.

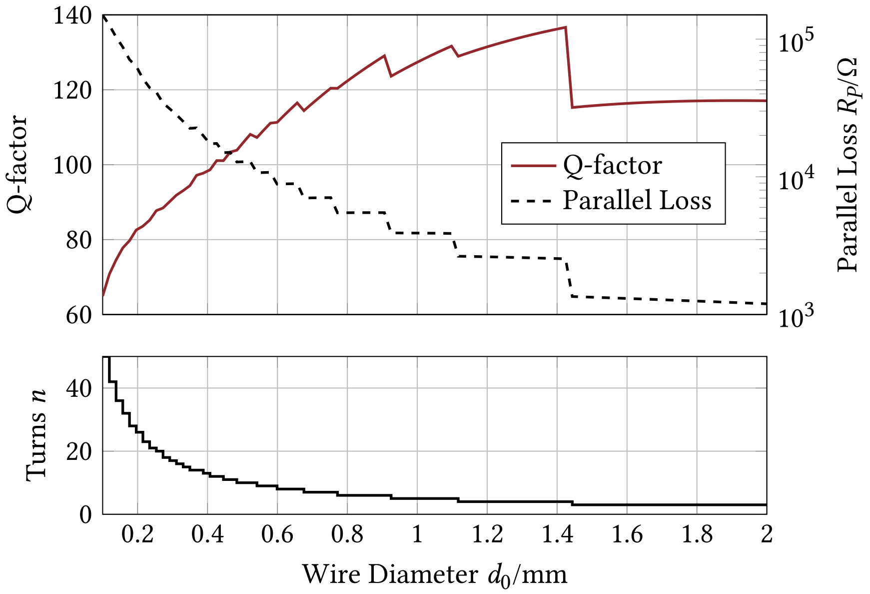

FIGURE 2.25: Finding optimum Q-factor as wire diameter is varied, following diameter and length constraints.

behind creating CuCCo was to provide a single tool that fills the gap between spice-like circuit simulation and FEM solver software. Instead of having to simulate coil geometries in FEM and convert them into electrical parameters for circuit simulation and link characterization, CuCCo aims to provide both functions with less overhead, by employing an analytic approach. The methods in this chapter are mostly included in CuCCo, to obviate the need for the reader to re-implement them themselves. The plots throughout this chapter have all been generated using calculated results from CuCCo. The following section is a design example, to demonstrate some of the capabilities of the software, and to show how to employ the principles in Sections 2.2 and 2.3 in an example application.

2.4.1 Design Example: Cochlear Implant

Constraints and Calculations

Typical cochlear implants require around 40 mW of power at the receiver, to be delivered through the skull by small coils aligned with a permanent magnet [122]. For this example, both coils should have diameters no larger than 20 mm, and should be within 4-6 mm in length. Typical temporal skull thicknesses range from 6- 12 mm [140]; the link should therefore function for coaxial D values in this range. Finally, PTE is a high priority for this example; higher PTE translates to a longer battery life, which is beneficial for the patient. For simplicity, a fixed-frequency non-adaptive driver running in the ISM band at 6.78 MHz is assumed. The receiving coil should feed a rectifier and produce at least 13 V (dc), to provide 12 V after regulation, for the stimulator circuit.

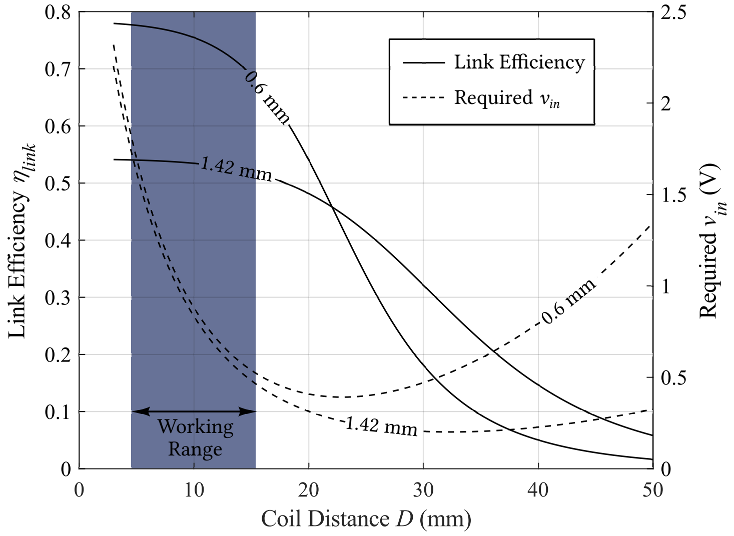

FIGURE 2.26: Curves to show link efficiency and the required input voltage to achieve 40 mW output from an SP configured link, coil geometries in accordance with the text and Figure 2.25, wire diameters noted on the curves.

To begin, the requirements of the receiver should be considered. If the implant requires 13 V, and will draw a maximum of 40 mW, this can be translated to a load:

$$R_{impl} = \frac{V^2}{P} = \frac{13^2}{40 \times 10^{-3}} = 4225\Omega\ . \tag{2.55}$$

Equation 2.55 gives the load presented by the implant after the rectifier. A simple method of including the effect of a single diode rectifier is given by Donaldson and Perkins [55], where the equivalent load seen by the link can be considered in terms of R_{impl}[3]:

$$R_L = \frac{R_{impl}}{2} \approx 2113\Omega\ . \tag{2.56}$$

Given this high value of R_L, a parallel resonant secondary is most appropriate for impedance matching (see Figure 2.21). The next step is to determine the optimum geometry given the constraints. Figure 2.25 shows the Q-factor, parallel loss resistance, and number of turns against changes in wire diameter for a single-layer solenoid, with minimum pitch, and its length limited to the 5 mm constraint. The number of turns is maximized to fill this length constraint. It should be noted that the coil series loss is assumed to have 50 mΩ added in series, to include losses from connecting PCB traces, solder joints etc. This small additional loss causes the drop in Q- factor as d_0 rises above 1.4 mm in Figure 2.25. The parallel loss resistance R_P can be computed from the series loss resistance R_S and the quality factor Q:

---

[3] It should be noted that this method is a simplification; relying on the assumption that a single diode rectifier acts as a perfect peak rectifier. For a more accurate result, a more thorough analysis would be necessary; nonetheless this method gives usable results for the design process.

TABLE 2.4: Cochlear Implant Example Link Specifications.

Parameter	**Value**
Coil diameter ($d_{1,2}$)	20 mm
Wire diameter ($d_{0(1,2)}$)	0.5 mm
Winding pitch ($p_{1,2}$)	0.6 mm
Number of turns ($n_{1,2}$)	8
Inductance ($L_{1,2}$)	1.87 μH
Capacitance ($C_{1,2}$)	295 pF
Tuned frequency ($f_{0(1,2)}$)	6.78 MHz
Output load (Z_{load})	2 kΩ

$$R_P \approx Q^2 R_S \, . \tag{2.57}$$

It follows from the maximum power transfer theorem that when $R_L = R_P$, the output power will be maximized. Figure 2.25 shows that to maximize PDL the optimum wire diameter is 1.42 mm; where the Q-factor is approximately 136, the coil has 4 turns, and the parallel loss is approximately 2.5 kΩ. While this receiver coil geometry maximizes PDL, the PTE will be limited to ≈ 50% since $R_P \approx R_L$. To increase the PTE therefore, the wire diameter should be reduced to a value that yields a higher parallel loss, without losing too much Q-factor. Reducing the wire diameter down to 0.6 mm for instance gives a 350% improvement in R_P (R_P = 8.85kΩ), at the cost of a 23% drop in Q-factor (Q = 111). Since the coils can be assumed to have good coaxial alignment, identical Tx and Rx coil geometries are suitable. Figure 2.26 shows the link efficiency difference between the 0.6 mm and 1.42 mm wire diameter coils, when configured as an SP link, as well as the input voltage required to maintain 40 mW in the 2.1 kΩ load. Since the relevant distances for this example are 6-12 mm, the 0.6 mm coils show much better performance, maintaining link efficiency from 73.6% to 77.3% over this range. By comparison, the 1.42 mm coils achieve a maximum efficiency of only 54% at 6 mm separation. In both cases, an input voltage of 0.5 V – 2.0 V is required; this can be implemented as a fixed 2.0 V input voltage, which can then be regulated at the receiver side. Alternatively, if the Rx can communicate with the Tx, the Rx can command the Tx to increase, decrease, or maintain the input voltage to perform regulation.

Experimental Validation

The proposed design was manufactured and measured to validate the predictions in the previous section. The measured parameters of the manufactured coils are given in Table 2.4. In this example, 0.5 mm diameter wire was used instead of 0.6 mm, but the pitch was maintained at 0.6 mm. The measured Q-factor of 127 shows a good correlation with the predicted Q of 115 from Figure 2.25. The link was arranged as shown in Figure 2.27, with the coils in coaxial alignment, separated by D mm. The signal generator used was an Agilent 33250A, and the oscilloscope was an Agilent

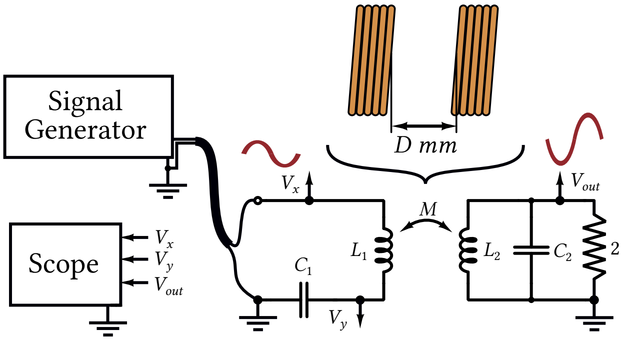

FIGURE 2.27: Diagram of the test arrangement, measured voltages are annotated.

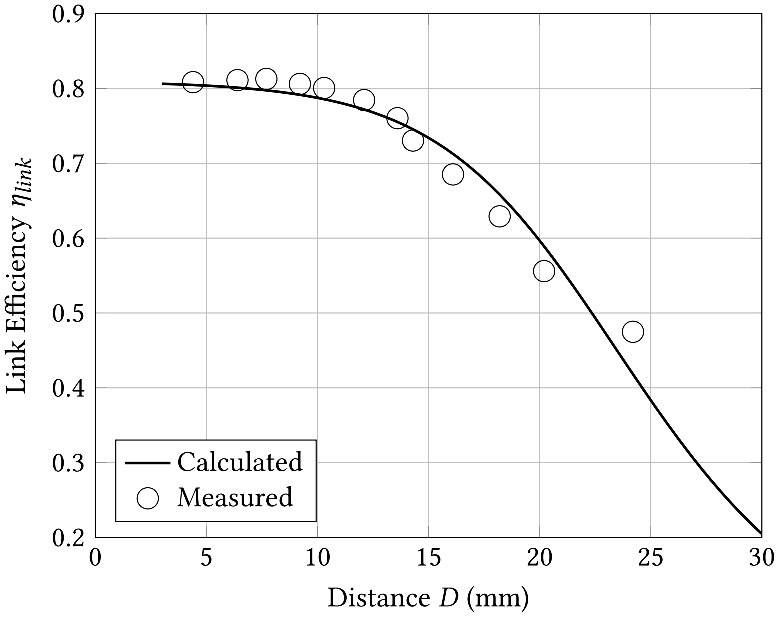

FIGURE 2.28: Measured and calculated link efficiency for the constructed link, maintaining 40 mW at a 2 kΩ load.

MSO6104A. V_{out} was measured to maintain a constant voltage of 9.0 V (p-p), translating to 40mW (p-p) at the output. All voltages in the testing process are sinusoid signals. By measuring the voltages V_x and V_y, i_1, and Z_{refl}. Using these, η_1 can be determined.

$$i_1 = \frac{V_y}{Z_{C_1}} = \frac{V_x - V_y}{Z_{L_1} + Z_{refl}} \tag{2.58}$$

$$\therefore Z_{refl} = \frac{V_x - V_y}{i_1} - Z_{L_1} \,. \tag{2.59}$$

Since $Z_{link} = Z_{L_1} + Z_{C_1} + Z_{refl}$, the results from Equations 2.58 and 2.59 can be applied to Equation 2.45 to determine η_1. Since the link is being operated at the resonant frequency of the Rx (and the Tx), it is simpler to determine η_2 by using the measured Q of the Rx, and the α parameter [65]:

$$\eta_2 = \frac{Q_2}{\alpha + Q_2} \tag{2.60}$$

where $\alpha = 2\pi f_0 C_2 R_{out}$, and f_0 is the resonant frequency of the Rx. The measured efficiency is shown in Figure 2.28, and is in good agreement with the calculated prediction.

2.5 Concluding Remarks

This chapter serves as a collection of the key formulae required to design, implement, and optimize inductive power links for biomedical applications. While some configurations were not considered, such as 3- or 4-coil links [61], [66], or solenoids with more than one layer, the most common methods were considered in sufficient detail to realise efficient inductive link designs, as shown in the example.

Of particular interest are some conclusions presented in this chapter that go against otherwise published canon. Firstly, the equation for finding the self resonant frequency of a solenoid given by Payne [103], based on the work of Knight [75]. This result entirely contradicts the prevailing wisdom regarding ‘inter-winding capacitance’, and the work of these two authors goes a long way to provide an alternative and compelling explanation for the self-resonance phenomenon in coils. Second is the conclusion shown in Figures 2.17 and 2.19, where the winding pitch[4] is shown to be a significant factor when determining the Q-factor of power transmission coils. By minimizing the coil pitch, more turns can be packed into the same space to boost the inductance, but at very tight pitches this extra inductance is offset by higher proximity effect losses. A coil with a fully packed winding pitch will generally have a much lower Q-factor than an otherwise identical coil with one or two fewer turns and a looser pitch. This is contrary to the conclusions drawn by analyses that neglect the proximity effect, where it is suggested that the pitch should be minimized [37].

---

[4] or w/s ratio in the case of PCB spirals.

While this chapter is not an exhaustive treatment of the subject, it gives a strong foundation of the theory and practice of inductive link design, providing simple analytic methods alongside a presentation of past and present work from the field.

Optimum Frequency Tracking for Power Transfer to Passive Implants

3

The work in this chapter was first published in the proceedings of the IEEE EMBC [119], and then in MDPI Sensors [120]. This chapter contains some further details not present in the original papers.

3.1 Introduction and Context

In fixed frequency WPT systems, uniform power delivery is commonly achieved by sensing the DC load voltage, transmitting its value to the transmitter via back-telemetry, and appropriately adjusting the supply voltage at the transmitter [26], [134], [141]. This method is suitable as long as the transmitter and receiver units are working close to resonance. Under overcoupled conditions, a significant increase in primary supply voltage is required to compensate for the occurrence of frequency splitting. This leads to a consequent drop in system efficiency. Alternative methods rely on careful optimization of the coil design to allow for coupling insensitive power transfer [118], but fail to address deviations from optimal operation arising from drifts in coil electrical parameters and geometric deformations. A number of adaptive systems have been described that accomplish power regulation in the secondary by electronically varying inductance [142], [143] or capacitance [144] in either the primary or the secondary tank circuit. However, component variations and drift may further reduce the link efficiency, in particular where flexible and stretchable coils are used, whose parameters may fall outside the available compensation range. In addition, the achievable frequency resolution is determined by the number of taps in the tuning circuit, which limits the improvement in system efficiency that can be obtained. A triple-loop automatic tuning system including transmitter and receiver tuning and power control is reported in [145]. In addition to the limited resolution available, this system is only suitable for operation at a fixed frequency, and relies heavily on back telemetry to inform local control units.

An alternative approach to these methods is to directly control the drive frequency of the WPT system [146]. This has the benefit of requiring no variable link components, only a variable frequency synthesizer. There are several benefits to this approach. Firstly, the design of the power transmitter can be considered largely separately from the design of the coils, as long as the frequency synthesizer has a wide range.

Secondly, a variable frequency synthesizer can be integrated on chip, saving valuable space in a compact transmitter, compared to variable link components. Additionally this approach requires no back-telemetry, the link state is measured and maintained from the primary side. This makes this method suitable for use with passive implants with no back-telemetry; the transmitter can determine the optimum frequency itself without needing to interrogate the receiver.

This chapter presents an active compensation method for frequency splitting, based on optimum frequency tracking (OFT) in the overcoupled regime [67], [119]. It can operate over a wide frequency range, and does not require the use of variable capacitors or inductors. A simple analytical derivation of the link gain is presented, that accounts for different coupling and load conditions. Theoretical link gain profiles are derived for a series-parallel link operating at fixed and variable frequency. A compact closed-loop automatic frequency tuning system is presented. The link efficiency is optimized by sensing the phase between the primary voltage and current, and adjusting the frequency of the transmitter power amplifier. This implementation uses a custom designed fully integrated power amplifier with an on-chip frequency synthesizer [147], which allows for very fine frequency resolution to be obtained.

The rest of the chapter is organised as follows. Section 3.2 reviews some of the relevant theory for this application. Section 3.3 describes the proposed system. Section 3.4 describes the testing methodology and the measured results from employing the OFT compensation method. Section 3.5 concludes the chapter, discussing the key aspects of the system and potential future developments.

3.2 Frequency Splitting in Passive Implants

The phenomenon of frequency splitting is discussed in §2.3.1; the fact that it can cause significant power drops in power single-frequency links is the primary motivation for the work in this chapter. In the case of active implants with back-telemetry, variations in coupling or load can be compensated for by communicating the status of the receiver voltage back to the primary side, and adjusting the transmitter accordingly. Such a scheme cannot be implemented for passive implants however, as there is no back-communication present [21], [148], [149].

This chapter considers the problem from the point of view of an SP link, driven by a voltage source, providing an output voltage to a fixed resistive load. While a real implant will present a load that looks more like a variable current source that is dependent on circuit activity, a resistive load is sufficient to give a rough approximation of the link behaviour, for a given circuit state.

Firstly the behaviour of a single-frequency power transfer link should be considered. By taking the equation for link gain (here we want A_{SP}) from earlier in Equation 2.42, we can rearrange to obtain:

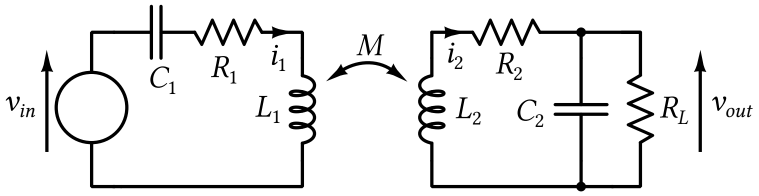

FIGURE 3.1: SP link with notation used throughout this chapter.

$$A = \frac{V_{out}}{V_{in}} = \frac{-j\omega M}{(Z_1 Z_2 + \omega^2 M^2)(j\omega C_2 + 1/R_L)} = \frac{-j\omega k\sqrt{L_1 L_2}}{(Z_1 Z_2 + \omega^2 k^2 L_1 L_2)(j\omega C_2 + 1/R_L)} \,. \tag{3.1}$$

Equation 3.1 gives a multivariate equation for A as a function of ω and k. At this point it is common to make a naïve assumption that if both sides are tuned to the same natural frequency $\left(\omega_0 = \left(2\pi\sqrt{L_1 C_1}\right)^{-1} = \left(2\pi\sqrt{L_2 C_2}\right)^{-1}\right)$ then the operating frequency can be fixed at ω_0 to achieve optimal performance. Chapter 2 shows that this is not the case; this assumption only holds when the link is critically coupled with the correct load. It is therefore important to consider different frequencies, distances, and loads. To analyse variations against frequency, Terman employs a 'gamma factor' $\gamma = \omega/\omega_0$ that considers the current frequency as a fraction of the tuned frequency [52].

The link gain can therefore be rearranged in terms of γ to obtain the following function for $A(\gamma, k)$:

$$Z_1 = R_1 + j\left(\omega L_1 - \frac{1}{\omega C_1}\right) = R_1 + j\omega L_1\left(1 - \frac{1}{\gamma^2}\right) \tag{3.2a}$$

$$Z_2 = R_2 + j\omega L_2 + \frac{1/R_L - j\omega C_2}{1/R_L^2 + (\omega C_2)^2} = R_2 + \frac{R_L}{1+\alpha} + j\left(\omega L_2 - \frac{\gamma^2 R_L^2}{\omega L_2(1+\alpha)}\right) \tag{3.2b}$$

$$A(\gamma, k) = \frac{-jk\sqrt{L_2/L_1}}{\left(\frac{1}{Q_1} + j\left(1 - \frac{1}{\gamma^2}\right)\right)\left(\gamma^2\left(\frac{1}{Q_2\sqrt{\alpha}} - 1 + j\left(\frac{1}{Q_2} + \frac{1}{\sqrt{\alpha}}\right)\right) + 1\right) + k^2\left(j\gamma^2 + \frac{1}{\sqrt{\alpha}}\right)} \tag{3.3}$$

Where $\alpha = (\omega C_2 R_L)^2$, as defined in [65], $Q_1 = \frac{\omega L_1}{R_1}$ and $Q_2 = \frac{\omega L_2}{R_2}$. The rearrangement to get 3.3 provides an equation for A that is essentially the same as the equation provided by Terman [52, Eq. 33, pg. 155], but takes into account the load R_L instead of assuming an unloaded SP link such that $R_L = \infty$. This rearrangement is not strictly necessary when using a machine to compute the value of A, it is more a method applicable to pencil and paper calculation. What this rearrangement *does* illuminate however, is the gain of the link is dependent entirely on k, Q, γ, and α, *not* on factors like the number of turns in the coils, or specific values of the link components.

The next step in the analysis is to translate between coupling factor k and coil separation distance d, by using Equations 2.18, 2.28, and 2.29. Working with real distances rather than abstract coupling factors is preferable, as it makes simulations and measured results more clearly applicable to the physical arrangement of the coils.

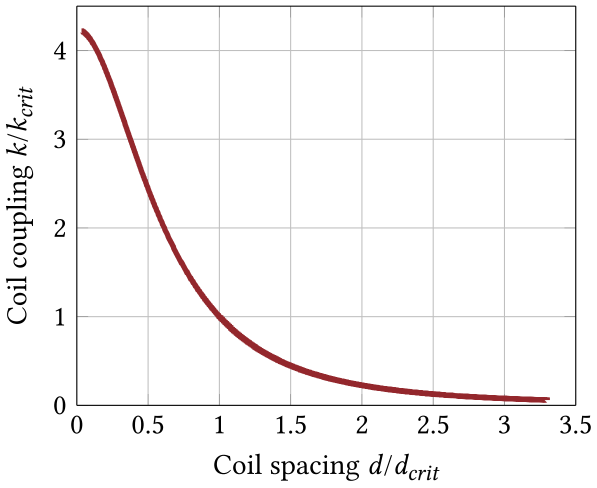

FIGURE 3.2: Relationship between coupling and distance, normalised.

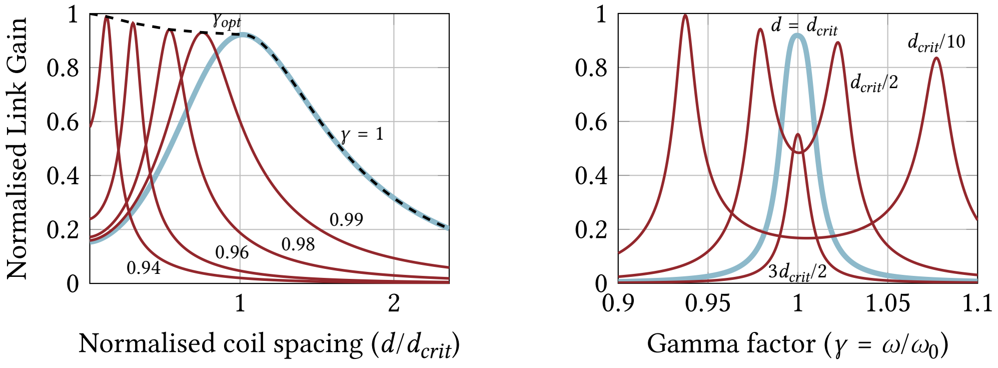

(A)

(B)

FIGURE 3.3: (A): Gain vs coil spacing against γ variations, (B): Gain vs γ against coil spacing variations.

Figure 3.2 shows the relationship between k and d for an example link. The example link values used here are the same as those measured later from Table 3.2. The key feature to note is that in the overcoupled region where $d < d_{crit}$, the coupling factor rises sharply with decreasing distance, and slowly drops in the undercoupled region, where $d > d_{crit}$.

Figure 3.3 shows how link gain is affected by sweeping d and γ; by maintaining a fixed frequency of ω_0, link gain is maximized only at d_{crit}. The plots in Figures 3.3a and 3.3b can be considered as cross-section slices of the 3 dimensional splitting plots in Figures 2.14 and 2.15. Figure 3.3a shows clearly that as the coil distance decreases below d_{crit}, the drive frequency must be adjusted appropriately to maintain a maximal gain. The optimum frequency is shown by the γ_{opt} trend on Figure 3.3a. This trend is essentially a root path, the same as those shown in Figure 2.16.

Figure 3.3b shows the double-peaked response resulting from frequency splitting; for this example link, the lower frequency peak gives a higher gain. Which peak gives the highest gain will depend on the specifics of the coil construction; since $Q \propto \omega L$, but also $Q \propto 1/R_S(\omega)$, depending on the coil construction and resonant frequency,

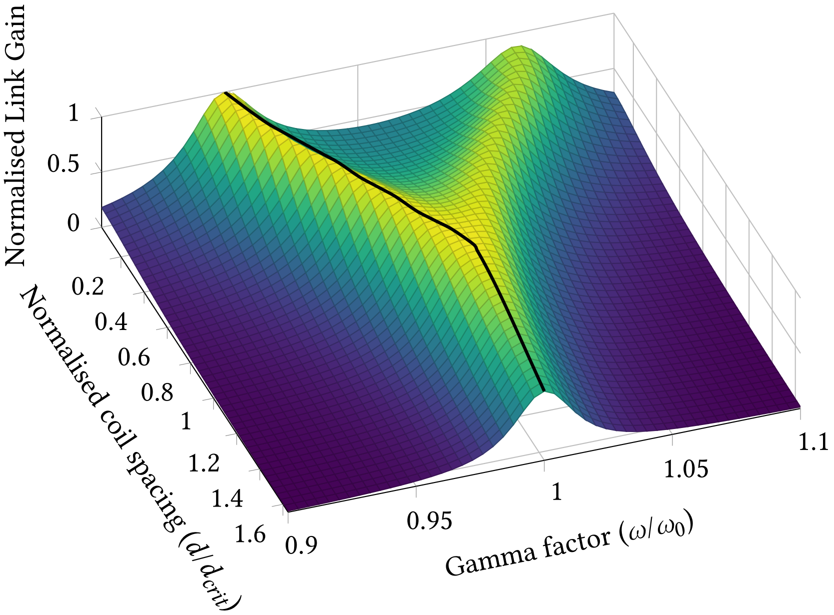

FIGURE 3.4: 3-dimensional plot of the slices from Figure 3.3.

either peak can yield a higher gain.

Figure 3.4 shows the full 3D representation of the plots in Figure 3.3; the black line shows the γ_{opt} root path moving across the surface of the plot. By adjusting the frequency to follow this path, gain is maximized and consistent through the overcoupled region.

3.3 System Design

Figure 3.5 shows a block diagram layout of the implemented variable frequency drive system. The system action was named 'optimum frequency tracking' (OFT), as the aim of the feedback loop was to track the optimum frequency ω_{opt} by monitoring whether or not the link was resonating and adjusting the frequency accordingly. The system action can be considered as a control loop, the behaviour of which is summarised as follows:

The link state is monitored at the primary side through the capacitive divider formed by C_a and C_b; the voltage tapped from this divider leads the primary current by 90°, and is compared against the PLL voltage with a phase detector. Measuring this phase difference allows detection of resonance in the primary, the target measured phase difference being 90° to achieve 0° between the primary voltage and current (resonance condition). Should the measured phase differ from the 90° target, the phase detector signal is amplified in the error amplifier, and fed to the microcontroller. With this information from the error amplifier, the microcontroller can adjust the drive frequency of the PLL such that $\omega \longrightarrow \omega_{opt}$ to try and pull the phase back to 90°. There is also a secondary control loop that allows a more general 'lock detection' to be performed. This is achieved by the combination of an envelope detector and a

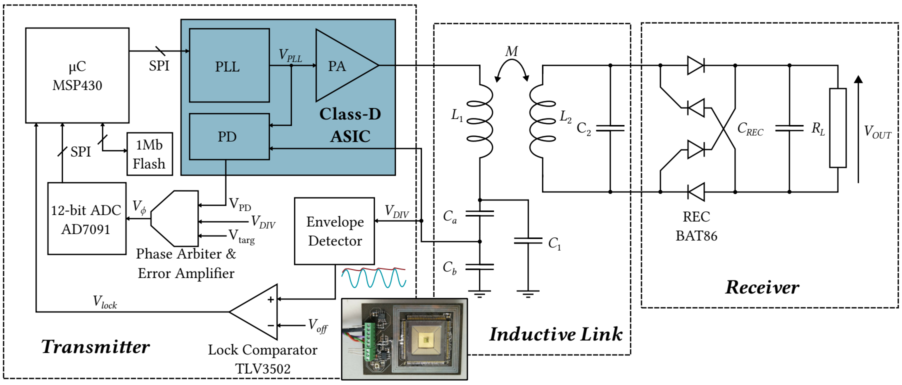

FIGURE 3.5: Block diagram to show the layout of the transmitter system. Inset: a compact transmitter prototype, with the chip fixed in the centre of the coil.

comparator, to provide a simple indication of whether the amplitude of the primary current is peaking sufficiently compared to a predetermined level. This provides a ‘coarse-grained’ mechanism that detects whether or not ω is within the correct frequency range.

The following subsections describe the blocks in Figure 3.5 in more detail.

3.3.1 Integrated Class-D Power Amplifier

The integrated class-D amplifier chip used is labelled ‘Class-D ASIC’ in Figure 3.5. The details of the chip’s implementation are well documented in [147]; key features used in this work are listed as follows:

- Power amplifier (PA) - for driving the link.
- Phase detector (PD) - for checking the phase of the primary current.
- Phase locked loop (PLL) - for clock synthesis that can be controlled via SPI.

Since the PLL is capable of generating a wide frequency range very accurately (0.875 MHz - 14 MHz with a sub-1 kHz resolution), it is ideal for very precisely tracking the optimum drive frequency ω_{opt}. While the PLL is ideal for this application, the on-chip phase detector however is not; it provides an absolute response to phase differences, i.e. the output voltage is the same regardless of whether the phase is a lead or a lag. Since the system must know if the current is leading or lagging the voltage to tell which way to adjust the frequency ω, the on-chip phase detector was supplemented with additional logic to add this functionality.

3.3.2 Phase and Lock Detection

The circuit described in Figure 3.6 complements the on-chip phase detector to allow differentiation between phase lag and phase lead. It also performs some amplification steps to make full use of the dynamic range available. The output of the amplifying stages is fed to a 12-bit ADC, which sends its values to the microcontroller via SPI.

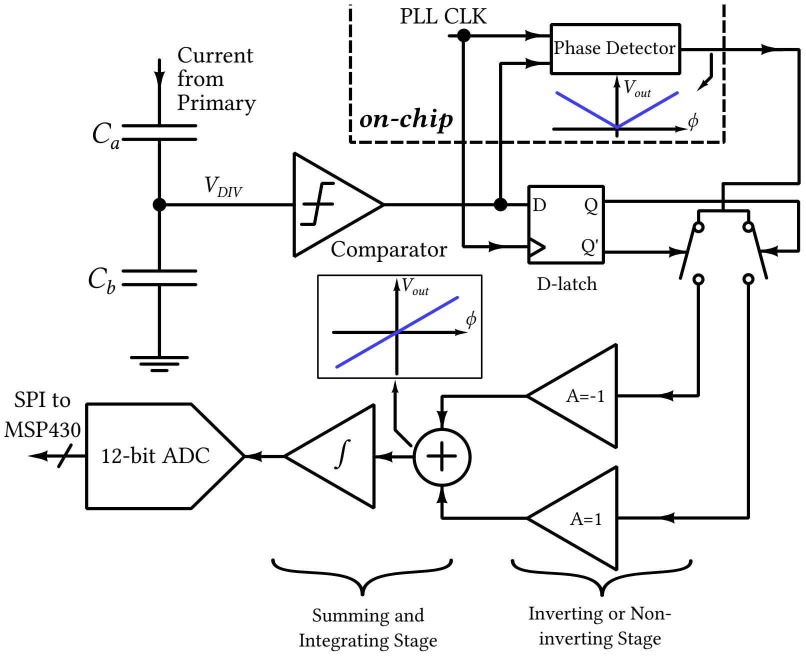

FIGURE 3.6: Details of the phase detection arbiter.

Figure 3.6 shows a simplified description of the circuit used for augmenting the phase detector and to drive the ADC feeding the microcontroller. The action of the circuit can be described as follows. The primary current is represented by the tapped voltage V_{DIV}, which is converted to a logic level signal by the comparator. This logic level signal is then fed to the on-chip phase detector, as well as the data input of a D-type latch. The on-chip phase detector compares the signal with the PLL clock, generating a voltage proportional to the difference in phase. However the voltage produced by the detector is proportional to the magnitude of the phase difference (see plot embedded in Figure 3.6). The purpose of the D-latch is to determine whether or not the phase difference between V_{DIV} and the PLL clock is a lag or a lead; if V_{DIV} leads V_{PLL} Q will be high, if it lags, Q' will be high. This latch acts as an arbiter to decide whether or not to invert the signal from the phase detector; the outputs control switches which feed the signal to inverting and non-inverting amplifiers respectively. The outputs of these two amplifiers are combined in a summing amplifier, achieving the desired response; phase lag is now represented by a negative voltage deviation, allowing the difference between phase lead and lag to be determined. Finally the output of the summing amplifier is fed to an integrating amplifier, the gain of which can be adjusted until the control loop of the system becomes stable. The output of the integrator is converted to a digital value via a 12-bit ADC, which communicates via SPI with the MSP430.

In short, the overall effect of the circuit is to provide the microcontroller with a value that corresponds to the phase difference between the primary current and

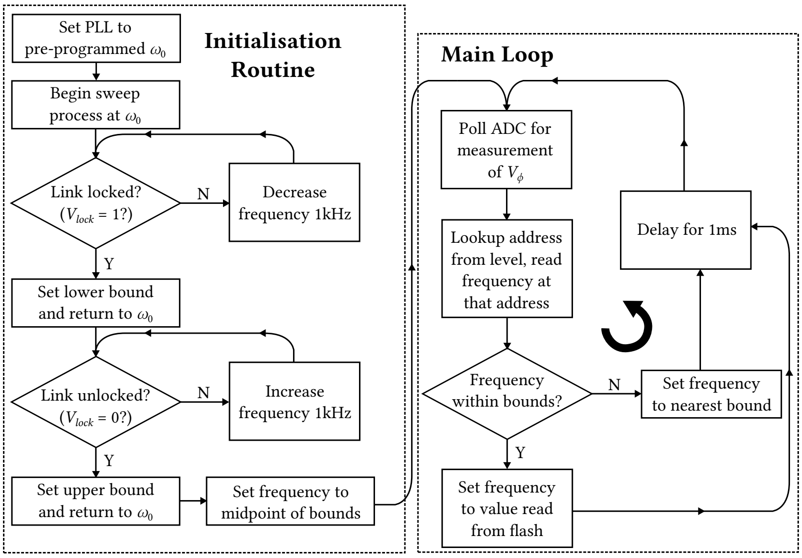

FIGURE 3.7: Flow diagram to show the behaviour of the microcontroller.

the PLL clock, which is essentially synchronised with the primary voltage[1]. Once the microcontroller knows this phase difference, it can proceed to adjust the drive frequency.

In addition to the phase information, the microcontroller takes a logic level signal from the lock detection circuit, to tell whether the link current is larger than a target amplitude. This allows a 'coarse grained' determination of whether the drive frequency ω is approaching ω_{opt}. This is useful for determining the range of useful drive frequencies for a given link, as well as determining whether or not the output of the phase detection circuit is reliable; if the amplitude of the primary current is too low, the output of the phase detector is essentially undefined, which would in turn lead to undefined loop behaviour.

The lock detection circuit is implemented with a simple RC envelope detector to generate a DC representation of the amplitude, which is then fed to a comparator to determine if it is large enough. This comparator feeds a logic level to the microcontroller, providing the lock state information.

3.3.3 Microcontroller Behaviour

The microcontroller makes use of the logic signal V_{LOCK}, and the phase difference value from the ADC. With these two signals, the microcontroller can determine the state of the link, and control the loop to maintain $\omega = \omega_{opt}$. Figure 3.7 gives a flowchart to describe the behaviour of the microcontroller when presented with these two signals.

Figure 3.7 shows how the controller's behaviour is split into an initialisation section and a main loop. The initialisation process can be summarised as essentially

---

[1] This is not strictly true, as there will inevitably be some small propagation delay from the PLL output to the output of the PA. This can be compensated for by adjusting V_{targ} (see Figure 3.5), which sets the target phase for the system to lock to.

TABLE 3.1: Table listing the geometric parameters generated for the test coil pair

Parameter	*Tx*	*Rx*
Outer diameter d_{out}	58.6 mm	20 mm
Inner diameter d_{in}	30 mm	2.2 mm
Track width w	0.9914 mm	0.2444 mm
Track spacing s	180 µm	180 µm
Number of turns N	12	21

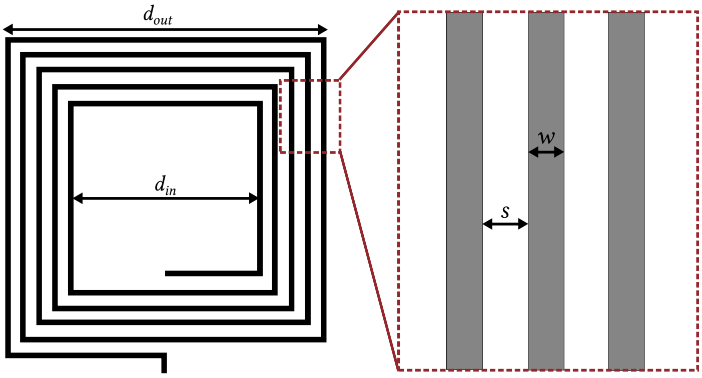

FIGURE 3.8: Diagram to demonstrate the geometry of a square spiral printed coil

sweeping through a preset range of frequencies to determine the actual working range of drive frequencies for the connected link. Once the working range is determined, the range of phase values can be translated to a range of frequencies. To program a given frequency the PLL needs to be sent a frequency code via the SPI bus; given the high resolution of the PLL, the full range of frequency codes are stored in an external flash chip wired to the MSP430.

The operation of the main loop consists of reading the current phase difference value, translating this to a frequency, reading the appropriate frequency code, and updating the PLL frequency. If the desired frequency is out of bounds it is set to the nearest bound. The controller sleeps for 1 ms each cycle to allow the loop to settle.

3.3.4 Coil Design and Implementation

The link was tested using square printed spiral coils, fabricated on a standard FR4 substrate, and optimised for 5 MHz operation. To obtain the design parameters for the coils, the iterative process described in [37] was employed through a script in MATLAB, to allow for easy replication of the coil designs. Initial constraints were applied to the following parameters: implanted coil outer diameter d_{o2}, typical load R_L, working coil spacing d, and minimum PCB track spacing s. The constraints were $d_{o2} = d =$20 mm, $R_L = 10\,k\Omega$, $s = 150\,\mu$m. The constraint on spacing was a conservative estimate of the limitations of the available PCB fabrication facility, while the other

TABLE 3.2: Measured coil parameters for operation at 5MHz.

		Tx Coil	Rx Coil
Outer Diameter	d_o	64.7 mm	20.0 mm
Inner Diameter	d_i	37.2 mm	4.7 mm
Number of Turns	n	12	13
Inductance	L	10.150 µH	2.255 µH
Q-factor	Q	47.5	26.0

constraints were common example values in the context of biomedical implant size, implantation depth, and power requirements [150]. Geometric details of these coils are given in Table 3.1 and Figure 3.8. The measured coil parameters of the fabricated coils are listed in Table 3.2.

The specs in Table 3.2 show that the Q-factor of the fabricated coils was relatively low at the operating frequency of 5 MHz. This was the result of the inter-turn spacing being very tight, increasing proximity effect losses, and the thin copper layer of the standard PCB material. The benefit of this kind of coil is consistency, since the stiff PCB material resists flexion and maintains a constant inductance.

3.4 Measured Results

3.4.1 Test Procedure

The operation of the closed-loop system was tested with a bench setup, in which the printed coils were mounted on a jig. This jig provided control over the coaxial displacement between the coils from 5 mm to 70 mm. The system efficiency was calculated in terms of the DC power drawn from the supply and the secondary voltage V_{OUT} across the load R_L. Therefore the efficiencies stated are *system* efficiencies, not link efficiencies.

Initially the coils were aligned on the jig, and placed far enough apart to ensure power transfer in the undercoupled region (d = 70 mm); the value of ω_0 could then be empirically determined through manual frequency adjustment. The distance between the coils was then manually adjusted between 5 mm and 50 mm in steps of 5 mm, and V_{OUT} at the load was measured with OFT disabled and enabled. In a second test the distance was varied as before, but the power supply was also manually adjusted such that V_{OUT} = 10 V; the efficiency was recorded. In a third test, the link coils were fixed in an overcoupled position (d = 5 mm), and the load R_L was varied; again V_{OUT} and system efficiency were recorded, with OFT enabled and disabled.

3.4.2 Link Measurements

Figure 3.9 shows measured results next to simulated results of the link gain as coil spacing and link load are varied. The trends clearly show that by enabling OFT, the

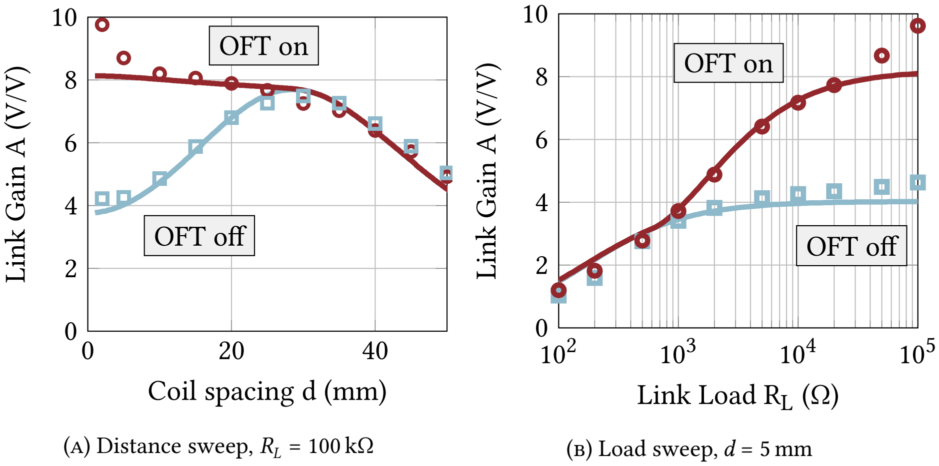

(A) Distance sweep, $R_L = 100\,\text{k}\Omega$

(B) Load sweep, $d = 5\,\text{mm}$

FIGURE 3.9: Plots to show experimental data against calculated behaviour for distance and load sweeps for the 5 MHz coils, with OFT enabled ($\omega = \omega_{opt}$) and OFT disabled ($\omega = \omega_0$)

link gain is maximized, and more power can be transmitted through the link. This improvement in gain link gain allows the Tx supply voltage to be reduced, while still achieving the desired V_{OUT}, allowing for reduced overall power consumption. The measured results do show some deviation from the simulated results, with higher gains at very close couplings and high loads. This is likely the result of the analytical model breaking down at very close spacings. This was initially considered to be the result of capacitive coupling between the flat printed coil traces [120], however a more likely explanation for this effect is as follows. Since the model considers each turn of the coil to be an infinitesimally thin conductive filament at the centre of each turn, this is a good approximation at reasonable distances, but as the coils come very close together, the variable current distribution in the PCB tracks becomes more apparent. Since the current is concentrated in the edges of the trace, it appears more like *two* thin conductive filaments in parallel with each other at the trace edges, rather than one in the centre of the trace. Qualitatively, this means that the coils would appear to have higher coupling when very tightly spaced than when they are coupled over larger distances.

Figure 3.10 shows the effect the OFT scheme has on system efficiency. When sweeping against distance (Figure 3.10a), the overcoupled region shows up to a 100% increase in system efficiency compared to the fixed frequency regime. When $\omega = \omega_{opt}$ losses in the driver are reduced as the reactive elements of the link are minimized. As the link approaches the critical coupling distance however, the system is less efficient when running in OFT mode than fixed frequency mode by ≈ 18%. This is expected, since the frequency tracking loop is made with many discrete components, and is not optimized for low power consumption. The behaviour could easily be improved through software optimization; for example, the microcontroller could include a routine to recognise when the frequency has stayed within a range for a certain period of time (indicating the coil positions are stable), and then swap to fixed-frequency

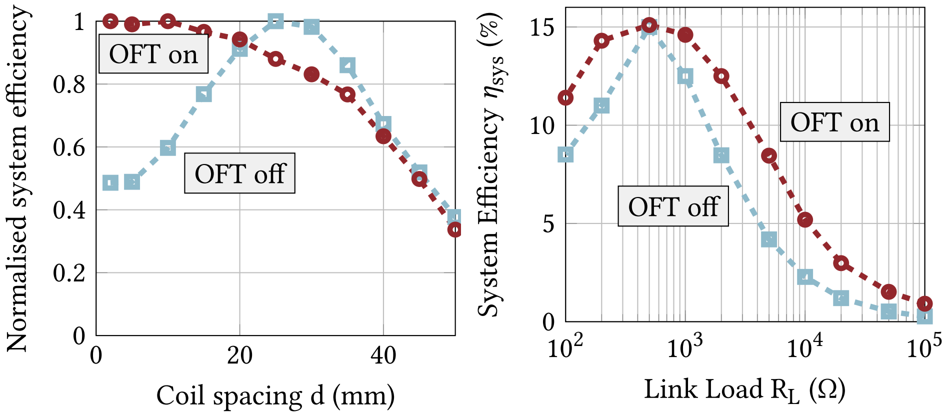

(A) Distance sweep, $R_L = 100\,\mathrm{k}\Omega$

(B) Load sweep, $d = 5\,\mathrm{mm}$

Figure 3.10: Plots to show experimental efficiency data for distance and load sweeps, with OFT enabled ($\omega = \omega_{opt}$) and OFT disabled ($\omega = \omega_0$)

mode to save power.

Figure 3.10b shows the effect of changing the receiver load on the system efficiency. At the optimum load of 500 Ω, the system efficiency is the same for both OFT and fixed frequency modes. For all other loads however, a nominal boost of 2.5% system efficiency is gained by using OFT. This is a result of changing load having an effect on the optimum frequency of the link, as it has a subtle effect on the coil resonance frequency. The effect of load on resonance is discussed in more detail in §4.2.8.

3.4.3 Realtime results

To demonstrate the transient operation of the system; scope screenshots are shown in Figure 3.11.

The plots in Figure 3.11 clearly show the difference between the OFT and fixed frequency schemes in the time domain. For the long traces (Figures 3.11a and 3.11b), the Tx and Rx coils were moved from a spacing of 20mm to 2mm, while monitoring the output voltage V_{OUT} and the divider voltage V_{DIV}. Figure 3.11a clearly shows that by using a fixed frequency scheme, the reduction in coil spacing leads to a substantial drop in V_{OUT}, and the reduction in the amplitude of V_{DIV} indicates a loss of resonance in the link. Figure 3.11b on the other hand shows that by employing OFT, the change in coil spacing results in a small *increase* in V_{OUT}. V_{DIV} remains the same, indicating that resonance is maintained. These transient results are consistent with the values shown in Fig. 3.9a. Figures 3.11c and 3.11d clearly demonstrate the phase difference resulting from $\omega = \omega_{opt}$ (3.11d) and $\omega \neq \omega_{opt}$ (3.11c). It should be noted that V_{DIV} will have a phase difference of 90° from the primary current I_{pri} due to it being on a capacitor. Therefore the 90° phase difference in Figure 3.11d is indicative of resonance ($\angle V_{PLL} = \angle I_{pri}$).

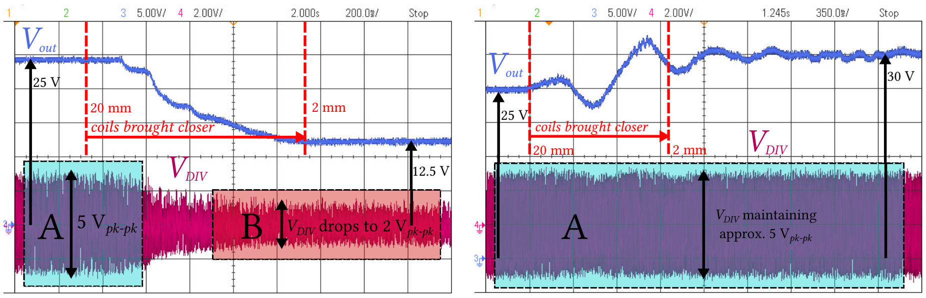

(A) OFT disabled (B) OFT enabled

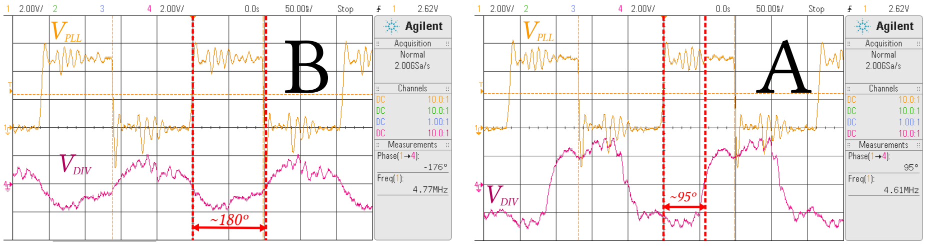

(C) OFT disabled (D) OFT enabled

FIGURE 3.11: Scope screenshots to show variation in output voltage against coil movement ((A),(B)), and the phase difference between V_{PLL} and V_{DIV} ((C),(D)), with OFT enabled and disabled.

It should be noted that there is some ringing and settling for the V_{OUT} trace in Figure 3.11b, this is likely the result of a combination of mechanical vibration in the coil displacement jig, but also some instability in the OFT control loop.

3.5 Concluding Remarks

Overall, the OFT system proved capable of compensating for coupling and load variations in an inductive link with printed coils, operating around a nominal frequency of 5 MHz. The system requires no variable capacitors or inductors, and is suitable for compact systems where space is valuable, such as for IMDs. Measurements showed close matching with the predicted behaviour of the system; discrepancies were only found at very tight couplings, where the mutual coupling model that was used is insufficiently precise. This system is suited to powering implanted medical devices, particularly those in which the receiver moves significantly with respect to the transmitter, and has time variant power requirements, such as in endoscopic capsules [151]. This approach could also be useful in the case of distributed implants [152], where the distances between the transmitter and the receivers are unpredictable. Additionally, in the case of implants employing flexible coils, the proposed OFT system would be capable of adapting to the altered link impedance presented by coil flexion [153]. OFT could also be used to interrogate remote units to establish the deviation in their true resonant frequencies from the designed value, or operate multiple receivers tuned at different frequencies [61]. Such an interrogation technique could also be used to confirm each receiver's post-implantation optimum frequency.

The work in this chapter could be improved by:

- Minimizing the power consumption of the control loop, to improve efficiency when running in OFT mode near critical coupling.
- More rigorous coil analysis, to determine why the model breaks down with printed coils, and improved coil designs.
- Full integration of the loop control system on-chip, for further miniaturization.

A Self-Oscillator for Remote Capacitive Sensing

4

The work in this chapter was first published in IEEE Transactions on Circuits and Systems I:Regular Papers [154]. This chapter contains further details not present in the original.

4.1 Context: Interrogating Remote Sensing Capacitors

Wireless sensing systems are becoming ubiquitous, particularly in biomedical and food monitoring applications. Biomedical application examples include neural monitoring [20], muscle pressure sensing [10], and glucose monitoring [12]. Some miniaturized devices can even perform multiple functions by incorporating multiple sensors on the same implant [7]. A food quality monitoring application in [155] has a passive receiver as part of an inductive link, but requires an impedance analyzer for interrogation. The same principle is demonstrated with a more general environmental sensor in [156], a biomedical pressure sensor in [157], and a humidity sensor in [158]. In all these cases an impedance analyzer is used to interrogate a passive resonant sensor.

A typical signal chain of a wireless sensor might include: analogue capacitive sensor interface, an analogue to digital converter and microprocessor, and a wireless digital transmission method [11], [159]–[162]. Alternatively for inductive link based systems, the signal chain consists of a capacitive sensor, an inductive link, and an impedance analyzer; generally implemented with large-scale lab equipment [155]–[158]. For example, Lee et al. [157] present an LC based implantable pressure sensor for sensing bladder pressure. Zhang et al. [158] propose a similar passive LC based sensor for detecting relative humidity. Figure 4.1 shows overviews of these two types of scheme; the standard digitizing type requires significant complexity, but passive sensors generally require bulky impedance analyzers.

In contrast to these previous designs, this work proposes a simple method for implementing a wireless capacitive sensor frontend in a single circuit block. This would allow a system to be implemented in a smaller size and with a lower power consumption, by leveraging the strengths of an inductive link. This approach has the benefit of being low power and highly miniaturized, particularly when compared with state of the art inductive link based wireless sensing systems [155]–[158].

The proposed system provides an integrated CMOS chip that allows interrogation of a capacitive sensor located at the primary or secondary side of an inductive link. The

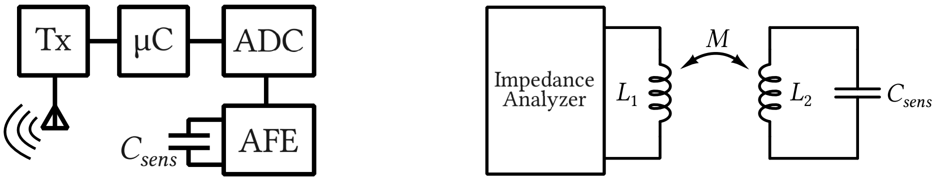

(A)

(B)

FIGURE 4.1: Typical sensor architectures. (A): a typical remote sensor chain with digital wireless transmitter. (B): an inductive link based remote interrogator, using an impedance analyzer.

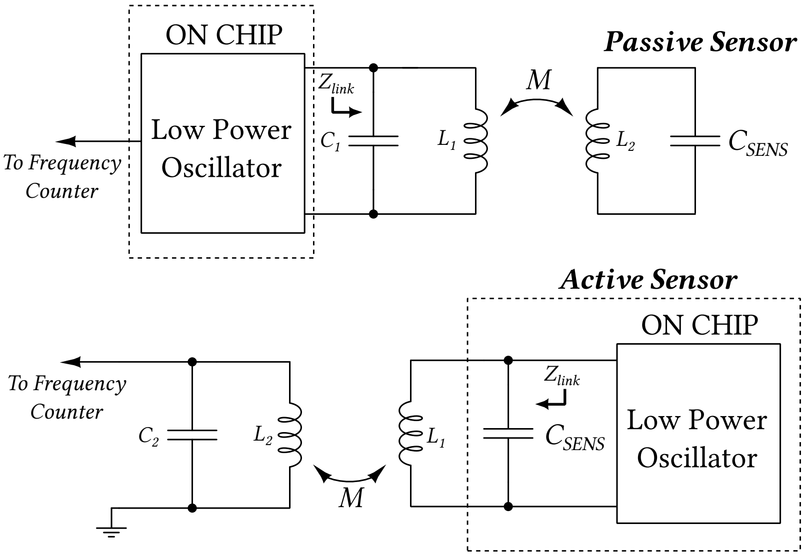

FIGURE 4.2: Passive and active sensor configurations with the proposed system.

system can be used as an interrogator for a remote passive sensor, or as a transmitter in an active sensing device. Figure 4.2 shows the two configurations that can be realised through this approach, referred to as active mode and passive mode. Capacitance to frequency conversion and wireless transmission are achieved in a single stage, by using a self-oscillator combined with an inductive link. Since passive mode allows for a remote sensor to be interrogated without an accompanying power source, it is well suited to applications where the power budget is critical, such as medical implants. Active mode would be more suited to applications where power is more available, where it is desirable to have many active elements (rather than a single active element and many passive sensors) to reduce the effect of a circuit failure, e.g. in the case of industrial food monitoring.

The rest of this chapter is structured as follows. Section 4.2 develops the inductive link theory required to describe the approach. Section 4.3 describes the design of the self-oscillating circuit, and Section 4.4 presents measured results of the system.

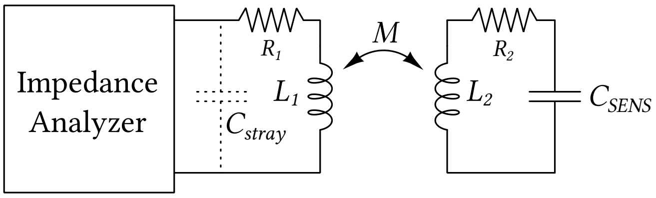

(A) Phase-dip measurement setup.

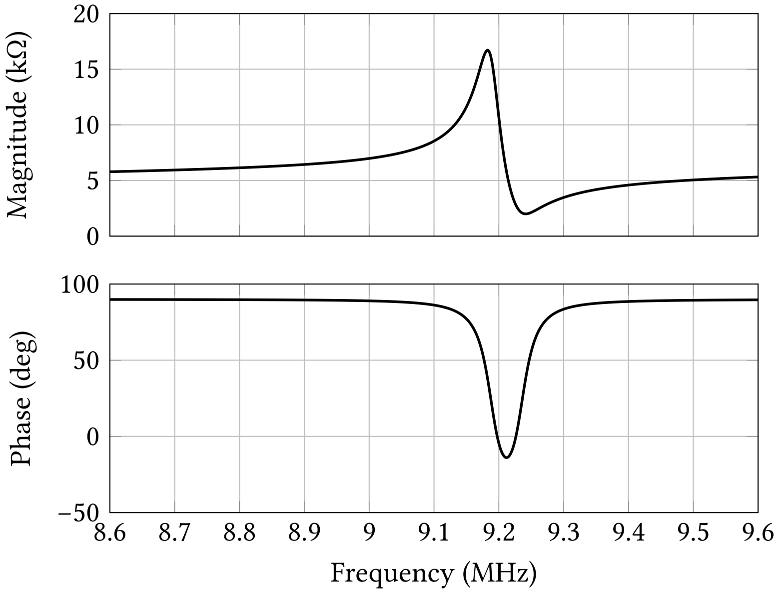

(B) Example link impedance measurement.

FIGURE 4.3: The phase-dip measurement approach for wireless capacitive sensing. $L_1 = 10\mu\text{H}$, $L_2 = 100\mu\text{H}$, $R_{1,2} = 2\Omega$, $M = 3.162\mu\text{H}$, $C_{SENS} = 3$ pF.

4.2 Direct Inductive Sensing

The approach presented in this chapter bears some similarity to 'traditional' inductive sensing methods such as those described in [157], [158], [163], but differs in terms of the basic principle of operation. In general, the method used for wireless inductive sensing makes use of an impedance analyzer; by sweeping frequency across the inductive link, its resonant characteristics can be determined. If the link is highly asymmetric (i.e. L_1 is much smaller than L_2 or vice versa), the response of a frequency sweep will show a local minima in the phase plot at the resonant frequency of the remote sensor. This local minima is appropriately referred to as a 'phase-dip' in [158]; as such this technique will be described as the 'phase-dip method' throughout. It is instructive to briefly consider the details of the phase-dip method for the purpose of comparison.

4.2.1 The Phase-Dip Method

The phase-dip method can be explained with the aid of Figure 4.3. Figure 4.3a illustrates a measurement arrangement, such that the value of C_{SENS} can be determined by

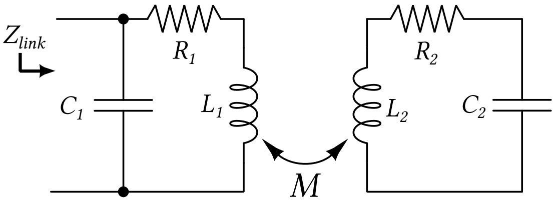

FIGURE 4.4: General case inductive link model.

reading the impedance plot generated by the impedance analyzer. The impedance plot in Figure 4.3b shows the characteristic phase-dip that occurs due to the resonance of L_2 and C_{SENS}. Assuming the link is sufficiently asymmetric, the frequency at which the phase dip occurs can be approximated as follows [158], [164]:

$$f_{dip} \approx \frac{1}{2\pi\sqrt{L_2 C_{SENS}}}, \tag{4.1}$$

where f_{dip} is the frequency at which the phase is minimized (see Figure 4.3b). As long as the frequency f_{dip} can be determined, and L_2 is known, the value of C_{SENS} can also be determined from Equation 4.1. The approximation in Equation 4.1 holds since L_1 has a limited effect on the resonance of L_2 and C_{SENS}. The phase-dip technique has problems however. Firstly it has limited sensitivity; since Equation 4.1 is an approximation, accurately determining small changes in C_{SENS} is difficult. Second, it requires a complex impedance analysis system to perform the measurement. When attempting to miniaturize the system, the requirement for L_1 to not affect the resonance of L_2 and C_{SENS} becomes more of a challenge. As the system size decreases, parasitic capacitance (C_{stray}) across L_1 becomes more relevant to the link impedance, therefore the assumptions required to perform a phase-dip measurement are no longer valid. The worst-case scenario for the phase-dip method therefore is the case of a symmetric link, such that $L_1 = L_2$ and $C_1 = C_2$.

Section 4.2.2 provides an exact analysis of Z_{link} with the goal of an expression that can accurately determine C_{SENS} for an arbitrary link, such that even a symmetric link can be successfully interrogated.

4.2.2 An Exact Method

The aim of the phase-dip method is to provide a close approximation of the value of C_{SENS}, as long as the value of L_2 is known. A more robust approach than the phase-dip method should attempt to provide the exact value of C_{SENS} for an arbitrary link arrangement. The proposed method determines the exact value of C_{SENS}, provided all other link parameters are known. Figure 4.4 shows the general case of a parallel-parallel dual resonant inductive link. In the case of a miniaturized system, this is a more realistic representation of the link than that shown in Figure 4.3a, since C_{stray} can no longer be ignored. By considering the circuit in Figure 4.4 in general terms, the conclusions can be applied to a link where either C_1 or C_2 is used as C_{SENS}, i.e. the

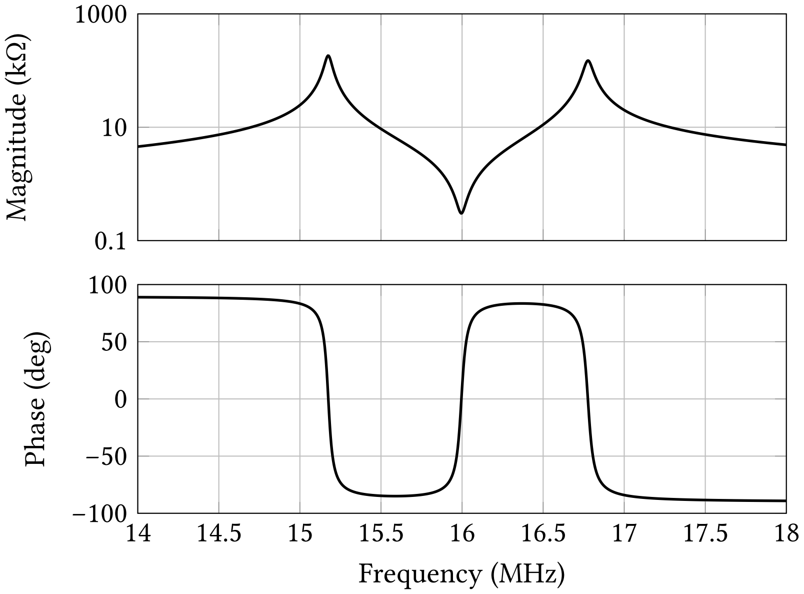

FIGURE 4.5: Impedance plots for a symmetric link. $L_{1,2} = 10\ \mu$H, $C_{1,2} = 10$ pF, $M = 1\mu$H, $R_{1,2} = 3\ \Omega$.

two cases of active and passive sensor (Figure 4.2). Figure 4.4 shows the impedance looking into the link Z_{link}, which is defined as follows:

$$Z_{link} = \left(\left(j\omega L_1 + R_1 + \frac{(\omega M)^2}{j\omega L_2 + \frac{1}{j\omega C_2} + R_2} \right)^{-1} + j\omega C_1 \right)^{-1} \tag{4.2}$$

where $L_{1,2}$ are the primary and secondary link inductances, $C_{1,2}$ are the primary and secondary capacitances, $R_{1,2}$ are the primary and secondary coil losses, M is the mutual inductance between the coils $L_{1,2}$, and ω is the angular frequency.

Z_{link} is always considered as the impedance looking into the link from the point of view of the oscillator, which can be considered as a negative resistance, which will generate an alternating current that drives the link I_{in}.

Figure 4.5 shows the magnitude and phase plots of Z_{link} for an example of a symmetric inductive link. The component values are given in the caption. These values are typical values that can be easily realised with small coils, and are comparable to the practical coils described in Section 4.3. It shows that the approximation made in Equation 4.1 is no longer valid for determining the value of C_2; calculating the result of Equation 4.1 will not correlate to a ‘dip’ in the phase plot. In this way, a symmetric link can be considered as a worst case scenario for the phase-dip method, as both sides of the link play a significant part in determining the resonant frequency. The plots in Figure 4.5 demonstrate the frequency-splitting phenomenon that occurs when M is sufficiently large; this effect has been previously discussed and analysed in the literature in detail [59], [116], [120], [165]. The features of interest are the two peaks and the trough that occur in the magnitude plot. These points will be referred to as the resonance and anti-resonance points respectively, and occur at corresponding

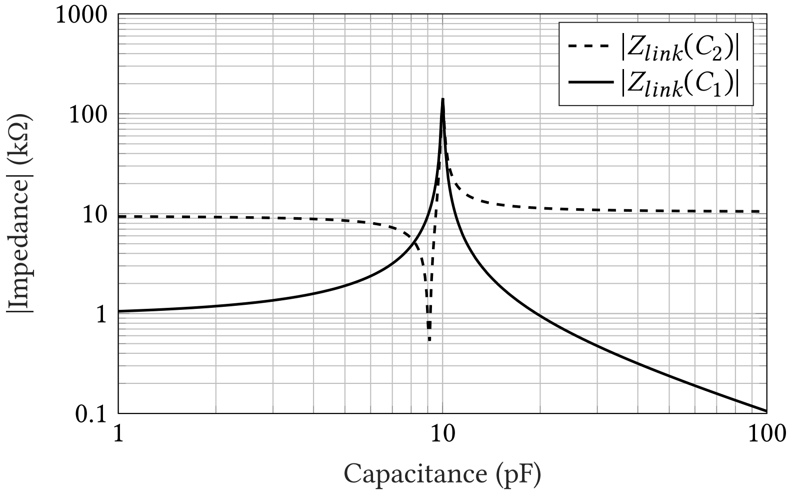

FIGURE 4.6: Magnitude of the link impedance for varying values of $C_{1,2}$.

resonance and anti-resonance frequencies.

Since the resonance and anti-resonance points are local maxima and minima in the function $|Z_{link}(\omega)| = \sqrt{\mathfrak{Re}\{Z_{link}\}^2 + \mathfrak{Im}\{Z_{link}\}^2}$, they can be determined by partial differentiation:

$$\frac{\partial\{|Z_{link}(\omega)|\}}{\partial\omega} = 0. \tag{4.3}$$

By solving Equation 4.3, the resonance ($\omega_{res(1,2)}$) and anti-resonance ($\omega_{antires}$) frequencies can be determined. The solution of Equation 4.3 results in a polynomial that is readily solvable numerically. If M is low enough that the link is undercoupled, there will be one positive real root corresponding to a single value for $\omega_{res(1)}$. If M is high enough that the link is overcoupled, there will be three positive real roots: $\omega_{res(1)} < \omega_{antires} < \omega_{res(2)}$. The exact boundary between the undercoupled and overcoupled conditions is defined by the critical coupling k_{crit} [52]:

$$k_{crit} = \frac{1}{\sqrt{Q_1 Q_2}} \tag{4.4a}$$

$$\therefore M_{crit} = k_{crit}\sqrt{L_1 L_2} \quad . \tag{4.4b}$$

For $k < k_{crit}$, the link is undercoupled, and for $k > k_{crit}$, the link is overcoupled.

It is possible to characterise the link in a similar way with respect to the capacitances C_1 and C_2, and observe how they are related to $\omega_{\mathrm{res}(1,2)}$ and $\omega_{antires}$. The link impedance can be considered a function of either C_1 or C_2: $(\left|Z_{link}(C_{1,2})\right|)$, and by substituting a known resonance frequency $\omega_{\mathrm{res}(1,2)}$, the link can be characterised in terms of C_1 or C_2.

Figure 4.6 shows $|Z_{link}|$ for the same link as in Figure 4.5, where $\omega = \omega_{\mathrm{res}(2)} =$ 16.78 MHz. The key feature of the plots in Figure 4.6 is that the curve of $|Z_{link}(C_1)|$

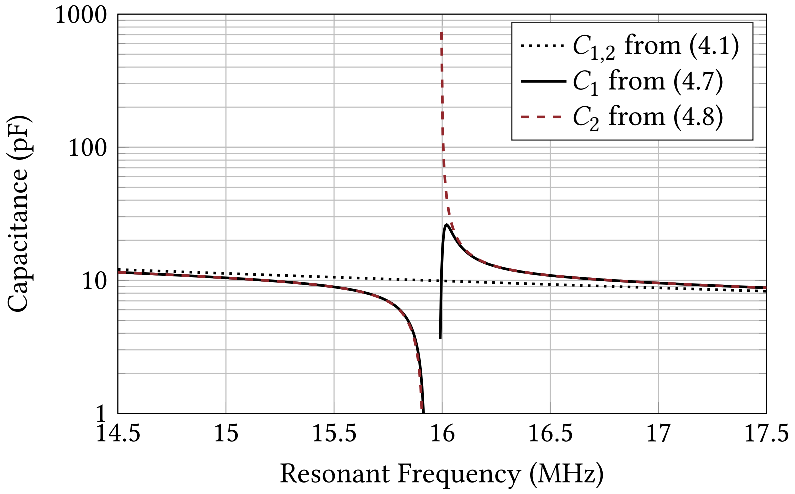

FIGURE 4.7: Determining capacitance through resonant frequency.

shows a single resonance point, and $|Z_{link}(C_2)|$ shows a resonance point and an anti-resonance point. By differentiation of $|Z_{link}|$ but with respect to C_1 or C_2, either capacitance can be determined, provided the other link parameters and the operating frequency ω is known. Solving

$$\frac{\partial\{|Z_{link}(\omega)|\}}{\partial C_1} = 0 \tag{4.5}$$

results in a closed form expression for C_1, shown in Equation 4.7. Similarly, solving:

$$\frac{\partial\{|Z_{link}(\omega)|\}}{\partial C_2} = 0 \tag{4.6}$$

results in two closed form expressions for C_2, corresponding to the resonance and anti-resonance points. The solution for the resonance point is relevant here, and is given in Equation 4.8.

Therefore, if either C_1 or C_2 has an unknown value, the link is known to be resonating, and all the other link parameters are known, the unknown capacitance can be determined using either Equations 4.7 or 4.8 respectively. To solve Equations 4.5 and 4.6 and generate Equations 4.7 and 4.8, the symbolic solver in SageMath was used, using the online CoCalc service [166].

Figure 4.7 shows the results of determining unknown capacitances C_1 or C_2, across a range of resonant frequencies, where all other parameters are the same as those used in Figure 4.5. For comparison, the solution according to Equation 4.1 has been added. This highlights the error that arises by using Equation 4.1; in particular where the resonant frequency is between 15.5 MHz and 16.5 MHz (i.e. the change in capacitance is small), the error between the two approaches becomes very significant; Equation 4.1 is no longer a suitable approximation. Note that Equations 4.7 and 4.8 have an asymptote with no solutions near the initial anti-resonance frequency of the link (see Figure 4.5). This is because, given the other link parameters, there is no

$$
\begin{aligned}
C_1 &= \frac{A}{B} \quad \text{where:} \\
A &= \left(C_2^2 L_1 L_2^2 - C_2^2 L_2 M^2\right)\omega^4 + \left(C_2^2 L_1 R_2^2 - 2\,C_2 L_1 L_2 + C_2 M^2\right)\omega^2 + L_1 \\
B &= \left(C_2^2 L_1^2 L_2^2 - 2\,C_2^2 L_1 L_2 M^2 + C_2^2 M^4\right)\omega^6 \\
&\quad + \left(C_2^2 L_2^2 R_1^2 + 2\,C_2^2 M^2 R_1 R_2 + C_2^2 L_1^2 R_2^2 - 2\,C_2 L_1^2 L_2 + 2\,C_2 L_1 M^2\right)\omega^4 \\
&\quad + \left(C_2^2 R_1^2 R_2^2 - 2\,C_2 L_2 R_1^2 + L_1^2\right)\omega^2 + R_1^2
\end{aligned}
\tag{4.7}
$$

$$
\begin{aligned}
C_2 &= \frac{A + \sqrt{B}}{C} \quad \text{where:} \\
A &= 2\left(C_1 L_1^2 L_2 - C_1 L_1 M^2\right)\omega^4 - \left(2\,C_1 L_2 R_1^2 + 4\,C_1 L_1 R_1 R_2 + 2\,L_1 L_2 - M^2\right)\omega^2 \\
&\quad + 2\,R_1 R_2 \\
B &= 4\left(C_1^2 M^4 R_1^2 + 2\,C_1^2 L_1^2 M^2 R_1 R_2 + C_1^2 L_1^4 R_2^2\right)\omega^6 \\
&\quad + \left(M^4 + 8\left(C_1^2 L_1^2 R_1^2 - C_1 L_1^3\right)R_2^2 + 8\left(C_1^2 M^2 R_1^3 - C_1 L_1 M^2 R_1\right)R_2\right)\omega^4 \\
&\quad + 4\,R_1^2 R_2^2 + 4\left(M^2 R_1 R_2 + \left(C_1^2 R_1^4 - 2\,C_1 L_1 R_1^2 + L_1^2\right)R_2^2\right)\omega^2 \\
C &= 2\left(\left(C_1 L_1^2 L_2^2 - 2\,C_1 L_1 L_2 M^2 + C_1 M^4\right)\omega^6\right. \\
&\quad - \left(C_1 L_2^2 R_1^2 + C_1 L_1^2 R_2^2 + L_1 L_2^2 - L_2 M^2 + 2\left(2\,C_1 L_1 L_2 - C_1 M^2\right)R_1 R_2\right)\omega^4 \\
&\quad \left.+ \left(2\,L_2 R_1 R_2 + \left(C_1 R_1^2 + L_1\right)R_2^2\right)\omega^2\right)
\end{aligned}
\tag{4.8}
$$

capacitance value for C_1 or C_2 that could allow link resonance in this frequency range.

4.2.3 Self-Oscillation

The key advantage of the analysis presented in Section 4.2.2 is that an unknown capacitance can be determined in an otherwise characterised resonating link with arbitrary characteristics; there is no requirement to have $L_1 \ll L_2$ as in the phase-dip method. Given that resonance is a requirement, a self-oscillating circuit can be employed in order to perform the measurement, in combination with a frequency counter. This is a much simpler solution than the impedance analyser required for a phase-dip measurement. Figure 4.8 illustrates the qualitative difference in $|Z_{link}|$

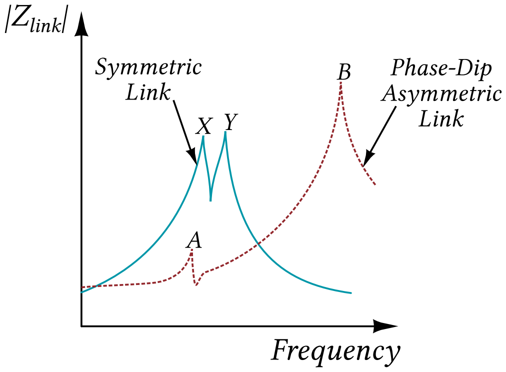

FIGURE 4.8: Symmetric vs asymmetric link impedances, resonance points marked.

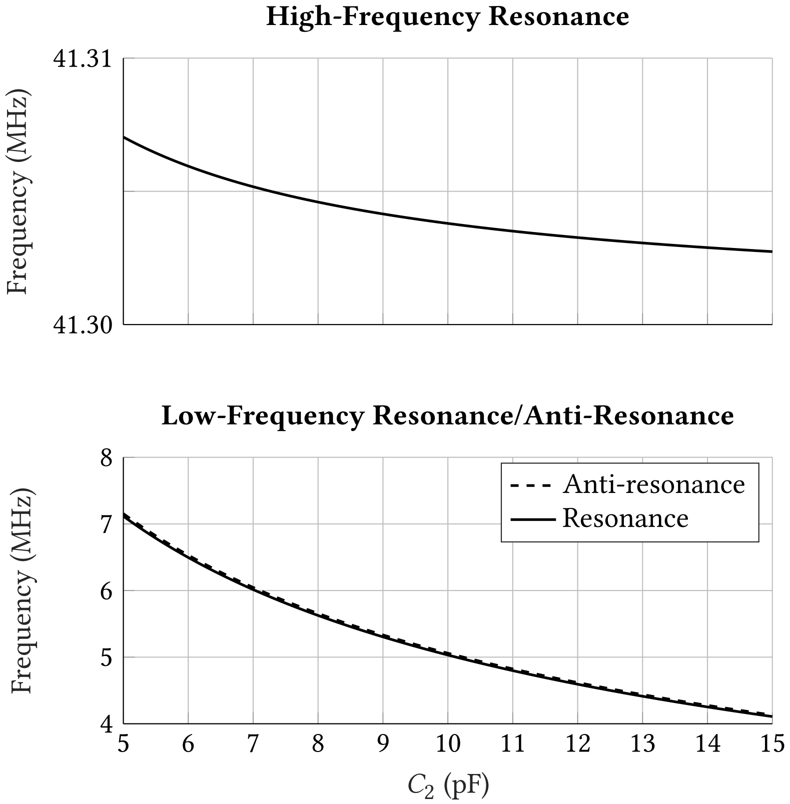

FIGURE 4.9: Lines of resonance and anti-resonance for an asymmetric link as C_2 is swept. Parameters are the same as in Figure 4.3 except C_{stray} = 1.5 pF.

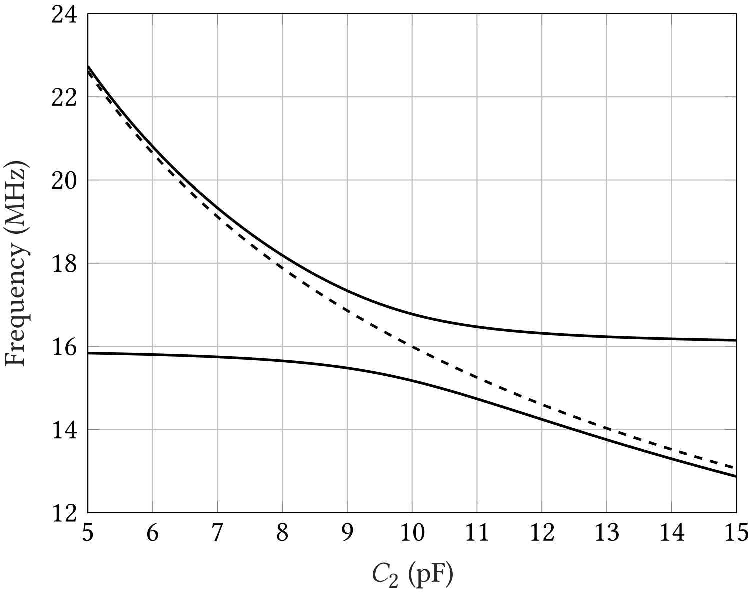

FIGURE 4.10: Lines of resonance and anti-resonance for a symmetric link as C_2 is swept. Parameters the same as in Figure 4.5.

for the asymmetric link used in the phase-dip method and a symmetric link. In the case of a self-oscillating circuit, a large resonance point impedance is required to maintain oscillation. In the asymmetric link, a self-oscillating circuit will oscillate at the higher-frequency peak, influenced mostly by the combination of L_1 and the negligible parasitic C_{stray} (C_1). While it is possible to use Equation 4.8 to determine the value of C_{SENS}, the sensitivity will be extremely poor. It is for this reason that the lower frequency peak (influenced mostly by the combination of L_2 and C_{SENS}) is used in the phase-dip method. In the case of the symmetric link however, both peaks are similarly affected by changes in capacitance at either C_1 or C_2. Therefore, regardless of which resonant peak the self-oscillator locks to, poor sensitivity is not an issue.

This difference in sensitivity is highlighted in Figures 4.9 and 4.10, where the resonance points (marked X,Y for the symmetric link and A,B for the asymmetric link in Figure 4.8) are plotted against changes in C_2. Figure 4.9 is split into two parts to highlight the full dynamic ranges of the low and high frequency lines. For the range of 5 pF $< C_2 <$ 15 pF, the high frequency line in Figure 4.9 shows a dynamic range of less than 10 kHz, whereas the low frequency line shows a dynamic range of approximately 3 MHz. In the symmetric link case as shown in Figure 4.10, it can be seen that both the high and low frequency lines of resonance show a large dynamic range of approximately 7 MHz and 3 MHz respectively. Whether the oscillator locks to the higher or lower frequency resonance point for a given capacitance is not a concern; there is no point at which the resonance lines can overlap and cause an ambiguous solution.

4.2.4 Link Coupling

The previous analysis has assumed a fixed mutual inductance M between the two coils, without considering how the value of M affects the link performance. In the active mode, variations in M affect the amplitude of the signal at the receiver, whereas in the passive mode variations in M primarily affect the sensitivity to changes in C_{SENS}. In both cases variations in M can cause measurement errors, since Equations 4.7 and 4.8 both depend on M as well as ω, changes in M can be misinterpreted as changes in C_{SENS}.

Link coupling is considered in terms of the unitless coupling coefficient k rather than mutual inductance M in some of this section, where:

$$k = M/\sqrt{L_1 L_2} \tag{4.9}$$

$k = 1$ indicates perfect coupling between L_1 and L_2 and $k = 0$ indicates that L_1 and L_2 are entirely uncoupled.

4.2.5 Active Mode

In the active mode, the coupling is the principal factor determining the amplitude of the signal at the receiver. As the coupling decreases, the gain also decreases. For the

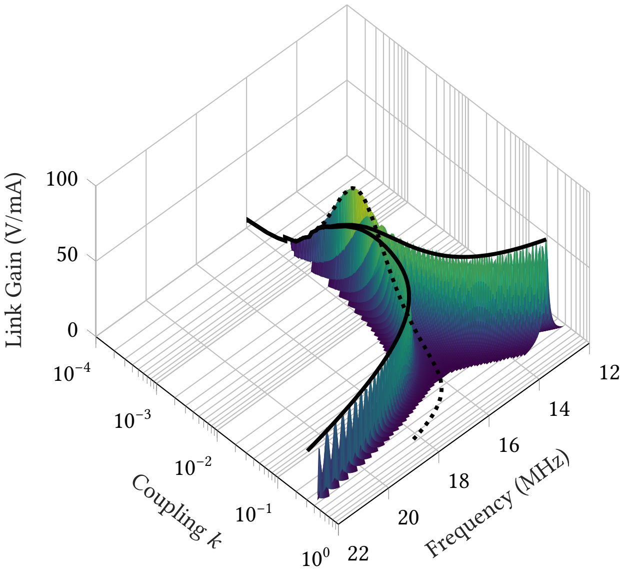

(A)

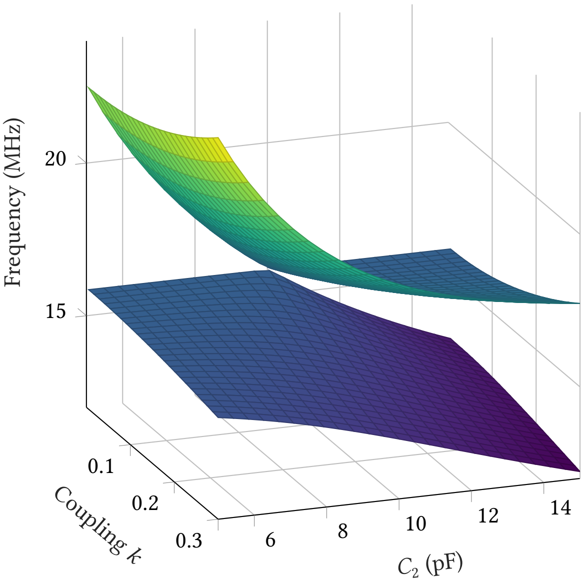

(B)

FIGURE 4.11: (A): Link gain vs coupling and frequency. Lines of resonance and anti-resonance are highlighted. (B):Planes of resonance against changes in C_2 and k.

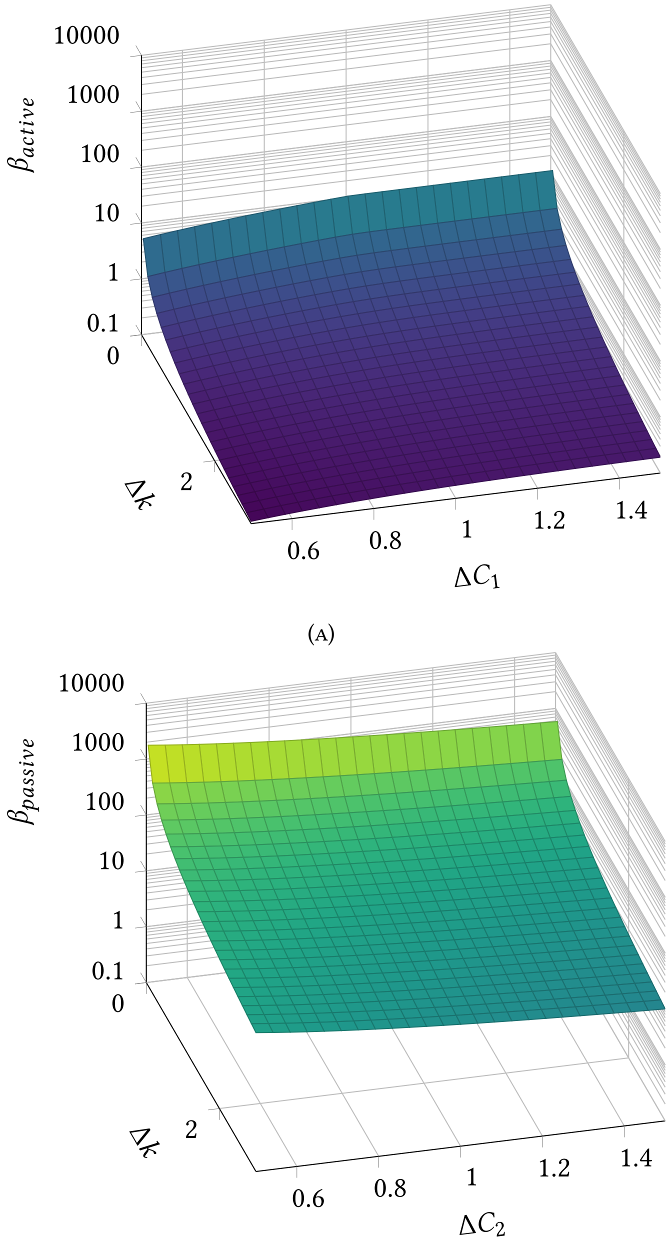

(A)

(B)

FIGURE 4.12: Plots of (A) β_{active} and (B) $\beta_{passive}$ against variations in Δk and $\Delta C_{(1,2)}$. Nominal parameters again are the same as in Figure 4.5, $k_{(nom)} = 0.1$, $C_{(1,2)_{(nom)}} = 10$ pF.

circuit in Figure 4.4, following the procedure defined in [52], the link gain is defined as:

$$\frac{V_{out}}{I_{in}} = \frac{-j\omega M\left(j\omega C_1 + \frac{1}{R_1+j\omega L_1+Z_{refl}}\right)^{-1}}{\left(R_1 + j\omega L_1 + Z_{refl}\right)\left(R_2 + j\omega L_2 + \frac{1}{j\omega C_2}\right)j\omega C_2} \tag{4.10}$$

where V_{out} is the voltage across the capacitor C_2, I_{in} is a constant ac input current with frequency ω in parallel with the input at C_1, and Z_{refl} is the impedance reflected from the secondary to the primary, where:

$$Z_{refl} = \frac{\omega^2 M^2}{R_2 + j\omega L_2 + \frac{1}{j\omega C_2}}. \tag{4.11}$$

Equation 4.10 shows how the link gain depends significantly on M. Figure 4.11a shows a plot of Equation 4.10 using the example values from Figure 4.5, sweeping coupling and frequency. The lines of resonance/anti-resonance are mapped onto the surface; as long as the coupling stays sufficiently high ($k \geq 0.005$ in this case) the gain stays maximized.

This analysis assumes a high impedance at the frequency counter input, hence the gain remaining high over a wide range of couplings. Further resistive loading across C_2 will reduce this gain particularly at lower couplings.

4.2.6 Passive Mode

In the passive mode, the coupling significantly affects the dynamic range (in Hz/F). Figure 4.11b shows the results of Equation 4.8 plotted against both k and C_2. Figure 4.11b demonstrates that, at low couplings, the resonance lines that lie furthest from the anti-resonance plane show an almost flat response compared with those at high couplings. While the resonance planes still show a wide dynamic range for the regions near the anti-resonance plane, the value of $|Z_{link}|$ for these points will be low (cf. the asymmetric plot in Figure 4.8). As a result, the oscillator will not oscillate in these regions, only in the flattened regions far from the anti-resonance plane.

4.2.7 Errors due to coupling variations

The aim of Equations 4.7 and 4.8, is to convert a measured $\Delta\omega$ to ΔC. However, ΔM will also correlate to a measured $\Delta\omega$.

To determine an ideal region of operation, the relative impacts of $\Delta C_{(1,2)}$ and ΔM on $\Delta\omega$ should be considered. First, the Δ quantities are defined as follows:

$$\Delta C_1 = C_1/C_{1_{(nom)}} \tag{4.12a}$$

$$\Delta C_2 = C_2/C_{2_{(nom)}} \tag{4.12b}$$

$$\Delta M = M/M_{(nom)} \tag{4.12c}$$

where (nom) denotes the nominal value. Equation 4.12 defines the Δ quantities as unitless proportional deviations from the norm, and thus ΔC and ΔM can be directly compared.

The relation in Equation 4.3 effectively provides a function that describes how changes in $|Z_{link}|$ parameters are converted to changes in ω. The positive real roots of this function for varying Z_{link} parameters can be considered as functions $\gamma_n(Z_{link})$, where n is the root number, and $n \in \mathbb{Z}^+$. Odd positive root numbers define resonance points, even root numbers define antiresonances. Here the resonance points are of interest, so from here $\gamma = \gamma_1$. Using partial differentiation, the sensitivity of γ to $\Delta C_{(1,2)}$ and ΔM can be determined. The relative sensitivities of γ to M and $C_{(1,2)}$ can be expressed as ratios:

$$\beta_{active} = \left(\frac{\partial\gamma}{\partial\Delta C_1}\right) \bigg/ \left(\frac{\partial\gamma}{\partial\Delta M}\right) \tag{4.13}$$

$$\beta_{passive} = \left(\frac{\partial\gamma}{\partial\Delta C_2}\right) \bigg/ \left(\frac{\partial\gamma}{\partial\Delta M}\right). \tag{4.14}$$

Equations 4.13 and 4.14 provide ratios for the sensitivity of ω to $\Delta C_{SENS}/\Delta M$ for the active (β_{active}) and passive ($\beta_{passive}$) modes respectively.

To minimize the effect of ΔM on the measured value of $\Delta\omega$, the link should be far more sensitive to changes in capacitance than coupling, i.e. β_{active} and $\beta_{passive}$ should both be large.

Figure 4.12 shows planes of β_{active} and $\beta_{passive}$ for sweeps of k and C_{SENS}. A notable difference is that the value of β_{active} is up to 1000× smaller than the value of $\beta_{passive}$. This indicates that in the active mode, the measurement is far more susceptible to errors due to Δk than in the passive mode. For example, the worst case β_{active} in Figure 4.12a is ≈ 0.1, indicating that the output frequency for this point is $\approx 10\times$ more sensitive to Δk than it is to ΔC_1, whereas for $\beta_{passive}$ the minimum value is ≈ 10. Both planes however share the trend that β improves as the coupling decreases; both curves show an improvement of two orders of magnitude as k is swept from 0.3 to 0.005. This reduction in coupling is at the cost of gain or dynamic range for the active and passive case respectively.

For the active case, the coupling should be minimized to minimize the error due to Δk, limited by ensuring the link gain is still sufficient for detection at the counter. In the passive case, again coupling should be minimized, but in this case limited by ensuring dynamic range is sufficient (see Figure 4.11b).

4.2.8 Series Losses

Section 4.2.2 provides an exact method for determining an unknown capacitance from the frequency of an otherwise characterized resonating link. However, errors can occur if there is a change in series loss (R_1 or R_2) in addition to a change in C_{SENS}. This is a valid concern given that, depending on the sensing method and substance

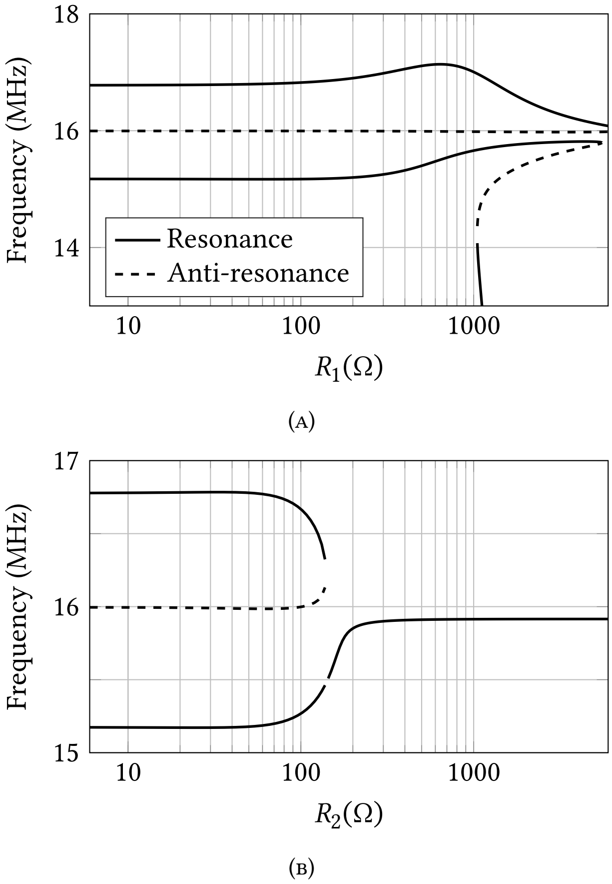

(a)

(b)

Figure 4.13: Lines of resonance and anti-resonance against changes in R_1 and R_2. Other link parameters the same as in Figure 4.5.

being sensed, a capacitive sensor may present a significant series loss compared to solid dielectrics or free space [167]–[169].

If the capacitive series loss resistance is large enough, it has a significant effect on the resonant frequency and would effectively stop an accurate measurement of capacitance from Equations 4.7 or 4.8. The frequency change would be due to a change in both C_{SENS} and R_1 or R_2. This effect is illustrated in Figure 4.13, where Equation 4.3 is solved against varying values of R_1 and R_2. As long as R_1 and R_2 remain below 100 Ω, the lines of resonance/antiresonance remain largely unaffected; they remain constant at the same frequencies as shown in Figure 4.5. However for larger values of series loss (≥ 100 Ω or so in this example), these lines suffer significant shifts. Therefore if a test substance introduces significant loss in addition to a change in capacitance, the capacitance change can no longer be reliably determined by using Equations 4.7 or 4.8.

The effect of series losses can be considered somewhat similarly to the issues arising from coupling variations. However there is no tradeoff in this case; ideally the loss should always be minimized to preserve the accuracy of the C_{SENS} measurement.

The preceding series loss analysis assumes that series loss in the capacitors $C_{1,2}$ can be lumped into the series loss of the coils, and simply added to $R_{1,2}$. It should be

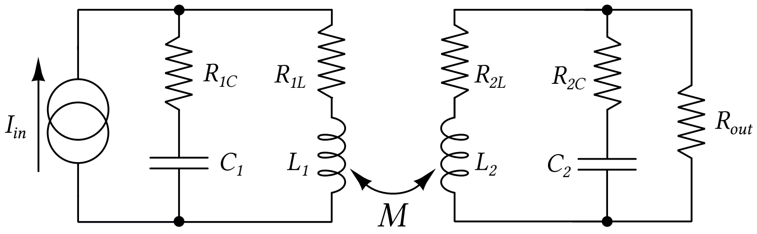

FIGURE 4.14: More detailed link diagram, including series loss in capacitors.

noted that this assumption is only valid for the link arrangement used here, a parallel-parallel link with a current-mode driver and a high (near infinite) load resistance.

Figure 4.14 shows a more detailed link diagram that includes the series loss resistance of both $C_{1,2}$ and $L_{1,2}$. If I_{in} has a very high output impedance, and R_{out} is also very large, then the R_C and R_L elements can be considered as singular combined losses $R_{1,2}$, as in Figure 4.4.

4.3 System Design

4.3.1 Oscillator Circuit

In order to test the method of measurement; a self-oscillating circuit, shown in Figure 4.15, was designed in 0.18 μm CMOS. It is a cross-coupled design, fed by a current source at its tail to control amplitude of oscillation.

The oscillator is controlled by complementary control signals *CTRL* and $\overline{CTRL}$. When *CTRL* goes high, the switches $M_{7,8}$ are turned on, connecting the oscillator to the transmission coil, and the transmission gate feeding M_0 is closed to allow bias current control. When *CTRL* goes low, $M_{5,6}$ turn on to force the gates of $M_{1,2}$ low and damp any oscillation during turnoff. The transmission gate feeding M_0 is also opened when *CTRL* goes low. The benefit of using a transmission gate here is when used in a round-robin arrangement (see §4.3.2), the required bias voltage for each oscillator will be held on the gate capacitance of M_0. This results in a faster startup time for each oscillator once it is selected. $M_{3,4}$ are long devices arranged to behave as a gate bias mechanism; these devices complement the fact that $M_{1,2}$ are 'native' enhancement mode NMOS devices, with $V_T \approx 0$ V. When the oscillator is on, the voltage at the drain of M_0 will always be a few mV above ground, this small voltage is enough to maintain $M_{3,4}$ in the subthreshold region, where they present a large pseudoresistance from gate to ground for $M_{1,2}$. $M_{3,4}$ also act in a loop to prevent the DC level of the gate voltages of $M_{1,2}$ from rising over time. This action can be considered as follows: if the gate voltage at M_1 rises slightly, the source voltage should also rise slightly, as M_0 will still be providing the same bias current. This slight rise in source voltage will reduce the resistance provided by M_4, bringing the gate voltage at M_1 back down. Since $M_{3,4}$ are long channel and operating in subthreshold, they do not respond to rapid changes at oscillation frequency, only to quasi-static drifts.

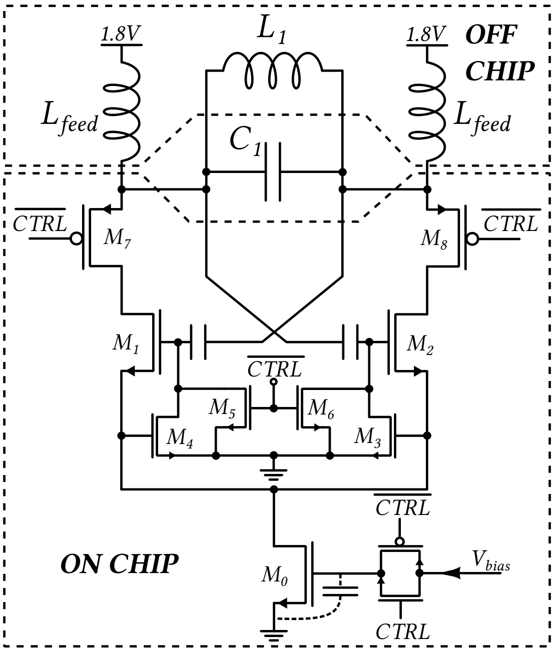

M_0	200μ/5μ
$M_{1,2}$	72μ/1μ
$M_{3,4}$	220n/10μ
$M_{5,6}$	2μ/350n
$M_{7,8}$	2048μ/300n

FIGURE 4.15: *Top*: Cross-coupled oscillator circuit. C_1 is on or off chip depending on active or passive configuration. *Bottom*: Table of device dimensions.

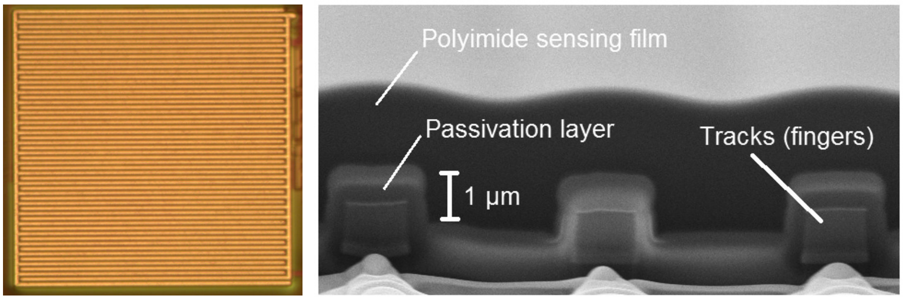

(A) *Top view.*

(B) *Side view.*

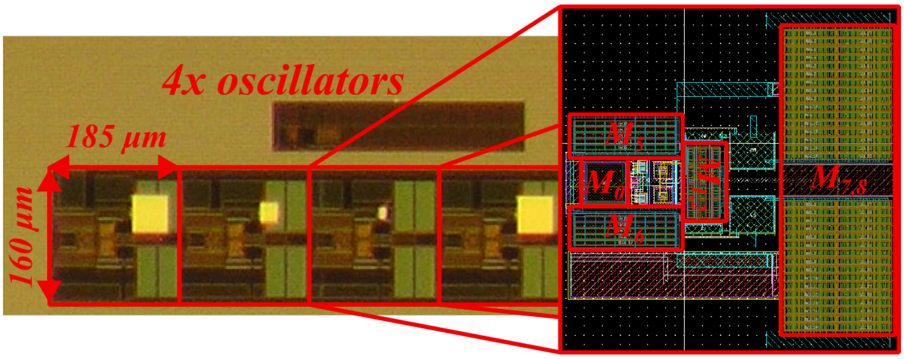

(C) *Chip photo, circuit elements highlighted.*

FIGURE 4.16: Microscope (a) and ion-beam (b) images of the humidity sensing capacitor. (c) shows a close-up image of the fabricated circuits and their area, layout detail is highlighted.

Figure 4.16c shows a photo of the fabricated chip, with 4 independent oscillator circuits visible, each occupying an area of 160 μm × 185 μm. An enlarged layout image is inset, highlighting the relative size of the key structures.

4.3.2 Round Robin Sensing

Figure 4.16c shows how there are 4 oscillators arranged in a group on the fabricated chip. This was part of the initial design that allowed these 4 oscillators to be automatically activated in a round-robin manner to interrogate 4 separate capacitors. Ultimately, this arrangement was not used; since the capacitors were buried under a thick layer of glass passivation, they were not sensitive enough to generate measurable capacitive changes in response to fluids placed on the chip or humidity changes in the environment. The overall architecture showed promise however, and is described in more detail here.

The round robin circuit is a simple counter driven by a ring oscillator at a fairly low frequency, which can be tuned digitally. Since each oscillator can be isolated from the coil by using the control switches $M_{7,8}$, they can all share a single inductive link across different time slots. To ensure each of these oscillators is running at a consistent low power level, a bias control loop was implemented, to allow the bias voltages to be adjusted such that the output amplitude envelope hits an external target value. Using the scheme as in Figure 4.17 requires the system to be used in active mode, since the sensing capacitors are attached directly to the oscillator circuits.

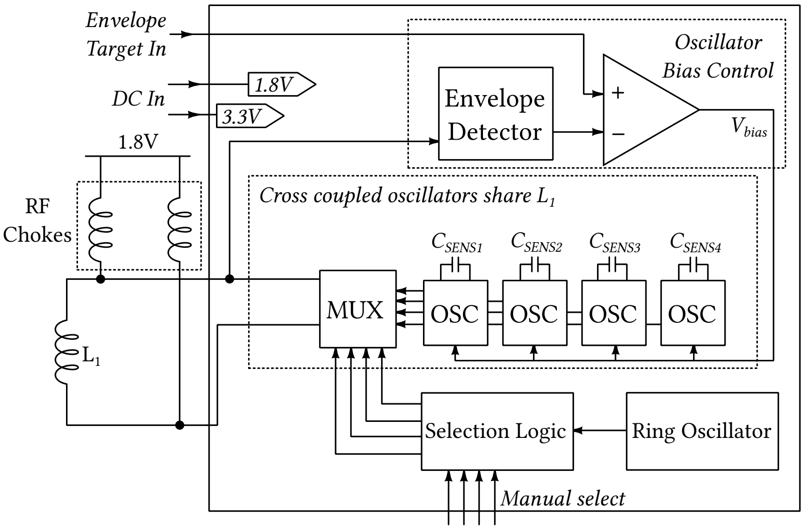

FIGURE 4.17: Full chip architecture; including round-robin selector and bias control loop.

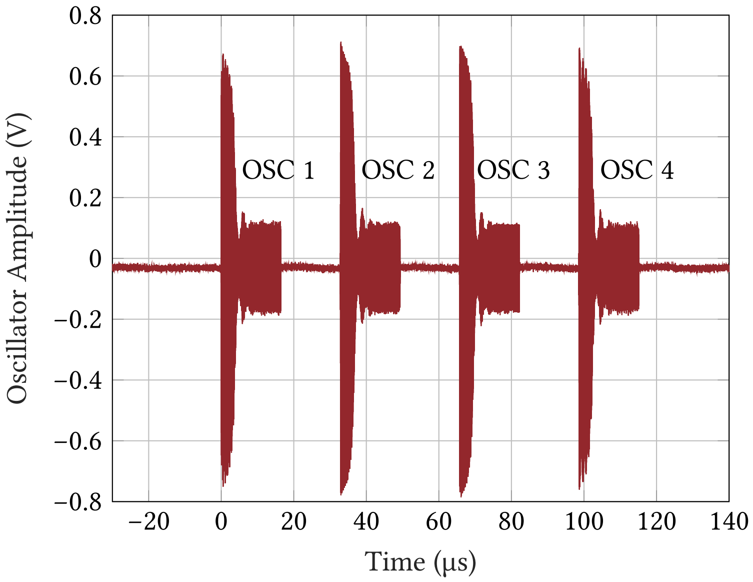

FIGURE 4.18: Output voltage at the transmission coil with 4 round robin oscillators running.

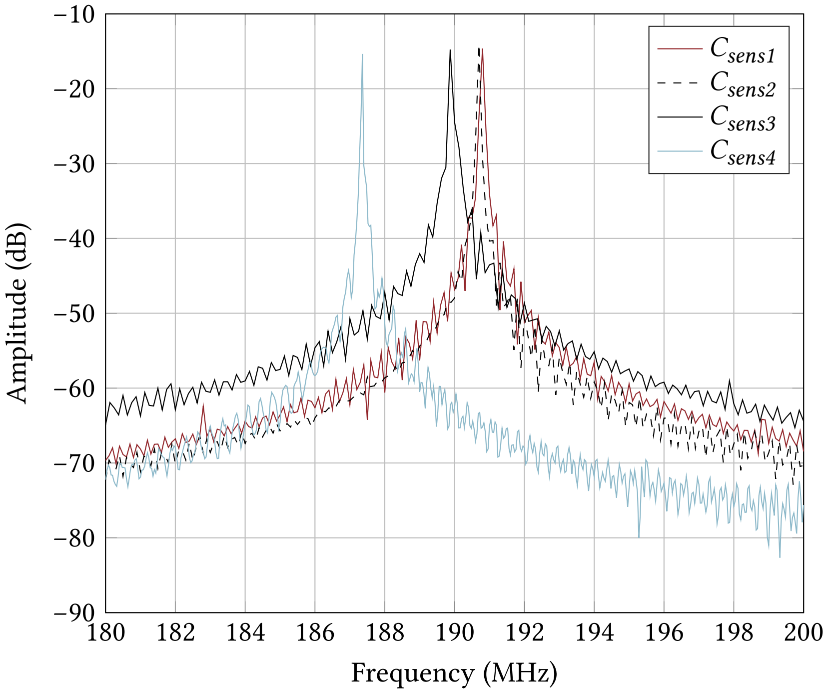

FIGURE 4.19: Post-layout simulated frequency spectra for each of the round robin bursts from Figure 4.18. Parasitic capacitance reduced the measured operating frequency to between 55 and 60 MHz.

Figure 4.18 shows measured output of the multiplexed oscillators. The ring oscillator is set to give each oscillator a 16.5 μs slot in which to run, with an empty slot between each. Each oscillator can be seen ramping up to a high power level initially, but is then quickly throttled down to the target amplitude by the bias regulation circuit.

Figure 4.19 shows how each oscillator generates a distinct resonant frequency, as a result of the integrated capacitors each being a different size[1]. While these capacitors failed to demonstrate sensing, they did demonstrate that the round-robin arrangement worked well, and each oscillator could be distinguished by its unique frequency relating to its unique capacitor.

4.3.3 Humidity Sensing Capacitors

Since the capacitors integrated into the round robin system were unsuitable, a standalone test oscillator[2] was used in combination with a humidity sensing capacitor [170]. The structure of this capacitor is illustrated in Figures 4.16a and 4.16b. The capacitor consists of interdigitated top metal fingers, with a polyimide film on the surface above the passivation. As the polyimide absorbs humidity from the environment, its dielectric constant changes, altering the capacitance. These on-chip capacitors were confirmed to have low series losses (< 1 Ω), and as such comply with the requirement for a low series loss sensing element as previously explained in Section 4.2.8.

---

[1] These tiny integrated capacitors are visible in Figure 4.16c, they are the bright yellow squares within the oscillator blocks.

[2] This oscillator is identical to the ones in Figure 4.16c and Figure 4.15, but is in a separate part of the chip from the round-robin and bias control circuits, and is manually controlled.

TABLE 4.1: Measured Nominal Link Parameters.

Common		*Active*		*Passive*	
$L_{1,2}$	7.34 μH	C_1	13.4 pF	C_1	18.7 pF
$R_{1,2}$	6.0 Ω†	C_2	19.5 pF	C_2	7.5 pF
k	0.217	β^*	0.588	β^*	1.950

†Measured coil loss, C_{SENS} series loss is neglected here.

*β values calculated from measured link parameters.

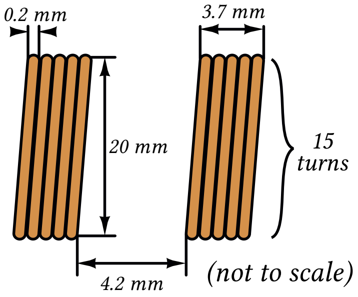

FIGURE 4.20: Nominal geometric specifications of the fabricated link coils. Both coils are circular, identical, and coaxially aligned.

The nominal capacitance of these capacitors is dependent on frequency, particularly at higher humidities [171], [172]. Here the capacitive variability is significantly reduced for frequencies beyond 1 MHz. In this work, the operating frequency is always higher than 10 MHz, therefore the nominal capacitive dependence on frequency can be neglected.

4.4 Measured Results

The system was tested in both the active and passive sensor configurations in order to determine the effectiveness of the method. The system was arranged as shown in Figure 4.21, and the nominal link parameters were measured. These link parameters are summarized in Table 4.1, as well as predicted values for β_{active} and $\beta_{passive}$. The link coils were single layer solenoids constructed from standard enamelled magnet wire, the details of their geometry are given in Figure 4.20. Most of the tests were conducted at a distance of 4.2 mm ($k = 0.217$), to obtain good dynamic range. Tests were also performed with 16.3 mm coil separation ($k = 0.056$); these are discussed later in this section.

In the active mode, the bulk of C_2 is formed by a 15 pF ceramic capacitor, the remaining capacitance comes from the parasitic capacitance of L_2 and the probe capacitances. C_1 is formed by C_{SENS} and parasitics at the oscillator. In the passive mode, C_1 consists of parasitics at the oscillator and the probe capacitances. C_2 is formed by C_{SENS} in addition to the parasitic capacitance of L_2.

In both cases, the parasitic capacitance at the oscillator is relevant; it is important therefore to maintain a constant bias current in the oscillator circuit, since the

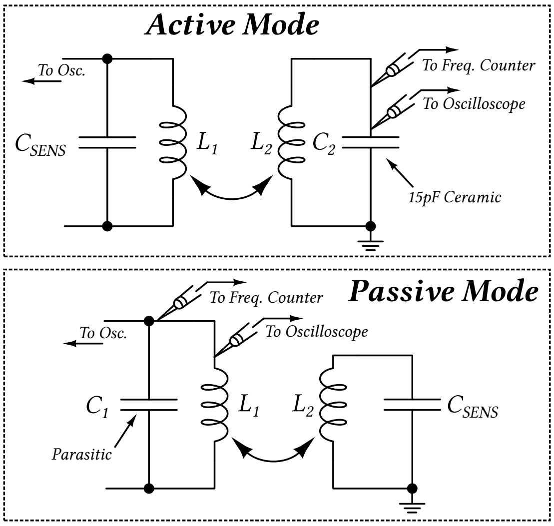

FIGURE 4.21: Test arrangements for the active and passive modes.

parasitic capacitance will depend on this bias. The correlation between bias and oscillation frequency is described in [173]; for the purposes of this work, increasing V_{bias} approximately generates an increasing shunt capacitance C_{shunt} that appears in parallel with the LC tank. This shunt capacitance is mostly the combination of junction capacitances at the sources of $M_{7,8}$. Since these junction capacitances are dependent on $M_{7,8}$'s V_{ds} values, which depend on their I_d values, which depend on V_{bias}, changing V_{bias} directly impacts the parasitic capacitances seen at the output nodes. By maintaining V_{bias} at a constant value, C_{shunt} will stay constant also.

Tests were performed in a climate controlled chamber (Binder KMF 115), for a range of humidities (20-90 %rh). The chamber was left to settle for 5 minutes after each change in humidity, and then 1000 samples were collected from the frequency counter (HP 53131A). The temperature was fixed at 35 °C.

Figure 4.22 shows measured data for the results of testing the system in active and passive mode, and a calibration plot, where the capacitor was measured by an impedance analyzer. The active mode and passive mode plots show that the same change in capacitance can be detected in both configurations, and matches well with the calibration plot. The error bars for the plots in Figure 4.22 are boxplots of the real data gathered from the counter. The boxplots show very little variation, with the maximum measured standard deviation occurring at 90% humidity in passive mode, where σ = 28 fF.

The main sources of error in this experiment are the stability of the humidity chamber itself and the phase noise of the oscillator, which is seen as capacitive measurement noise after being converted by Equation 4.7 or Equation 4.8. The worst case σ of 28 fF at 90 %rh in passive mode suggests a minimum resolvable relative humidity step of < 2 %rh. Given that the specified humidity fluctuation of the chamber is ≤ 2.5 %rh, it is possible that this variance is due to the chamber rather than the circuit.

Figure 4.23 shows the relative measured capacitive change for the active and

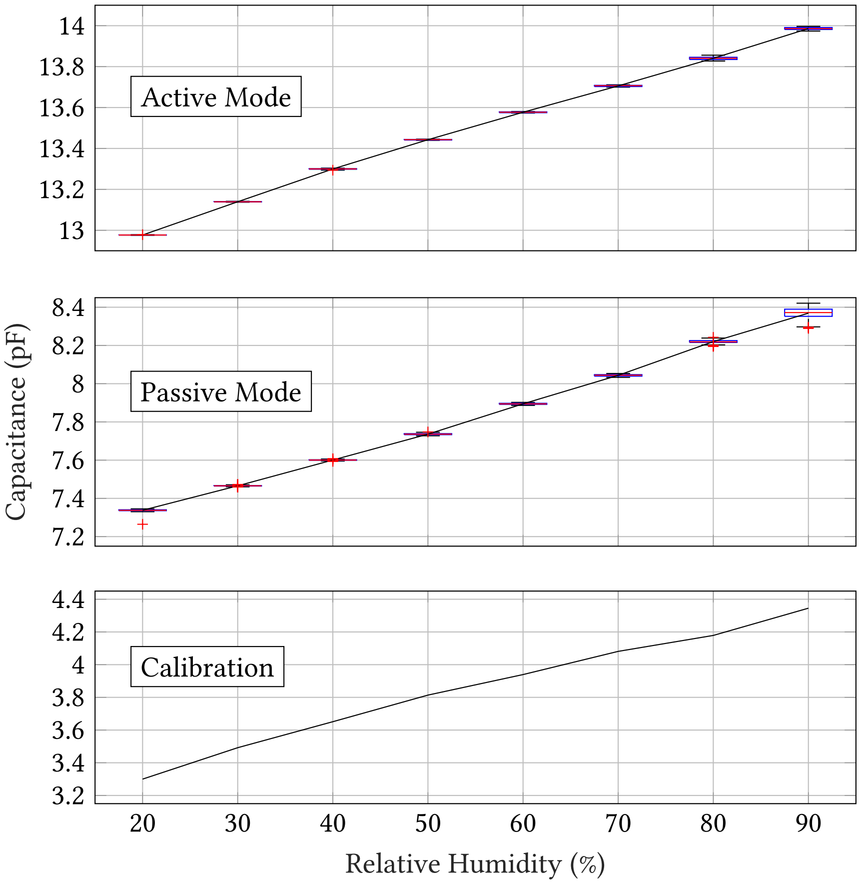

Figure 4.22: Raw relative humidity data from the system in active and passive mode, compared with calibration data from the capacitive sensor.

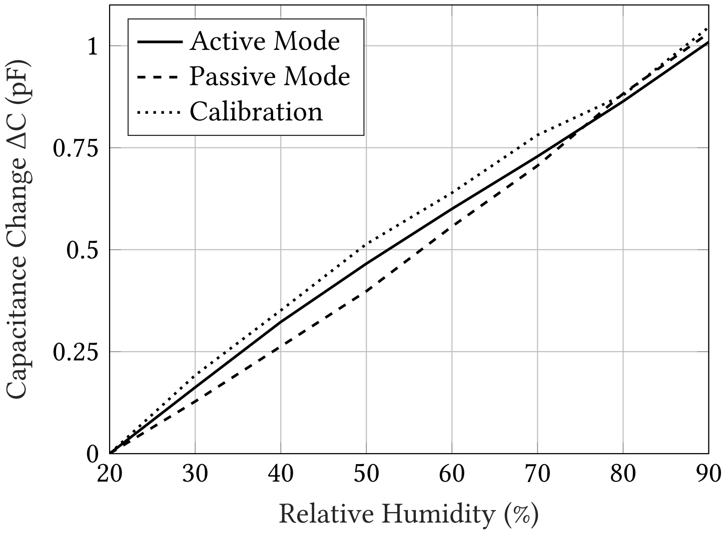

Figure 4.23: Capacitive deviation as a function of relative humidity for the active and passive modes.

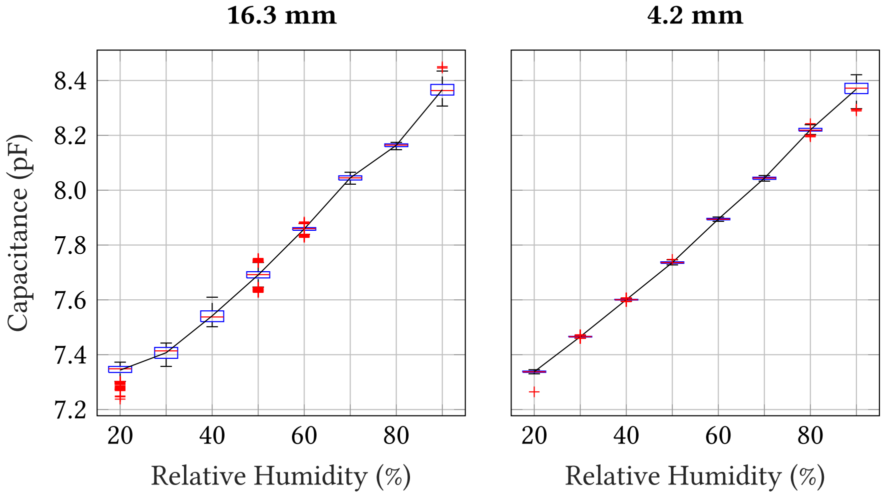

FIGURE 4.24: Passive mode capacitance measurements for different coil spacings.

passive modes compared to the impedance analyzer measurement. The worst case difference is an error of 0.1 pF between the passive mode and the calibration plot occurring at 50 %rh.

Table 4.2 summarizes the magnitude errors (mean and standard deviation) and correlation coefficients for the active and passive mode results, compared with those from the calibration run (based on the data in Figure 4.23). These statistical results from the system show good correlation with the calibration run; the worst case mean magnitude error of 55.5 fF correlates to a humidity sensing error of 3.9 %rh, with respect to the calibration run with the impedance analyzer.

4.4.1 Reduced Coupling

To assess the effect of reducing the coupling on system performance, the distance between the coils was increased from 4.2 mm to 16.3 mm, and the system was tested in passive mode. Figure 4.24 shows measured capacitance against humidity for 4.2 mm and 16.3 mm coil spacings. While the overall trend remains the same, as the distance is increased the accuracy is reduced. This is shown by the boxplots for each humidity value having larger spreads than those from the shorter range tests.

The reason for this increased spread in the results can be explained by increased phase noise in the oscillator as the distance between the coils is increased. This is illustrated in Figure 4.25. This increase in frequency variability directly translates

TABLE 4.2: Summary of correlation and error between system measurements and calibration measurements.

	Magnitude Error (pF)	*r Value*
Active Mode	μ = 0.0311 σ = 0.0172	0.9991
Passive Mode	μ = 0.0555 σ = 0.0437	0.9925

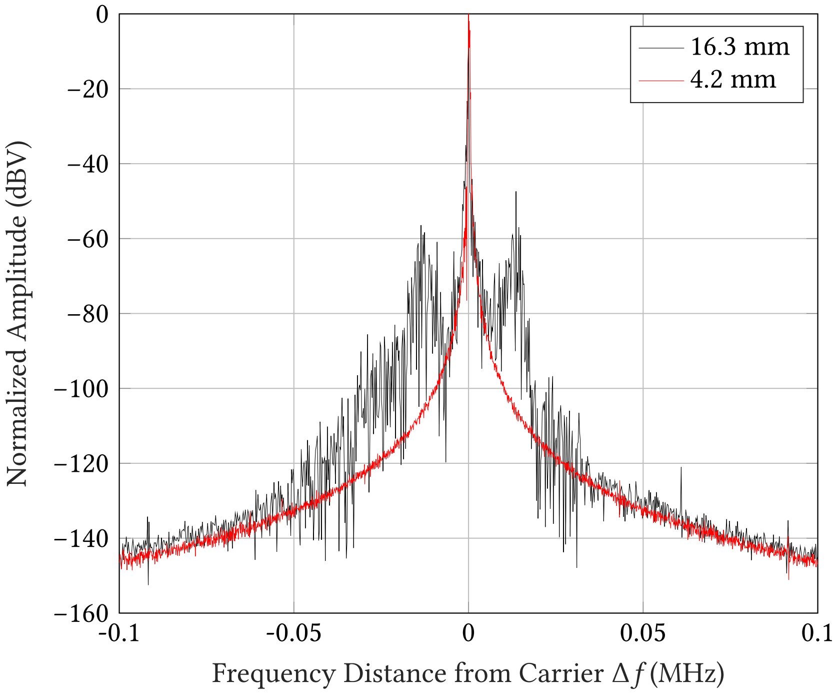

FIGURE 4.25: Output spectra for different coil spacings.

to an increase in measurement variability, increasing the overall uncertainty. It is therefore important to consider the effect of coil coupling on the phase noise of the oscillator, as it has a direct impact on the measurement accuracy.

4.4.2 Power Consumption

The total current consumption of the circuit was also measured, and compared with the average current consumption in postlayout simulation. Since the consumption of the system is strongly dependent on V_{bias}, it was measured for a range of V_{bias} values.

Figure 4.26 shows the average current consumption of the circuit from a 1.8 V supply as V_{bias} is varied from 0.85 V to 1.5 V, and the peak to peak voltage output at the oscillator. The curves show that the output starts compressing at $V_{bias} > 1.2$ V; the bias was therefore fixed here to maximize the output without wasting power in distortion. The measured current consumption for $V_{bias} = 1.2$ V was 0.8 mA, or 1.44 mW total power dissipation. The minimum power dissipation at $V_{bias} = 0.85$ V is 72 μW.

4.5 Conclusion

This chapter has presented a method for performing short-range wireless sensing of a capacitive sensing element, requiring only a self-oscillating circuit and a frequency counter. The developed theory has been verified through circuit fabrication and experiment, with the results suggesting good accuracy. Compared with the current state of the art, this approach bridges the gap between miniaturized wireless measurement

TABLE 4.3: Comparison with other recent wireless sensing systems.

Parameter	**This Work**	Ahmadi et. al. 2009 [12]	Lee et. al. 2016 [157]	Zhang et. al. 2015 [158]
Size	Miniature	Miniature	Benchtop	Benchtop
Power	Low (72 μW – 1.44 mW†)	Low (198 μW††)	High	High
Complexity	Low	High	Moderate	Moderate
Method	Direct C to f Conversion and FM Wireless Transmission	Glucose to Current Conversion, A2D Encoding, and Digital Wireless Transmission	Frequency Sweep Impedance Interrogation	Frequency Sweep Impedance Interrogation
Active/Passive	Active or Passive	Active* Only	Passive Only	Passive Only
Sensitivity	Passive: 635 Hz/%rh, Active: 1.188 kHz/%rh	1.25 – 8.8 nA/mM	304 kHz/kPa	18.71 kHz/%rh
Frequency Range	12 – 14 MHz	DC Sensing, 13.56 MHz RF Carrier	160 – 170 MHz	35 – 37 MHz
Operating Distance (Max)	16.3 mm	4 cm	20 mm	5 mm

†Not including frequency counter.
††Not including RF transmitter.

*While the modulation scheme is technically 'passive' (load-shift keying), the direction is one way from the remote side to the local side; this is therefore comparable to the active mode in this work.

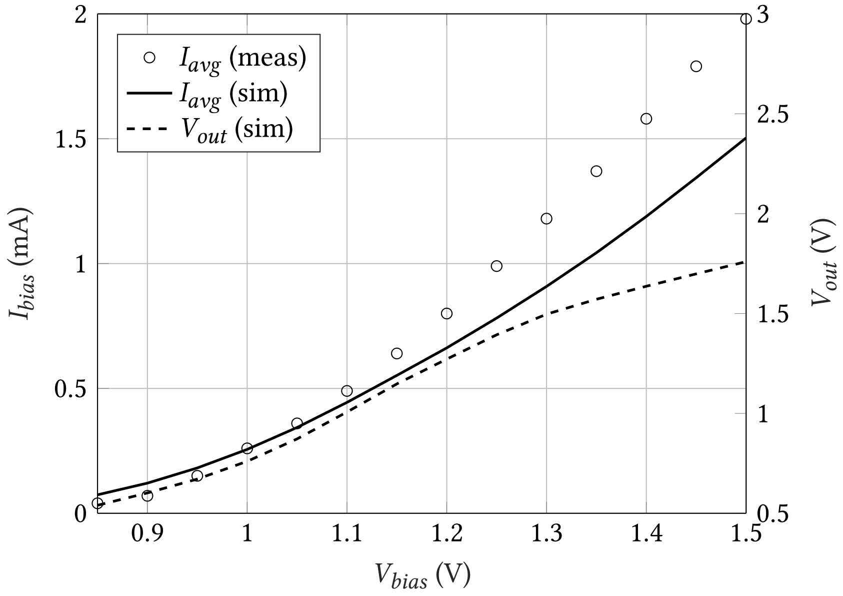

FIGURE 4.26: Measured and simulated average current consumption (I_{avg}) and oscillator output amplitude (V_{out}) as V_{bias} is varied.

systems, that require complex signal processing chains, and direct inductive link based measurement systems, that require benchtop impedance analyzers.

A comparison with the state of the art is provided in Table 4.3. The key elements to note are that the method presented in this chapter is suitable for miniaturized implementations at low power consumptions, without the associated complexity that otherwise is required. In addition, the method is reversible; the same fundamental circuits are used for both active and passive modes.

Given that the method presented here is flexible and low complexity, and the circuits are miniaturizable and low power, they would be well placed in a variety of fast-growing wireless sensing applications, for example in the biomedical, food quality, and environmental monitoring domains.

In addition, the system could be extended to contain many multiplexed oscillators over a single link, running in active mode. By running in this way, low resolution imaging systems (1 oscillator per pixel), or multi-purpose sensing systems (different sensing targets per oscillator/capacitor pair) could be realised. These would have the benefit of limited complexity at the remote side, to minimize remote side power consumption.

4.6 Addendum: Application to Power Transfer

While the methods presented in this chapter primarily apply to sensing, they have the potential to be very useful for power transfer as well. Chapter 3 describes a system for zero-phase tracking in order to maintain the optimum frequency for power transfer, regardless of the link coupling. The downside of the system from chapter 3 is its complexity; it requires multiple blocks to capture the phase information, process it into data for the microcontroller, and then convert that data into commands to adjust the PLL. A much more elegant way to ensure that the power transmitter is maintaining the optimum frequency is to use a self-oscillating circuit, such as the one in Figure 4.15. By scaling the transistors to be large enough, fairly high powers can be delivered efficiently, with the frequency maintained at the optimum value. An example of such a system was presented by Ahn et al. [174], where an integrated self-oscillating transmitter was combined with an integrated adaptive active rectifier to achieve high efficiency.

The work presented in this chapter could provide a unique addition to this method however. By applying the analysis used to determine unknown capacitances (Equations 4.7 and 4.8) to an unknown mutual inductance, this allows the displacement between the link coils to be determined when the link is overcoupled.

$$\frac{\partial\{|Z_{link}(\omega)|\}}{\partial M} = 0 \tag{4.15}$$

By using Equation 4.15, one can obtain a function to relate the current oscillation frequency to the coil distance. This will in turn give information about the value of Z_{refl}. This information can be used to adjust the primary side voltage for output load regulation, without the need for back-telemetry. When the link is undercoupled, the amplitude of the primary current with respect to the primary supply can be used as an indicator of distance. Whether a drop in primary current indicated a reduced distance $< k_{crit}$ or an increased distance $> k_{crit}$ would no longer be ambiguous; the oscillation frequency removes this ambiguity by being dependent on the link being under- or over-coupled.

Power and Data Transfer using Stagger Tuning and PPSK

5

The work in this chapter forms a part of the work published in IEEE Transactions on Biomedical Circuits and Systems [175]. What is presented here serves to expand on and clarify the relevant parts of that paper.

5.1 Data Transfer for IMDs

Up to this point we have focused on inductive links for power transfer. However, it is often convenient to use inductive links for data transmission as well, especially if the power link can be repurposed for simultaneous data transfer. When it comes to designing links for data transfer however, different considerations must be made. This is particularly true for shared power/data links, where features must be carefully traded off against each other. The rest of this section will briefly discuss the topic of data transfer for IMDs, and describe some of the key difficulties that can arise.

5.1.1 Shared Link Solutions

Shared link solutions involve transmitting data over an inductive link that is already transmitting power. They can provide uplink (implant ⟶ transmitter) or downlink (transmitter ⟶ implant) communications, and are usually limited to half-duplex operation. This half-duplex limitation arises because most of the schemes involve amplitude-modulation of the power carrier, so uplink and downlink have to share the same transmission channel.

A good example of a half-duplex bidirectional shared link data transmission solution is given by Jiang et al. [175], where on-off keying (OOK) is used for the downlink, and passive phase-shift keying (PPSK) is used for the uplink.

OOK is implemented here by modulating the power driver for the link on or off, to encode 0- and 1-bits. This appears at the receiver coil as a drop in the received power envelope, which can be recovered using an amplitude demodulator. PPSK can be considered as a special form of load-shift keying (LSK) [176]. In both cases the fundamental principle involves short-circuiting the receiver side of the link for a short period to encode bits. Each time it is shorted in this way, the reflected load seen at the transmitter side is modified, which can be detected at the primary side by monitoring the load current. Figure 5.1 gives a high level overview of an OOK-LSK style system.

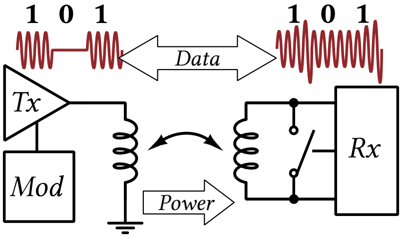

FIGURE 5.1: Simple overview of an OOK-LSK style shared link solution.

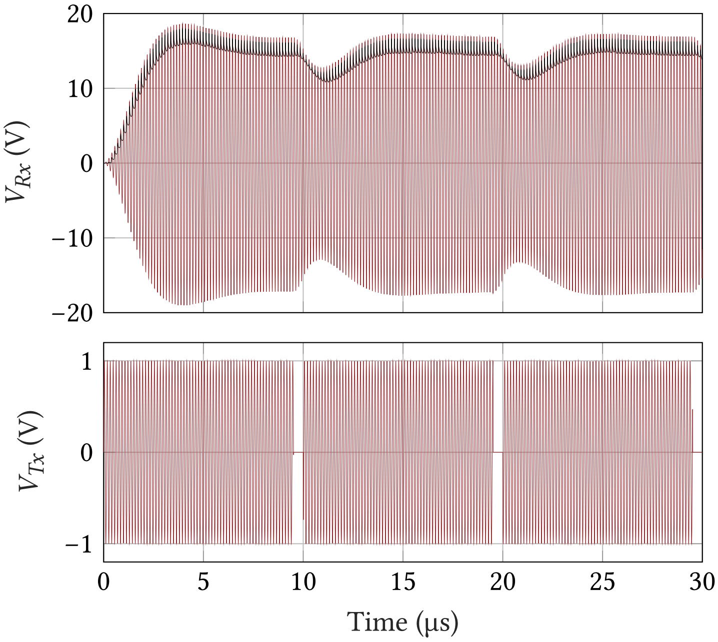

FIGURE 5.2: OOK modulation, 6.78 MHz carrier, 100 kHz datastream. Black trace is the envelope.

This kind of system is not without pitfalls however. Considering the OOK downlink, each time a 0-bit is encoded, the power transmitter must be disabled; this can starve the receiver if the power drops by too much. Reducing the duty cycle of the OOK modulation can mitigate this drop in power somewhat, however it requires careful consideration of the link bandwidth. If the link coils have a very high Q, the receiver will need more time to register a bit, as the energy from the receiving tank will drain more slowly. Considered in terms of bandwidth, power transfer requires *high-Q*, *low bandwidth* links, whereas data transfer requires *low-Q*, *high bandwidth* links. Compromises must be made to perform both functions.

Figures 5.2 and 5.3 show example waveforms for OOK transmission through an inductive link, using the same link parameters as in Table 2.4, but with a coupling coefficient of 0.05. For low data rates, a high duty cycle can suffice; Figure 5.2 has a 95% duty cycle in V_{Tx}, giving an average V_{Rx} amplitude of 13 V, with clear dips in the received envelope encoding transmitted bits. By increasing the data rate to 500 kHz however, the duty cycle must be reduced to 50% to achieve a reasonable depth of envelope at the receiver (see Figure 5.3). This also comes at the cost of the power

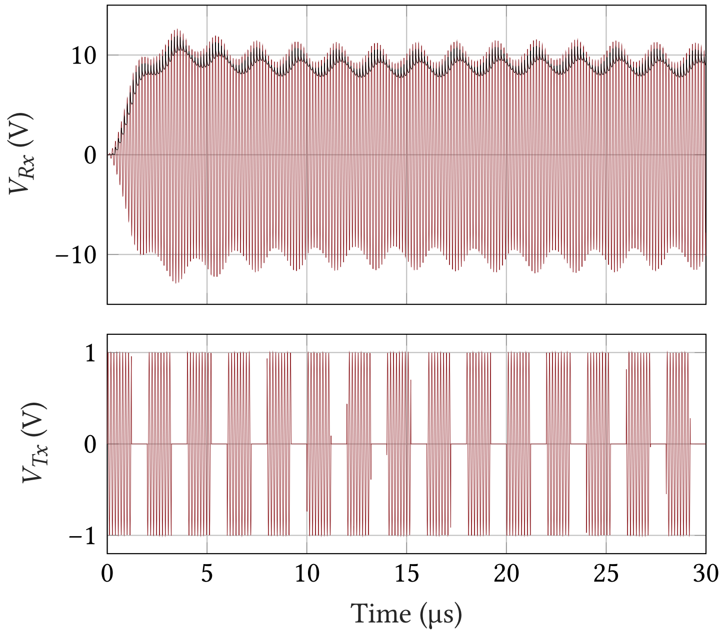

FIGURE 5.3: OOK modulation, 6.78 MHz carrier, 500 kHz datastream.
Black trace is the envelope.

transmitted; with a 50% duty cycle the average amplitude at the receiver is only 9 V.

LSK suffers from similar problems to OOK; data rate and modulation depth are hindered by the link having a high-Q, requiring higher duty cycles over which the receiver must be cut off from power. In addition, since LSK essentially modulates the reflected impedance, it is more dependent than OOK on having a high coupling coefficient to achieve good modulation depths at the transmitter.

Yet another issue suffered by both schemes is that they lack displacement tolerance. Since they both rely on AM, and the gain of the link is dependent on the coupling coefficient, a sudden displacement of a coil can appear as a rogue bit. A worst case situation would be vibration in the link, as a mechanical vibration with enough amplitude could easily cause a k modulation large enough to appear as a phantom bitstream at the vibration frequency.

5.1.2 Dedicated Link Solutions

If higher data rates are required, a dedicated link solution is preferable to a shared link. Full duplex operation can be achieved by using a pair of dedicated data links in parallel; one for uplink, one for downlink.

This kind of arrangement has significant benefits over a shared link scheme, at the cost of complexity. The data links can be optimized with high-bandwidth in mind, so can have moderate to low Q-factors, while the power link can be designed with a high Q-factor for increased PTE. This allows for higher data rates to be achieved than the few Mbps shared links can manage. For example Lu et al. [46] demonstrate 8 Mbps transmission with a 13.56 MHz carrier, by using offset quadrature phase shift keying (OQPSK). Schemes like PSK and FSK are also more resilient to displacement

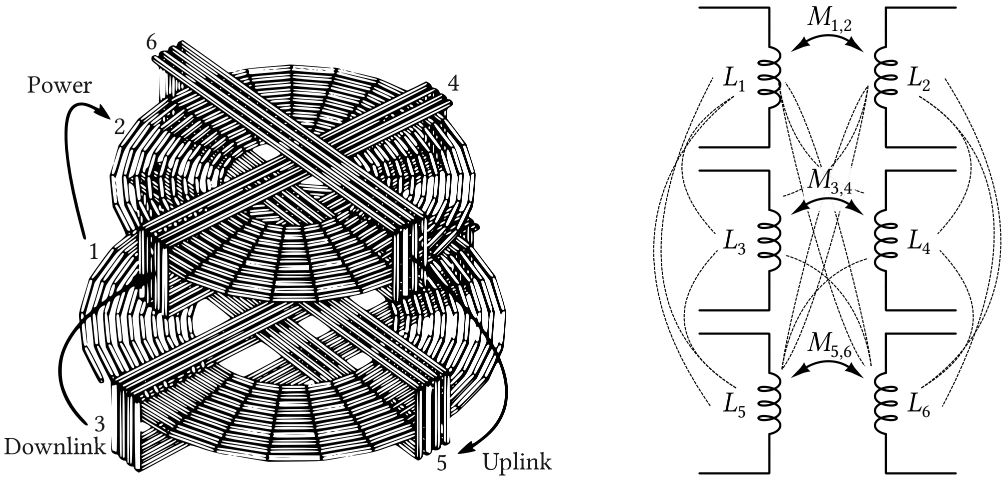

(A) Orthogonal coils

(B) Cross-coupling of 6 coils

FIGURE 5.4: (A): Remastered from [179], an arrangement to minimize unwanted couplings between coils in a power + full duplex data link arrangement. (B): Circuit representation of the arrangement; desirable couplings are labelled, undesirable couplings are marked with thin dashed lines.

than AM based schemes, as the phase and frequency are entirely independent of coupling. FSK and PSK based schemes also require a carrier to be generated at the transmitter side, and a local oscillator (LO) for recovery at the receiver side. This will require progressively more power budget as the carrier frequency increases. To avoid this extra power consumption from carrier and LO generation, an impulse radio (IR) based scheme can be used, such as pulse harmonic modulation (PHM) [49], [177], [178], pulse delay modulation (PDM) [50], or short-range quality-factor modulation (SQuirM)[1].

For both continuous wave and impulse based systems however, there is the problem of cross-coupling. By adding additional links in parallel, all coils in close proximity to each other will be coupled to some degree, whether it is intended or not. Figure 5.4 illustrates cross coupling in a full-duplex power and data inductive link arrangement, as well as a an orthogonal coil placement arrangement designed to minimize undesirable cross-coupling [179]. The exception to this is in the case of PDM, where cross-coupling is intentionally used; a dedicated link is used for impulse transmission, with the goal of disrupting the zero-crossings of the power carrier to encode bits. PDM can be considered a hybrid between a dedicated- and shared-link solution, with some of the pros and cons of each.

5.2 Problem Definition: NEUWalk

The rest of this chapter describes the design of an inductive link for use as part of the NEUWalk project [175], [180], [181], capable of transferring both power and data to an implanted stimulator unit over a single inductive link. The purpose of the NEUWalk

---

[1] See Chapter 6

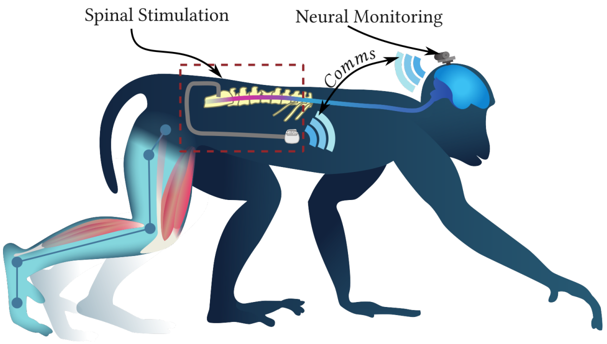

FIGURE 5.5: Adapted from [181], overview of the closed-loop spinal stimulator concept.

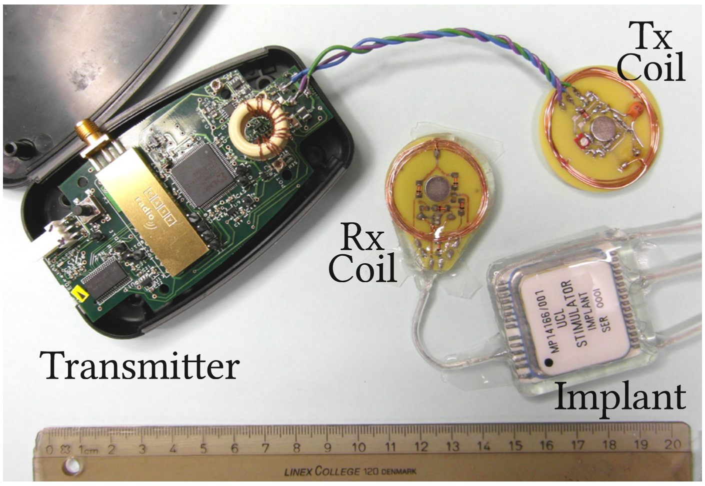

FIGURE 5.6: Implanted stimulator and external transmitter.

project was ultimately to develop a closed-loop spinal stimulation system, capable of restoring leg function in a paraplegic patient, based on monitoring neural activity and controlling an implanted stimulator based on those recordings. Figure 5.5 shows the concept behind the project; the first prototype was to be implanted in a monkey with a spinal lesion, aiming to restore movement to its right leg.

The overall project would require several components to work in concert[2], including the communications, neural recording, and stimulation elements. The component that was developed in this work was the inductive link between the implanted stimulator and parts of the external stimulator controller. Figure 5.6 shows the final transmitter design next to the implantable stimulator unit, with each side connected to an inductive link coil. The transmitter needed to be able to deliver power, send stimulator commands via OOK, and receive information from the stimulator via PPSK. Figure 5.7 shows a block diagram overview of the system in Figure 5.6. C_1 is implemented with a pair of capacitors in series for two reasons: to reduce the voltage seen by the recovery circuit to a safer level (5 V amplitude max or so), and to reduce the effect of capacitive loading from the recovery circuit on the primary capacitance.

---

[2] The majority of these components were developed by other members of the analogue and biomedical electronics group, and the implanted devices group, both at UCL. More details of the whole system are described in [175]

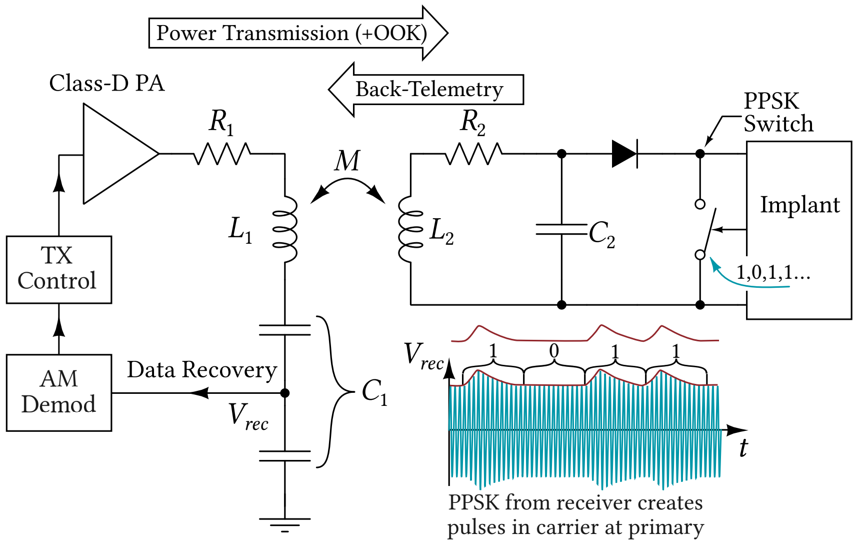

FIGURE 5.7: Block diagram of the transmitter/implant/link arrangement.

The requirements of the inductive link were as follows:

- Nominal working distance of 8 mm, with a functional range of 3-11 mm.
- Power carrier frequency of 9.6 MHz.
- Maximum implanted coil diameter of ≈30 mm.
- Sufficient voltage gain and power delivery to be able to run the implant from an external 3.8 V lithium cell.
- Resilience to coupling variations inherent to live implantation.
- Sufficient bandwidth to transmit uplink data via PPSK and downlink programming information via OOK.

With reference to Chapter 2, this list of requirements can be seen to have internal conflicts. Bandwidth should be minimized for power telemetry, but maximized for data telemetry. To improve resilience, generally efficiency or PDL has to be sacrificed. In order to meet all the requirements adequately, the link was designed using the principle of ‘stagger tuning’, as described by Galbraith et al. [47].

5.3 Passive Phase Shift Keying

Up to this point, PPSK has been mentioned but not described. This section describes the principles of PPSK in some more detail, illustrating the methodology itself, as well as differences between LSK and PPSK.

PPSK was first reported by Zhou and Donaldson [48] as a refined form of LSK, with the goal of maximizing the modulation depth, and minimizing the transient response

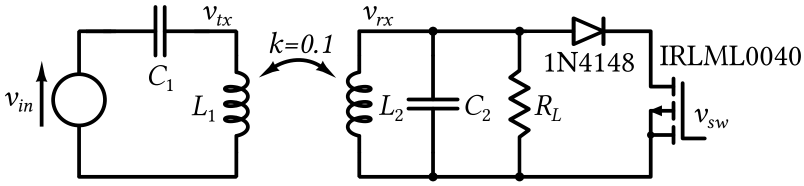

FIGURE 5.8: Circuit setup for LSK/PPSK simulation, R_L =1344 Ω, link specifications otherwise the same as in Table 5.1.

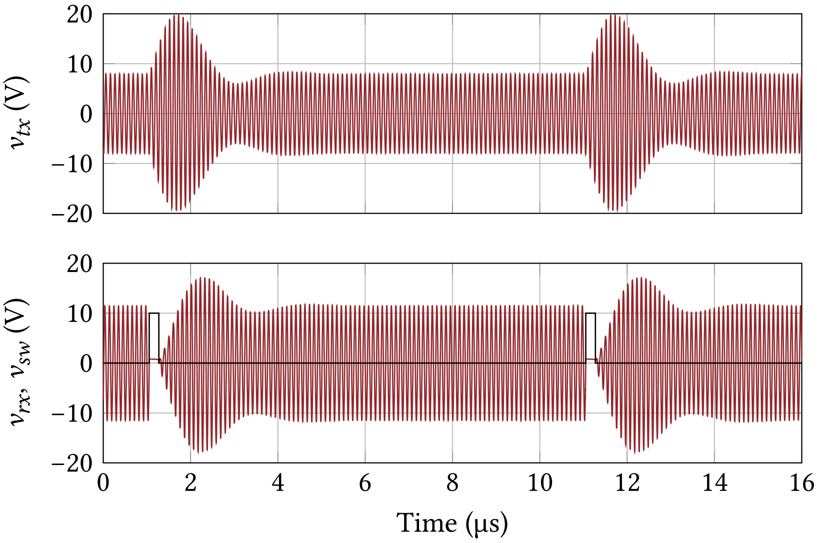

FIGURE 5.9: Simulated waveforms for an LSK arrangement.

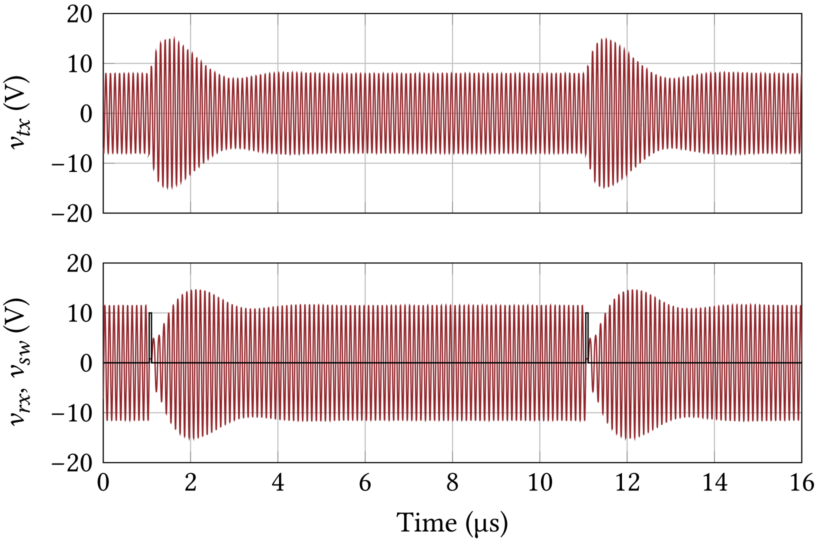

FIGURE 5.10: Simulated waveforms for a PPSK arrangement.

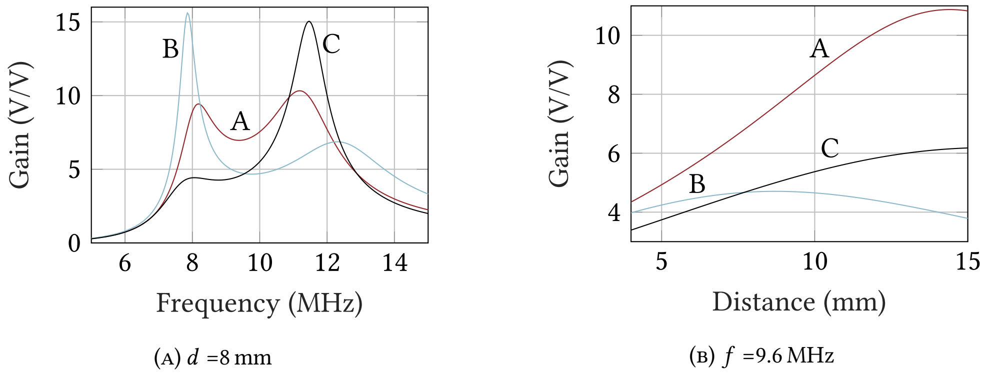

(A) d =8 mm

(B) f =9.6 MHz

FIGURE 5.11: Link gain responses for different stagger setups. Link arrangement is SP, $R_1 = 0.77\Omega$, $R_2 = 1.14\Omega$, $R_L = 1344\Omega$. Other specifications are given in Table 5.1.

time. In both LSK and PPSK, the receiver communicates back to the transmitter by shorting the receiving coil temporarily.

Figure 5.8 shows the circuit used to simulate behaviour of both LSK and PPSK modulation in a 9.6 MHz centre tuned link. Figure 5.9 shows waveforms for this link in an LSK modulated arrangement. By shorting the receiver coil for a period, the impedance seen at the transmitter is altered, and the voltage envelope builds. This can be detected as a bit by using an AM demodulator. Holding the switch closed for a longer time allows the envelope to build more, and be more easily detected, but reduces the maximum bit-rate, and further limits power delivery through the link. PPSK involves carefully pulsing the shorting switch *on* for an odd number of half-cycles[3], instead of an arbitrary pulse length. When timed in this way, the current in the receiver coil performs a phase reversal, and it rapidly returns to leading the coil voltage by 90° when the switch is released. As a result, the envelope at v_{tx} builds more quickly, the received voltage is disrupted less, and higher data rates can be achieved than in the case of regular LSK.

5.4 Stagger Tuning for Power and Data Transfer

Stagger tuning a link is a simple but effective method of designing an inductive link so as to strike a balance between resilience and power delivery. Due to the nature of staggering, it also produces an increase in bandwidth when the link is overcoupled. While this increase in bandwidth was not part of Galbraith's original intention, it is certainly useful for shared power and data links.

The principle of staggered link design as originally described by Galbraith involves designing a link around a desired centre frequency, then altering the resonant capacitor values through trial and error to achieve the desired level of staggering. Figure 5.11 shows the effect of different capacitor skews on the gain of an example link, in accordance with Table 5.1. The load value of $R_L = 1344\Omega$ was used as a good approximation for the load presented by the implant [175]. Maximum gain is achieved

---

[3] Ideally 1 half cycle, as is used in this example.

by using a centre tuned link at 9.6 MHz (skew **A**), however this comes with a large amount of variability in gain against coupling (see Figure 5.11b). Skew **B** increases the primary and reduces the secondary capacitance. This reduces the overall gain, but also greatly reduces the variability against coupling variations within the working range. It also shows a moderate increase in bandwidth compared with the centre tuned configuration. Skew **C** demonstrates how not all stagger setups produce a useful result. There is no real bandwidth increase compared with the centre tuned case, and while the gain variability against distance is reduced, it is only reduced moderately. To produce a good design with stagger tuning, some amount of iterative design and trial and error is required.

5.5 Link Design and Gain Measurements

The first element of the link design that must be considered is the diameter of the receiver: it must be no larger than 30 mm. The receiver coil was designed with a diameter of 28 mm, to be mounted on a 30 mm diameter PCB with 1 mm of extra space at the edges. With this fixed, the transmitter coil diameter was set to a diameter of 32 mm, in accordance with the following equation from Ko et al. [54]:

$$d_1 = \sqrt{d_2^2 + 4D^2}\,. \tag{5.1}$$

Where d_1 and d_2 are the transmitter and receiver diameters respectively, and D is the nominal coil distance, Equation 5.1 provides a transmitter diameter that maximizes the coil coupling for a given separation distance D. Maximizing the coil coupling is useful for PTE, but also useful in this case for PPSK operation, where higher coupling coefficients enable higher data rates.

This link was designed before the CuCCo software was developed, therefore in order to determine optimum turn ratios, a sequence of transmitter and receiver coils were constructed, with turn numbers (n_1 and n_2 for Tx and Rx turns) ranging from 3 to 9. All of these coils were then measured using an impedance analyzer, and the inductance and resistance values at 9.6 MHz were extracted. Using these extracted values, link gain vs coupling was calculated for all combinations of these coils. The best combination[4] was found to be $n_1 = 5$ and $n_2 = 7$. Details for the chosen coils are

TABLE 5.1: Table of stagger configurations, with inductance and capacitance values.

		Capacitances		
	Inductances	**A**	**B**	**C**
Primary	1.73 µH	159.0 pF	174.0 pF	144 pF
Secondary	2.56 µH	107.2 pF	92.2 pF	122.2 pF

---

[4] The combination with the highest link gain across the operating range.

TABLE 5.2: Measured parameters of the link coils. Measurements were performed at 9.6 MHz.

Parameter	**Tx Coil**	**Rx Coil**
Turns ($n_{1,2}$)	5	7
Diameter ($d_{1,2}$)	32 mm	28 mm
Inductance ($L_{1,2}$)	1.864 µH	2.529 µH
Series Resistance ($R_{1,2}$)	1.04 Ω	1.38 Ω
Quality Factor ($Q_{1,2}$)	107	108

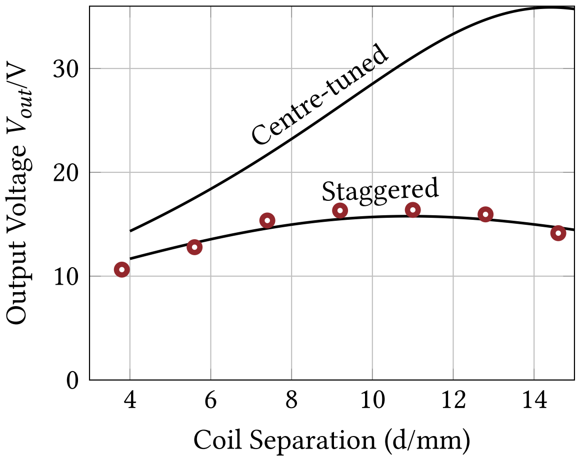

FIGURE 5.12: Plot to show experimental values of V_{out} against coil separation d, with drive frequency $f = 9.6$ MHz. Black lines are calculations, red circles are measurements.

summarised in Table 5.2.

These coils were paired with undersized tuning capacitors (100 pF at the Tx and 68 pF at the Rx) in parallel with trimmable capacitors. This allowed for both sides of the link to be tuned to either side of the centre frequency.

The link was then adjusted through an iterative trial and error procedure, sweeping the coil coupling, and adjusting the tuning capacitors, until a flattened gain response was achieved across the working range. After achieving the desired gain response, the link was measured across a range of frequencies and coil coupling distances, to determine its full gain characteristic. The results of these measurements are plotted in Figures 5.12 and 5.13. The staggered capacitances used were approximately $C_1 = 133$ pF and $C_2 = 110$ pF, and the output stage of the Class-D was powered from a 3.3 V supply. The output voltage was measured with a 1344 Ω load connected, to approximate the load presented by the implant [175].

Figure 5.12 in particular shows the benefits of stagger-tuning when considering output voltage stability against coupling variations. While the centre-tuned configuration achieves significantly more gain, the output voltage when driven from the 3.3 V Class-D ranges from less than 15 V up to 37 V, a total range of 22 V. Since the implant uses an LDO to down-regulate the received voltage, receiving high voltages

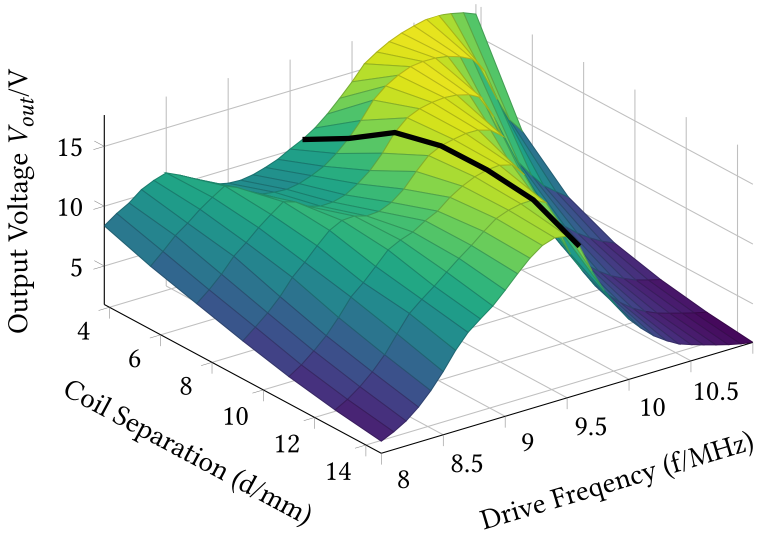

FIGURE 5.13: Plot to show experimental values of V_{out} against frequency f and coil separation d.

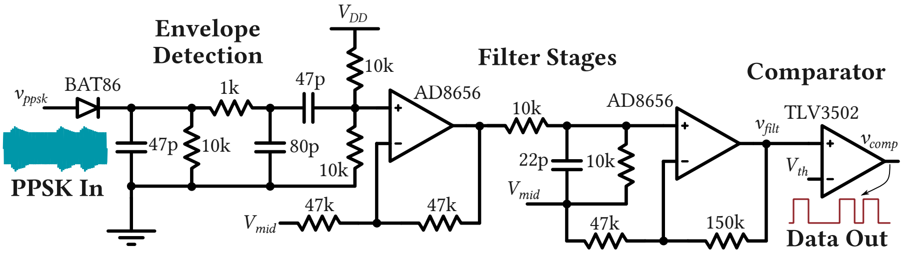

FIGURE 5.14: PPSK demodulation circuit.

leads to a drop in efficiency, since the regulator has to burn off the difference as heat. The staggered link however, varies across a range of only 5.8 V. As such, it maintains similar system efficiency across the whole working range.

Figure 5.13 shows the output voltage of the link[5] against both coupling and frequency variations. The 9.6 MHz results from Figure 5.12 are highlighted with a black line. The mesh here also shows that the link retains a fairly wide bandwidth over the whole working range. The overall response shows milder frequency splitting than in a centre-tuned link however; the centre frequencies retain more gain at close coupling, and the ridges are less pronounced.

5.6 AM Demodulator

In order to recover data sent through the link at the transmitter side, an AM demodulator was designed to be capable of handling datastreams with speeds of up to 1.35 Mbps. Details of the demodulator circuit are shown in Figure 5.14.

The response of the demodulator circuit is a bandpass, with −3 dB cutoffs at 135 kHz and 4.8 MHz, yielding a bandwidth of 4.67 MHz, more than sufficient to recover a 1.35 Mbps datastream. V_{mid} and V_{th} were generated by resistive dividers

---

[5] Again with a 3.3 V supply at the power amplifier.

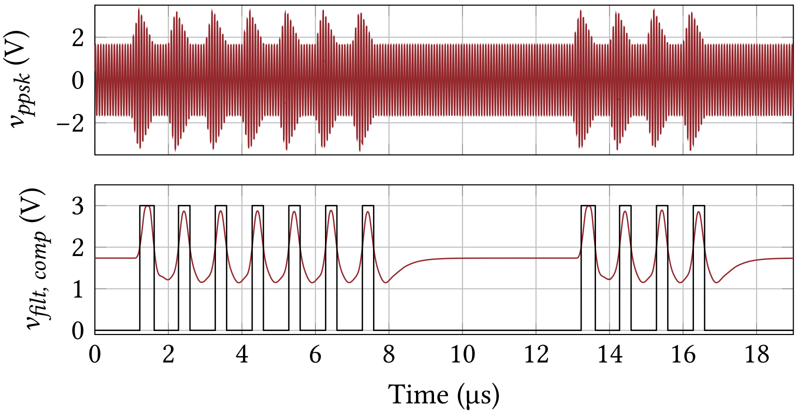

FIGURE 5.15: Simulated demodulator waveforms.

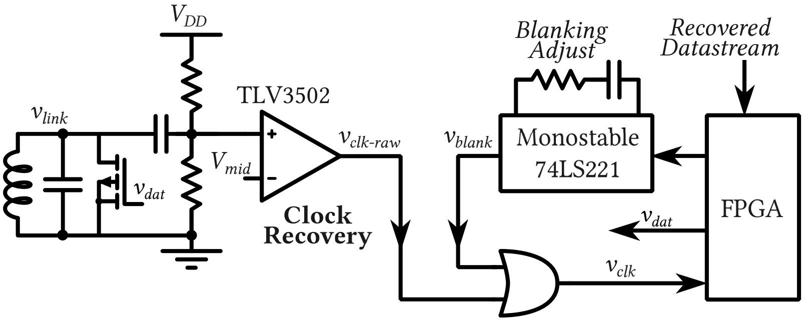

FIGURE 5.16: PPSK modulator for BER testing.

with unity gain buffers added. V_{mid} was defined as $V_{DD}/2$, so that a single-rail supply could be used. V_{th} was a variable reference that could be adjusted to an appropriate level with respect to the DC average of V_{filt}. Figure 5.15 shows simulated behaviour of the demodulator, using a 1 Mbps datastream. Overall the two amplifying stages provide a combined gain of 8, allowing the comparator to easily detect and output the recovered bits.

5.7 Data Transfer Testing

The data transfer capabilities of the system were tested by sending an OOK instruction from the transmitter to set the implant into handshake mode. This would cause the implant to send a continuous stream of handshake packets back via PPSK. The system was tested at a data rate of 600 kbps, and found to perform successful handshakes and data transfer. This was assessed through visual inspection of the output waveforms of the implant, ensuring that the returning bits were successfully recovered by the AM demodulator.

In order to further test the capabilities of the link and the demodulator circuit, a discrete PPSK modulator circuit was constructed. This modulator circuit imitated the functions of the implant data subsystem, but provided a pseudorandom bitstream back through the link to test the BER of the system.

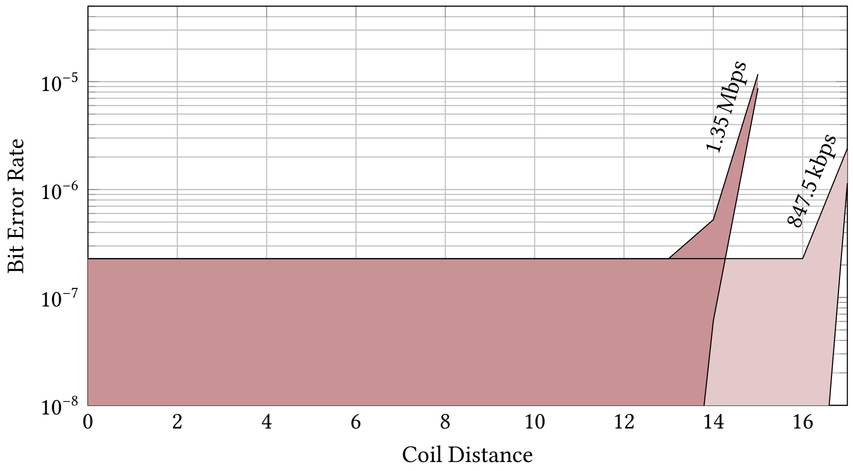

FIGURE 5.17: BER test results, upper and lower bounds shown to 95% confidence.

Figure 5.16 shows the circuit schematic for the modulator. The link carrier is used to generate a clock for the FPGA after being recovered by a comparator. This is passed through an OR-gate in order to allow the FPGA to disable its own clock when sending PPSK bits through a blanking control mechanism. Since PPSK disrupts the clock frequency, it is important to prevent the clock from being fed to the FPGA as v_{dat} is brought high. The datastream is then recovered by the demodulator at the Tx side of the link, and brought back to the FPGA for comparison, where any bit errors can be counted.

Figure 5.17 shows the recorded bit error rates for the PPSK system as the coil distance is varied, for different data rates. Upper and lower bounds were calculated to confidence levels of 95%, using Wilson's adjusted method [182][6]. Each distance was tested with a pseudorandom stream of $2^{24} - 1$ bits. It is likely that better nominal BER values could have been verified, however given the low overall data rate of the system, this would have taken many hours to send the required number of bits at each coil distance.

5.8 Discussion and Conclusions

This chapter has presented a stagger tuning based inductive link design for transferring power and data. The link proved to reduce variation in output voltage against variations in coupling significantly compared to a centre tuned design, while still providing sufficient voltage to power the implant across the working range. The link gain was measured across a range of couplings and frequencies, and these measurements were found to have good agreement with calculations. BER was also measured with data rates of 847.5 kbps and 1.35 Mbps, and was found to be good throughout the working range, with measured values largely better than 2.3×10^{-7}.

---

[6] This statistical method is described in more detail in Chapter 6.

While stagger tuning was found to be largely helpful in achieving a link that is coupling insensitive, and capable of carrying both data and power, the method itself still has some drawbacks and room for improvement. From the viewpoint of reproducibility, stagger tuning is not a good method. Since the design procedure involves trial and error, any small alteration in the design could easily make an existing stagger configuration invalid. A valuable improvement could come from determining a repeatable procedure for designing stagger tuned links to meet given targets of bandwidth, gain, and insensitivity to coupling variations.

The work in this chapter also highlighted the value of software tools as part of the design process. Since the link here was designed before CuCCo (see Appendix B) was written, many link coils were constructed and measured in the lab, in order to characterize the design space. This process would have been far more efficient if it was modelled in software first. This was, in part, the motivation for writing the CuCCo software for link design [2].

6

Shortrange Quality-Factor Modulation (SQuirM)

The work in this chapter was first published in the conference proceedings of BioCAS 2017 [183]. This chapter contains further information, including experimental results.

It is often desirable for IMDs to send out large amounts of recorded data from within a patient; this is particularly the case for neural recording applications [16], [40], [184]. Figure 6.1 shows an example arrangement for a neural recording implant, with many recording needles. Using this 'Utah' array as an example, if we assume each of the 100 needles records at the same time, over a bandwidth of 10 kHz, this would require a bare minimum sample rate of 20 kHz. Then assuming each sample is encoded in 8-bits, this results in a bit rate requirement of 100 × 20 kHz × 8 bits = 16 Mbps. This is already a much greater data rate than can be supported by a simple OOK/FSK system modulating a power link [175]. If more resolution or oversampling are desired, the data rate increases accordingly, for example, Lopez et al. present a system with 455 recording electrodes, with 10 b 120 kS/s ADCs [184]. Recording from all electrodes in this system at once would produce 546 Mbps of data!

One approach to reduce the volume of data produced by these systems is to employ compressive sensing techniques. For example, Harrison et al. present a 'spike-driven' system [15], where the sampling rate is kept low, until a spike-event occurs. This triggers an increase in sampling rate, so that the spike can be captured in detail, without wasting samples on useless information. The problem with this kind of compressive sensing is that potentially useful information can be lost; the quality of the data depends on the quality of the compressive algorithm.

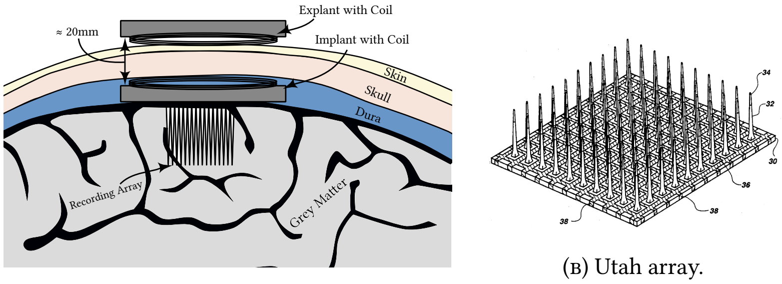

(B) Utah array.

(A) Neural implant.

FIGURE 6.1: Neural implant diagram, with many recording electrodes, and a 'Utah' electrode array, for neural recording [185].

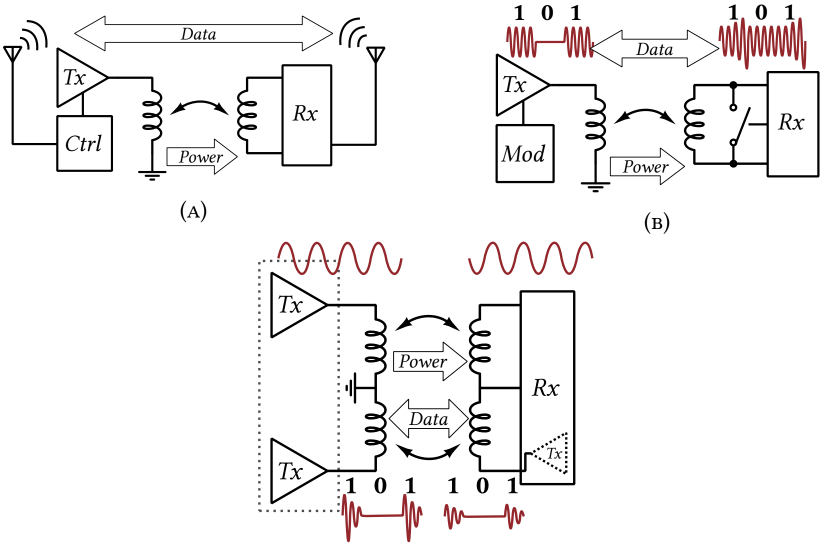

(A) (B) (C)

Figure 6.2: Inductive WPT with (A): WiFi-style data link, (B): data-modulated power link, and (C): dedicated data link.

Therefore, if the data is captured non-compressively, or the system has many compressed channels, a high-speed data link of some form must be employed.

6.1 Existing Techniques

Existing methods for high-speed data transfer can be classified as non-inductive, or inductive; these were discussed earlier in Chapters 1 and 2, and are revisited briefly here. General differences between approaches, and their respective pros and cons, are listed in Table 6.1.

Non-inductive data-transfer methods are those that use far-field omnidirectional transmission; e.g. Bluetooth, ZigBee, WiFi etc (see Figure 6.2a). These have the benefit of being widely used technologies, with CotS chips and designs available for easy implementation. These kinds of solution also have large working ranges, and capacity for high data rates. However this all comes at the cost of power consumption. To transmit large quantities of high-rate data using something like a WiFi transmitter requires power in the range of 100s of milliwatts to a watt [186]. This is far too much continuous power consumption for an IMD. In addition, the high frequencies (usually 915 MHz or 2.4 GHz) used by far-field transmitters suffer significant loss due to absorption by body tissues [187, pp. 59]. As a result, non-inductive data telemetry systems are less popular than inductive ones in the context of IMDs.

Inductive data-transfer methods can be considered in two categories; those that modulate an existing inductive power link (Figure 6.2b), and those that make use of a dedicated inductive link for data transfer (Figure 6.2c).

Modulated power links are an attractive option for low-data rate applications, as they are fairly simple to implement, and can make further use of the power link that

Table 6.1: Pros and cons for the schemes shown in Figure 6.2

Method	Pros	Cons
Non-inductive	• High data rate • Easy implementation • Long range	• *Prohibitively high power consumption*
Modulated power link	• Compact implementation • Fairly efficient	• Low data rate • Reduces power transfer
Dedicated link	• Supports higher data rate • Can be fairly efficient†	• Needs a dedicated link • Potential crosstalk

†Depends on implementation details.

is already in place. The example in Figure 6.2b shows a typical arrangement using OOK modulation for downlink data, and LSK modulation for uplink data (Chapter 5 presents a similar scheme as part of the NEUWalk system). These systems can also operate with little power; they do not need to generate their own carrier. However, since they must modulate the power carrier to transmit data, they are limited by the frequency of the power carrier with respect to data rate. For a typical power carrier frequency of 13.56 MHz, sending data at rates beyond 2 Mbps or so becomes difficult; each symbol needs several carrier cycles to be correctly demodulated [175]. In addition, as the transmitted data rate increases, the power transfer efficiency of the link gets worse. Take for example an OOK modulated transmitter sending data at full capacity, such that it has a 50% duty cycle; this reduces the average transmitted power to 50% as well (see Figure 6.3). These limitations render modulated power links unattractive for continuous transmission of high speed data.

On the other hand, dedicated link solutions are not limited in this way. By using a separate link, data can be transmitted in its own channel, without impacting power delivery. There are a number of ways to implement dedicated link solutions, but here we can broadly classify them as continuous-wave (CW), or impulse-radio (IR)[1] styles.

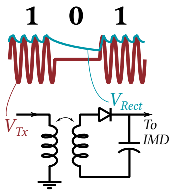

Figure 6.3: V_{rect} drooping due to high data rate

CW systems require generation of a continuous carrier in the transmitter side, which can then be modulated using ASK, FSK, PSK, etc to transmit data, in the same way as any traditional radio system. Simard et al. [179] give a good example of such a system, where 3 links are used in parallel: one for power, one for data uplink, and one for data downlink. While this

---

[1] Note that 'impulse-radio' is also used when referring to impulse-radio ultra-wide-band (IR-UWB) transmission methods, as described in [188]. While IR-UWB and close range IR are both impulse-driven, they should be considered to be distinct methodologies.

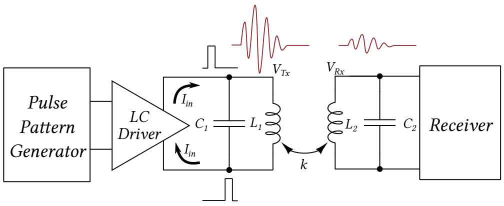

Figure 6.4: PHM system block diagram.

system is shown to work with a data rate of 4.15 Mbps, it requires continuous carrier generation, and still does not efficiently saturate the carrier with data. The system in [179] could theoretically boost its data rate by increasing the carrier frequency from 13.56 MHz, but this would inevitably require faster and more power hungry local oscillators; not an acceptable solution for low power IMDs.

IR based systems sidestep the problem of power hungry carrier (re-)generation by dispensing with the carrier completely. They rely on the fact that by striking a high-Q resonant circuit with an impulse, it will ring at its natural frequency for a period of time, and then fade away. In effect this can be considered both a carrier and a symbol. If the resonant circuit is a transmitting coil of an inductive link, this ringing can be easily detected in a closely coupled receiver coil. Inanlou et al. [49] give an excellent example of a short-range IR based system, using his method of pulse-harmonic modulation (PHM) [177]. PHM has been shown to achieve data transmission rates of up to 20 Mbps [178], using small closely coupled coils, in the presence of an interfering power carrier; all without requiring power hungry local oscillators for carrier (re-)generation.

Since PHM has the benefits of low power consumption and high speed, it is an excellent fit for IMD data subsystems. However, it suffers from some limitations, particularly regarding inter-symbol interference (ISI), that can increase power consumption and implementation complexity. The SQuirM method was developed as a system inspired by PHM, with the goal of eliminating the issues relating to ISI and simplifying the circuit implementation.

6.2 Theory

6.2.1 Fundamentals

It is worth covering the fundamental principles of both PHM and SQuirM, to show the differences in their theories of operation, and how SQuirM tackles some of PHM's problems.

PHM

A simplified block diagram of a PHM system is shown in Figure 6.4. The key elements are the pulse-pattern-generator and bidirectional LC-driver, that allow precise current pulses to be injected into the transmission coil. Figure 6.5 shows the nature of the

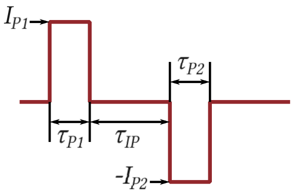

Param	**Value**
τ_{P1}	5 ns
τ_{P2}	5 ns
I_{P1}	1 mA
I_{P2}	0.9 mA
τ_{IP}	21 ns

Param	**Value**
$L_{1,2}$	129 nH
$C_{1,2}$	15 pF
$R_{1,2}$	0.6 Ω
k	0.1
R_L	50 Ω

FIGURE 6.5: Pulse-driving mechanism for PHM, with tables of values for an example system.

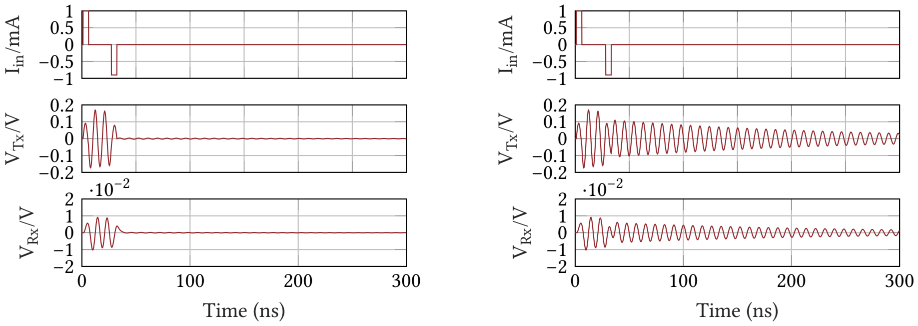

(A) τ_{IP} =21 ns (B) τ_{IP} =22 ns

FIGURE 6.6: (A): Ideal PHM waveforms, (B): Erroneous PHM waveforms.

pulses transmitted by the LC driver, the first pulse is the *activation pulse*, and the second is the *suppression pulse*. The aim of these two pulses is firstly to begin an oscillation in the transmission coil with the activation pulse, then by sending a perfectly timed suppression pulse in the opposite direction, a counter oscillation perfectly cancels the first oscillation. This generates a short oscillatory burst, which can be detected as a symbol by the receiver coil (see Figure 6.6a).

For this to work however, the activation and suppression pulses must be perfectly formed and synchronized. Inanlou provides an exact expression for the impulse response of a PP inductive link, and an associated expression for finding the ideal value of τ_{IP}, which 'should be an integer multiple of $[1/f_0]$ plus a half cycle'[177, Eq. 12]. Figure 6.6b shows the effect of a 1 ns error in the inter-pulse delay for the example system specified in Figure 6.5. The short symbol becomes extended into a long ringing signal, which would result in extreme ISI if sending a data sequence with a period any shorter than 300 ns in this case (any faster than ≈3 Mbps). While this kind of pulse-desynchronization can occur as a result of process or temperature variation in the pulse generator, the optimum value of τ_{IP} is also strongly dependent on the exact link state i.e. the values of L, C, R, k and R_L. This is a significant problem; the quality of the data link can suffer significantly due to changes in coupling and load. This fundamentally reduces the resilience of PHM as a method for data transfer, particularly for the case of IMDs, as there is no guarantee that the link state will remain stable[2].

A final point to note, is that in order for PHM to work well, the secondary must be loaded by a fairly small resistance R_L, in this example 50 Ω. This is necessary; without the effect of this load resistance, the secondary coil would contain a freewheeling current that would return to the coupled primary, undoing the effect of the suppression pulse. This load resistor has the unwanted side-effect of significantly reducing the link gain, since it has the effect of reducing the secondary side quality factor by an order of magnitude or more.

SQuirM

In contrast to PHM's twin-pulse cancellation strategy, the operating principle for SQuirM is based on the idea of successively *striking* and *damping* a PP inductive link.

Figure 6.7a gives a simplified block diagram of a SQuirM architecture, the theory of operation is as follows. An incoming datastream is fed to both the impulse generator and the transmit-side damping switch, M_{Txd}. Pulling the data line high represents a '1', and the pulse width of these incoming '1's determines how long the transmit side remains undamped. Sending longer data-in pulses gives more time for the Tx oscillation amplitude (and therefore the received oscillation amplitude) to build up, at the cost of data rate. Once the oscillation has been detected in the receiver, and V_{Rx} reaches sufficient amplitude, the receiver can detect its envelope and produce an output pulse. This pulse can then be *re-used* in order to damp the secondary coil once a bit has been received. Since the link is being damped from both sides, it means that the secondary coil can be terminated in a high impedance; the freewheeling current that would flow back to the primary instead terminates into the damping switch when it turns on. The benefit of this high impedance termination is a great increase in link gain compared with the PHM setup, where the secondary side Q must be reduced to achieve short symbols. For comparison, the received voltage of the example SQuirM system in Figure 6.7 is ≈ 100 mV, whereas for the PHM example it is ≈ 10 mV.

The purpose of the damping switches is to modulate the Q-factor of both sides of the link; when a bit is to be transferred, they are open so the Q is high. When a bit has been transmitted and received, the switches close, reducing the Q of both sides and clearing the remaining energy from the transmission channel.

The benefits of SQuirM can be summarized as follows:

- **Reduced power consumption:** The transmitter only needs to generate one sharp pulse instead of two; the amplitude at the receiver is higher, therefore the receiver requires less gain.

---

[2] The link coupling is most likely to vary here due to patient movement. Inductances can change due to flexion, and capacitances can drift due to temperature and age.

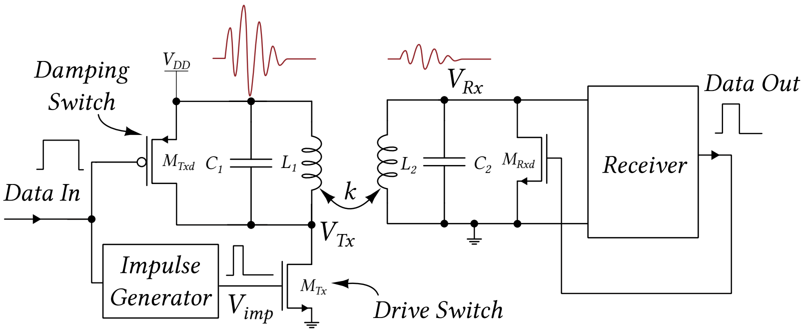

(A)

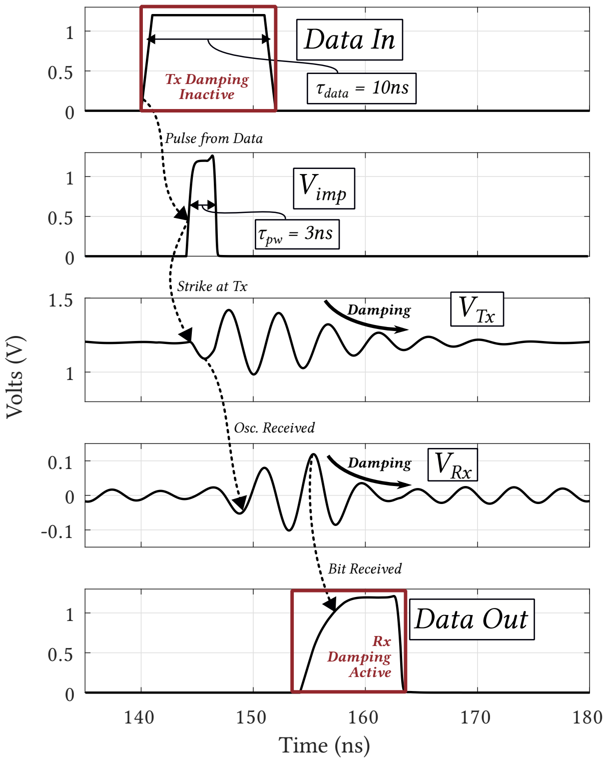

(B)

FIGURE 6.7: (A): Block and (B): timing diagrams for SQuirM.

- **Reduced complexity:** Timing requirements are far less strict, with only monopolar pulsing. Therefore no need for precise timing circuitry or bidirectional drivers.
- **Improved resilience:** Small errors in impulse generation, or deviations in link parameters have far less impact on data transmission than in PHM. Striking and damping pulses in SQuirM do not need to be *precise*, they only need to be 'good enough'.

6.3 Transmitter and Receiver Circuit

The transmitter and receiver were designed in AMS 0.35 µm CMOS, capable of operating with supplies between 1.2 V and 3.6 V. Figure 6.8 shows the layout and dimensions of the final circuits. The following sections describe the individual circuits in more detail.

6.3.1 Transmitter Details

Figure 6.9 shows the transmitter circuit in detail. The circuit is fundamentally quite simple, with three key parts, the impulse generator, the trimmable output switch (M_{Tx}), and the damping switch (M_{Txd}). The sizing of the output stage is not critical, but was approached using the following design principles. In the case of the damping switch, its size is a tradeoff between wanting a small value for r_{on} (to sufficiently damp the transmission coil), and having a small enough switch so as not to cause charge-injection problems (see §6.3.3), or overload the data input with gate-capacitance. We can find a target value of r_{on} by using the principle of loaded Q from Chapter 2. Assume for example we have a 120 nH transmission coil with a Q-factor of 100 at 300 MHz, $\therefore R_S = 2.26\Omega$; the loaded Q is:

$$Q_L = \frac{R_D\,(Q + 1/Q)}{\omega L\,(Q + 1/Q) + R_D}, \tag{6.1}$$

where R_D is the on-resistance of the damping switch. By rewriting Q_L as Q/α, we can rearrange Equation 6.1 into an expression for R_D, that will make the Q smaller by a factor of α:

$$R_D = \frac{\omega L}{\frac{\alpha}{Q} - \frac{1}{Q+\frac{1}{Q}}}. \tag{6.2}$$

If we wish to de-Q our example coil 10 times, Equation 6.2 returns the minimum value of R_D to be 2.5 kΩ. The on-resistance of M_{Txd} was simulated to be 1.6 kΩ; more than sufficient to de-Q the example coil.

The output switch M_{Tx} has a similar tradeoff problem. The switch should be large enough to draw a large current burst through the transmission coil, but must have a low enough gate capacitance for the impulse generator to be able to drive it. If M_{Tx} is

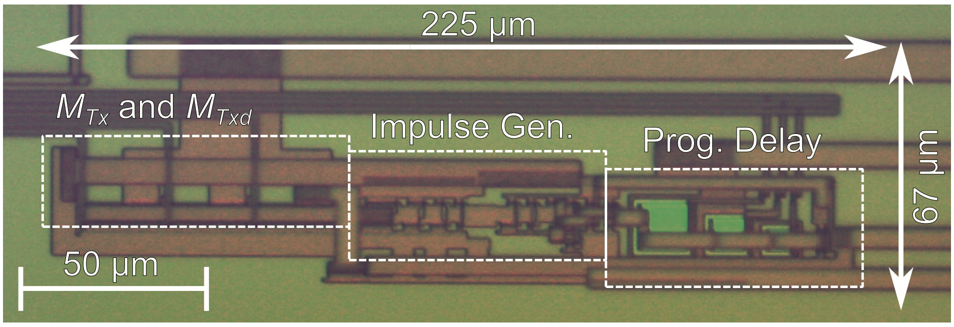

(A) Transmitter

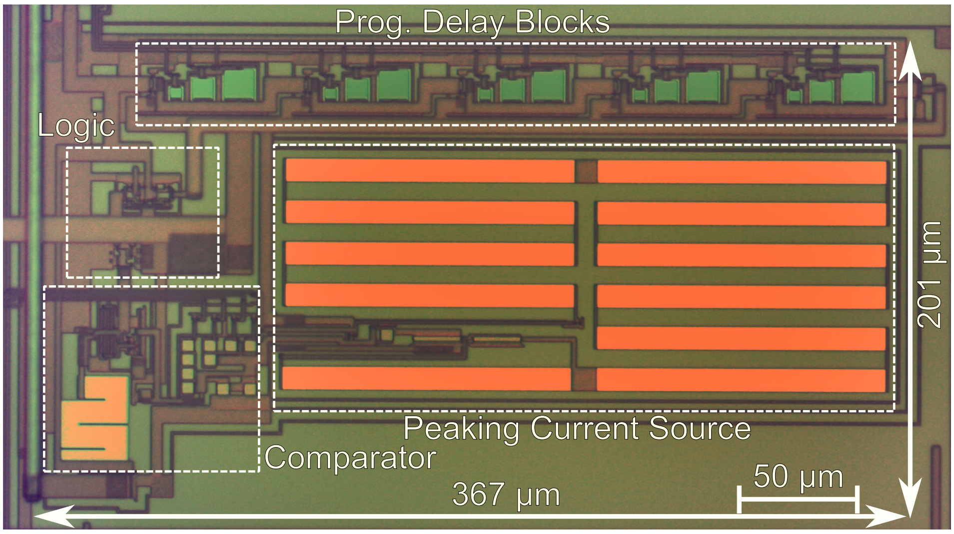

(B) Receiver

FIGURE 6.8: Microphotographs of the fabricated transmitter and receiver circuits, highlighting the active areas.

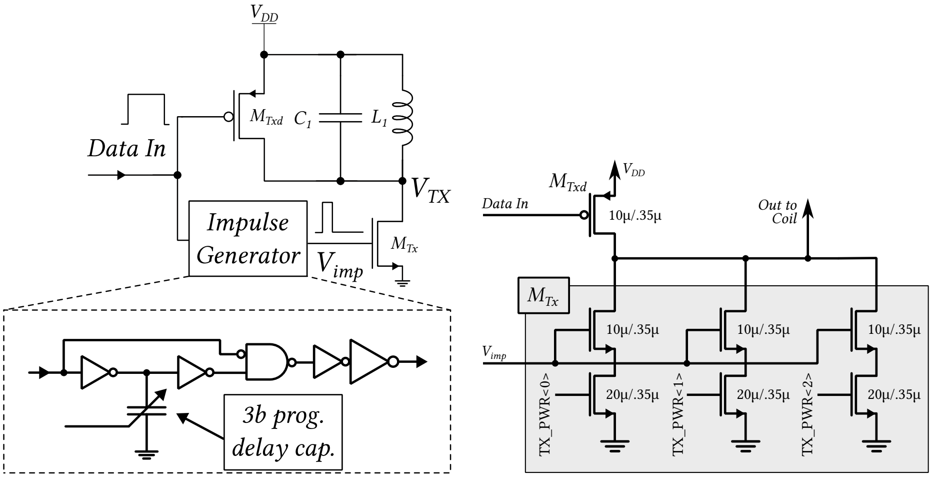

FIGURE 6.9: *Left:* Detailed transmitter circuit block diagram. *Right:* Expanded view of the output stage. M_{Tx} has 3 taps to alter the output power. The 3b trimcap is binary weighted, with 40,80, and 160 fF MIM capacitors.

made large enough, the capacitance at its drain will impact the resonant frequency of the transmission coil; C_{DD} will add to C_1, so this should also be considered. M_{Tx} was made fairly small in this implementation in the interests of saving power. With all three power taps switched on, the peak drain current into M_{Tx} is approx. 2 mA.

The impulse generator is based on logic blocks; by splitting the incoming signal into two paths, with and without a delay, and taking the difference, a short pulse is generated. The pulse-width is mainly dependent on the length of the delay set by the delay capacitor, but also has some dependence on the rise-time of the incoming data. To avoid errors in pulse timing, the data rise time should be as consistent as possible. Figure 6.10 shows postlayout simulated pulse widths for the impulse generator against changing capacitor codes with a Monte Carlo spread included (20 runs per code). The wide spread of the boxplots shows the weakness of the logic-gate based method; small variations in the trip-threshold of the gates can lead to comparatively large variations in delay. However, it is a small low-power design, which is more valuable than extremely refined pulse-width control in the context of IMDs.

To generate maximum output amplitude, the drive pulse width should ideally be exactly one-half cycle of the Tx coil natural frequency [49]:

$$\tau_{pw(opt)} = \pi\sqrt{L_1 C_1} = \frac{1}{2f_0}\,. \tag{6.3}$$

A drive impulse formed in accordance with Equation 6.3 will draw current through the inductor up until the maximum current is reached. This is illustrated in Figure 6.11; the falling edge of I_D aligns perfectly with the peak negative current in I_L. A shorter pulse will give a lower amplitude, but also save power, since less current is being injected. A pulse longer than $\tau_{pw(opt)}$ will have a reduced amplitude, since some of the freewheeling current in the tank will be drawn away by M_{Tx}. If the pulse generator cannot generate a short enough pulse, a compromise solution is to make the pulse

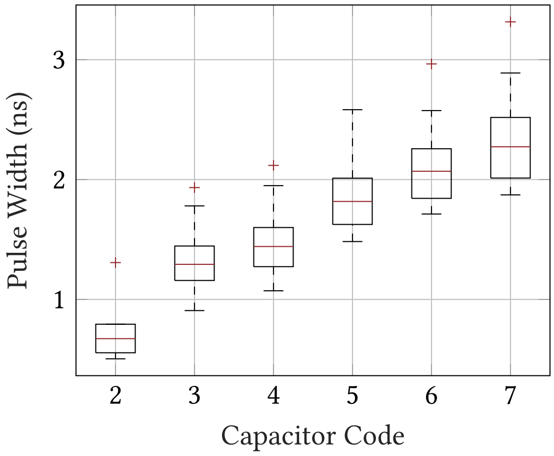

FIGURE 6.10: Postlayout Monte Carlo spread of pulse widths from the impulse generator in Figure 6.9

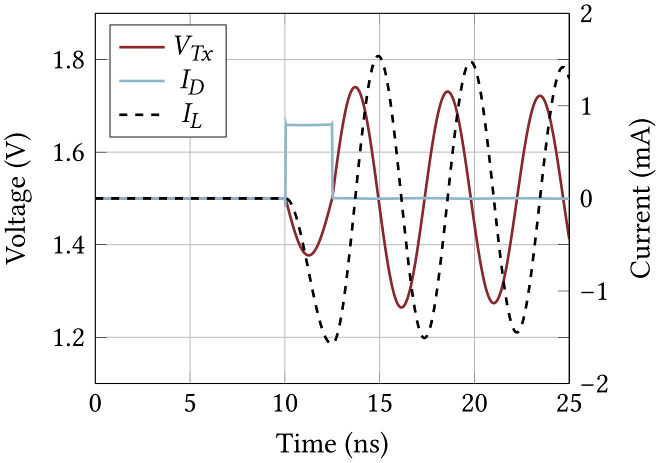

FIGURE 6.11: A well-timed current pulse into a resonant circuit, f_0 = 205.5 MHz.

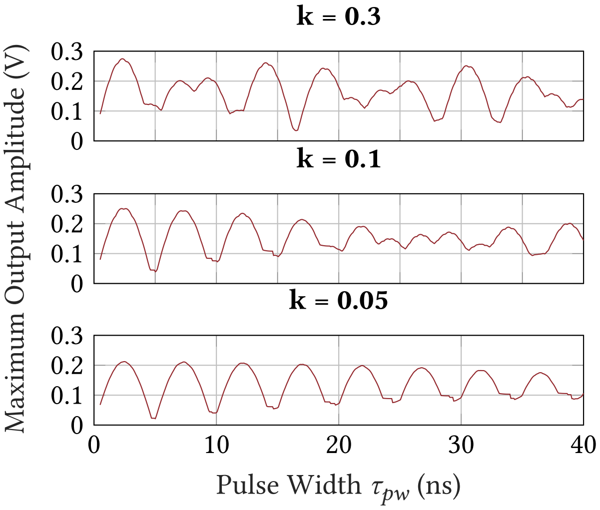

FIGURE 6.12: Simulated data of maximum amplitude seen at the receiver, for varying pulse widths and coupling factors, for two coupled tanks with f_0 = 205.5 MHz, $\tau_{pw(opt)} \approx$ 2.433ns.

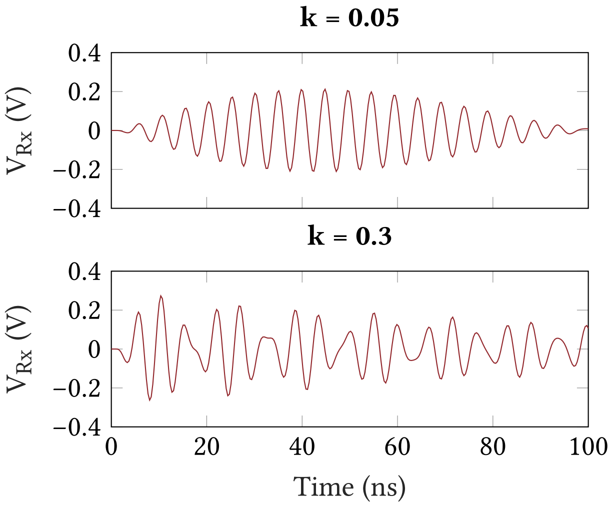

FIGURE 6.13: Output voltage responses of the example link at low and high coupling factors. The response shows a mix of the two peak frequencies at high coupling.

width close to any other odd multiple of half-cycles. By doing this, the falling edge of I_D will still align with a maximum negative coil current, and achieve a higher amplitude than otherwise. This relationship does not hold perfectly when taking into account the coupled receiver however, particularly at higher coupling factors. The effect of higher coupling factors is illustrated in Figure 6.12; at lower coupling factors, the odd-multiple half-cycle rule holds, but breaks down as the coupling factor increases. This effect must be accounted for when tuning the drive pulse-width with tightly coupled coils.

The reason this behaviour occurs at high coupling factors is because of the double-peaked impedance curve that the link has due to frequency splitting. After a link with a split response is struck with an impulse, instead of both sides ringing at f_0, they will ring at a combination of the two peak frequencies. Double peak ringing is illustrated in Figure 6.13.

6.3.2 Receiver Details

Details of the receiver circuits are given in Figure 6.14; the key components are the input comparator, and the programmable delay-reset block. The comparator design is a ground-referenced common-gate based comparator, based on a design by Guo et al. [189]. While any AM-demodulator would be able to recover the received datastream, this comparator-only approach was chosen because it is low power and effective. The comparator works by balancing two common-gate amplifiers that push-pull the output stage. The trip-threshold of the comparator can be adjusted by modifying the sizes of the PMOS devices driven by V_{bias}. By unbalancing the current flowing in each branch, a the ΔV required to trip the comparator will differ, depending on the difference in the quiescent branch currents. The offset can also be fine-tuned by adding a resistor in series with one of the inputs; here a 500 Ω was used to give a small

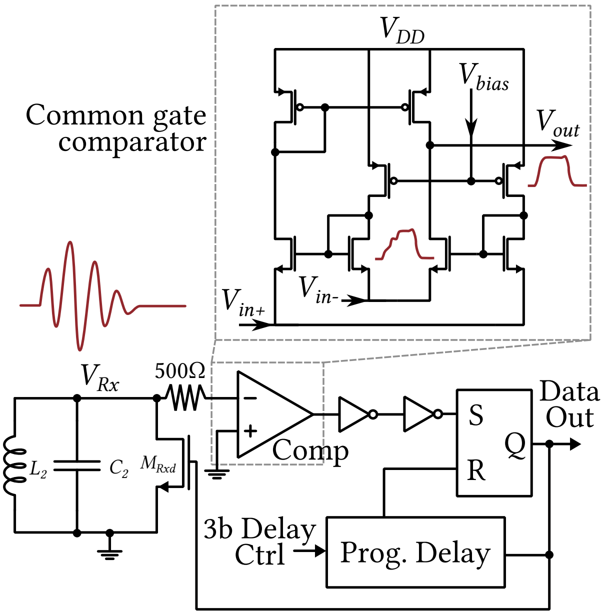

FIGURE 6.14: Details of the receiver circuitry.

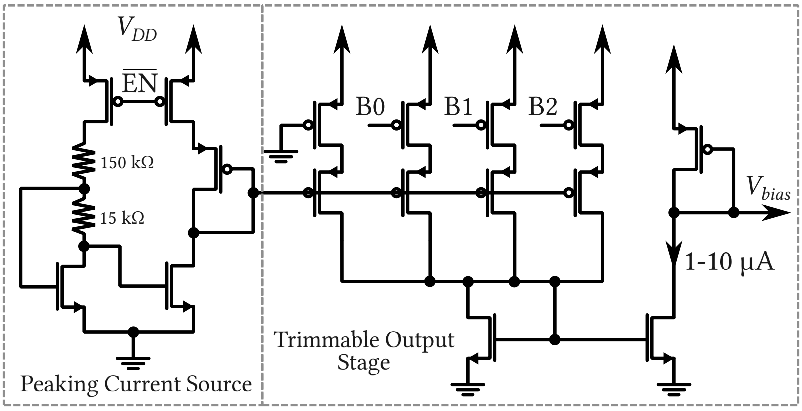

FIGURE 6.15: Trimmable peaking current source, with 3 equally weighted output taps.

offset, as well as some isolation between the receiving tank and the comparator input. V_{bias} was generated with a peaking current source with a trimmable output stage; a schematic is shown in Figure 6.15. The output taps allow for some control over the bias current, which can help compensate for process variation in the comparator devices. The taps controlled by B0-2 are the same size as the enable switches controlled by $\overline{\text{EN}}$, to retain matching in the mirror devices. The design could be improved by using an alternative bias generation scheme; the current circuit requires a lot of area to be used for the peaking source resistors.

Figure 6.16 shows simulated waveforms for the receiver chain blocks. The 'push' PMOS in the push-pull output stage of the comparator generates more current than the 'pull' NMOS; as a result, the comparator output voltage gets pushed further up with each cycle at the input, rather than returning fully to ground each cycle. In this way the comparators perform both amplification and a crude form of envelope detection in a single circuit. The inverters at the output of the comparator square up

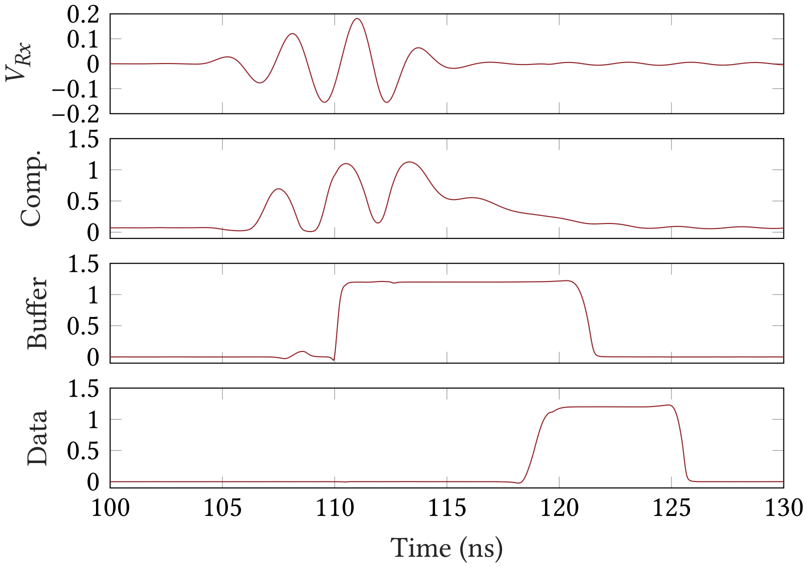

FIGURE 6.16: Simulated voltages for the receiver chain, with a short delay set in the delay block. All vertical axis units are Volts.

the glitchy output, to be fed to the output data latch.

The output data latch is set whenever the comparator buffer swings high, offering further protection from glitches in the comparator output. The programmable delay block determines how long output data bits are held on the latch before they are cleared. Since the received pulses are directly used to damp the receiver coil, setting this width also controls the time that the coil is damped for. Longer delays will damp the receiver more, but will also reduce the maximum achievable data rate.

6.3.3 Charge Injection When Damping

A final important consideration is the role that charge injection can play in the damping switches. When a damping switch is turned on, it draws current away from the tank it is damping and through itself. However, once these switches stop conducting, their conductive channels collapse, injecting charge carriers into the nodes at the source and drain [190, pg. 421]. This can be a problem particularly at the receiver side of a SQuirM system if the damping switch is large. The current injected from the collapsing channel of M_{Rxd} will provide an impulse to the tank and make it ring, which can appear like an incoming bit if there is too much current injected.

In the design presented here, this was not a significant problem as the damping switches were chosen to be fairly small; the current they inject on switch-off is not enough to generate a large ringing signal. Figure 6.17 shows the difference between two types of receiver damping scheme. Figure 6.17a shows the regular damping method; when the switch turns off, the source current will flow to ground, but the drain current must flow through the tank. This will inevitably cause ringing, but the amplitude is determined by switch size, so for a small switch the performance may still be acceptable. By using a pair of differential matched damping switches however

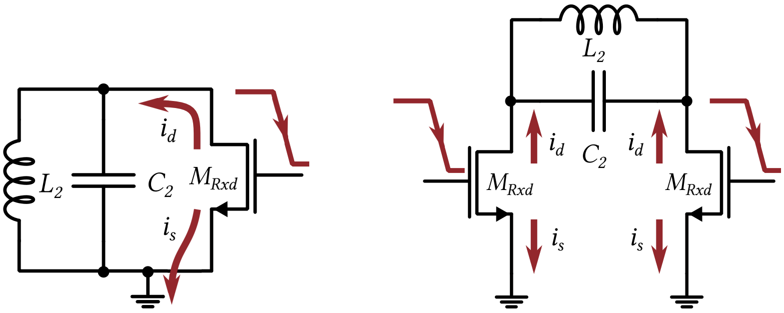

(A)

(B)

FIGURE 6.17: (A): Regular receiver damping scheme, i_d injects a pulse into the coil. (B): Differential damping, equivalent i_d pulses cancel each other.

(Figure 6.17b), the drain currents they inject into the tank are equal and opposite, so no net current should flow in the tank. A downside of this technique however is that the coil needs to be connected to two floating pads, increasing the stray capacitance to ground that it sees, and reducing f_0.

6.3.4 Regulatory Considerations

In the case of power transfer, transmissions can be kept in a regulated band (e.g. 6.78 MHz or 13.56 MHz), however, the intermittent bursts generated by SQuirM inevitably produce a broad spectrum in the frequency domain. This can pose a problem from a regulatory perspective, as a SQuirM system would be considered as an intentional UWB radiator under FCC Title 47 regulations [191]. Intentional UWB radiators must limit their transmit power to stay within these regulations; this would not be a significant problem for SQuirM, since it requires very little transmit power to operate. However, should the SRF of the link coils be <960 MHz (as they are in this implementation), the emissions would be out of the FCC regulated UWB band. This doesn't guarantee that such a system would be illegal to operate, but there is no explicit guidance on maximum allowable transmit power at these lower frequencies. If used in medical devices some restrictions can be waived, but again since UWB systems operating in this frequency range aren't described in the regulations, the precise details are unclear. If SQuirM were to be used in a product, these potential regulatory pitfalls would be an important consideration.

6.4 Chip Measurements

6.4.1 Experimental Setup

Figure 6.18 shows the circuit arrangement for performing measurements. One chip was used as a dedicated transmitter, and one as a dedicated receiver, each with it's own isolated board. Since both circuits have trimmable elements, these were controlled by an on-chip SPI register to reduce the overall pin count on the chip package. This

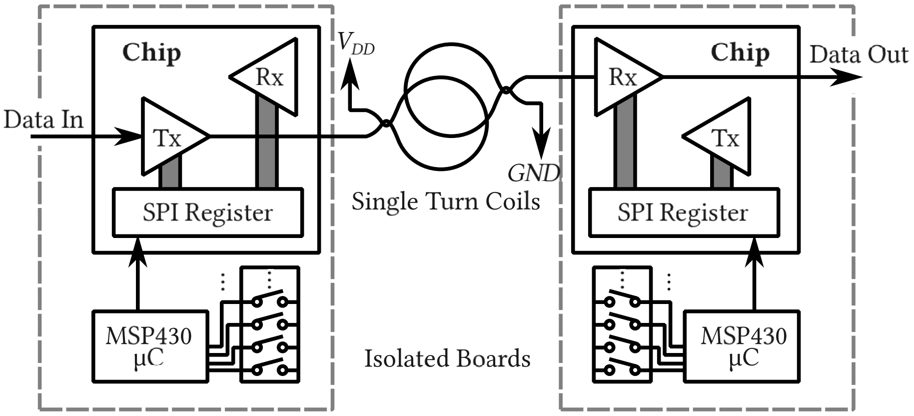

FIGURE 6.18: Experimental setup.

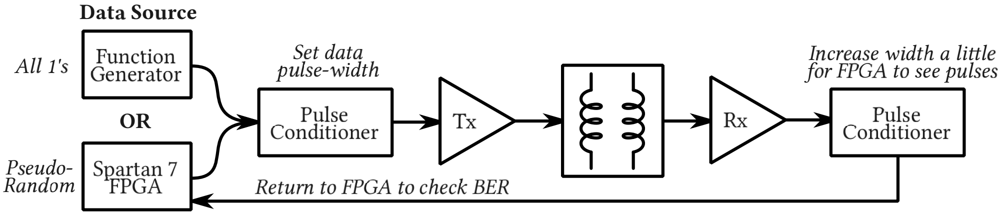

FIGURE 6.19: Equipment setup for producing and recovering datastreams.

SPI register was controlled by a MSP430 microcontroller, which periodically reads the state of a bank of toggle switches. This allowed the trimmable bits to be controlled easily during the experiments. Each board was also equipped with fully adjustable power supplies, with inline current monitoring. This allowed the chips to be tested with a wide range of supply voltages, and their power consumption to be monitored accurately. The single turn coils were 28 mm in diameter, wound using standard 0.7 mm diameter magnet wire. They were directly soldered to pads as close as possible to the chip, to minimize parasitics. The length of the PCB traces for the Tx and Rx coils were closely matched, so that any parasitic losses should be similar.

The coils were both measured to have inductances of 70 nH ±1 nH, with negligible losses at frequencies below 30 MHz, measured using a Wayne Kerr 6500B impedance analyzer. Due to the 30 MHz limit of the instrument, it was difficult to measure the quality factor and self-resonant frequency f_0 of these coils directly. By inspecting the resonant bursts from running the system however, the resonant frequency of these coils in parallel with all other system parasitics was found to be 181.8 MHz. This would suggest a total in-system parallel capacitance of 10.95 pF; it is not feasible to measure this precisely however. Substituting this value for f_0 back into Equation 6.3 yields a value of $\tau_{pw(opt)} = 2.75$ ns. This is well within the capabilities of the impulse generator (see Figure 6.10).

Figure 6.19 shows the arrangement that was used for generating input data streams, and recovering them in the case of bit-error rate (BER) tests. A function generator (Agilent 33250A) was used to generate strings of repeated 1's to determine the maximum data rate the link could handle. To test the BER of the system, a Spartan 7 FPGA

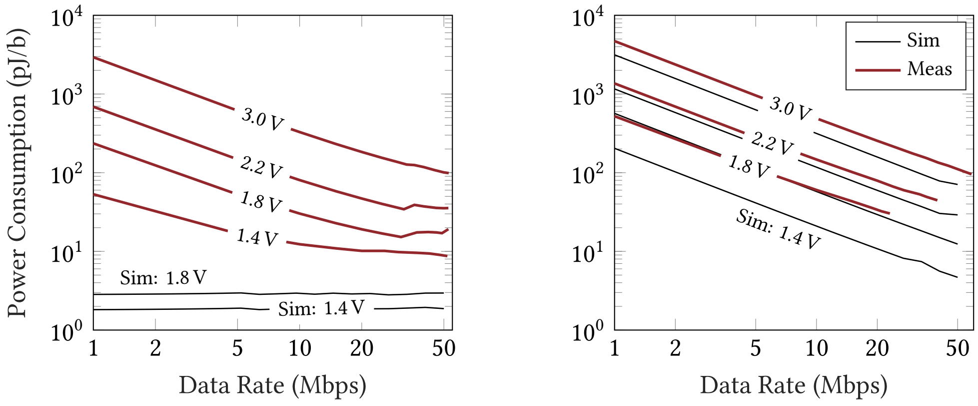

(A) Tx

(B) Rx

FIGURE 6.20: Measured and simulated power consumption per bit for (A): transmitter and (B): receiver circuits. The receiver consumes far more quiescent power than the transmitter.

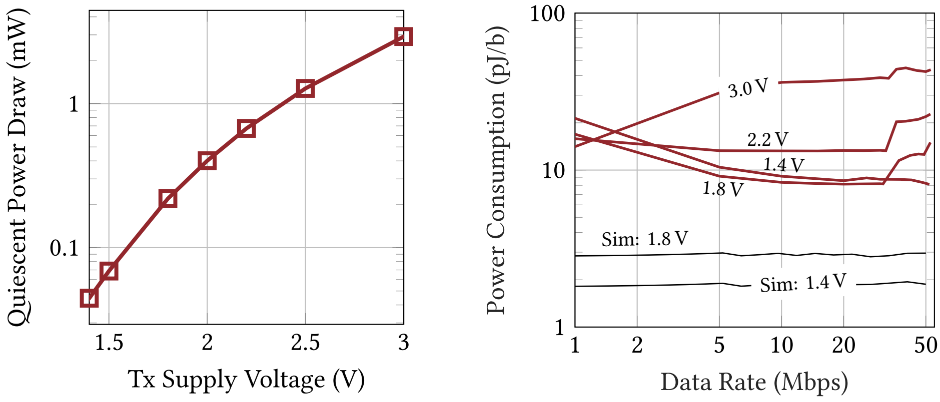

(A)

(B)

FIGURE 6.21: Quiescent power draw in the overall circuit (A), and inferred measured power without quiescent draw (B).

was used to generate (8.6 Gb) pseudorandom sequences, which can be fed back to the FPGA for comparison after they have been transmitted through the system. Any non-matching bits can be counted, and a BER calculated.

6.4.2 Power Consumption

The first priority was to test the power consumption of both circuits, using a range of supply voltages. Figure 6.20 shows the results of these tests; the data rate was a stream of continuous 1's, to use a maximal amount of power and determine the theoretical worst case.

Figure 6.20a shows that at low supply voltages and high data rates, the transmitter mostly consumes dynamic power, with the best recorded Tx power consumption being 8.72 pJ/b, with a data rate of 52 Mbps at 1.4 V supply voltage. At higher supply voltages, V_{Tx} is larger, but at the cost of more quiescent power being dissipated. This extra quiescent power is mostly drawn by the unpowered Rx circuit however, since both circuits are linked to the same supply pad, and the Rx circuit has quiescent draw even when disabled.

By measuring the current draw when the Rx circuit in the Tx side is powered down, a quiescent power baseline with respect to supply voltage was determined. This is shown in Figure 6.21a, where a steady increase in power consumption can be seen against increasing supply voltage. By subtracting this baseline from the measured results in Figure 6.20a, we get an approximation of the true power consumption of the Tx (see Figure 6.21b). The results in Figure 6.21 show much more clearly that the Tx power consumption is almost purely dynamic. However, the measured power consumption is still significantly higher than the simulated case, with the best recorded value being 8.11 pJ/b at 52 Mbps at 1.4 V. This extra power draw is likely due to parasitic capacitances that were not fully accounted for in the simulation. The anomalous changes in gradient of the measured results at high and low data rates are also difficult to explain. These anomalies could, at least partially, be the result of the process of removing the quiescent baseline, since it assumes that incoming data to the Tx does not affect the power draw of the disabled Rx, which may or may not be the case. Another factor could be that there are unaccounted sources of power leakage in the system, such as parasitic capacitance in the PCB, chip-package or connectors.

Figure 6.20b shows power consumption curves for the Rx circuit; for all supply voltages the consumption is almost completely quiescent. Reducing the supply voltage here gives significant power savings, but at the cost of maximum data rate. At a supply voltage of 3.0 V, the receiver could recover a maximum data rate of 58.6 Mbps, but could only reach a maximum of 23.1 Mbps with a 1.8 V supply.

It should be noted that while both circuits were designed to ideally operate from 1.2 V supplies, this voltage was found experimentally to be too low for them to operate well. While the transmitter generates successful V_{Tx} pulses, the transmission range is seriously limited. From the receiver point of view, it was found to be essentially inoperable at supply voltages below 1.8 V. This is likely due to process variation; significant differences in the receiver transistors could easily manifest as a large input offset that would worsen at low supply voltages.

6.4.3 Bit Error Rate and Resilience

Figure 6.22 shows the measured maximum operating distance of the system for a range of Tx supply voltages. For each distance step, the supply voltage was reduced and the datastream was visually inspected, if significant jitter or dropped bits were apparent[3], then the supply was backed off by a few mV and noted. The plot shows a sudden drop in range for Tx supplies lower than 1.8 V, this is somewhat expected, since the 0.35 µm process is designed for 3 V operation. Since the losses in the Tx are almost entirely dynamic losses, implementing the design in a smaller process node, e.g. 65 nm, could yield better performance[4] at lower supply voltages.

---

[3] These kind of errors were easily spotted by using the ∞ persist option on the oscilloscope.

[4] In terms of both bit energy and maximum achievable data rate.

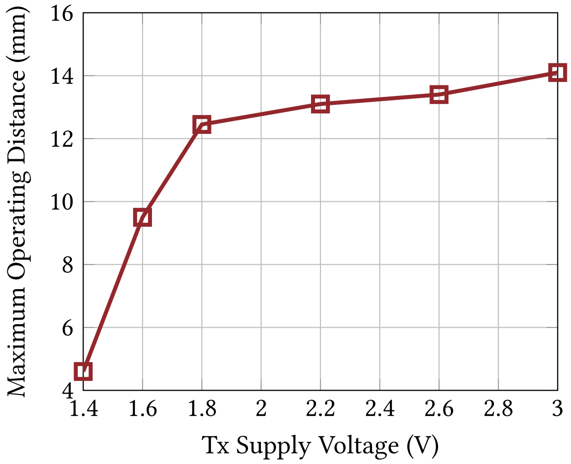

FIGURE 6.22: Maximum coil distance vs Tx supply voltage.

The Rx supply was swept in these tests, but since it has no real effect on gain, rather on the maximum data rate that can be recovered, it has no real impact on the maximum operating distance. The Rx supply voltage was therefore fixed at 3.0 V for these tests, and a 40 Mbps pseudorandom stream was used. A clean example sequence is shown in Figure 6.23, where several hundred captures are overlaid to demonstrate jitter. The input stream has approx. 0.5 ns of jitter, which becomes approx. 1 ns at the output. Keeping jitter low is crucial in an asynchronous system such as this.

The BER performance of the system was tested by using the arrangement in Figure 6.19. The FPGA was configured to generate an ≈ 8.59 Gb long pseudorandom sequence, generated by a 33 bit linear feedback shift register. This sequence was passed through the system at a range of distances and data rates, and the number of errors was counted.

Bit error rates were determined to a 95% confidence level by using Wilson's score interval [182], the interval boundaries are evaluated as follows:

$$\frac{\hat{p} + z^2/2n}{1 + z^2/n} \pm \frac{z}{1 + z^2/n}\sqrt{\frac{\hat{p}\,(1-\hat{p})}{n} + \frac{z^2}{4n^2}}\,. \tag{6.4}$$

Where $\hat{p}$ is $\frac{\text{number of errors observed}}{\text{number of bits sent}}$, n is the total number of bits sent (2^{33} in this case), and $z = 1.96$[5].

Figure 6.24 shows the recorded results of the BER testing, the upper and lower black lines are the upper and lower confidence levels, respectively, the regions between these lines are shaded. For data rates of 49.5 Mbps and below, the calculated BER is less than 4.472×10^{-10}. The exception is when the coil distance increases to 14.5 mm, where it increases slightly at some lower data rates, e.g. 14.5 mm, 37.5 Mbps, the calculated BER is between 7.151×10^{-10} and 2.293×10^{-9}. Overall the BER results here show a very slight dependence on coil distance: the maximum data rate (before rapid

---

[5] The z value defines the desired level of confidence of the result, and should be picked in accordance with the table of values provided by Wilson [182].

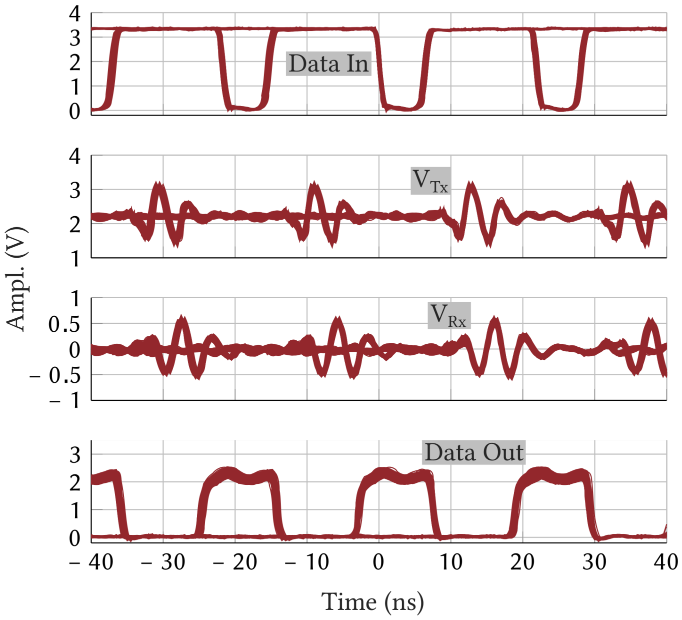

FIGURE 6.23: Measured waveforms for a 40 Mbps pseudorandom data sequence, demonstrating a low level of jitter over time.

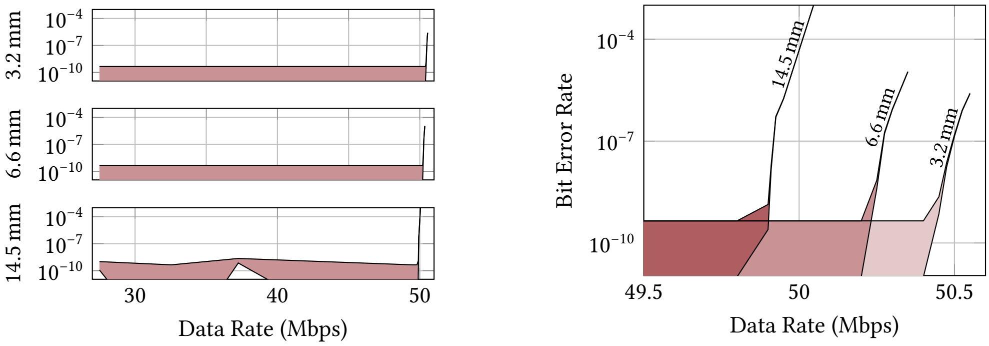

(A) BER vs Data Rate

(B) Zoomed plot

FIGURE 6.24: (A): BER results across a range of coil spacings and data rates. (B): Zoomed in view of the point at which many errors occur. The regions between the upper and lower confidence levels are shaded. In the case the lower bound is zero, the shaded area continues downward forever.

Table 6.2: Table of comparison for inductive data telemetry schemes.

Ref.	**Scheme**	**Range**	**Data Rate (Mbps)**	**Tx Power (pJ/b)**	**BER**	**FoM**
[49]	PHM	10 mm	10.2	345	6.3×10^{-8}	4.69×10^{21}
[178]	PHM	10 mm	20	180	8.7×10^{-8}	1.27×10^{22}
[179]	OQPSK	5 mm	4.16	?	2×10^{-6}	?
[192]	TTC†	70 mm	50	0.475	$< 1 \times 10^{-3}$	7.36×10^{21}
[193]	LSK	20 mm	2.8	35.7	$< 10^{-6}$	1.56×10^{21}
[50]	PDM	10 mm	13.56	960	4.3×10^{-7}	3.28×10^{20}
This Work	SQuirM	14.5 mm	50	8.11	$< 4.5 \times 10^{-10}$	1.98×10^{26}

†Transmission Time Control.

increase in BER) for 3.2 mm is ≈50.4 Mbps, whereas for 14.5 mm it is ≈49.7 Mbps, a difference of only 1.4%.

6.5 Discussion and Conclusions

Table 6.2 shows how SQuirM compares to other inductive link based data transmission schemes. SQuirM achieves far better performance than other methods mainly used in the biomedical circuits field (LSK, OQPSK, PHM) in terms of data rate, power consumption, and BER, while working at a similar range. While the TTC scheme presented by Lee et al. [192] is superior in terms of power consumption and range, its BER performance is sub-par, and it appears to require a separate channel for a synchronized clock to be shared between the Tx and Rx. The FoM defined in Table 6.2 is based on the range in meters, the data rate in bits per second, the BER, and the transmitter power consumption in joules per bit, in accordance with the following formula:

$$\text{FoM} = \frac{\text{Data Rate} \times \text{Range}}{\text{BER} \times \text{Tx Power}}. \tag{6.5}$$

SQuirM was found to achieve a FoM that is better than the next best system [178] by 4 orders of magnitude.

Overall, the work in developing a SQuirM transceiver for short-range low-power high data-rate biomedical telemetry was successful. The power consumption, data rate, and BER results are of particular note, as they are represent a significant improvement over the results of previous impulse-based PHM systems (e.g. [178]). In addition, given the simplicity of the scheme, SQuirM lends itself to easy adoption without the need for complex tuning and trimming. Given its capacity for high data rate transmission, which can be further increased by using smaller coils with a higher SRF, SQuirM also lends itself to consumer applications where large amounts of data need to be transferred over a short distance.

Future work could include re-implementation in smaller CMOS nodes, to improve performance, as well as re-designing the receiver to have a more robust architecture that is less affected by process variations. This could also include redesign of the impulse generator to be less process dependent, making it easier to drive different coils with different SRF values.

6.6 Addendum: Impulse-Driven Clock Generation

During the design of the SQuirM system, a clock generation circuit was devised. While unrelated to inductive-link telemetry, it makes use of the same principle: maximising the amplitude of the ringing response in a resonator by striking it with a well timed impulse. The goal of this clock circuit design was to determine if the power consumption of a resonator based clock circuit could be traded off against phase-noise, for applications where power consumption is more important, and how this would compare to a regular cross-coupled LC oscillator design. Details of this clock circuit have been published in the proceedings of ISCAS 2018 [194]. As this work is adjacent to the rest of the thesis rather than directly related, it will only be discussed briefly here.

6.6.1 Theory

The theory of impulse-driven resonators is essentially the same as previously discussed in this chapter. However, for SQuirM it is sufficient to consider only a few cycles after the impulse, whereas for clock generation, we must consider many cycles after the impulse. After a resonator is struck with an impulse, it will immediately ring at its resonant frequency f_0, but should the f_0 of the resonator depend in some way on the amplitude of oscillation, as the oscillation is damped, the resonant frequency changes as well. This principle is illustrated in Figure 6.25. This effect arises prominently in the case of an LC tank controlled by MOSFETs, as their voltage dependent parasitic capacitances contribute significantly to the value of f_0. A traditional oscillator using positive feedback can be considered as ‘undamped’, since the gain of the feedback block cancels out the damping inherent to the resonator. The damped response of an impulse-driven resonator can be seen to deviate from the ideal undamped response increasingly over time.

The benefit of driving a resonator with an impulse compared to a constant gain block however is in terms of power consumption. Since an impulse driver effectively acts like a switch, losses only occur when changing between the ‘on’ and ‘off’ states. This is much more efficient than in the case of a simple Colpitts or Hartley oscillator, where the transistors are effectively working as Class-A amplifiers.

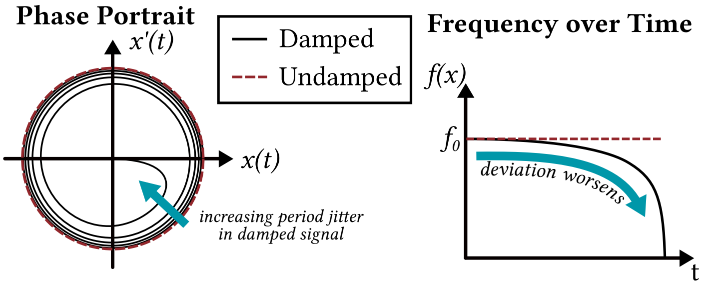

FIGURE 6.25: Damped vs continuous oscillations. $x(t)$ is the resonator current, $f(x)$ is the instantaneous frequency.

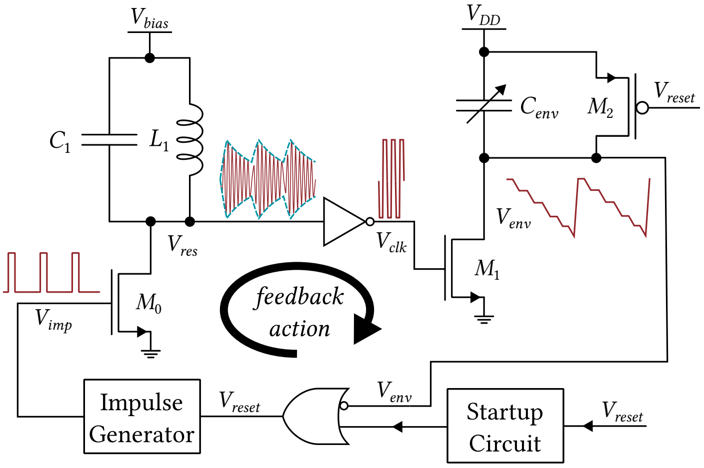

FIGURE 6.26: Simplified circuit diagram of the impulse-driven clock circuit.

6.6.2 Circuit Details

To implement an oscillator using an impulse-driven resonator, the design as shown in Figure 6.26 was devised, and implemented in 65 nm CMOS.

The action of the circuit is to first strike the resonator with an impulse, which will cause a ringing oscillation. This is then fed to an inverter to generate a clock signal; the resonator is supplied from a voltage $V_{bias} = V_{inverter\text{-}th}$, so that any oscillation will easily trip the inverter. Each positive clock half-cycle will enable current to flow through M_1, adding a packet of charge to C_{env} each time. This will eventually reduce V_{env} beyond the logic level of the reset OR-gate, and the impulse generator will be triggered again. The value of C_{env} should be carefully tuned to ensure the impulse generator strikes the tank at the perfect time, to minimize further phase noise that could be caused by generating an impulse with too little or too much delay.

Figure 6.27 shows the layout of the clock circuit; the layout requires 32 μm × 30 μm, with most of the area taken by the impulse generator and trimmable envelope capacitor. External circuits would be required for setting V_{bias} and controlling the digital taps for C_{env}.

Figure 6.28 shows postlayout simulation results for the clock circuit, using a standard LCR resonator with the following specifications: $L = 80$ nH, $C = 50$ fF, $R = 10\,\Omega$. The clock frequency generated here was 2.015 GHz, at a cost of 412 μW of power,

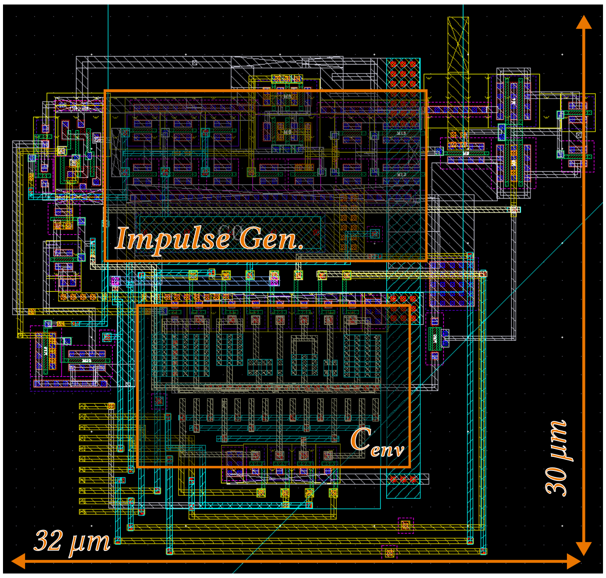

FIGURE 6.27: Screenshot of circuit layout, key blocks are highlighted.

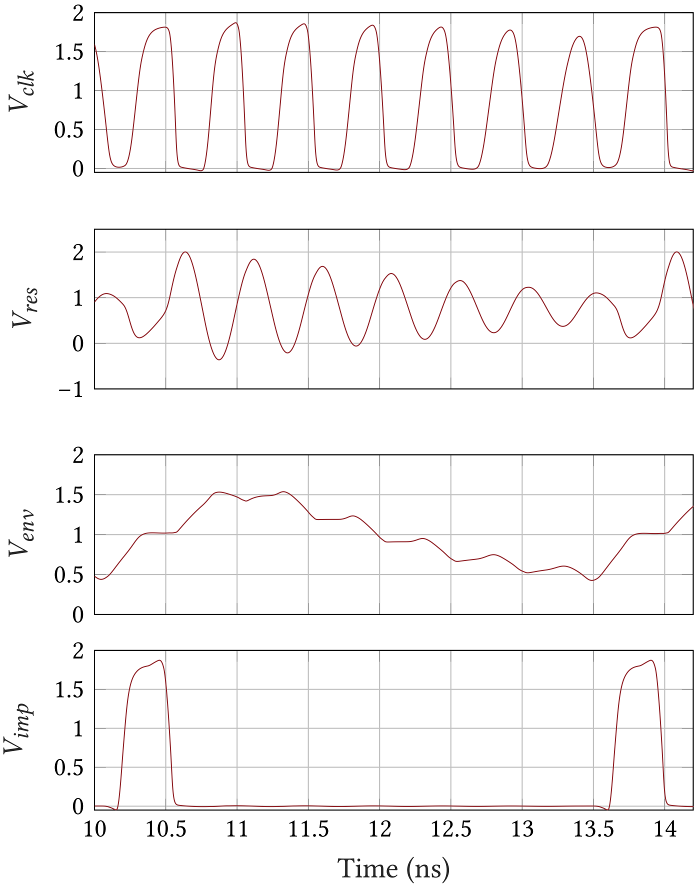

FIGURE 6.28: Simulated waveforms for the clock circuit.

yielding a FOM of 4.89 GHz/mW. The chip has been sent for fabrication by TSMC, and will need to undergo testing to confirm its performance with measurements.

Closing Discussion, Conclusions, and Future Work

7

This thesis has described a series of developments in the field of short range telemetry for IMDs, for both power and data, using short-range inductive links. Comprising both methodological work and circuit designs, it has addressed several problems faced by inductive telemetry systems, such as poor resilience to displacement, data rate limitations, and limited PTE and PDL.

The first sections focused primarily on the underlying theory of coupled inductors for power transfer, and the accompanying calculations that are required. The problem of modelling coils in a simple and accurate manner is one that can still be considered under investigation; indeed there is still contention as to the underlying principle of coil self-resonance [75], [103], [195]. The aim of the theoretical sections in Chapter 2 therefore, was to draw upon the existing knowledge in the literature and collect it, providing a practical analytic procedure for the design and analysis of coils for ICPT systems. To complement this theoretical description the CuCCo [2] software was developed, to further simplify the design process. Since the software is based on the same simple expressions and definitions, results can be produced far more quickly than by using FEM modelling methods; this allows for design spaces to be quickly mapped with iterative calculations.

The next two chapters provided methods and systems that tackle the problem of frequency splitting in tightly coupled inductive link systems. Increasingly overcoupled inductive link coils, tuned at a centre frequency ω_0, will suffer from a considerable drop in power delivery if driven at ω_0. The optimum frequency tracking system was devised in order to automatically detect the frequency at which the link should be driven to maximise power delivery, and adjust a power amplifier to this frequency automatically. This system was fabricated and tested, with measurements yielding significant improvements in system efficiency and power delivery for an overcoupled link, compared to driving it at ω_0. The system produced here was complex, but performed well. After considering frequency splitting from the point of view of power transfer, it was analysed in further detail and applied to the problem of remote sensing. By taking a PP link that has all components characterized, apart from one tank capacitor, it was shown that the value of the tank capacitor can be determined from the link's self resonance frequency. This would translate to one of the optimum frequencies that would be selected by the OFT system. It was demonstrated that by driving the such a link with a self-oscillating circuit, a remote sensing capacitor could be accurately interrogated, by counting the oscillation frequency. The sensitivity was found to be positively correlated to the coupling factor, but also susceptible to errors if the coupling factor changes during the measurement.

The final chapters provided implementations of data transfer over inductive links; a dual-purpose link for power and data, employing stagger tuning, and a dedicated data transfer link based on a novel impulse-based transmission system, SQuirM. By employing stagger tuning, it was demonstrated that a link can be designed with a good compromise of tolerance against coupling and load variations, improved bandwidth for data transfer, and sufficient power transfer capability to power an attached implant. The data subsystem was tested with pseudorandom bit sequences at 847 kbps and 1.35 Mbps, and found to be better than 1×10^{-7} over most operating distances. Since the method of stagger tuning is based on trial and error however, it is less repeatable than other designs. Further analysis towards a method for determining the best stagger tuning for a given design would be a useful development. On the other hand, the SQuirM methodology presented in Chapter 6 demonstrates the strengths of using a dedicated data link to achieve high speed data transmission, with a low power consumption. It was shown that by modulating the Q-factor of both sides of the link, bits could be transferred rapidly and efficiently; high-Q coils allow easily detectable bits to be transferred, with little input energy, and low-Q coils allow remaining bit energy to be rapidly quenched to make way for the next bit. This unique approach allowed for data to be transferred at up to 52 Mbps, with a power consumption of only 8.11 pJ/b. The recorded BER was also found to be excellent, with a measured figure of $< 4.472 \times 10^{-10}$ across the working range (95% confidence level).

In summary, the work presented in this thesis has provided the following:

- Practical treatment of the theory behind inductive power links, with an accompanying software package, with the aim being to simplify the topic of ICPT for the uninitiated.
- Investigations into the design of an adaptive power transfer system, to compensate for coupling and load variations, as well a compromise link employing stagger tuning for resilient power and data transfer.
- Development of a methodology, and accompanying test system, for measuring a remote sensing capacitor through an inductive link, without the need for a digitizing front-end circuit.
- Development of a methodology, and accompanying test system, for high-speed low-power data transfer over near field inductive links, that pushes the state of the art in terms of data rate, BER, and power consumption.

7.1 Future Work and Outlook

The work developed so far has several potential avenues of further investigation, these are detailed in this final section.

7.1.1 Further Coil Modelling

While the analyses in Chapter 2 and implementations in CuCCo [2] were found to be effective when predicting the parameters for single-layer solenoids and PCB coils, the calculations involved in accurately determining parameters such as the self-resonant frequency, and parameters for arbitrary coil geometries are still lacking, e.g. square solenoids, multi-layer solenoids, and figure-8 coils. In particular the following areas are in need of improvement:

- Proximity effect losses in coil types other than single layer wirewound solenoids.
- Mutual inductance calculation for arbitrary alignments.
- Self-resonant frequency prediction.

For example, while calculating the inductance of an arbitrary solenoid is quite feasible[1], determining proximity effect losses becomes significantly more complex[2], especially as more layers are added. The proximity effect analysis for PCB coils is also lacking; the current analysis is based on approximations informed by measurements, that give reasonable estimates of R_{prox}, but are far less accurate than for wirewound coils. Calculation of arbitrary coil mutual inductances is another aspect that is feasible, by solving the appropriate integral for all coupled filaments and summing the total result [72]. However this comes at a far greater computational cost than for the coaxially aligned case. Further investigation into whether mutual inductance calculations for arbitrary displacements can be simplified could greatly improve these computation times. Finally, a better understanding of the principles of self-resonance in coils would also be of great use. As it stands, the literature has been labouring under the misconception that self-resonance in coils is due to an ‘inter-winding capacitance’, that adds up across the windings of a coil’s length, forming a parallel resonant tank with its inductance. However the formulae for calculating this inter-winding capacitance tend to give very poor results; SRF therefore is usually something that is measured after coils have been fabricated, or must be estimated with FEM. While Payne [103] gives a useful approximation based on theory and some regression of empirical measurements, the full picture is still unclear.

A good direction for this work to be developed in therefore, would be to close these gaps in modelling, aiming towards a complete analytic model for coupled coil

---

[1] As long as the structure can be deconstructed into a series of filaments, with a known arrangement, that can then be substituted into Equation 2.1, and summed up, correcting for mutual-self-inductance between the turns.

[2] The procedure provided by Kim et al. [86] no longer holds, as the assumptions for the single layer case that allow the external H-field to be assumed to be monodirectional is no longer valid.

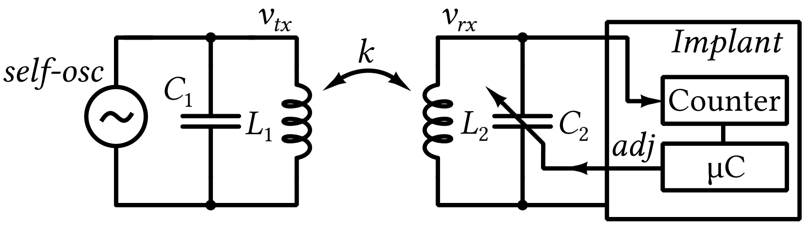

FIGURE 7.1: Potential configuration of a self-oscillating driver, with an adjustable receiver capacitor.

systems that is both practical and accurate. This would greatly improve the capacity of CuCCo to assist in rapid design of effective inductive power links.

7.1.2 Self-oscillating drivers for power transfer

In Chapter 3, the OFT tracking system was presented, that compensated for changes in coupling coefficient by adjusting the drive frequency to maintain itself at an optimum level. However, the system was complex, with many interacting parts and therefore many potential points of failure. Later in Chapter 4, a self-oscillating circuit was described, that was capable of driving an inductive link and tracking the optimum frequency automatically through positive feedback. By employing a cross-coupled oscillator as in the case of Chapter 4 to power transfer, a much simpler OFT system could be achieved.

A further development in this vein however could combine the theory from both of these chapters, and develop a system that can automatically compensate for coupling variations, but also adjust the link to maintain an fixed frequency; this could be useful if wishing to drive the link at a fixed 13.56 MHz or 6.78 MHz frequency. A potential implementation is shown in Figure 7.1. By counting the current drive frequency at the receiver, and employing the relations in Chapter 4, C_2 can be adjusted automatically at the receiver to force the self-oscillation frequency back to the desired value.

The benefit of this kind of scheme is that the output power can be maximized, the circuit implementation is fairly simple, and no back-telemetry is required. In addition, the frequency should stay fixed at a set value; useful if trying to stay within a regulated transmission band.

7.1.3 Improvements to SQuirM and Other Applications

Chapter 6 presented the SQuirM system for inductive data transfer. The system achieved transfer rates in excess of 50 Mbps, with excellent BER figures, and a low power consumption. However, at present the system is limited by being unidirectional, and purely a physical layer device with no software protocol. The system could be greatly improved by multiplexing of the transmit and receive coils, to create a half-duplex bidirectional data link. Full duplex transmission would also be possible in theory, however this would require two fully isolated inductive links. Practically this kind of implementation would be very prone to crosstalk, unless using figure-8 or orthogonal coils, or some other form of shielding between channels. The system could also be refined and implemented in a smaller CMOS node, for example 65 nm or 40 nm. This would allow much sharper pulses to be generated, to drive higher frequency resonant links and achieve higher data rates. These high-SRF coils would also have the benefit of a smaller coil size.

Another potential application for SQuirM could be in 3D chip interconnects. Where through-silicon-vias (TSVs) can be challenging to fabricate and prone to failure [196], using a surface level array of coils to communicate from chip to chip with SQuirM could be used as an alternative where TSVs are not feasible to implement. SQuirM could also find application in consumer electronics, for things like SD cards, remote control fobs, and other short range devices. The benefit of employing something like SQuirM in an SD card would be the potential to make the device fully waterproof very easily. A similar approach aimed at waterproof interfaces for storage devices is proposed by Kosuge et al. [197].

Useful Formulae for Link Design

A

A.1 Cumulative H-field Calculation

A summary of the method for determining the cumulative H-field experienced by a coil as a function of its geometry, given in [86] is presented below. First, each individual conductor (turn) is considered as being surrounded by immediately neighboring conductors, of which each will be put into either the pair group or the asymmetric group. The pair group consists of the conductors where a conductor on the left/right of the target conductor has a corresponding conductor on the right/left. The asymmetric group consists of the other conductors with no such corresponding conductor (see [86, Fig. 3]). The field on a conductor m from left and right pair conductors i and j is defined as:

$$H_{m,pair}(i,j) = -\frac{I_0}{2\pi}\sqrt{\frac{p_{im}^2 + r_0^2}{\left(p_{im}^2 - r_0^2\right)^2} + \frac{p_{mj}^2 + r_0^2}{\left(p_{mj}^2 - r_0^2\right)^2} - \frac{2\left(p_{im}p_{mj} - r_0^2\right)}{\left(p_{im}^2 - r_0^2\right)\left(p_{mj}^2 - r_0^2\right)}}\,, \tag{A.1}$$

where p_{im} is the pitch between i and m, and p_{mj} is the pitch between j and m. $H_{m,pair}$ must be calculated according to the following rules:

$$H_{m,pair} = \begin{cases} 0, & \text{for } m = 1 \text{ and } n \\ \sum_{i=1}^{m-1} H_{m,pair}(i,j), & \text{for } 1 < m \leqslant n/2 \\ \sum_{i=2m-n}^{m-1} H_{m,pair}(i,j), & \text{for } n/2 < m < n\,. \end{cases} \tag{A.2}$$

Where n is the number of conductors (turns). The field from the asymmetric group is calculated similarly; the field on a conductor m from an asymmetrically adjacent conductor k is defined as:

$$H_{m,asy}(k) = -\frac{I_0}{2\pi}\frac{p_{mk}}{p_{mk}^2 + r_0^2}\,, \tag{A.3}$$

where p_{mk} is the distance between the conductors m and k. $H_{m,asy}$ must also be calculated in accordance with the following rules:

$$H_{m,asy} = \begin{cases} 0, & \text{for } m = n/2 \\ \sum\limits_{k=2m}^{n} H_{m,asy}(k), & \text{for } 1 \leqslant m \leqslant n/2 \\ \sum\limits_{k=1}^{2m-n-1} H_{m,asy}(k), & \text{for } n/2 < m < n \\ \sum\limits_{k=1}^{n-1} H_{m,asy}(k), & \text{for } m = n\,. \end{cases} \tag{A.4}$$

The total magnitude can then be calculated from the sum of the symmetric and asymmetric group fields:

$$H_m = H_{m,pair} + H_{m,asy} \tag{A.5}$$

and the total field H can be defined as the sum of all the H_m values:

$$H = \sum_{m=1}^{n} H_m\,. \tag{A.6}$$

The result of Equation A.6 can be substituted back into Equation 2.11 in order to predict proximity effect losses.

A.2 Table of Reference

Table A.1 summarizes the formulae presented throughout the paper, as a point of reference for the designer.

TABLE A.1: Common Link Design Formulae: Table of Reference

	Wire Solenoid	**PCB Spiral**
Inductance	$L = \frac{\mu_0 \pi r^2 n^2 \kappa}{l}$, $\kappa = z_k \left(ln \left(1 + \frac{1}{z_k} \right) X \right)$, where $X = \frac{1}{\left(k_0 + k_1 \left(\frac{l}{d} \right) \right) + k_2 \left(\frac{l}{d} \right)^2 + \frac{w_1}{(\lvert w_2 \rvert + d/l)^v}}$ and $z_k = l/(\pi r)$, $k_0 = 2.30038$, $k_1 = 3.437$, $k_2 = 1.76356$, $w_1 = -0.47$, $w_2 = 0.755$, and $v = 1.44$.	$L_{circ} = \frac{\mu n^2 d_{avg}}{2} \left(ln \left(\frac{2.46}{\beta} \right) + 0.2\beta^2 \right)$, $L_{sq} = \frac{1.27 \mu n^2 d_{avg}}{2} \left(ln \left(\frac{2.07}{\beta} \right) + 0.18\beta + 0.13\beta^2 \right)$, $L_{hex} = \frac{1.09 \mu n^2 d_{avg}}{2} \left(ln \left(\frac{2.23}{\beta} \right) + 0.17\beta^2 \right)$, $L_{oct} = \frac{1.07 \mu n^2 d_{avg}}{2} \left(ln \left(\frac{2.29}{\beta} \right) + 0.19\beta^2 \right)$,
Skin Effect Loss	$R_{skin} = \frac{l_c \rho}{\pi(d_0 - \delta)\delta}$, $\delta = \sqrt{\frac{2\rho}{\omega\mu}}$	$R_{skin} = R_{DC} \frac{t_0}{\delta \left(1 - e^{-\frac{t_0}{\delta}} \right)} \frac{1}{1 + \frac{t_0}{w}}$, $\delta = \sqrt{\frac{2\rho}{\omega\mu}}$
Proximity Effect Loss	$R_{prox} = \frac{2P_{prox}}{I_0^2} \approx 2R_{DC}\pi^2 r_0^2 \left(\frac{2r_0}{\delta} - 1 \right) \frac{H^2}{I_0^2}$	$R_{prox} = \frac{R_{DC}}{10} \left(\frac{\omega}{\omega_{crit}} \right)^2$, $\omega_{crit} = \frac{3.1}{\mu_0} \frac{(w + s)\rho}{w^2 t_0}$

Mutual Inductance (coaxial)	$M_{coax} = \mu_0 \sqrt{ab} G(\aleph)$, $G(\aleph) = \left(\frac{2}{\aleph} - \aleph \right) K(\aleph) - \frac{2}{\aleph} E(\aleph)$, $\aleph = \sqrt{\frac{4ab}{(a + b)^2 + D^2}}$ a and b are loop radii, D is the coaxial distance

	SS	**SP**	**PS**	**PP**
Link Impedance	$Z_{L1} + \frac{1}{j\omega C_1} + \frac{(\omega M)^2}{Z_{L2} + \frac{1}{j\omega C_2} + Z_{load}}$	$Z_{L1} + \frac{1}{j\omega C_1} + \frac{(\omega M)^2}{Z_{L2} + \frac{1}{j\omega C_2 + 1/Z_{load}}}$	$\frac{1}{j\omega C_1 + \frac{1}{Z_{L1} + \frac{(\omega M)^2}{Z_{L2} + \frac{1}{j\omega C_2} + Z_{load}}}}$	$\frac{1}{j\omega C_1 + \frac{1}{Z_{L1} + \frac{(\omega M)^2}{Z_{L2} + \frac{1}{j\omega C_2 + 1/Z_{load}}}}}$
Link Gain	$\frac{-j\omega M Z_{load}}{Z_{link} \left(Z_{L2} + \frac{1}{j\omega C_2} + Z_{load} \right)}$	$\frac{-j\omega M}{Z_{link}(Z_{L2}(j\omega C_2 + 1/Z_{load}) + 1)}$	$\frac{-j\omega M Z_{load} Z_{link}}{\left(Z_{L1} + Z_{refl} \right) \left(Z_{L2} + \frac{1}{j\omega C_2} + Z_{load} \right)}$	$\frac{-j\omega M Z_{link}}{\left(Z_{L1} + Z_{refl} \right) (Z_{L2}(j\omega C_2 + 1/Z_{load}) + 1)}$

Link Efficiency	$\eta_1 = \frac{P_{Z_{refl}}}{P_{in}} = \frac{\lvert i_1 \rvert^2 \mathfrak{R}\{Z_{refl}\}}{\lvert i_{in} \rvert^2 \mathfrak{R}\{Z_{link}\}} = \frac{\lvert i_1 \rvert^2 \mathfrak{R}\{Z_{refl}\} \lvert Z_{link} \rvert^2}{\lvert v_{in} \rvert^2 \mathfrak{R}\{Z_{link}\}}$, $\eta_2 = \frac{P_{out}}{P_{Z_{refl}}} = \frac{\lvert v_{out} \rvert^2 \mathfrak{R}\{Z_{load}\}}{\lvert i_1 \rvert^2 \mathfrak{R}\{Z_{refl}\} \lvert Z_{load} \rvert^2}$, $\eta_{link} = \frac{P_{out}}{P_{in}} = \frac{P_{Z_{refl}} P_{out}}{P_{in} P_{Z_{refl}}} = \eta_1 \eta_2 = \frac{\lvert v_{out} \rvert^2}{\lvert v_{in} \rvert^2} \cdot \frac{\lvert Z_{link} \rvert^2 \mathfrak{R}\{Z_{load}\}}{\lvert Z_{load} \rvert^2 \mathfrak{R}\{Z_{link}\}} = \frac{\lvert v_{out} \rvert^2}{\lvert i_{in} \rvert^2} \cdot \frac{\mathfrak{R}\{Z_{load}\}}{\lvert Z_{load} \rvert^2 \mathfrak{R}\{Z_{link}\}}$.

CuCCo: The Coupled Coil Configurator

B

The information provided here is also available on Github at `https://github.com/schormans/CuCCo`*; where the latest version of the software can also be downloaded.*

CuCCo provides a series of MATLAB scripts that allow for calculation of 2-coil inductive link parameters, based on geometric coil definitions. Currently, wirewound solenoid coils and PCB-based spiral coils are supported. CuCCo allows seamless geometric ⟶ electrical parameter conversion to allow links to be designed without the need for FEM simulations.

B.1 Features

Given a geometric parameter definition for solenoid or PCB coils, CuCCo can calculate the following parameters:

Coil Parameters:

- Inductance
- Series resistance and Q-factor
- Parallel Capacitance and Self-resonant frequency
- Required capacitance to form a resonant tank

Link Parameters:

- Gain
- Efficiency
- Mutual Inductance and Coupling coefficient

B.2 Function Descriptions

B.2.1 Coil Object Definitions

Currently two coil objects classes are implemented: `SolWireCoil` and `PCBCoil`. Each is constructed from geometric parameters, an input frequency, and a predicted source resistance. Upon construction, the electrical parameters for the coils are calculated and held as object properties. Details are summarized below.

`SolWireCoil.m`

Implements a single-layer solenoid wirewound coil.

Inputs:

- `n` : Number of turns.
- `r_0` : Wire cross-sectional radius.
- `p` : Turn pitch, this can be set to zero to assume a minimum pitch (adjacent wires touching).
- `r` : Coil radius.
- `f` : Drive frequency (this can be a vector, to test over a range).
- `CP` : Parallel capacitance. If this is set to zero, the constructor will attempt to predict a parallel capacitance based on geometry, this will lose accuracy for low turn counts and strange geometries.
- `sourceres` : Additional resistance expected to be inherent to the design. For a Tx coil this should include the source resistance, for an Rx coil this should include connecting trace resistances. This can be set to zero, but neglecting to include this resistance may produce over-optimistic Q-factor predictions.

Outputs:

- `l` : Coil length, depends on `n` and `p` .
- `L` : Inductance
- `Rs` : Series loss resistance.
- `Q` : Q-factor ($\mathfrak{Im}\{Z\}/\mathfrak{Re}\{Z\}$).
- `C` : Tank capacitance required for the coil to resonate at the drive frequency `f` .
- `fSRF` : Self-resonant frequency; either calculated from a user-supplied `CP` value, or predicted from geometry.
- `CP` : If not user supplied, this will be calculated from the predicted `fSRF` .
- `coilZ` : Total coil impedance, considering `L` , `Rs` , `CP` , and `f` .

Note: If `f` is supplied as a vector, `Rs` , `Q` , `C` , and `coilZ` will be created as vectors of the same length, with each value corresponding to the values of `f` in the input vector.

`PCBCoil.m`

Implements a PCB-based spiral coil, assuming standard 1oz copper on FR4 substrate. `PCBCoil` objects are generated in the same way as `SolWireCoil` objects, the only real difference being the input geometry parameters.

Inputs:

- `dout` : The outer diameter of the spiral (edge to edge).
- `fillfact` : The 'fill factor', defining the amount of the spiral outer diameter that is filled with turns, defining the inner diameter `din` in the process.
- `s` : Spacing between turns (edge to edge).
- `w` : Track width.
- `f` : Drive frequency (this can be a vector, to test over a range).
- `shape` : String, can be 'square', 'circ', 'hex', or 'oct'.
- `sourceres` : Additional resistance expected to be inherent to the design. For a Tx coil this should include the source resistance, for an Rx coil this should include connecting trace resistances. This can be set to zero, but neglecting to include this resistance may produce over-optimistic Q-factor predictions.

Outputs are the same as for `SolWireCoil.m` , but with `din` instead of `l` .

B.2.2 Link Parameter Functions

With coils defined, link parameters can be determined with the following functions. The simplest way to characterize a link currently is to use `linkcharvsdist.m` . This gives gain, efficiency, and impedance parameters for an inductive link across a range of distances. Alternatively, specific parameters can be calculated by using individual functions.

`linkcharvsdist.m`

Characterizes a link at a single frequency, over a range of distances. This function will output the key performance metrics: gain, efficiency, and maximum theoretical efficiency. It will also output the link impedance and reflected impedance, as these can be of interest when designing transmitter and receiver circuits.

Inputs:

- `coil1` , `coil2` : The input coil objects, can be `SolWireCoil` or `PCBCoil` .
- `dists` : A vector containing coaxial distances between the two coil objects, e.g. `linspace(1e-3,10e-3,100)` for 100 distance points between 1 mm and 10 mm.

- `config` : can be `'SS'` , `'SP'` , `'PS'` , `'PP'` , corresponding to each possible link arrangement.
- `Zout` : The output load attached to the link.
- `freq` : Drive frequency in Hz.
- `C1` , `C2` : Resonant capacitances, these can be manually supplied to tweak the resonance to your liking. The most simple method is to use `coil.C` , where coil is one of your coil input objects. To improve resonance for parallel connected coils `coil.C - coil.CP` allows you to use the parallel capacitance of the coil as part of the resonant capacitance.

Outputs:

- `gainout` : Link gain, for SP,SS units are V/V, for PS,PP units are V/A. This is a complex number, use `abs(gainout)` to get the absolute value.
- `effout` : Link efficiency.
- `zlinkout` : Full link impedance as viewed from the input coil.
- `zreflout` : Reflected impedance into the input coil from the coupled coil.
- `effmax` : Maximum theoretical link efficiency, given the values of `Q` and `k` .

`linkcharvslat.m`

Fundamentally the same as `linkcharvsdist.m` , but uses `mutualLat.m` to include a lateral misalignment as well as a distance variable.

`mutualIdeal.m`

Determines the mutual inductance and coupling factor of two coaxially aligned coils, separated by a distance `dist` . The two coil objects must currently be of the same class.

Inputs:

- `coil1` , `coil2` : The input coil objects, can be `SolWireCoil` or `PCBCoil` .
- `dist` : The coaxial distance between the two coil objects.

Outputs:

- `M` : Mutual inductance between the coils.
- `k` : Coupling factor (`M` normalized to geometric mean of the two coil inductances).

`mutualLat.m`

Determines the mutual inductance and coupling factor of two parallel coils with a lateral displacement lat, separated by a distance dist. The two coil objects must currently be of the same class.

Inputs:

- `coil1` , `coil2` : The input coil objects, can be `SolWireCoil` or `PCBCoil` .
- `lat` : The lateral misalignment between the two coil centers.
- `dist` : The coaxial distance between the two coil objects.

Outputs:

- `M` : Mutual inductance between the coils.
- `k` : Coupling factor (`M` normalized to geometric mean of the two coil inductances).

`zlink.m`

Determines the link impedance of two coupled coils.

Inputs:

- `config` : can be `'SS'` , `'SP'` , `'PS'` , `'PP'` , corresponding to each possible link arrangement.
- `ZL1` , `ZL2` : impedances of coil1 and coil2 respectively.
- `M` : mutual inductance between the two coils.
- `omega` : angular drive frequency.
- `Zout` : connected output impedance (load).
- `C1` , `C2` : resonant tank capacitors for `coil1` and `coil2` .

Outputs:

- `zlinkval` : the impedance looking into the link. given as a Cartesian complex number.

`gain.m`

Determines the link gain of two coupled coils.

Inputs:

- `config` : can be `'SS'` , `'SP'` , `'PS'` , `'PP'` , corresponding to each possible link arrangement.
- `ZL1` , `ZL2` : impedances of coil1 and coil2 respectively.
- `M` : mutual inductance between the two coils.
- `omega` : angular drive frequency.
- `Zout` : connected output impedance (load).
- `C1` , `C2` : resonant tank capacitors for `coil1` and `coil2` .
- `Zlink` : Link impedance seen at the input of the link.

Outputs:

- `gainval` : the gain of the link, either a voltage gain or a transimpedance, depending on the configuration of the link.

`linkeff.m`

Determines the link efficiency for a given link arrangement, derived from the config, gain, and impedances.

Inputs:

- `config` : can be `'SS'` , `'SP'` , `'PS'` , `'PP'` , corresponding to each possible link arrangement.
- `linkgain` : link gain, as produced by `gain.m` .
- `Zlink` : link impedance, as produced by `zlink.m` .
- `Zout` : connected load impedance.

Outputs:

- `effout` : Link efficiency.

`etamax.m`

Determines the maximum theoretical efficiency of a given link, based on the *kQ* product.

Inputs:

- `k` : coupling factor.
- `Q1` , `Q2` : the Q-factors of the two link coils.

Outputs:

- `max_eff` : the maximum theoretical efficiency of the link with the given input parameters.

`resonance.m`

Returns peak and trough frequencies in the link impedance function of the given link. Ensure to account for changing frequency when providing the coil impedance values.

Bibliography

[1] M. Schormans, V. Valente, and A. Demosthenous, “Practical inductive link design for biomedical wireless power transfer: A tutorial”, *IEEE Transactions on Biomedical Circuits and Systems*, vol. 12, no. 5, pp. 1112–1130, Oct. 2018, ISSN: 1932-4545. DOI: 10.1109/TBCAS.2018.2846020.

[2] (2018). CuCCo: The coupled coil configurator, [Online]. Available: https://github.com/schormans/CuCCo.

[3] O Aquilina, “A brief history of cardiac pacing.”, *Images in paediatric cardiology*, vol. 8, no. 2, pp. 17–81, Apr. 2006, ISSN: 1729-441X. [Online]. Available: http://www.ncbi.nlm.nih.gov/pubmed/22368662http://www.pubmedcentral.nih.gov/articlerender.fcgi?artid=PMC3232561.

[4] W. Greatbatch and C. Holmes, “History of Implantable Devices”, *IEEE Engineering in Medicine and Biology Magazine*, vol. 10, no. 3, pp. 38–41, Sep. 1991, ISSN: 0739-5175. DOI: 10.1109/51.84185. [Online]. Available: http://ieeexplore.ieee.org/document/84185/.

[5] W. M. CHARDACK, A. A. GAGE, and W GREATBATCH, “A transistorized, self-contained, implantable pacemaker for the long-term correction of complete heart block.”, *Surgery*, vol. 48, no. 4, pp. 643–54, Oct. 1960, ISSN: 0039-6060. DOI: 10.5555/URI:PII:0039606060903184. [Online]. Available: http://www.ncbi.nlm.nih.gov/pubmed/13692461.

[6] Medtronic, “Medtronic Micra Specification Sheet”, 2014. [Online]. Available: http://www.medtronic.co.uk/wcm/groups/mdtcom_sg/@mdt/@crdm/documents/documents/micra-patient-pdf.pdf.

[7] Y.-j. Huang, T.-h. Tzeng, T.-w. Lin, C.-w. Huang, P.-w. Yen, P.-h. Kuo, C.-t. Lin, and S.-s. Lu, “A Self-Powered CMOS Reconfigurable Multi-Sensor SoC for Biomedical Applications”, *IEEE Journal of Solid-State Circuits*, vol. 49, no. 4, pp. 851–866, 2014.

[8] Z. Xiao, X. Tan, X. Chen, S. Chen, Z. Zhang, H. Zhang, J. Wang, Y. Huang, P. Zhang, L. Zheng, and H. Min, “An implantable RFID sensor tag toward continuous glucose monitoring”, *IEEE Journal of Biomedical and Health Informatics*, vol. 19, no. 3, pp. 910–919, 2015, ISSN: 21682194. DOI: 10.1109/JBHI.2015.2415836.

[9] S. Guan, J. Gu, Z. Shen, J. Wang, Y. Huang, and A. Mason, "Wireless powered implantable bio-sensor tag system-on-chip for continuous glucose monitoring", *2011 IEEE Biomedical Circuits and Systems Conference, BioCAS 2011*, pp. 193–196, 2011. DOI: `10.1109/BioCAS.2011.6107760`.

[10] N. J. Cleven, J. A. Müntjes, H. Fassbender, U. Urban, M. Görtz, H. Vogt, M. Gräfe, T. Göttsche, T. Penzkofer, T. Schmitz-Rode, and W. Mokwa, "A novel fully implantable wireless sensor system for monitoring hypertension patients", *IEEE Transactions on Biomedical Engineering*, vol. 59, no. 12 PART2, pp. 3124–3130, 2012, ISSN: 00189294. DOI: `10.1109/TBME.2012.2216262`.

[11] N. T. Trung and P. Häfliger, "A submicrowatt implantable capacitive sensor system for biomedical applications", *IEEE Transactions on Circuits and Systems II: Express Briefs*, vol. 62, no. 2, pp. 209–213, 2015, ISSN: 15497747. DOI: `10.1109/TCSII.2014.2368260`.

[12] M. M. Ahmadi and G. a. Jullien, "A wireless-implantable microsystem for continuous blood glucose monitoring", *Biomedical Circuits and Systems, IEEE Transactions on*, vol. 3, no. 3, pp. 169–180, 2009, ISSN: 1932-4545. DOI: `10.1109/TBCAS.2009.2016844`. [Online]. Available: `http://www.ncbi.nlm.nih.gov/pubmed/23853218`.

[13] A. D. DeHennis and K. D. Wise, "A wireless microsystem for the remote sensing of pressure, temperature, and relative humidity", *Journal of Microelectromechanical Systems*, vol. 14, no. 1, pp. 12–22, 2005, ISSN: 10577157. DOI: `10.1109/JMEMS.2004.839650`.

[14] P. Cong, N. Chaimanonart, W. H. Ko, and D. J. Young, "A Wireless and Batteryless 10-Bit Implantable Blood Pressure Sensing Microsystem With Adaptive RF Powering for Real-Time Laboratory Mice Monitoring", *IEEE Journal of Solid-State Circuits*, vol. 44, no. 12, pp. 3631–3644, Dec. 2009, ISSN: 0018-9200. DOI: `10.1109/JSSC.2009.2035551`. [Online]. Available: `http://ieeexplore.ieee.org/document/5342353/`.

[15] R. R. Harrison, P. T. Watkins, R. J. Kier, R. O. Lovejoy, D. J. Black, B. Greger, and F. Solzbacher, "A Low-Power Integrated Circuit for a Wireless 100-Electrode Neural Recording System", *IEEE Journal of Solid-State Circuits*, vol. 42, no. 1, pp. 123–133, 2007.

[16] C. W. Chang and J. C. Chiou, "A wireless and batteryless microsystem with implantable grid electrode/3-dimensional probe array for ECoG and extracellular neural recording in rats.", *Sensors*, vol. 13, no. 4, pp. 4624–4639, 2013, ISSN: 14248220. DOI: `10.3390/s130404624`.

[17] A. M. Sodagar, G. E. Perlin, Y. Yao, K. Najafi, and K. D. Wise, "An implantable 64-channel wireless microsystem for single-unit neural recording", *IEEE Journal of Solid-State Circuits*, vol. 44, no. 9, pp. 2591–2604, 2009, ISSN: 00189200. DOI: `10.1109/JSSC.2009.2023159`.

[18] Z. Xiao, C.-M. Tang, C. M. Dougherty, and R. Bashirullah, “A 20μW Neural Recording Tag with Supply-Current-Modulated AFE in 0.13μm CMOS”, in *IEEE International Solid-State Circuits Conference*, vol. 17, 2010, pp. 560–561, ISBN: 9781424460342.

[19] C. M. Lopez, A. Andrei, S. Mitra, M. Welkenhuysen, W. Eberle, C. Bartic, R. Puers, R. F. Yazicioglu, and G. G. E. Gielen, “An Implantable 455-Active-Electrode 52-Channel CMOS Neural Probe”, *IEEE Journal of Solid-State Circuits*, vol. 49, no. 1, pp. 248–261, Jan. 2014, ISSN: 0018-9200. DOI: `10.1109/JSSC.2013.2284347`. [Online]. Available: `http://ieeexplore.ieee.org/document/6642150/`.

[20] Y. Zhang, F. Zhang, Y. Shakhsheer, J. D. Silver, A. Klinefelter, M. Nagaraju, J. Boley, J. Pandey, A. Shrivastava, E. J. Carlson, A. Wood, B. H. Calhoun, and B. P. Otis, “A Batteryless 19 μW MICS / ISM-Band Energy Harvesting Body Sensor Node SoC for ExG Applications”, *IEEE Journal of Solid-State Circuits*, vol. 48, no. 1, pp. 199–213, 2013.

[21] J. Charthad, T. C. Chang, Z. Liu, A. Sawaby, M. J. Weber, S. Baker, F. Gore, S. A. Felt, and A. Arbabian, “A mm-Sized wireless implantable device for electrical stimulation of peripheral nerves”, *IEEE Transactions on Biomedical Circuits and Systems*, vol. 12, no. 2, pp. 257–270, 2018, ISSN: 19324545. DOI: `10.1109/TBCAS.2018.2799623`.

[22] M. Ortmanns, A. Rocke, M. Gehrke, and H. J. Tiedtke, “A 232-Channel Epiretinal Stimulator ASIC”, *IEEE Journal of Solid-State Circuits*, vol. 42, no. 12, pp. 2946–2959, 2007, ISSN: 00189200. DOI: `10.1109/JSSC.2007.908693`.

[23] Medtronic, “Activa RC Implant Manual”, Tech. Rep., 2008.

[24] H.-m. Lee, H. Park, and M. Ghovanloo, “A Power-Efficient Wireless System With Adaptive Supply Control for Deep Brain Stimulation”, *IEEE Journal of Solid-State Circuits*, vol. 48, no. 9, pp. 2203–2216, 2013.

[25] H.-m. Lee, K. Y. Kwon, and W. Li, “A Power-Efficient Switched-Capacitor Stimulating System for Electrical / Optical Deep Brain Stimulation”, *IEEE Journal of Solid-State Circuits*, vol. 50, no. 1, pp. 1–15, 2015.

[26] G. Wang, W. Liu, M. Sivaprakasam, and G. A. Kendir, “Design and analysis of an adaptive transcutaneous power telemetry for biomedical implants”, *IEEE Transactions on Circuits and Systems I: Regular Papers*, vol. 52, no. 10, pp. 2109–2117, 2005, ISSN: 10577122. DOI: `10.1109/TCSI.2005.852923`.

[27] H.-g. Rhew, J. Jeong, J. A. Fredenburg, S. Dodani, P. G. Patil, and M. P. Flynn, “A Fully Self-Contained Logarithmic Closed-Loop Deep Brain Stimulation SoC With Wireless Telemetry and Wireless Power Management”, *IEEE Journal of Solid-State Circuits*, vol. 49, no. 10, pp. 2213–2227, 2014.

[28] D. Jiang, D. Cirmirakis, M. Schormans, T. Perkins, N. Donaldson, and A. Demosthenous, “An Integrated Passive Phase-Shift Keying Modulator for Biomedical Implants With Power Telemetry Over a Single Inductive Link”, *IEEE Transactions on Biomedical Circuits and Systems*, vol. 11, no. 1, pp. 64–77, 2016, ISSN: 19324545. DOI: `10.1109/TBCAS.2016.2580513`.

[29] Y. P. Lin, C. Y. Yeh, P. Y. Huang, Z. Y. Wang, H. H. Cheng, Y. T. Li, C. F. Chuang, P. C. Huang, K. T. Tang, H. P. Ma, Y. C. Chang, S. R. Yeh, and H. Chen, “A Battery-Less, Implantable Neuro-Electronic Interface for Studying the Mechanisms of Deep Brain Stimulation in Rat Models”, *IEEE Transactions on Biomedical Circuits and Systems*, vol. 10, no. 1, pp. 98–112, 2015, ISSN: 19324545. DOI: `10.1109/TBCAS.2015.2403282`.

[30] T Mussivand, P. J. Hendry, R. G. Masters, K. S. Holmes, A Hum, and W. J. Keon, “A remotely controlled and powered artificial heart pump”, *Artificial organs*, vol. 20, no. 12, pp. 1314–1319, 1996, ISSN: 0160-564X (Print). [Online]. Available: `http://www.ncbi.nlm.nih.gov/pubmed/8947455`.

[31] O. Knecht, R. Bosshard, and J. W. Kolar, “High-Efficiency Transcutaneous Energy Transfer for Implantable Mechanical Heart Support Systems”, *IEEE Transactions on Power Electronics*, vol. 30, no. 11, pp. 6221–6236, Nov. 2015, ISSN: 0885-8993. DOI: `10.1109/TPEL.2015.2396194`. [Online]. Available: `http://ieeexplore.ieee.org/document/7018986/`.

[32] J. Charthad, M. J. Weber, T. C. Chang, and A. Arbabian, “A mm-Sized Implantable Medical Device (IMD) With Ultrasonic Power Transfer and a Hybrid Bi-Directional Data Link”, *IEEE Journal of Solid-State Circuits*, vol. 50, no. 8, pp. 1741–1753, Aug. 2015, ISSN: 0018-9200. DOI: `10.1109/JSSC.2015.2427336`. [Online]. Available: `http://ieeexplore.ieee.org/document/7109955/`.

[33] J. S. Ho, S. Kim, and A. S. Y. Poon, “Midfield wireless powering for implantable systems”, *Proceedings of the IEEE*, vol. 101, no. 6, pp. 1369–1378, 2013, ISSN: 00189219. DOI: `10.1109/JPROC.2013.2251851`.

[34] S. A. Mirbozorgi, P. Yeon, and M. Ghovanloo, “Robust Wireless Power Transmission to mm-Sized Free-Floating Distributed Implants”, *IEEE Transactions on Biomedical Circuits and Systems*, vol. 11, no. 3, pp. 692–702, 2017, ISSN: 19324545. DOI: `10.1109/TBCAS.2017.2663358`.

[35] S. Stoecklin, A. Yousaf, T. Volk, and L. Reindl, “Efficient Wireless Powering of Biomedical Sensor Systems for Multichannel Brain Implants”, *IEEE Transactions on Instrumentation and Measurement*, vol. 65, no. 4, pp. 754–764, 2016, ISSN: 00189456. DOI: `10.1109/TIM.2015.2482278`.

[36] N. Kyungmin, J. Heedon, S. K. Oruganti, and F. Bien, “An improved wireless power transfer system with adaptive technique for Implantable Biomedical Devices”, in *Microwave Workshop Series on RF and Wireless Technologies for*

Biomedical and Healthcare Applications (IMWS-BIO), 2013 IEEE MTT-S International, 2013, pp. 1–3, ISBN: 9781467360968. DOI: `10.1109/IMWS-BIO.2013.6756136`.

[37] U.-m. Jow and M. Ghovanloo, "Design and Optimization of Printed Spiral Coils for Efficient Inductive Power Transmission", in *Electronics, Circuits and Systems, 2007. ICECS 2007. 14th IEEE International Conference on*, vol. 2, 2007, pp. 70–73, ISBN: 1424413788.

[38] C. Zheng, H. Ma, J.-s. Lai, and L. Zhang, "Design Considerations to Reduce Gap Variation and Misalignment Effects for the Inductive Power Transfer System", *IEEE Transactions on Power Electronics*, vol. 30, no. 11, pp. 6108–6119, Nov. 2015, ISSN: 0885-8993. DOI: `10.1109/TPEL.2015.2424893`. [Online]. Available: `http://ieeexplore.ieee.org/document/7091005/`.

[39] S. Y. R. Hui, Z. Wenxing, and C. K. Lee, "A critical review of recent progress in mid-range wireless power transfer", *IEEE Transactions on Power Electronics*, vol. 29, no. 9, pp. 4500–4511, 2014, ISSN: 0885-8993. DOI: `10.1109/TPEL.2013.2249670`.

[40] R. R. Harrison, H. Fotowat, R. Chan, R. J. Kier, R. Olberg, A. Leonardo, and F. Gabbiani, "Wireless Neural / EMG Telemetry Systems for Small Freely Moving Animals", *IEEE Transactions on Biomedical Circuits and Systems*, vol. 5, no. 2, pp. 103–111, 2011.

[41] C.-c. Peng, Z. Xiao, and R. Bashirullah, "Toward Energy Efficient Neural Interfaces", *IEEE Transactions on Biomedical Engineering*, vol. 56, no. 11, pp. 2697–2700, 2009.

[42] A. M. Sodagar, K. D. Wise, and K. Najafi, "A wireless implantable microsystem for multichannel neural recording", *IEEE Transactions on Microwave Theory and Techniques*, vol. 57, no. 10, pp. 2565–2573, 2009, ISSN: 00189480. DOI: `10.1109/TMTT.2009.2029957`.

[43] H.-m. Lee and M. Ghovanloo, "A Power-Efficient Wireless Capacitor Charging System Through an Inductive Link", *IEEE Transactions on Circuits and Systems II: Express Briefs*, vol. 60, no. 10, pp. 707–711, 2013.

[44] M. Fu, H. Yin, X. Zhu, and C. Ma, "Analysis and Tracking of Optimal Load in Wireless Power Transfer Systems", *IEEE Transactions on Power Electronics*, vol. 30, no. 7, pp. 3952–3963, Jul. 2015, ISSN: 0885-8993. DOI: `10.1109/TPEL.2014.2347071`. [Online]. Available: `http://ieeexplore.ieee.org/document/6876181/`.

[45] Y. Wang, D. Ye, L. Lyu, Y. Xiang, H. Min, and C.-J. R. Shi, "A 13.56MHz Wireless Power and Data Transfer Receiver Achieving 75.4% Effective-Power-Conversion Efficiency with 0.1% ASK Modulation Depth and 9.2mW Output Power", *2018 IEEE International Solid - State Circuits Conference - (ISSCC)*,

pp. 142–144, 2018. DOI: `10.1109/ISSCC.2018.8310224`. [Online]. Available: `http://ieeexplore.ieee.org/document/8310224/`.

[46] Z. Lu and M. Sawan, “An 8 Mbps data rate transmission by inductive link dedicated to implantable devices”, *Proceedings - IEEE International Symposium on Circuits and Systems*, vol. 3, no. 1, pp. 3057–3060, 2008, ISSN: 02714310. DOI: `10.1109/ISCAS.2008.4542103`.

[47] D. C. Galbraith, M. Soma, and R. L. White, “A Wide-Band Efficient Inductive Transdermal Power and Data Link with Coupling Insensitive Gain”, *IEEE Transactions on Biomedical Engineering*, no. 4, pp. 265–275, 1987.

[48] L. Zhou and N. Donaldson, “A Fast Passive Data Transmission Method for ENG Telemetry”, *Neuromodulation*, vol. 6, no. 2, pp. 116–121, 2003.

[49] F. Inanlou, M. Kiani, and M. Ghovanloo, “A 10.2 Mbps pulse harmonic modulation based transceiver for implantable medical devices”, *IEEE Journal of Solid-State Circuits*, vol. 46, no. 6, pp. 1296–1306, 2011, ISSN: 00189200. DOI: `10.1109/JSSC.2011.2134570`.

[50] M. Kiani and M. Ghovanloo, “A 13.56-mbps pulse delay modulation based transceiver for simultaneous near-field data and power transmission”, *IEEE transactions on biomedical circuits and systems*, vol. 9, no. 1, pp. 1–11, 2015, ISSN: 1940-9990. DOI: `10.1109/TBCAS.2014.2304956`. [Online]. Available: `http://www.ncbi.nlm.nih.gov/pubmed/24760945`.

[51] F. E. Terman, *Radio Engineering*. 1937, pp. xiii, 813, ISBN: 9781848212961.

[52] ——, *Radio Engineers’ Handbook*. McGraw-Hill Book Company, 1943.

[53] U.-m. Jow and M. Ghovanloo, “Modeling and Optimization of Printed Spiral Coils in Air , Saline , and Muscle Tissue Environments”, *IEEE Transactions on Biomedical Circuits and Systems*, vol. 3, no. 5, pp. 339–347, 2009.

[54] W. H. Ko, S. P. Liang, and C. D. F. Fung, “Design of radio-frequency powered coils for implant instruments”, *Medical & Biological Engineering & Computing*, vol. 15, no. 6, pp. 634–640, 1977.

[55] N. d. N. Donaldson and T. A. Perkins, “Analysis of resonant coupled coils in the design of radio frequency transcutaneous links”, *Medical & Biological Engineering & Computing*, vol. 21, no. September, pp. 612–627, 1983.

[56] K. Fotopoulou and B. W. Flynn, “Wireless power transfer in loosely coupled links: Coil misalignment model”, *IEEE Transactions on Magnetics*, vol. 47, no. 2 PART 2, pp. 416–430, 2011, ISSN: 00189464. DOI: `10.1109/TMAG.2010.2093534`.

[57] B. X. Nguyen, D. M. Vilathgamuwa, G. H. Foo, P. Wang, A. Ong, U. K. Madawala, and T. D. Nguyen, “An Efficiency Optimization Scheme for Bidirectional Inductive Power Transfer Systems”, *IEEE Trans. Power Electron.*, vol. 30, no. 11, pp. 6310–6319, 2015, ISSN: 0885-8993. DOI: `10.1109/TPEL.2014.2379676`.

[58] M. E. Halpern and D. C. Ng, “Optimal Tuning of Inductive Wireless Power Links: Limits of Performance”, *IEEE Transactions on Circuits and Systems I: Regular Papers*, vol. 62, no. 3, pp. 725–732, 2015, ISSN: 1549-8328. DOI: `10.1109/TCSI.2014.2386771`. [Online]. Available: `http://ieeexplore.ieee.org/lpdocs/epic03/wrapper.htm?arnumber=7024943`.

[59] W.-Q. Niu, J.-X. Chu, W. Gu, and A.-D. Shen, “Exact Analysis of Frequency Splitting Phenomena of Contactless Power Transfer Systems”, *IEEE Transactions on Circuits and Systems I: Regular Papers*, vol. 60, no. 6, pp. 1670–1677, 2013, ISSN: 1549-8328. DOI: `10.1109/TCSI.2012.2221172`. [Online]. Available: `http://ieeexplore.ieee.org/lpdocs/epic03/wrapper.htm?arnumber=6363491`.

[60] W. Zhong, C. K. Lee, and S. Y. Ron Hui, “General analysis on the use of tesla’s resonators in domino forms for wireless power transfer”, *IEEE Transactions on Industrial Electronics*, vol. 60, no. 1, pp. 261–270, 2013, ISSN: 02780046. DOI: `10.1109/TIE.2011.2171176`.

[61] S. a. Mirbozorgi, H. Bahrami, M. Sawan, and B. Gosselin, “A smart multi-receiver power transmission system for long-term biological monitoring”, *2014 IEEE Biomedical Circuits and Systems Conference (BioCAS) Proceedings*, pp. 412–415, 2014. DOI: `10.1109/BioCAS.2014.6981750`. [Online]. Available: `http://ieeexplore.ieee.org/lpdocs/epic03/wrapper.htm?arnumber=6981750`.

[62] Y. Ahn, I. Jeon, and J. Roh, “A Multiphase Buck Converter With a Rotating Phase-Shedding Scheme For Efficient Light-Load Control”, *IEEE Journal of Solid-State Circuits*, vol. 49, no. 11, pp. 2673–2683, 2014.

[63] Z. Dang, Y. Cao, and J. A. Abu Qahouq, “Reconfigurable Magnetic Resonance-Coupled Wireless Power Transfer System”, *IEEE Transactions on Power Electronics*, vol. 30, no. 11, pp. 6057–6069, 2015, ISSN: 0885-8993. DOI: `10.1109/TPEL.2015.2422776`. [Online]. Available: `http://ieeexplore.ieee.org/lpdocs/epic03/wrapper.htm?arnumber=7084654`.

[64] E. Moradi, T. Björninen, L. Sydänheimo, and J. M. Rabaey, “Analysis of Wireless Powering of mm-Size Neural Recording Tags in RFID-inspired Wireless Brain-Machine Interface Systems”, in *IEEE International Conference on RFID*, 2013, pp. 8–15, ISBN: 9781467357500.

[65] K. Van Schuylenbergh and R. Puers, Eds., *Inductive Powering*. Dordrecht: Springer Netherlands, 2009, ISBN: 978-90-481-2411-4. DOI: `10.1007/978-90-481-2412-1`. [Online]. Available: `http://link.springer.com/10.1007/978-90-481-2412-1`.

[66] M. Kiani, U. M. Jow, and M. Ghovanloo, “Design and optimization of a 3-coil inductive link for efficient wireless power transmission”, *IEEE Transactions on Biomedical Circuits and Systems*, vol. 5, no. 6, pp. 579–591, 2011, ISSN: 19324545. DOI: `10.1109/TBCAS.2011.2158431`.

[67] A. P. Sample, D. a. Meyer, and J. R. Smith, "Analysis, experimental results, and range adaptation of magnetically coupled resonators for wireless power transfer", *IEEE Transactions on Industrial Electronics*, vol. 58, no. 2, pp. 544–554, 2011, ISSN: 02780046. DOI: `10.1109/TIE.2010.2046002`.

[68] N. Hoang and I. A. Johnson, "Splitting Frequency Diversity in Wireless Power Transmission", *IEEE Transactions on Power Electronics*, vol. 30, no. 11, pp. 6088–6096, 2015, ISSN: 00135127. DOI: `10.1109/TPEL.2015.2424312`.

[69] K. Agarwal, R. Jegadeesan, Y.-X. Guo, and N. V. Thakor, "Wireless Power Transfer Strategies for Implantable Bioelectronics", *IEEE Reviews in Biomedical Engineering*, vol. 10, pp. 136–161, 2017, ISSN: 1937-3333. DOI: `10.1109/RBME.2017.2683520`. [Online]. Available: `http://ieeexplore.ieee.org/document/7879807/`.

[70] H. A. Wheeler, "Simple inductance formulas for radio coils", *Proceedings of the Institute of Radio Engineers*, vol. 16, no. 10, pp. 1398–1400, 1928, ISSN: 07315996. DOI: `10.1109/JRPROC.1928.221309`.

[71] F. W. Grover, *Inductance Calculations.* Dover Publications Inc., 1962.

[72] P. Silvester, *Modern Electromagnetic Fields.* 1968. [Online]. Available: `https://archive.org/details/ModernElectromagneticFields`.

[73] W. G. Hurley, M. C. Duffy, J. Zhang, I. Lope, B. Kunz, and W. H. W, "A Unified Approach to the Calculation of Self- and Mutual-Inductance for Coaxial Coils in Air", *IEEE Transactions on Power Electronics*, vol. 30, no. 11, pp. 6155–6162, 2015. DOI: `10.1109/TPEL.2015.2413493`.

[74] K. A. Wirgau, "Inductance calculation of an air-core disk winding", *IEEE Transactions on Power Apparatus and Systems*, vol. 95, no. 1, pp. 394–400, 1976, ISSN: 00189510. DOI: `10.1109/T-PAS.1976.32117`.

[75] D. W. Knight, *An Introduction to the Art of Solenoid Inductance Calculation.* 2016, pp. 1–86, ISBN: 0471585513. [Online]. Available: `http://g3ynh.info/zdocs/magnetics/Solenoids.pdf`.

[76] S. S. Mohan, M. D. M. Hershenson, S. P. Boyd, and T. H. Lee, "Simple accurate expressions for planar spiral inductances", *IEEE Journal of Solid-State Circuits*, vol. 34, no. 10, pp. 1419–1420, 1999.

[77] H. B. Dwight, "Skin Effect in Tubular and Flat Conductors", *Transactions of the American Institute of Electrical Engineers*, vol. XXXVII, no. 2, pp. 1379–1403, Jul. 1918, ISSN: 0096-3860. DOI: `10.1109/T-AIEE.1918.4765575`. [Online]. Available: `http://ieeexplore.ieee.org/lpdocs/epic03/wrapper.htm?arnumber=4765575`.

[78] J. Cockcroft, "Skin Effect in Rectangular Conductors at High Frequencies", *Proceedings of the Royal Society of London. Series A, Containing Papers of a Mathematical and Physical Character*, vol. 122, no. 790, pp. 533–542, 1928. [Online]. Available: `http://www.jstor.org/stable/95158`.

[79] J. Lammeraner and M. Stafl, *Eddy Currents.* Iliffe Books Ltd., 1966, ISBN: 978-0592050164.

[80] P. Meyer, P. Germano, and Y. Perriard, “FEM Modeling of Skin and Proximity Effects for Coreless Transformers”, in *International Conference on Electrical Machines and Systems*, 2012, pp. 1–6.

[81] I. Lope, C. Carretero, J. Acero, R. Alonso, and J. M. Burdío, “AC power losses model for planar windings with rectangular cross-sectional conductors”, *IEEE Transactions on Power Electronics*, vol. 29, no. 1, pp. 23–28, 2014, ISSN: 08858993. DOI: `10.1109/TPEL.2013.2256928`.

[82] G. K. Felic, D. Ng, and E Skafidas, “Investigation of frequency-dependent effects in inductive coils for implantable electronics”, *IEEE Transactions on Magnetics*, vol. 49, no. 4, pp. 1353–1360, 2013, ISSN: 00189464. DOI: `10.1109/TMAG.2012.2231091`.

[83] R. C. Fernandes, A. Albano, and D. O. Jr, “Iterative Design Method of Weakly Coupled Magnetic Elements for Inductive Power Transfer”, pp. 1088–1094, 2013.

[84] S.-H. Lee and R. D. Lorenz, “Development and Validation of Model for 95%-Efficiency 220-W Wireless Power Transfer Over a 30-cm Air Gap”, *IEEE Transactions on Industry Applications*, vol. 47, no. 6, pp. 2495–2504, Nov. 2011, ISSN: 0093-9994. DOI: `10.1109/TIA.2011.2168555`. [Online]. Available: `http://ieeexplore.ieee.org/document/6022774/`.

[85] Z. Pantic and S. Lukic, “Computationally-efficient, generalized expressions for the proximity-effect in multi-layer, multi-turn tubular coils for wireless power transfer systems”, *IEEE Transactions on Magnetics*, vol. 49, no. 11, pp. 5404–5416, 2013, ISSN: 00189464. DOI: `10.1109/TMAG.2013.2264486`.

[86] J. Kim and Y. Park, “Approximate Closed-Form Formula for Calculating Ohmic Resistance in Coils of Parallel Round Wires with Unequal Pitches”, *IEEE Transactions on Industrial Electronics*, vol. 0046, no. c, pp. 3482–3489, 2014, ISSN: 0278-0046. DOI: `10.1109/TIE.2014.2370943`. [Online]. Available: `http://ieeexplore.ieee.org/lpdocs/epic03/wrapper.htm?arnumber=6960849`.

[87] W. B. Kuhn and N. M. Ibrahim, “Analysis of current crowding effects in multi-turn spiral inductors”, *IEEE Transactions on Microwave Theory and Techniques*, vol. 49, no. 1, pp. 31–38, 2001, ISSN: 00189480. DOI: `10.1109/22.899959`.

[88] H. Wheeler, “Formulas for the Skin Effect”, *Proceedings of the IRE*, vol. 30, no. 9, pp. 412–424, Sep. 1942, ISSN: 0096-8390. DOI: `10.1109/JRPROC.1942.232015`. [Online]. Available: `http://ieeexplore.ieee.org/document/1694542/`.

[89] B. H. Choi, E. S. Lee, J. Huh, and C. T. Rim, “Lumped Impedance Transformers for Compact and Robust Coupled Magnetic Resonance Systems”, *IEEE Transactions on Power Electronics*, vol. 30, no. 11, pp. 6046–6056, Nov. 2015, ISSN:

0885-8993. DOI: `10.1109/TPEL.2015.2394242`. [Online]. Available: `http://ieeexplore.ieee.org/document/7015574/`.

[90] J. T. Boys, G. Covic, and a.W. Green, "Stability and control of inductively coupled power transfer systems", *IEE Proceedings - Electric Power Applications*, vol. 147, no. 1, p. 37, 2000, ISSN: 13502352. DOI: `10.1049/ip-epa:20000017`.

[91] Q. Ke, W. Luo, G. Yan, and K. Yang, "Analytical Model and Optimized Design of Power Transmitting Coil for Inductive Coupled Endoscope Robot", *IEEE Transactions on Biomedical Engineering*, vol. 63, no. 4, pp. 694–706, 2015, ISSN: 0018-9294. DOI: `10.1109/TBME.2015.2469137`. [Online]. Available: `http://ieeexplore.ieee.org/lpdocs/epic03/wrapper.htm?arnumber=7206546`.

[92] G. A. Kendir, W. Liu, G. Wang, M. Sivaprakasam, R. Bashirullah, M. S. Humayun, and J. D. Weiland, "An Optimal Design Methodology for Inductive Power Link With Class-E Amplifier", *IEEE Transactions on Circuits and Systems I: Regular Papers*, vol. 52, no. 5, pp. 857–866, 2005.

[93] M. Bartoli, N. Noferi, A. Reatti, and M. K. Kazimierczuk, "Modeling Litz-wire Winding Losses in High-Frequency Power Inductors", in *IEEE Annual Power Electronics Specialists Conference*, vol. 2, 1996, pp. 1690–1696, ISBN: 0780335007. DOI: `10.1109/PESC.1996.548808`.

[94] C. Carretero, J. Acero, and R. Alonso, "Tm-Te Decomposition of Power Losses in Multi-Stranded Litz-Wires Used in Electronic Devices", *Progress In Electromagnetics Research*, vol. 123, no. September 2011, pp. 83–103, 2012, ISSN: 1559-8985. DOI: `10.2528/PIER11091909`. [Online]. Available: `http://www.jpier.org/PIER/pier.php?paper=11091909`.

[95] M. Etemadrezaei and S. Lukic, "Coated-Strand Litz Wire for Multi-MHz Frequency Applications", *IEEE Transactions on Magnetics*, vol. 9464, no. c, pp. 1–11, 2016, ISSN: 0018-9464. DOI: `10.1109/TMAG.2016.2550425`. [Online]. Available: `http://ieeexplore.ieee.org/lpdocs/epic03/wrapper.htm?arnumber=7447774`.

[96] J. Acero, P. J. Hernández, J. M. Burdío, R. Alonso, and L. A. Barragán, "Simple resistance calculation in litz-wire planar windings for induction cooking appliances", *IEEE Transactions on Magnetics*, vol. 41, no. 4, pp. 1280–1288, 2005, ISSN: 00189464. DOI: `10.1109/TMAG.2005.844844`.

[97] E. W. Weisstein. (2019). Kelvin functions, [Online]. Available: `http://mathworld.wolfram.com/KelvinFunctions.html`.

[98] A. J. Palermo, "Distributed capacity of single-layer", *Proceedings of the Institute of Radio Engineers*, vol. 22, no. 7, pp. 897–905, 1934, ISSN: 0096-8390. DOI: `10.1109/JRPROC.1934.226741`.

[99] Z. Jiang, P. S. Excell, and Z. M. Hejazi, "Calculation of distributed capacitances of spiral resonators", *IEEE Transactions on Microwave Theory and Techniques*, vol. 45, no. 1, pp. 139–142, 1997, ISSN: 00189480. DOI: `10.1109/22.552045`.

[100] J. Biela and J. W. Kolar, "Using transformer parasitics for resonant converters - A review of the calculation of the stray capacitance of transformers", *IEEE Transactions on Industry Applications*, vol. 44, no. 1, pp. 223–233, 2008, ISSN: 00939994. DOI: `10.1109/TIA.2007.912722`.

[101] M. B. Shadmand and R. S. Balog, "Determination of parasitic parameters in a high frequency magnetic to improve the manufacturability, performance, and efficiency of a PV inverter", *Conference Record of the IEEE Photovoltaic Specialists Conference*, pp. 1368–1372, 2012, ISSN: 01608371. DOI: `10.1109/PVSC.2012.6317854`.

[102] D. W. Knight, *An Introduction to the Art of Solenoid Inductance Calculation.* 2016, pp. 1–86, ISBN: 0471585513. [Online]. Available: `http://g3ynh.info/zdocs/magnetics/Solenoids.pdf`.

[103] Payne Alan, "Self-resonance in coils and the self-capacitance myth", vol. 6, pp. 1–11, 2014.

[104] J Groszkowski, *Frequency of Self-Oscillations.* Elsevier Science, 1964, ISBN: 9781483280301. [Online]. Available: `https://books.google.co.uk/books?id=H_ZFBQAAQBAJ`.

[105] M. Soma, D. C. Galbraith, and R. L. White, "Radio-Frequency Coils in Implantable Devices : Misalignment Analysis and Design Procedure", *IEEE Transactions on Biomedical Engineering*, vol. BME-34, no. 4, pp. 276–282, 1987.

[106] J. S. Ho, A. J. Yeh, E. Neofytou, S. Kim, Y. Tanabe, B. Patlolla, R. E. Beygui, and A. S. Y. Poon, "Wireless power transfer to deep-tissue microimplants", *Proceedings of the National Academy of Sciences*, vol. 111, no. 22, pp. 7974–7979, Jun. 2014, ISSN: 0027-8424. DOI: `10.1073/pnas.1403002111`. [Online]. Available: `http://www.pnas.org/cgi/doi/10.1073/pnas.1403002111`.

[107] F. C. Flack, E. D. James, and D. M. Schlapp, "Mutual inductance of air-cored coils: Effect on design of radio-frequency coupled implants", *Medical & Biological Engineering*, vol. 9, no. 2, pp. 79–85, Mar. 1971, ISSN: 0025-696X. DOI: `10.1007/BF02474736`. [Online]. Available: `http://link.springer.com/10.1007/BF02474736`.

[108] C. M. Zierhofer and E. S. Hochmair, "Geometric approach for coupling enhancement of magnetically coupled coils", *IEEE Transactions on Biomedical Engineering*, vol. 43, no. 7, pp. 708–714, 1996, ISSN: 00189294. DOI: `10.1109/10.503178`.

[109] T. Ohira, "The kQ Product as Viewed by an Analog Circuit Engineer", *IEEE Circuits and Systems Magazine*, vol. 17, no. 1, pp. 27–32, 2017, ISSN: 1531636X. DOI: `10.1109/MCAS.2016.2642698`.

[110] K. Hata, T. Imura, and Y. Hori, “Simplified measuring method of kQ product for wireless power transfer via magnetic resonance coupling based on input impedance measurement”, in *IECON 2017 - 43rd Annual Conference of the IEEE Industrial Electronics Society*, vol. 1, IEEE, Oct. 2017, pp. 6974–6979, ISBN: 978-1-5386-1127-2. DOI: `10.1109/IECON.2017.8217219`. [Online]. Available: `http://ieeexplore.ieee.org/document/8217219/`.

[111] T. Ujihara, Q. T. Duong, and M. Okada, “KQ-product analysis of inductive power transfer system with two transmitters and two receivers”, *WPTC 2017 - Wireless Power Transfer Conference*, no. 1, pp. 2–5, 2017. DOI: `10.1109/WPT.2017.7953861`.

[112] A. Barchanski, “Simulations of Low-Frequency Electromagnetic Fields in the Human Body .”, *Organization*, p. 111, 2007. [Online]. Available: `http://tuprints.ulb.tu-darmstadt.de/888/1/promotion_barchanski.pdf`.

[113] X. P. Ripoll, “Electrical Properties of Human Tissues Applied to Wearable Antenna Design”, 2012.

[114] A. Trigui, S. Hached, F. Mounaim, and A. C. Ammari, “Inductive Power Transfer System With Self-Calibrated Primary Resonant Frequency”, *IEEE Transactions on Power Electronics*, vol. 30, no. 11, pp. 6078–6087, 2015, ISSN: 0885-8993. DOI: `10.1109/TPEL.2015.2399417`.

[115] S. J. Thomas and M. S. Reynolds, “A 96 Mbit / sec , 15 . 5 pJ / bit 16-QAM Modulator for UHF Backscatter Communication”, in *IEEE International Conference on RFID*, 2012, pp. 185–190, ISBN: 9781467303286.

[116] Yiming Zhang and Zhengming Zhao, “Frequency Splitting Analysis of Two-Coil Resonant Wireless Power Transfer”, *IEEE Antennas and Wireless Propagation Letters*, vol. 13, no. 4, pp. 400–402, 2014, ISSN: 1536-1225. DOI: `10.1109/LAWP.2014.2307924`. [Online]. Available: `http://ieeexplore.ieee.org/document/6747365/`.

[117] Y. Zhang, Z. Zhao, and K. Chen, “Frequency-Splitting Analysis of Four-Coil Resonant Wireless Power Transfer”, *IEEE Transactions on Industry Applications*, vol. 50, no. 4, pp. 2436–2445, Jul. 2014, ISSN: 0093-9994. DOI: `10.1109/TIA.2013.2295007`. [Online]. Available: `http://ieeexplore.ieee.org/document/6682994/`.

[118] Y.-l. Lyu, F.-y. Meng, G.-h. Yang, B.-j. Che, Q. Wu, L. Sun, D. Erni, and J. L.-w. Li, “A Method of Using Nonidentical Resonant Coils for Frequency Splitting Elimination in Wireless Power Transfer”, *IEEE Transactions on Power Electronics*, vol. 30, no. 11, pp. 6097–6107, Nov. 2015, ISSN: 0885-8993. DOI: `10.1109/TPEL.2014.2387835`. [Online]. Available: `http://ieeexplore.ieee.org/document/7001689/`.

[119] M. Schormans, V. Valente, and A. Demosthenous, “Efficiency optimization of class-D biomedical inductive wireless power transfer systems by means of frequency adjustment”, *Proceedings of the Annual International Conference of the IEEE Engineering in Medicine and Biology Society, EMBS*, vol. 2015-Novem, no. 1, pp. 5473–5476, 2015, ISSN: 1557170X. DOI: `10.1109/EMBC.2015.7319630`.

[120] ——, “Frequency splitting analysis and compensation method for inductive wireless powering of implantable biosensors”, *Sensors*, vol. 16, no. 8, 2016, ISSN: 1424-8220. DOI: `10.3390/s16081229`. [Online]. Available: `http://www.mdpi.com/1424-8220/16/8/1229`.

[121] B. Lee, D. Ahn, and M. Ghovanloo, “Three-Phase Time-Multiplexed Planar Power Transmission to Distributed Implants”, *IEEE Journal of Emerging and Selected Topics in Power Electronics*, vol. 4, no. 1, pp. 263–272, 2016, ISSN: 21686785. DOI: `10.1109/JESTPE.2015.2436391`.

[122] F.-G. Zeng, S. Rebscher, W. Harrison, X. Sun, and H. Feng, “Cochlear implants: System design, integration, and evaluation”, *IEEE Reviews in Biomedical Engineering*, vol. 1, no. dc, pp. 115–142, 2008, ISSN: 1937-3333. DOI: `10.1109/RBME.2008.2008250`. [Online]. Available: `http://ieeexplore.ieee.org/document/4664429/`.

[123] R. Carta and R. Puers, “Wireless power and data transmission for robotic capsule endoscopes”, in *2011 18th IEEE Symposium on Communications and Vehicular Technology in the Benelux (SCVT)*, 2011, pp. 1–6, ISBN: 978-1-4577-1289-0. DOI: `10.1109/SCVT.2011.6101305`. [Online]. Available: `http://ieeexplore.ieee.org/lpdocs/epic03/wrapper.htm?arnumber=6101305`.

[124] M. R. Basar, M. Yazed, J. Cho, and F. Ibrahim, “A Wireless Power Transmission System for Robotic Capsule Endoscopy : Design and Optimization”, no. 1, pp. 2–4, 2014.

[125] Y. Yang, X. Xie, G. Li, Y. Huang, and Z. Wang, “A Combined Transmitting Coil Design for High Efficiency WPT of Endoscopic Capsule”, pp. 97–100, 2015.

[126] K. Bocan and E. Sejdić, “Adaptive Transcutaneous Power Transfer to Implantable Devices: A State of the Art Review”, *Sensors*, vol. 16, no. 3, p. 393, 2016, ISSN: 1424-8220. DOI: `10.3390/s16030393`. [Online]. Available: `http://www.mdpi.com/1424-8220/16/3/393`.

[127] K. Sasaki, S. Sugiura, and H. Iizuka, “Distance adaptation method for magnetic resonance coupling between variable capacitor-loaded parallel-wire coils”, *IEEE Transactions on Microwave Theory and Techniques*, vol. 62, no. 4, pp. 892–900, 2014, ISSN: 00189480. DOI: `10.1109/TMTT.2013.2280130`.

[128] M. Kiani and M. Ghovanloo, “A Closed Loop Wireless Power Transmission System Using a Commercial RFID Transceiver for Biomedical Applications”, in *Annual International Conference of the IEEE EMBS*, 2009, pp. 3841–3844. DOI: `10.1109/IEMBS.2009.5332564`.

[129] R. Jegadeesan and Y.-X. Guo, “Topology Selection and Efficiency Improvement of Inductive Power Links”, *IEEE Transactions on Antennas and Propagation*, vol. 60, no. 10, pp. 4846–4854, Oct. 2012, ISSN: 0018-926X. DOI: `10.1109/TAP.2012.2207325`. [Online]. Available: `http://ieeexplore.ieee.org/document/6236050/`.

[130] M. W. Baker and R. Sarpeshkar, “Feedback Analysis and Design of RF Power Links for Low-Power Bionic Systems”, *IEEE Transactions on Biomedical Circuits and Systems*, vol. 1, no. 1, pp. 28–38, 2007.

[131] Q. Li and Y. C. Liang, “An Inductive Power Transfer System With a High-Q Resonant Tank for Mobile Device Charging”, *IEEE Transactions on Power Electronics*, vol. 30, no. 11, pp. 6203–6212, 2015. DOI: `10.1109/TPEL.2015.2424678`.

[132] P. Aqueveque, M. Saez, J. E. Rodriguez, and E. Pino, “An inductive-link with a regulated secondary voltage based on frequency adjustment”, in *2012 Annual International Conference of the IEEE Engineering in Medicine and Biology Society*, IEEE, Aug. 2012, pp. 1671–1674, ISBN: 978-1-4577-1787-1. DOI: `10.1109/EMBC.2012.6346268`. [Online]. Available: `http://ieeexplore.ieee.org/document/6346268/`.

[133] M. Catrysse, B. Hermans, and R. Puers, “An inductive power system with integrated bi-directional data-transmission”, *Sensors and Actuators A: Physical*, vol. 115, no. 2-3, pp. 221–229, Sep. 2004, ISSN: 09244247. DOI: `10.1016/j.sna.2004.02.016`. [Online]. Available: `http://linkinghub.elsevier.com/retrieve/pii/S0924424704001335`.

[134] M. Kiani and M. Ghovanloo, “An RFID-based closed-loop wireless power transmission system for biomedical applications”, *IEEE Transactions on Circuits and Systems II: Express Briefs*, vol. 57, no. 4, pp. 260–264, 2010, ISSN: 15497747. DOI: `10.1109/TCSII.2010.2043470`.

[135] V. Valente, C. Eder, N. Donaldson, and A. Demosthenous, “A High-Power CMOS Class-D Amplifier for Inductive-Link Medical Transmitters”, *IEEE Transactions on Power Electronics*, vol. 30, no. 8, pp. 4477–4488, 2015.

[136] L. Cheng, W. H. Ki, Y. Lu, and T. S. Yim, “Adaptive On/Off Delay-Compensated Active Rectifiers for Wireless Power Transfer Systems”, *IEEE Journal of Solid-State Circuits*, vol. 51, no. 3, pp. 712–723, 2016, ISSN: 00189200. DOI: `10.1109/JSSC.2016.2517119`.

[137] Y. Lu and W. H. Ki, “A 13.56 MHz CMOS active rectifier with switched-offset and compensated biasing for biomedical wireless power transfer systems”, *IEEE Transactions on Biomedical Circuits and Systems*, vol. 8, no. 3, pp. 334–344, 2014, ISSN: 19324545. DOI: `10.1109/TBCAS.2013.2270177`.

[138] E. Waffenschmidt, "Dynamic Resonant Matching Method for a Wireless Power Transmission Receiver", *IEEE Transactions on Power Electronics*, vol. 30, no. 11, pp. 6070–6077, 2015. DOI: `10.1109/TPEL.2015.2401977`.

[139] *Gnu general public license*, version 3, Free Software Foundation, Jun. 29, 2007. [Online]. Available: `http://www.gnu.org/licenses/gpl.html`.

[140] O. Ozturan, A. Yenigun, E. Senturk, O. F. Calim, F. Aksoy, and S. B. Eren, "Temporal Scalp Thickness, Body Mass Index, and Suprafascial Placement of Receiver Coil of the Cochlear Implant", *Journal of Craniofacial Surgery*, vol. 28, no. 8, e781–e785, Nov. 2017, ISSN: 1049-2275. DOI: `10.1097/SCS.0000000000003999`. [Online]. Available: `http://insights.ovid.com/crossref?an=00001665-201711000-00109`.

[141] X. Li, C. Y. Tsui, and W. H. Ki, "A 13.56 MHz Wireless Power Transfer System With Reconfigurable Resonant Regulating Rectifier and Wireless Power Control for Implantable Medical Devices", *IEEE Journal of Solid-State Circuits*, vol. 50, no. 4, pp. 978–989, 2015, ISSN: 00189200. DOI: `10.1109/JSSC.2014.2387832`.

[142] B Lenaerts, F Peeters, and R Puers, "Closed-loop transductor-compensated class e driver for inductive links", in *TRANSDUCERS and EUROSENSORS '07 - 4th International Conference on Solid-State Sensors, Actuators and Microsystems*, 2007, pp. 65–68.

[143] S. Aldhaher, P. Chi-kwong Luk, and J. F. Whidborne, "Tuning Class E Inverters Applied in Inductive Links Using Saturable Reactors", *IEEE Transactions on Power Electronics*, vol. 29, no. 6, pp. 2969–2978, 2014.

[144] P. Si, A. P. Hu, S. Malpas, and D. Budgett, "A Frequency Control Method for Regulating Wireless Power to Implantable Devices", *IEEE Transactions on Biomedical Circuits and Systems*, vol. 2, no. 1, pp. 22–29, 2008.

[145] B. Lee, M. Kiani, and M. Ghovanloo, "A Triple-Loop Inductive Power Transmission System for Biomedical Applications", *IEEE Transactions on Biomedical Circuits and Systems*, vol. 10, no. 1, pp. 138–148, Feb. 2016, ISSN: 1932-4545. DOI: `10.1109/TBCAS.2014.2376965`. [Online]. Available: `http://ieeexplore.ieee.org/lpdocs/epic03/wrapper.htm?arnumber=7031455http://ieeexplore.ieee.org/document/7031455/`.

[146] M. A. Hannan, H. A. Hussein, S. Mutashar, S. A. Samad, and A. Hussain, "Automatic frequency controller for power amplifiers used in bio-implanted applications: Issues and challenges", *Sensors*, vol. 14, no. 12, pp. 23 843–23 870, 2014, ISSN: 14248220. DOI: `10.3390/s141223843`.

[147] V. Valente, C. Eder, N. Donaldson, and A. Demosthenous, "A High-Power CMOS Class-D Amplifier for Inductive-Link Medical Transmitters", *IEEE Transactions on Power Electronics*, vol. 30, no. 8, pp. 4477–4488, 2014.

[148] V. Valente, C. Eder, A. Demosthenous, and N. Donaldson, “Towards a Closed-Loop Transmitter System with Integrated Class-D Amplifier for Coupling-Insensitive Powering of Implants”, in *Electronics, Circuits and Systems (ICECS), 2012 19th IEEE International Conference on*, 2012, pp. 29–32, ISBN: 9781467312608.

[149] S. Ha, M. L. Khraiche, G. A. Silva, and G. Cauwenberghs, “Direct Inductive Stimulation for Energy-efficient Wireless Neural Interfaces”, in *Annual International Conference of the IEEE EMBS*, 2012, pp. 883–886, ISBN: 9781457717871.

[150] H. Xu, J. Handwerker, and M. Ortmanns, “Telemetry for Implantable Medical Devices”, *IEEE Solid-State Circuits Magazine*, pp. 60–63, 2014.

[151] B. Lenaerts and R. Puers, “An inductive power link for a wireless endoscope.”, *Biosensors & bioelectronics*, vol. 22, no. 7, pp. 1390–5, Feb. 2007, ISSN: 0956-5663. DOI: `10.1016/j.bios.2006.06.015`. [Online]. Available: `http://www.ncbi.nlm.nih.gov/pubmed/16904885`.

[152] B. Lee, D. Ahn, and M. Ghovanloo, “Three-Phase Time-Multiplexed Planar Power Transmission to Distributed Implants”, *IEEE Journal of Emerging and Selected Topics in Power Electronics*, pp. 1–1, 2015, ISSN: 2168-6777. DOI: `10.1109/JESTPE.2015.2436391`. [Online]. Available: `http://ieeexplore.ieee.org/lpdocs/epic03/wrapper.htm?arnumber=7111213`.

[153] B. Lenaerts, F. Peeters, and R. Puers, “Closed-loop transductor-compensated class e driver for inductive links”, in *TRANSDUCERS and EUROSENSORS ’07 - 4th International Conference on Solid-State Sensors, Actuators and Microsystems*, 2007, pp. 65–68, ISBN: 1-4244-0841-5. DOI: `10.1109/SENSOR.2007.4300072`.

[154] M. Schormans, V. Valente, and A. Demosthenous, “A low-power, wireless, capacitive sensing frontend based on a self-oscillating inductive link”, *Circuits and Systems I: Regular Papers, IEEE Transactions on*, vol. 65, no. 9, pp. 2645–2656, Jul. 2018. DOI: `10.1109/TCSI.2018.2835148`.

[155] E. L. Tan, W. N. Ng, R. Shao, B. D. Pereles, and K. G. Ong, “A Wireless, Passive Sensor for Quantifying Packaged Food Quality”, *Sensors*, vol. 7, no. 9, pp. 1747–1756, 2007, ISSN: 1424-8220. DOI: `10.3390/s7091747`. [Online]. Available: `http://www.mdpi.com/1424-8220/7/9/1747/`.

[156] K. G. Ong and C. A. Grimes, “A resonant printed-circuit sensor for remote query monitoring of environmental parameters”, *Smart Materials and Structures*, vol. 9, no. 4, p. 421, 2000.

[157] H. Y. Lee, B. Choi, S. Kim, S. J. Kim, W. J. Bae, and S. W. Kim, “Sensitivity-Enhanced LC Pressure Sensor for Wireless Bladder Pressure Monitoring”, *IEEE Sensors Journal*, vol. 16, no. 12, pp. 4715–4724, 2016, ISSN: 1530437X. DOI: `10.1109/JSEN.2016.2533262`.

[158] C. Zhang, L. F. Wang, J. Q. Huang, and Q. A. Huang, “An LC-type passive wireless humidity sensor system with portable telemetry unit”, *Journal of Microelectromechanical Systems*, vol. 24, no. 3, pp. 575–581, 2015, ISSN: 10577157. DOI: `10.1109/JMEMS.2014.2333747`.

[159] F. Chen, F. Lim, O. Abari, A. Chandrakasan, and V. Stojanovic, “Energy-aware design of compressed sensing systems for wireless sensors under performance and reliability constraints”, *IEEE Transactions on Circuits and Systems I: Regular Papers*, vol. 60, no. 3, pp. 650–661, Mar. 2013, ISSN: 1549-8328. DOI: `10.1109/TCSI.2012.2215738`.

[160] Y. P. Lin, C. Y. Yeh, P. Y. Huang, Z. Y. Wang, H. H. Cheng, Y. T. Li, C. F. Chuang, P. C. Huang, K. T. Tang, H. P. Ma, Y. C. Chang, S. R. Yeh, and H. Chen, “A Battery-Less, Implantable Neuro-Electronic Interface for Studying the Mechanisms of Deep Brain Stimulation in Rat Models”, *IEEE Transactions on Biomedical Circuits and Systems*, vol. 10, no. 1, pp. 98–112, 2016, ISSN: 19324545. DOI: `10.1109/TBCAS.2015.2403282`.

[161] J. V. Ham, I. E. Naert, and R. Puers, “Design and packaging of a fully autonomous medical monitoring system for dental applications”, *IEEE Transactions on Circuits and Systems I: Regular Papers*, vol. 54, no. 1, pp. 200–208, Jan. 2007, ISSN: 1549-8328. DOI: `10.1109/TCSI.2006.886791`.

[162] M. H. Ghaed, G. Chen, R. u. Haque, M. Wieckowski, Y. Kim, G. Kim, Y. Lee, I. Lee, D. Fick, D. Kim, M. Seok, K. D. Wise, D. Blaauw, and D. Sylvester, “Circuits for a cubic-millimeter energy-autonomous wireless intraocular pressure monitor”, *IEEE Transactions on Circuits and Systems I: Regular Papers*, vol. 60, no. 12, pp. 3152–3162, Dec. 2013, ISSN: 1549-8328. DOI: `10.1109/TCSI.2013.2265973`.

[163] F. Wang, X. Zhang, M. Shokoueinejad, B. J. Iskandar, J. E. Medow, and J. G. Webster, “A Novel Intracranial Pressure Readout Circuit for Passive Wireless LC Sensor”, *IEEE Transactions on Biomedical Circuits and Systems*, vol. 11, no. 5, pp. 1123–1132, Oct. 2017, ISSN: 1932-4545. DOI: `10.1109/TBCAS.2017.2731370`. [Online]. Available: `http://ieeexplore.ieee.org/document/8010343/`.

[164] M. Nowak, N. Delorme, F. Conseil, and G. Jacquemod, “A novel architecture for remote interrogation of wireless battery-free capacitive sensors”, *Proceedings of the IEEE International Conference on Electronics, Circuits, and Systems*, pp. 1236–1239, 2006. DOI: `10.1109/ICECS.2006.379685`.

[165] R. Huang, B. Zhang, D. Qiu, and Y. Zhang, “Frequency splitting phenomena of magnetic resonant coupling wireless power transfer”, *IEEE Transactions on Magnetics*, vol. 50, no. 11, 2014, ISSN: 00189464. DOI: `10.1109/TMAG.2014.2331143`.

[166] (). CoCalc - Collaborative Calculation in the Cloud, [Online]. Available: `https://cocalc.com`.

[167] R. Bartnikas, “Dielectric Losses in Solid-Liquid Insulating Systems—Part I”, *IEEE Transactions on Electrical Insulation*, vol. EI-5, no. 4, pp. 113–121, 1970, ISSN: 00189367. DOI: `10.1109/TEI.1970.299119`.

[168] J. B. Whitehead, “Liquid insulators”, *Transactions of The Electrochemical Society*, vol. 65, no. 1, pp. 35–46, 1934. DOI: `10.1149/1.3498042`. eprint: `http://jes.ecsdl.org/content/65/1/35.full.pdf+html`.

[169] C. G. Garton, “Dielectric loss in thin films of insulating liquids”, *Journal of the Institution of Electrical Engineers - Part III: Communication Engineering, including the Proceedings of the Wireless Section of the Institution*, vol. 88, no. 1, pp. 23–40, Mar. 1941. DOI: `10.1049/ji-3-1.1941.0006`.

[170] C. Eder, V. Valente, N. Donaldson, and A. Demosthenous, “A CMOS smart temperature and humidity sensor with combined readout”, *Sensors*, vol. 14, no. 9, pp. 17 192–17 211, 2014, ISSN: 14248220. DOI: `10.3390/s140917192`.

[171] A. Tripathy, S. Pramanik, A. Manna, S. Bhuyan, N. F. Azrin Shah, Z. Radzi, and N. A. Abu Osman, “Design and development for capacitive humidity sensor applications of lead-free ca,mg,fe,ti-oxides-based electro-ceramics with improved sensing properties via physisorption”, *Sensors*, vol. 16, no. 7, 2016, ISSN: 1424-8220. DOI: `10.3390/s16071135`. [Online]. Available: `http://www.mdpi.com/1424-8220/16/7/1135`.

[172] R. Akram, “Frequency dependence of electrical parameters of an organic-inorganic hybrid composite based humidity sensor”, *Electronics*, vol. 5, no. 2, 2016, ISSN: 2079-9292. DOI: `10.3390/electronics5020023`. [Online]. Available: `http://www.mdpi.com/2079-9292/5/2/23`.

[173] J. Groszkowski, *Frequency of Self-Oscillations*. Macmillan, 1964.

[174] D. Ahn and S. Hong, “Wireless power transmission with self-regulated output voltage for biomedical implant”, *IEEE Transactions on Industrial Electronics*, vol. 61, no. 5, pp. 2225–2235, 2014, ISSN: 02780046. DOI: `10.1109/TIE.2013.2273472`.

[175] D. Jiang, D. Cirmirakis, M. Schormans, T. A. Perkins, N. Donaldson, and A. Demosthenous, “An Integrated Passive Phase-Shift Keying Modulator for Biomedical Implants with Power Telemetry over a Single Inductive Link”, *IEEE Transactions on Biomedical Circuits and Systems*, vol. 11, no. 1, pp. 64–77, 2017, ISSN: 19324545. DOI: `10.1109/TBCAS.2016.2580513`.

[176] U. Bihr, T. Liu, M. Ortmanns, H. Xu, and J. Handwerker, “Telemetry for Implantable Medical Devices”, *IEEE Solid-State Circuits Magazine*, pp. 47–51, 2014.

[177] F. Inanlou and M. Ghovanloo, “Wideband near-field data transmission using pulse harmonic modulation”, *IEEE Transactions on Circuits and Systems I: Regular Papers*, vol. 58, no. 1, pp. 186–195, 2011, ISSN: 15498328. DOI: `10.1109/TCSI.2010.2055351`.

[178] M. Kiani and M. Ghovanloo, "A 20-Mb / s Pulse Harmonic Modulation Transceiver for Wideband Near-Field Data Transmission", *IEEE Transactions on Circuits and Systems II: Express Briefs*, vol. 60, no. 7, pp. 382–386, 2013. DOI: `10.1109/TCSII.2013.2261182`.

[179] G. Simard, M. Sawan, and D. Massicotte, "High-speed OQPSK and efficient power transfer through inductive link for biomedical implants", *IEEE Transactions on Biomedical Circuits and Systems*, vol. 4, no. 3, pp. 192–200, 2010.

[180] *NEUwalk Project*, 2014. [Online]. Available: `neuwalk.eu`.

[181] (2016). Neuwalk research project: New hope for paraplegic patients, [Online]. Available: `https://ec.europa.eu/digital-single-market/en/news/neuwalk-research-project-new-hope-paraplegic-patients`.

[182] E. B. Wilson, "Probable inference, the law of succession, and statistical inference", *Journal of the American Statistical Association*, vol. 22, no. 158, pp. 209–212, 1927. DOI: `10.1080/01621459.1927.10502953`.

[183] M. Schormans, V. Valente, and A. Demosthenous, "Single-pulse harmonic modulation for short range biomedical inductive data transfer", in *Biomedical Circuits and Systems Conference (BioCAS), 2017 IEEE*, IEEE, 2017, pp. 1–4.

[184] C. M. Lopez, A. Andrei, S. Mitra, M. Welkenhuysen, W. Eberle, C. Bartic, R. Puers, R. F. Yazicioglu, and G. G. E. Gielen, "An implantable 455-active-electrode 52-channel CMOS neural probe", *IEEE Journal of Solid-State Circuits*, vol. 49, no. 1, pp. 248–261, 2014, ISSN: 00189200. DOI: `10.1109/JSSC.2013.2284347`.

[185] R. A. Normann, P. K. Campbell, and K. E. Jones, *Three-dimensional electrode device*, US Patent 5,215,088, Jun. 1993.

[186] L. Sun, R. K. Sheshadri, W. Zheng, and D. Koutsonikolas, "Modeling wifi active power/energy consumption in smartphones", in *Distributed Computing Systems (ICDCS), 2014 IEEE 34th International Conference on*, IEEE, 2014, pp. 41–51.

[187] R. Kitchen, *RF and microwave radiation safety handbook*. Newnes, 2001.

[188] M. Z. Win and R. A. Scholtz, "Impulse radio: How it works", *IEEE Communications letters*, vol. 2, no. 2, pp. 36–38, 1998.

[189] S. Guo and H. Lee, "An efficiency-enhanced CMOS rectifier with unbalanced-biased comparators for transcutaneous-powered high-current implants", *IEEE Journal of Solid-State Circuits*, vol. 44, no. 6, pp. 1796–1804, 2009, ISSN: 00189200. DOI: `10.1109/JSSC.2009.2020195`.

[190] B. Razavi, *Design of Analog CMOS Integrated Circuits*. McGraw-Hill, 2005.

[191] T. F. C. Commission. (2015). Code of federal regulations: Title 47: Part 15, [Online]. Available: `https://www.govinfo.gov/content/pkg/CFR-2015-title47-vol1/pdf/CFR-2015-title47-vol1-part15.pdf`.

[192] S. Lee, K. Song, J. Yoo, and H. J. Yoo, “A low-energy inductive coupling transceiver with Cm-Range 50-Mbps data communication in mobile device applications”, *IEEE Journal of Solid-State Circuits*, vol. 45, no. 11, pp. 2366–2374, 2010, ISSN: 00189200. DOI: `10.1109/JSSC.2010.2065850`.

[193] S. Mandal and R. Sarpeshkar, “Power-efficient impedance-modulation wireless data links for biomedical implants”, *IEEE Transactions on Biomedical Circuits and Systems*, vol. 2, no. 4, pp. 301–315, 2008.

[194] M. Schormans, V. Valente, and A. Demosthenous, “Intermittent excitation of high-q resonators for low-power high-speed clock generation”, in *2018 IEEE International Symposium on Circuits and Systems (ISCAS)*, IEEE, 2018, pp. 1–4.

[195] B. D. W. Knight, *The self-resonance and self-capacitance of solenoid coils The self-resonance and self-capacitance of solenoid coils*, May. 2010, vol. 01, pp. 1–29, ISBN: 0486495779. DOI: `10.13140/RG.2.1.1472.0887`.

[196] M. Motoyoshi, “Through-silicon via (tsv)”, *Proceedings of the IEEE*, vol. 97, no. 1, pp. 43–48, 2009.

[197] A. Kosuge, J. Hashiba, T. Kawajiri, S. Hasegawa, T. Shidei, H. Ishikuro, T. Kuroda, and K. Takeuchi, “An inductively powered wireless solid-state drive system with merged error correction of high-speed wireless data links and nand flash memories”, *IEEE Journal of Solid-State Circuits*, vol. 51, no. 4, pp. 1041–1050, 2016.